

# THE BELL SYSTEM

## *Technical Journal*

DEVOTED TO THE SCIENTIFIC AND ENGINEERING  
ASPECTS OF ELECTRICAL COMMUNICATION

---

VOLUME XXXVII

JULY 1958

NUMBER 4

---

Transmission Characteristics of a Three-Conductor Coaxial Transmission Line with Transpositions

G. RAISBECK AND J. M. MANLEY 835

Synthesis of Series-Parallel Network Switching Functions

WARREN SEMON 877

Circular Waveguide Taper of Improved Design

HANS-GEORG UNGER 899

The Nonuniform Transmission Line as a Broadband Termination

IRA JACOBS 913

Using Contact Resistance to Measure Adsorption of Gases on Metals

P. KIELIUK 925

Shot Noise in p-n Junction Frequency Converters

A. UHLIR, JR. 951

Gain and Noise Figure of a Variable-Capacitance Up-Converter

D. LÉENOV 989

Nonstationary Velocity Estimation

T. M. BURFORD 1009

Amplitude Modulation Suppression in FM Systems

C. L. RUTHROFF 1023

Oxide Semiconductors with Partially Filled 3d Levels

F. S. MORIN 1047

---

Recent Bell System Monographs

1085

Contributors to This Issue

1088

## THE BELL SYSTEM TECHNICAL JOURNAL

### ADVISORY BOARD

A. B. GOETZ, *President, Western Electric Company*

M. J. KELLY, *President, Bell Telephone Laboratories*

E. J. McNEELY, *Executive Vice President, American Telephone and Telegraph Company*

### EDITORIAL COMMITTEE

B. McMILLAN, *Chairman*

S. E. BRILLHART

A. J. BUSCH

L. R. COOK

A. C. DICKIESON

R. L. DIETSOLD

E. E. GOULD

E. I. GREEN

H. K. HONAMAN

R. B. HOUGH

J. R. PIERCE

### EDITORIAL STAFF

W. D. BULLOCH, *Editor*

C. POLOGE, *Production Editor*

J. T. MYSAK, *Technical Illustrations*

T. H. POPE, *Circulation Manager*

THE BELL SYSTEM TECHNICAL JOURNAL is published six times a year by the American Telephone and Telegraph Company, 195 Broadway, New York 7, N. Y. F. R. Kappel, President; S. Whitney Landon, Secretary; John J. Scanlon, Treasurer. Subscriptions are accepted at \$5.00 per year. Single copies \$1.35 each. Foreign postage is 65 cents per year or 11 cents per copy. Printed in U.S.A.



# THE BELL SYSTEM TECHNICAL JOURNAL

---

VOLUME XXXVII

JULY 1958

NUMBER 4

---

*Copyright 1958, American Telephone and Telegraph Company*

## Transmission Characteristics of a Three-Conductor Coaxial Transmission Line with Transpositions

By G. RAISBECK and J. M. MANLEY

(Manuscript received October 30, 1957)

*This paper describes in detail the manufacture of, measurements on, and computations about a three-conductor coaxial cable with transpositions. By reducing skin-effect losses in the central conductor, this three-conductor line achieves 17 per cent lower attenuation at a particular frequency than does a two-conductor line of the same outer diameter. The matrix method used for analysis can easily be extended to n-conductor lines. Suggestions for making improved three-conductor coaxial lines are made.*

### I. SUMMARY

Most of the loss in a simple coaxial cable is due to series resistance in the center conductor. At high frequencies this resistance is aggravated by the skin effect, which causes conduction currents to concentrate in a thin layer on the surface of the conductor. Because of the skin effect, the effective cross-sectional area of a conductor is smaller than its geometric cross section at high frequencies.

The effective cross section of the center conductor of a new coaxial line has been increased by dividing the conductor into two parts, a solid central member and a concentric thin shell insulated from the center member. Over a certain range of frequencies, conduction currents are distributed throughout the whole thickness of the thin cylindrical shell

and a layer one skin-depth thick on the surface of the solid center member.

The total current in the composite center conductor is divided into two components, one flowing in the solid center member and one flowing in the thin cylindrical shell. The effective resistance of the composite center conductor is less than that of a solid conductor only when these two current components are approximately equal both in phase and in magnitude, and then only over a limited frequency range. The desired division of current has been achieved by electrical transposition of the two parts of the inner conductor at intervals of less than one-eighth of a wavelength.

Several thousand feet of such a three-conductor transmission line have been constructed with transpositions at various intervals. Detailed measurements and calculations have been made, and the three-conductor cable has been compared directly with a similarly constructed conventional two-conductor cable. The three-conductor cable has lower attenuation than the two-conductor cable at frequencies between 1 and 10 mc with transpositions 9 feet apart or less. Near 4 mc, the three-conductor cable has 17 per cent less attenuation than does the two-conductor cable. The agreement between measurements and computations is excellent. The improvement in the three-conductor cable can be increased to 25 per cent by changing the relative dimensions of the parts of the center conductor, and the frequency range over which it surpasses a two-conductor cable can be increased thereby to 20:1.

## II. BACKGROUND

### 2.1 *Introduction*

A transmission line with three parallel conductors can support two modes of transmission at low frequency.<sup>1</sup> Each mode has a well-defined phase velocity and attenuation at every frequency. It might be assumed that the transmission losses on such a line are minimized if power is transmitted only in the mode having the lower attenuation. If the line is sufficiently long, this is true; but for short sections of line it is not. The losses in a short section of line may be reduced, under some circumstances, by a judicious combination of pure modes.

The reason why the losses may be smaller for a combination of pure modes than for any of the modes separately depends on constructive and destructive interference. If two pure modes propagate with different wave velocities, the currents which they induce in the conductors will

be successively in phase, out of phase, in phase again, and so on. When the currents are in phase, the losses are greater than when the currents are out of phase. Over a long length of line, the phases will pass through many cycles, and the amount of power lost will average out to be the same as if the pure modes were propagated independently.

If two modes are propagated over a short length of line so that there is substantial cancellation of currents, the losses will be reduced *so long as the currents do cancel substantially*. When the differential phase shift between modes begins to be appreciable, it will be necessary to terminate the line, draw off the power and launch it in a new length of line. If this is not done, the reduction in losses will be offset precisely by an increase in losses when the currents of the two modes become in phase.

This phenomenon can be used to combat losses due to skin effect in a coaxial line. In a simple coaxial line, most of the effective resistance of the line is in the center conductor. This effective resistance can be reduced if the center conductor is replaced by a smaller center conductor surrounded by a thin coaxial tubular conductor, provided the magnitudes and phases of the currents in these two inner conductors bear the right relation. As will be shown, this can be accomplished by transposing the two parts of the center conductor, which is equivalent to the process described in the previous paragraph.

The problem of losses in a three-conductor transmission line has much in common with that of losses in a two-conductor line that has standing waves. The three-conductor line has four waves, one forward and one backward in each distinct mode of propagation, and these four waves may beat in various forms of destructive and constructive interference. In order to get an intuitive grasp of the performance of such a line, it is convenient to subdivide the problem into two parts: finding the loss in the line for a given distribution of currents, and determining how the current distribution which yields the lowest losses for a given power transfer can be attained. The answer to the first question tells how much a coaxial line can be improved; the answer to the second tells how to do it.

## 2.2 Losses in a Three-Conductor Coaxial Having a Given Current Distribution

In the next section an accurate calculation of properties of a three-conductor coaxial will be made. But a good idea of how much the loss may be reduced in this kind of line, under the proper conditions, may be obtained by assuming a simple model for the line, as shown in Fig. 1, and also assuming that the currents in the three conductors are known.

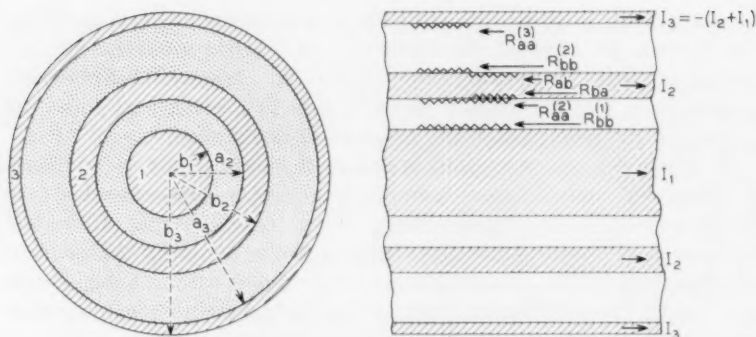


Fig. 1 — Three-conductor coaxial transmission line: cross section and schematic longitudinal section showing surface resistance.

The loss in such a line is given approximately by

$$L = \frac{1}{2} |I_1|^2 R_{bb}^{(1)} + \frac{1}{2} [ |I_1|^2 R_{aa}^{(2)} + (I_1 \bar{I}_3 + \bar{I}_1 I_3) R_{ab}^{(2)} + |I_3|^2 R_{bb}^{(2)} ] + \frac{1}{2} |I_3|^2 R_{aa}^{(3)},$$

where  $I_1$  and  $I_3$  are the current amplitudes in the inner and outer conductors respectively and the resistances are the surface resistances calculated from formulas (83) in Schelkunoff's paper<sup>2</sup> on cylindrical transmission lines.\* The superscripts in parentheses refer to the particular conductor being considered;  $R_{aa}$  is the resistance of the inner surface of a tube per unit length to current which is returned entirely inside the surface,  $R_{bb}$  is the resistance of an outer surface of a tube per unit length to current which is returned entirely outside the surface and  $R_{ab}$  is the transfer resistance from one surface of a tube to the other.

Of the five terms in the equation above, the first is the ohmic loss in the center conductor. The second, third and fourth terms are the loss in the intermediate conductor. The resistances  $R_{aa}$ ,  $R_{ab}$  and  $R_{bb}$  are real functions.

It is obvious that only one of the five loss terms depends on the relative phases of  $I_1$  and  $I_3$ . This is the third term, which contains the factor

$$(I_1 \bar{I}_3 + \bar{I}_1 I_3) = 2 |I_1| |I_3| \cos \theta,$$

\* The reader should note that the first-order correction terms in Schelkunoff's formulas (82) are in error; formulas (75), from which they were derived, are correct. Briefly,  $Z_{aa}$ ,  $Z_{ab}$ ,  $Z_{ba}$  and  $Z_{bb}$  are the ratios of longitudinal electric field strength on the inner or the outer surface of a tubular conductor to the part of the total current returning either inside or outside the tube. The real parts are denoted by  $R$  with the same subscripts. For details, see Ref. 2, pp. 554-558.

where  $\theta$  is the phase difference between  $I_1$  and  $I_3$ . Any reduction in losses depends on having  $R_{ab}$  large and choosing  $I_1$  and  $I_3$  so that the term containing  $R_{ab}$  is negative.

These theoretical calculations show that the losses in a coaxial transmission line can be reduced by using a third conductor. Suppose, for example, that the skin depth, the thickness of the inner dielectric layer and the thickness of the intermediate conductor, are all small relative to the radius of the center conductor. Then the various loss formulas are simplified and it is easy to compare the losses in the two innermost conductors with the loss in a solid conductor of the same over-all dimensions. This comparison is made in Fig. 2. Here, the dotted and dashed curves show the resistances of the two conductors compared to the resistance of a single solid conductor. For the dotted curve, the distribution of currents is chosen to minimize the resistance. The required distribution is shown in the solid curve, which gives the best ratio  $I_3/I_1$ . The dashed curve shows the relative resistance if the current is divided equally in the two inner conductors. In either case, the resistance may be reduced to 65 per cent of that of a solid wire for a particular frequency.

In a normal coaxial line 78 per cent of the effective resistance is in the

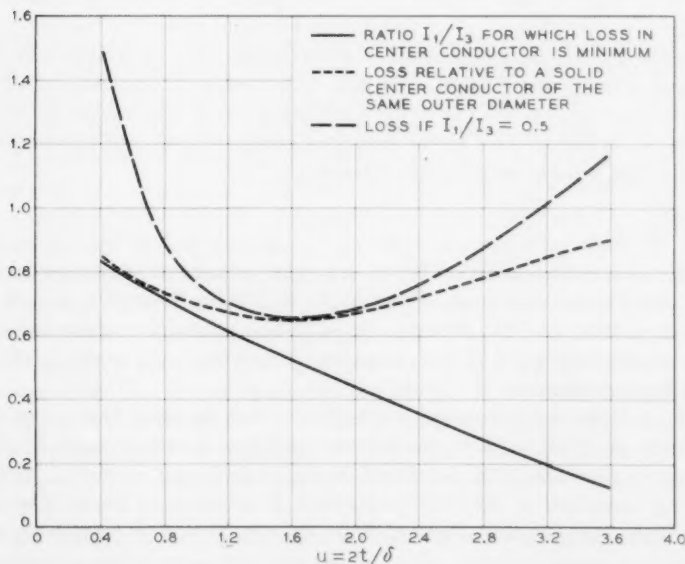


Fig. 2 — Comparison of losses in simple and compound center conductors for certain current distributions.



center conductor and 22 per cent is in the outer conductor. When the center conductor resistance is reduced 35 per cent, the attenuation is reduced not 35 per cent but roughly  $78 \text{ per cent} \times 35 \text{ per cent} = 27 \text{ per cent}$ .

From the curves of Fig. 2 we can conclude that, if the current in a suitably proportioned three-conductor coaxial line can be distributed so that the two innermost conductors carry equal currents, at one particular frequency the attenuation can be reduced to 73 per cent of the attenuation of a two-conductor coaxial line of the same over-all dimensions and made of the same materials. The attenuation of the three-conductor line will be less than that of the two-conductor line over a 20:1 range of frequencies, but at extremely low or extremely high frequencies it will have higher attenuation.

### 2.3 *How Can the Desired Current Distribution Be Achieved?*

The previous section shows that a coaxial transmission line having three conductors, the two innermost of which are very close together, will have lower losses than a conventional coaxial cable if the currents in the two innermost conductors are approximately equal. Two independent ways to achieve this equal division of current have been suggested. One way\* is to alter the dimensions and dielectric constants so that the line has a natural mode of propagation with approximately the desired current distribution. The other proposal is to transpose conductors in the manner of a litz wire to get the desired distribution by brute force, so to speak. This paper describes computations and experiments with a line having such transpositions.

### 2.4 *History*

The idea of transposition between a solid cylindrical conductor and a concentric tube is at least as old as U. S. Patent 1,088,902, issued on March 3, 1914, to P. V. Hunter. Fig. 4 of that patent shows a transposition similar to Fig. 15 of the present text, and the exact wording of the specification states:

*"If it is desired to arrange the feeders so that the leads have equal impedance, the cable may be divided into an even number of equal lengths, the inner conductor a of one length being, as indicated in Fig. 4 [of the patent] connected to the other conductor b of the adjacent length. This arrangement also prevents alteration to the division of current between the two leads by unequal inductive effects on the two leads of currents in adjacent feeders or earth."*

\* Proposed by H. S. Black and S. P. Morgan, Jr.

Hunter was concerned with power distribution systems. The increase in resistance at high frequency resulting from the skin effect is not mentioned in his patent. This is reasonable, for at a frequency of 50 cycles per second the increase in resistance of a copper conductor even as large as one-half inch in diameter is only 0.34 per cent. One can easily understand, therefore, why Hunter did not apply his technique to the reduction of skin resistance.

Later, when the nonuniformity of current distribution at high frequencies became a matter of concern, stranded conductors<sup>3,4,5</sup> were used rather than transposed coaxial cylinders. At frequencies below one megacycle per second, stranded conductors may be quite advantageous. Above that frequency, the fineness and large number of the strands required makes the technique less rewarding.

The work reported in this paper stems from a systematic search for ways to combat skin and proximity effects. The beginning of this search was stimulated largely by W. H. Doherty during his tenure as Director of Research-Electrical Communications at Bell Telephone Laboratories.

### 2.5 *Early Experimental Results*

The first three-conductor coaxial line with transpositions was made with a center conductor devised by W. McMahon and fabricated by him and G. R. Johnson as shown in Fig. 3. Starting with a bare wire 30 mils in diameter, flat sections 8 in. long, 120 mils wide and 5 mils thick were formed at regular intervals along the wire so that they were separated by a length slightly greater than 8 in. This was done by placing the wire on a hardened steel plate and passing the plate and wire through a rolling mill. The flat sections were then formed into channels in a simple die. Then the round sections of the wire were insulated with a wrapping of plastic tape. Finally, two such conductors were placed side by side so that the flat sections (now channels) of one were matched with the round sections of the other, as shown in the figure. The round sections were laid in the channels, and the whole structure was passed through a die of diameter such that it caused the flat sections to be wrapped completely around the insulated round sections. Thus, the conductors alternate as inner and outer conductors along the line, as shown in the figure.

Resistances measured at various frequencies were compared with computations based on the approximate formulas of Section 2.2, which were, at that time, the best available. The results are shown in Figs. 4, 5 and 6. While the correspondence between the measured and computed

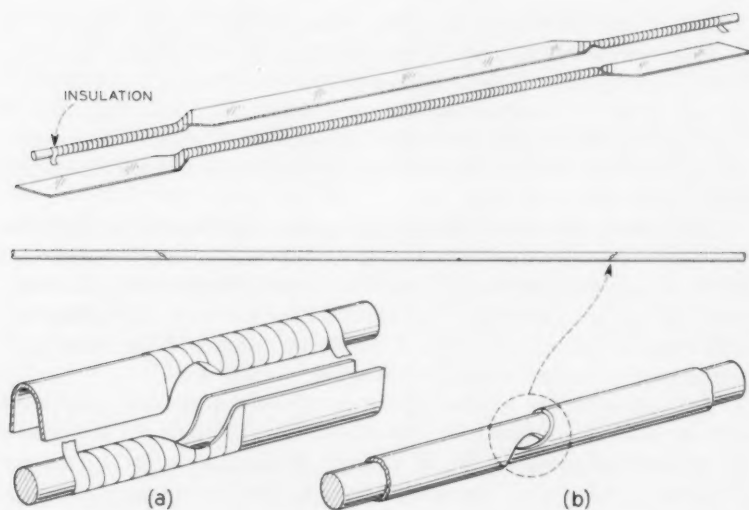


Fig. 3 — Method suggested by W. McMahon for making a transposed compound conductor.

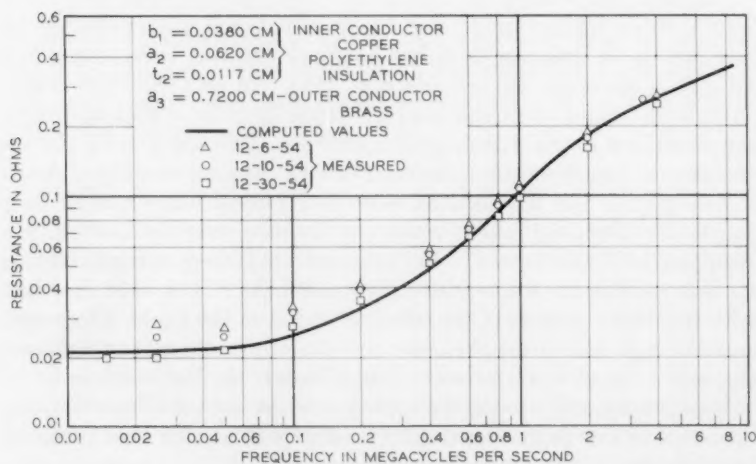


Fig. 4 — Effective resistance of a 1-meter length of coaxial line with a transposed copper center conductor.

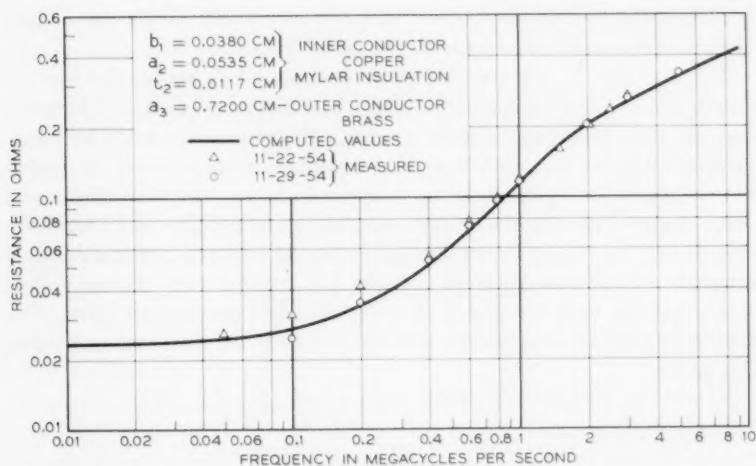


Fig. 5 — Effective resistance of a 1-meter length of coaxial line with a transposed copper center conductor of different size.

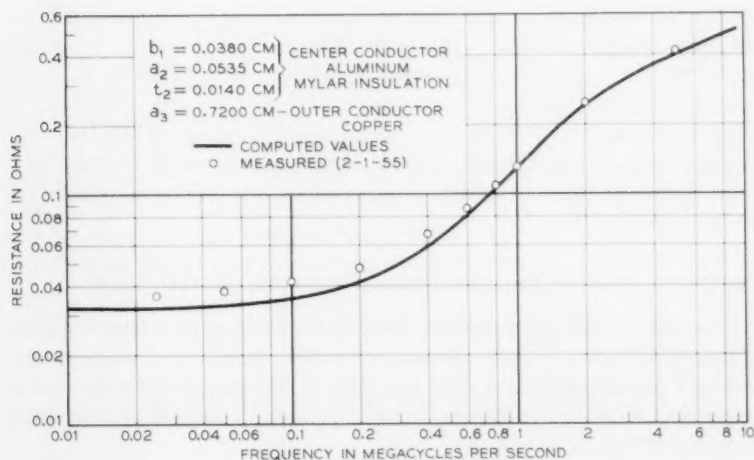


Fig. 6 — Effective resistance of a 1-meter length of coaxial line with a transposed aluminum center conductor.

values is not perfect, it is clear that the computed curves are a good qualitative approximation to the measured values.

At that time, it was decided to make a long test sample for further measurement. The experimental length was chosen so that: (1) different transposition intervals could be studied, (2) attenuation could be measured directly in a straight-through transmission measurement, (3) termination effects would be small in comparison to transmission effects and (4) a control experiment on a two-conductor coaxial line could be easily carried out. As this cable was being fabricated and measured, a detailed analysis and computation procedure was worked out. Actually, the measurements were completed six months before the computations. The results of this last experiment and computation are the main subject of this paper.

### 2.6 *Plan of the Paper*

Following this introduction, we shall make a thorough analysis of the three-conductor transposed line. In Section III, the propagation properties of a uniform three-conductor line are expressed in matrix form. In Section IV, a unit of transposed line, made by combining two equal lengths of this uniform line and a transposition, is described. A cascade of these units is then analyzed as a periodic transmission medium to find its new traveling waves and propagation constants. In general, the expressions are complicated and numerical analysis is necessary to obtain useful results. However, if the spacing between transpositions becomes very small, quite tractable forms appear. Further, an approximation to these forms yields a very simple understandable picture of the behavior of these lines. Following this, Section V is a description of experimental work and final results. Details of calculation and tables of results are given in Section VI.

## III. PROPAGATION IN UNIFORM THREE-CONDUCTOR COAXIAL LINES

Consider the line with transpositions to be made up of a large number of equivalent sections each containing a certain length  $2l$  of transmission line and one transposition. For the sake of preserving symmetry, it is convenient to place the transposition in the center, flanked by two equal lengths  $l$  of line, as in Fig. 7.

It is convenient to use matrix notation to describe the transformation of voltages and currents from one end of each of these elements to the other because the matrix of the transformation of any number of linear networks in cascade is simply the product of the matrices of the individ-



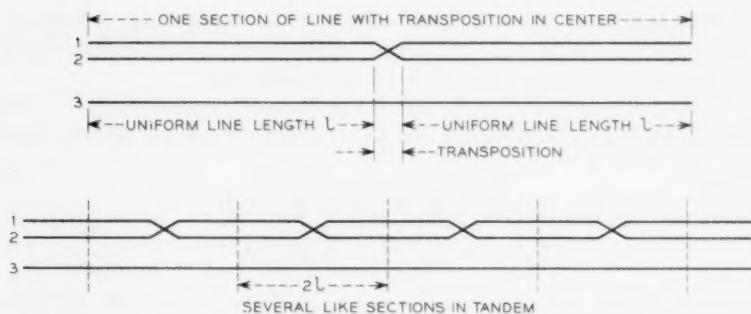


Fig. 7 — Schematic representation of a three-conductor transmission line with several transpositions.

ual transformations, even though the individual networks are not identical (Ref. 6, p. 337).

First, we will obtain a suitable matrix for the length  $l$  of uniform line, starting from the differential equations. Carson and Gilbert<sup>1</sup> and Schelkunoff<sup>2</sup> have shown how to derive a first integral of Maxwell's equations for a structure consisting of uniform concentric cylinders and shells. For the purpose of studying three-conductor coaxial lines it is only necessary to adapt Schelkunoff's general results to the specific case at hand.

Suppose the cross section of the transmission line is as shown in Fig. 1. Let the conductors be numbered, from the innermost out, 1, 2 and 3. Let the currents in the several conductors be  $i_1 e^{j\omega t}$ ,  $i_2 e^{j\omega t}$  and  $i_3 e^{j\omega t}$ . Note that small letters are used instead of the capital letters used before, and that the dependence on longitudinal distance  $x$  is included. Let the voltages of the various conductors be  $v_1 e^{j\omega t}$ ,  $v_2 e^{j\omega t}$  and  $v_3 e^{j\omega t}$ . To avoid ambiguity, we may suppose that voltages are measured radially inward from the outermost conductor. It follows that  $i_3 = -i_1 - i_2$  and  $v_3 = 0$ , and we can eliminate  $i_3$  and  $v_3$  when desirable.

Following Schelkunoff, in analogy to his equation (52), we can find

$$\frac{j\omega\mu i_1}{2\pi} \log \frac{a_2}{b_1} = E_x(a_2) - E_x(b_1) - \frac{\partial}{\partial x} (v_2 - v_1), \quad (1)$$

$$\frac{j\omega\mu(i_1 + i_2)}{2\pi} \log \frac{a_3}{b_2} = E_x(a_3) - E_x(b_2) - \frac{\partial}{\partial x} (v_3 - v_2),$$

$$v_2 - v_1 = -\frac{1}{2\pi(g + j\omega\epsilon)} \log \frac{a_2}{b_1} \frac{\partial i_1}{\partial x}, \quad (2)$$

$$v_3 - v_2 = -\frac{1}{2\pi(g + j\omega\epsilon)} \log \frac{a_3}{b_2} \frac{\partial}{\partial x} (i_1 + i_2).$$

Here  $a_n$  and  $b_n$  are the inside and outside radii, respectively, of conducting shell  $n$ , and  $E_x(a_n)$ ,  $E_x(b_n)$  are the longitudinal electric field strengths at the inner and outer surfaces of the  $n$ th conductor.

To these equations must be added Schelkunoff's equation (74) (modified appropriately in notation) for determining the surface electric fields  $E_x$ :

$$\begin{aligned} E_x(a_n) &= Z_{aa}^{(n)} I_a^{(n)} + Z_{ab}^{(n)} I_b^{(n)}, \\ E_x(b_n) &= Z_{ba}^{(n)} I_a^{(n)} + Z_{bb}^{(n)} I_b^{(n)}, \end{aligned} \quad (3)$$

where  $I_a^{(n)}$  and  $I_b^{(n)}$  are the parts of  $i_n$  which flow back inside and outside the  $n$ th conductor and the  $Z$ 's are the artificial surface impedances,\* the resistances of which were used above. We see from Fig. 1 that

$$\begin{aligned} I_a^{(n)} + I_b^{(n)} &= i_n, \\ I_a^{(n)} &= -\sum_1^{n-1} i_n, \\ I_b^{(n)} &= -\sum_{n+1}^{\infty} i_n = \sum_1^n i_n = -I_a^{(n+1)}, \\ I_a^{(1)} &= 0. \end{aligned} \quad (4)$$

The terms on the left of the first two equations (1) above are the inductive reactance voltages resulting from the magnetic field between conductors. To simplify the writing, let  $X_{a1}$  and  $X_{a2}$  be these reactances so that

$$\begin{aligned} \frac{\omega\mu}{2\pi} \log \frac{a_2}{b_1} &= X_{a1}, \\ \frac{\omega\mu}{2\pi} \log \frac{a_3}{b_2} &= X_{a2}. \end{aligned} \quad (5)$$

In the second pair of equations (2), voltages and currents are related by the radial admittances  $Y_1$  and  $Y_2$  of the dielectric between conductors. That is,

$$\begin{aligned} \frac{2\pi(g + j\omega\epsilon)}{\log(a_2/b_1)} &= Y_1, \\ \frac{2\pi(g + j\omega\epsilon)}{\log(a_3/b_2)} &= Y_2. \end{aligned} \quad (6)$$

\* Formulae for the surface impedances for the cylindrical line are given in Section VI.

Equations (1) and (2) may now be written

$$\begin{aligned}\frac{\partial i_1}{\partial x} &= Y_1 v_1 - Y_1 v_2, \\ \frac{\partial i_2}{\partial x} &= -Y_1 v_1 + (Y_1 + Y_2) v_2, \\ \frac{\partial v_1}{\partial x} &= (Z_{22} + Z_{11} - 2Z_{ab}) i_1 + (Z_{22} - Z_{ab}) i_2, \\ \frac{\partial v_2}{\partial x} &= (Z_{22} - Z_{ab}) i_1 + Z_{22} i_2,\end{aligned}\quad (7)$$

where

$$Z_{11} = Z_{bb}^{(1)} + Z_{aa}^{(2)} + jX_{a1} \quad (8)$$

is the effective series impedance of the simple coaxial line consisting of conductors 1 and 2 only, and where

$$Z_{22} = Z_{bb}^{(2)} + Z_{aa}^{(3)} + jX_{a2} \quad (9)$$

is the effective series impedance of the simple coaxial line consisting of conductors 2 and 3 only. The coefficients in these equations are all per unit length of line.

In matrix notation (7) is

$$\begin{bmatrix} \frac{\partial i_1}{\partial x} \\ \frac{\partial i_2}{\partial x} \\ \frac{\partial v_1}{\partial x} \\ \frac{\partial v_2}{\partial x} \end{bmatrix} = A' \begin{bmatrix} i_1(x) \\ i_2(x) \\ v_1(x) \\ v_2(x) \end{bmatrix}. \quad (10)$$

This system has four eigenvalues, which are the roots of the characteristic equation of the matrix (Ref. 6, p. 314; Ref. 7, p. 111):

$$\text{determinant } [A' - \gamma I] = 0.$$

To each eigenvalue  $\gamma_j$  ( $j = 1, 2, 3, 4$ ) corresponds an eigenvector,

$$\begin{bmatrix} I_j \\ V_j \end{bmatrix} = \begin{bmatrix} i_{j1}(x) \\ i_{j2}(x) \\ v_{j1}(x) \\ v_{j2}(x) \end{bmatrix}, \quad j = 1, 2, 3, 4 \quad (11)$$

such that

$$A' \begin{bmatrix} i_{j1} \\ i_{j2} \\ v_{j1} \\ v_{j2} \end{bmatrix} = \gamma_j \begin{bmatrix} i_{j1} \\ i_{j2} \\ v_{j1} \\ v_{j2} \end{bmatrix}, \quad j = 1, 2, 3, 4, \quad (12)$$

where the notations

$$V(x) = \begin{bmatrix} v_1(x) \\ v_2(x) \end{bmatrix} \quad \text{and} \quad \underline{V}(x) = [v_1(x), v_2(x)]$$

are used for column and row matrices respectively.

The following convention regarding subscripts will be used in the rest of this paper: If a voltage or a current bears two subscripts, the first refers to the number of the eigenvector or mode, and the second to the number of the conductor.

### 3.1 Traveling Waves and Eigenvectors

A set of certain simple solutions of the system (10) can be expressed in the form

$$\begin{aligned} i_1(x + \xi) &= \lambda i_1(x) = e^{\gamma \xi} i_1(x), \\ i_2(x + \xi) &= \lambda i_2(x) = e^{\gamma \xi} i_2(x), \\ v_1(x + \xi) &= \lambda v_1(x) = e^{\gamma \xi} v_1(x), \\ v_2(x + \xi) &= \lambda v_2(x) = e^{\gamma \xi} v_2(x). \end{aligned} \quad (13)$$

To a transmission engineer, each such solution is a *traveling wave* with a *propagation constant*  $\gamma$ . To a mathematician, each such solution is an *eigenvector* with an *eigenvalue*  $\lambda$ . More general solutions can be expressed as linear combinations of such elementary solutions. In this particular case, as we saw above, there are four traveling waves or eigenvectors, and the solutions are

$$\begin{aligned} i_1(x) &= i_{11} e^{\gamma_1 x} + i_{21} e^{\gamma_2 x} + i_{31} e^{\gamma_3 x} + i_{41} e^{\gamma_4 x}, \\ i_2(x) &= i_{12} e^{\gamma_1 x} + i_{22} e^{\gamma_2 x} + i_{32} e^{\gamma_3 x} + i_{42} e^{\gamma_4 x}, \\ v_1(x) &= v_{11} e^{\gamma_1 x} + v_{21} e^{\gamma_2 x} + v_{31} e^{\gamma_3 x} + v_{41} e^{\gamma_4 x}, \\ v_2(x) &= v_{12} e^{\gamma_1 x} + v_{22} e^{\gamma_2 x} + v_{32} e^{\gamma_3 x} + v_{42} e^{\gamma_4 x}. \end{aligned} \quad (14)$$

The eigenvalues  $\gamma_j$ , corresponding to the  $j$  normal traveling waves of

the system described by  $A'$ , are isolated and shown clearly by factoring  $A'$  into the canonical form (Ref. 6, p. 314; Ref. 7, p. 111):

$$A' = L\Gamma L^{-1}, \quad (15)$$

where

$$\Gamma = \begin{bmatrix} \gamma_1 & 0 & 0 & 0 \\ 0 & \gamma_2 & 0 & 0 \\ 0 & 0 & \gamma_3 & 0 \\ 0 & 0 & 0 & \gamma_4 \end{bmatrix} \quad (16)$$

and

$$L = \begin{bmatrix} i_{11} & i_{21} & i_{31} & i_{41} \\ i_{12} & i_{22} & i_{32} & i_{42} \\ v_{11} & v_{21} & v_{31} & v_{41} \\ v_{12} & v_{22} & v_{32} & v_{42} \end{bmatrix} = \begin{bmatrix} I_1 & I_2 & I_3 & I_4 \\ V_1 & V_2 & V_3 & V_4 \end{bmatrix}. \quad (17)$$

Because  $A'$  has special properties, in particular,

$$A' = \begin{bmatrix} 0 & Y \\ Z & 0 \end{bmatrix} \quad (18)$$

the set of four equations (10) can be reduced by further differentiation to two separate sets of two equations:

$$\begin{bmatrix} \frac{\partial^2 i_1}{\partial x^2} \\ \frac{\partial^2 i_2}{\partial x^2} \end{bmatrix} = YZ \begin{bmatrix} i_1 \\ i_2 \end{bmatrix}, \quad \begin{bmatrix} \frac{\partial^2 v_1}{\partial x^2} \\ \frac{\partial^2 v_2}{\partial x^2} \end{bmatrix} = ZY \begin{bmatrix} v_1 \\ v_2 \end{bmatrix}. \quad (19)$$

Because  $YZ$  is the transpose of  $ZY$ , the eigenvalues of these two systems are the same. Further, because the solutions have the forms (13) and must satisfy a relation like (12), we have

$$YZ \begin{bmatrix} i_{j1} \\ i_{j2} \end{bmatrix} = \gamma_j^2 \begin{bmatrix} i_{j1} \\ i_{j2} \end{bmatrix}. \quad (20)$$

Since the eigenvalues  $\gamma_1^2$  and  $\gamma_3^2$  of (19) are the squares of those of (10), we have

$$\gamma_1 = -\gamma_2, \quad \gamma_3 = -\gamma_4. \quad (21)$$



They may be calculated from

$$\text{determinant } [YZ - \gamma^2 I] = 0, \quad (22)$$

as indicated above.

The ratios of magnitudes of the several traveling waves in the two conductors may be calculated from (20) and a similar equation for the voltages after the  $\gamma$ 's have been found.

It may be noticed that if  $Z_{ab} = 0$ , we have  $\gamma^2 = Y_1 Z_{11}$  or  $Y_2 Z_{22}$ , corresponding to two independent coaxial lines. This would be the case if the intermediate conductor tube were very thick or the frequency very high.

The above results may be extended to any number of concentric tubes. For each added tube, two more equations are added to the original set of four, and one additional distinct natural mode which may travel forward or backward appears. The number of homogeneous equations [corresponding to (20)] is one less than the number of conductors.

The computation for the three-conductor case we considered was done by machine. The results will be described in Sections V and VI.

#### IV. TRANSMISSION PROPERTIES OF LINES WITH TRANSPOSITIONS

In order to combine sections of uniform line and transpositions as indicated at the beginning of Section III, we need the relation between currents and voltages into and out of a line section of length  $l$ . This is

$$\begin{bmatrix} i_1(x+l) \\ i_2(x+l) \\ v_1(x+l) \\ v_2(x+l) \end{bmatrix} = A \begin{bmatrix} i_1(x) \\ i_2(x) \\ v_1(x) \\ v_2(x) \end{bmatrix}. \quad (23)$$

The matrix  $A$  is related to the matrix  $A'$  discussed in Section III by

$$A = LAL^{-1}, \quad (24)$$

where\*

$$\Lambda = \exp(\Gamma l)$$

is a diagonal matrix with elements  $\lambda_i = e^{\gamma_i l}$ . This throws into clear view the relation between the differential equations of the line and the trans-

\* The form (23) is derived from that of (10) by considering  $n$  sections of length  $\Delta x$  in cascade, calculating  $i(x_0 + n\Delta x)$  from  $[i(x_0 + n\Delta x) - i(x_0)]/\Delta x$ , and then keeping  $n\Delta x = l$  while  $\Delta x \rightarrow 0$ . This is a case of Sylvester's theorem. A treatment is found in Ref. 7, p. 119, where polynomial functions are considered. A general proof for converging power series, including exponential series as a special case, follows by taking the limit as the sum of a polynomial series.

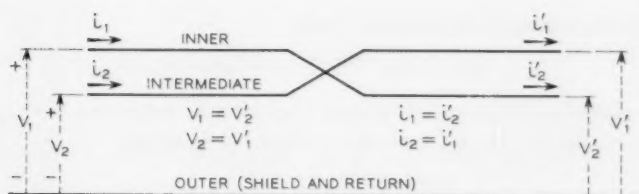


Fig. 8—Schematic representation of a transposition in a three-conductor transmission line.

mission properties of a finite length. The eigenvectors are the same, and the eigenvalues are related through the equation

$$\lambda_i = e^{\gamma_i l}, \quad (25)$$

where  $\lambda_1 = 1/\lambda_2$  and  $\lambda_3 = 1/\lambda_4$  correspond to (21).

The transposition shown in Fig. 8, whose matrix we shall call  $T$ , is governed by the equations

$$\begin{aligned} v_1 &= v_2', \\ v_2 &= v_1', \\ i_1 &= i_2', \\ i_2 &= i_1', \end{aligned} \quad (26)$$

where the primed and unprimed letters refer respectively to the two sets of terminals of the six-terminal network. In matrix notation,

$$T = \begin{bmatrix} 0 & 1 & 0 & 0 \\ 1 & 0 & 0 & 0 \\ 0 & 0 & 0 & 1 \\ 0 & 0 & 1 & 0 \end{bmatrix}. \quad (27)$$

The line with transpositions is made up of a large number of equivalent sections, each containing a certain length  $2l$  of transmission line and one transposition at the center, as in Fig. 7. The matrix of the transformation becomes

$$ATA = L\Lambda L^{-1}TL\Lambda L^{-1}.$$

Remember that  $\Lambda$  depends on the length of the section of line, although  $L$ ,  $L^{-1}$  and  $T$  do not.

The characteristic equation becomes

$$\det [L\Lambda L^{-1}TL\Lambda L^{-1} - \nu I] = 0. \quad (28)$$

The matrix can be modified without changing its determinant by multiplying on the left by  $L^{-1}$  and on the right by  $L$ , to get

$$\det [\Lambda L^{-1}TL\Lambda - \nu I] = 0. \quad (29)$$

Inasmuch as the matrices  $Z$  and  $Y$  [see (7)] are both symmetrical,  $ZY$  is the transpose of  $YZ$ . Consequently, there is a set of orthogonality relations among the respective eigenvectors, as follows:

$$\underline{I_j V_k} = i_{j1} v_{k1} + i_{j2} v_{k2} = 0$$

if

$$\gamma_j \neq \pm \gamma_k \quad \text{or} \quad \lambda_j + 1/\lambda_j \neq \lambda_k + 1/\lambda_k$$

and

$$\underline{I_j V_k} + \underline{V_j I_k} = 0$$

if

$$\gamma_j \neq \gamma_k \quad \text{or} \quad \lambda_j \neq \lambda_k.$$

The use of these relations simplifies the calculation of  $L^{-1}TL$  considerably. The first step is to find  $L^{-1}$ :

$$L^{-1} = \begin{bmatrix} p_1 v_{11} & p_1 v_{12} & p_1 i_{11} & p_1 i_{12} \\ p_2 v_{21} & p_2 v_{22} & p_2 i_{21} & p_2 i_{22} \\ p_3 v_{31} & p_3 v_{32} & p_3 i_{31} & p_3 i_{32} \\ p_4 v_{41} & p_4 v_{42} & p_4 i_{41} & p_4 i_{42} \end{bmatrix} = \begin{bmatrix} p_1 \underline{V_1} & p_1 \underline{I_1} \\ p_2 \underline{V_2} & p_2 \underline{I_2} \\ p_3 \underline{V_3} & p_3 \underline{I_3} \\ p_4 \underline{V_4} & p_4 \underline{I_4} \end{bmatrix}, \quad (30)$$

where

$$p_j = \frac{1}{2 \underline{I_j V_j}}. \quad (31)$$

Using, in addition, the relations (21) and consequences, straightforward but tedious multiplication yields for the characteristic equation (29)

$$\begin{aligned} & \nu^4 - \nu^3 Q_1 (\lambda_1^2 + \lambda_2^2 - \lambda_3^2 - \lambda_4^2) \\ & + \nu^2 [2Q_1^2 - (Q_1^2 + Q_2^2)(\lambda_2^2 \lambda_4^2 + \lambda_1^2 \lambda_3^2) \\ & - (Q_1^2 - Q_3^2)(\lambda_2^2 \lambda_3^2 + \lambda_1^2 \lambda_4^2)] \\ & - \nu Q_1 (\lambda_1^2 + \lambda_2^2 - \lambda_3^2 - \lambda_4^2) + 1 = 0, \end{aligned} \quad (32)$$

where

$$\begin{aligned} Q_1 &= (v_{12}v_{32} - v_{11}v_{31})/\Delta, \\ Q_2 &= [\sqrt{p_1/p_3}(v_{11}^2 - v_{12}^2) + \sqrt{p_3/p_1}(v_{32}^2 - v_{31}^2)]/2\Delta, \\ Q_3 &= [\sqrt{p_1/p_3}(v_{11}^2 - v_{12}^2) - \sqrt{p_3/p_1}(v_{32}^2 - v_{31}^2)]/2\Delta, \\ \Delta &= v_{11}v_{32} - v_{12}v_{31}. \end{aligned}$$

Equation (31) defines  $p_1$  and  $p_3$ , and

$$Q_1^2 + Q_2^2 - Q_3^2 = 1.$$

As anticipated, the equation has symmetrical coefficients, which means that the roots occur in symmetrical pairs, and also means that a substitution  $v + 1/v = \xi$  reduces the degree to two. The roots  $v_i$  of the characteristic equation (32) are the eigenvalues of the system and are related to the effective propagation constants  $\gamma_{Ti}$  of a transposed line by  $v_i = e^{\gamma_{Ti}l}$ . By this means, the propagation constants of the transposed line were derived from the eigenvectors and propagation constants of a section without transposition, with the aid of matrix properties of the line. The actual numerical computation was performed on a large electronic computer for several different transposition intervals, and the results are given both graphically and in tabular form in Sections V and VI.

#### 4.1 Infinitesimal Spacing of Transpositions

A special case of the general results just given yields results with much less numerical calculation and throws interesting light on the whole subject. From it, a very simple picture of the action of transposed lines is derived.

Consider the situation when the uniform line sections on either side of a transposition have length  $dx$  instead of  $l$ . The matrix  $A$  now may be formed from  $A'$  by calculating  $i_1(x + dx)$ , etc., from  $di_1/dx$ . In this way we get

$$A = \begin{bmatrix} 1 & 0 & Y_1 dx & -Y_1 dx \\ 0 & 1 & -Y_1 dx & (Y_1 + Y_2) dx \\ (Z_{22} + Z_{11} - 2Z_{ab}) dx & (Z_{22} - Z_{ab}) dx & 1 & 0 \\ (Z_{22} - Z_{ab}) dx & Z_{22} dx & 0 & 1 \end{bmatrix}.$$

From this, the matrix  $ATA$  for an element of transposed line is obtained easily. But, for present purposes, it is desirable to maintain the positions of  $i_1(x)$ ,  $i_2(x)$ , etc., in the column matrices of (23), and so we will consider a unit of length  $4 dx$  having a matrix  $ATAATA$ .

Just as was found in Section III, it is easier to handle a system like (10) with matrix  $A'$  when the line is divided into equivalent sections of infinitesimal length. To do this,  $4\partial i_{T1}/\partial x$  is calculated from  $[i_{T1}(x + 4dx) - i_{T1}(x)]/dx$ , etc. The transposed line composed of these very short elements is described, as in (10), by

$$\begin{bmatrix} \frac{\partial I_T}{\partial x} \\ \frac{\partial V_T}{\partial x} \end{bmatrix} = A_T' \begin{bmatrix} I_T \\ V_T \end{bmatrix}, \quad (33)$$

where

$$A_T' = \begin{bmatrix} 0 & Y_T \\ Z_T & 0 \end{bmatrix}, \quad Y_T = \begin{bmatrix} 2Y_1 + Y_2/2 & -Y_1 \\ -Y_1 & 2Y_1 + Y_2/2 \end{bmatrix},$$

and

$$Z_T = \begin{bmatrix} Z_{22} + Z_{11}/2 - Z_{ab} & Z_{22} - Z_{ab} \\ Z_{22} - Z_{ab} & Z_{22} + Z_{11}/2 - Z_{ab} \end{bmatrix}.$$

The eigenvalues  $\gamma_{Tj}$  of (33) occur in pairs and are calculated from determinant  $[Y_T Z_T - \gamma_T^2 I] = 0$ . The eigenvectors  $I_{Tj}$  and  $V_{Tj}$  are calculated from

$$Y_T Z_T \begin{bmatrix} i_{Tj1} \\ i_{Tj2} \end{bmatrix} = \gamma_{Tj}^2 \begin{bmatrix} i_{Tj1} \\ i_{Tj2} \end{bmatrix}, \text{ etc.}, \quad (34)$$

as before. The results are

(Low loss mode)

$$\begin{aligned} \gamma_{T1}^2 &= Y_2(Z_{22} - Z_{ab} + Z_{11}/4), & \gamma_{T2} &= -\gamma_{T1}, \\ i_{11} &= i_{12} = v_{11}Y_2/2\gamma_{T1} = v_{12}Y_2/2\gamma_{T1}, \\ i_{21} &= i_{22} = v_{21}Y_2/2\gamma_{T2} = v_{22}Y_2/2\gamma_{T2}, \end{aligned} \quad (35)$$

(High loss mode)

$$\begin{aligned} \gamma_{T3}^2 &= (Y_1 + Y_2/4)Z_{11}, & \gamma_{T4} &= -\gamma_{T3}, \\ i_{31} &= -i_{32} = v_{31}(4Y_1 + Y_2)/2\gamma_{T3} = -v_{32}(4Y_1 + Y_2)/2\gamma_{T3}, \\ i_{41} &= -i_{42} = v_{41}(4Y_1 + Y_2)/2\gamma_{T4} = -v_{42}(4Y_1 + Y_2)/2\gamma_{T4}, \end{aligned}$$

where the  $T$  subscript on the voltage and current components has been dropped for simplicity.



It is clear in this case that one mode has the expected current distribution, i.e.,  $i_{11} = i_{12}$ , in which equal currents flow in the two inner conductors. This confirms the heuristic analysis in an earlier section, where we assumed that such a current distribution could be achieved and conjectured that it could be achieved by transposition at sufficiently short intervals. A detailed comparison with the estimate of loss  $L$  in Section 2.2 shows that the predicted loss is the same as estimated before. However, the present analysis is more revealing, because it not only tells the loss of the desired mode, but also shows the losses and current and voltage distributions of both modes. A knowledge of the current and voltage distributions is necessary to launch one mode without exciting the other. In this case, connecting the two inner conductors together, so that  $v_1 = v_2$  at the launching point, is enough to guarantee that the unwanted mode cannot be excited, for in the unwanted mode  $v_{31} - v_{32}$  does not equal zero.

#### 4.2 Simple Picture of Attenuation in the Transposed Line

An interesting picture of the operation of the transposed three-conductor line can be obtained from (35) for  $\gamma_{T1}$  when the transposition interval is very small, ( $\gamma_{T1}$  being the propagation constant for the low-loss mode). In this expression,  $Y_2 = jS_2$  may be taken as the radial admittance and  $Z_{22} - Z_{ab} + Z_{11}/4$  as the series impedance of an equivalent two-conductor coaxial. If the series impedance is  $R + jX$  and  $R$  is very much less than  $X$ , we have approximately

$$\gamma_{T1} = \frac{R}{2} \sqrt{\frac{S_2}{X}} + j\sqrt{S_2 X}.$$

The attenuation (r.p.  $\gamma_T$ ) is proportional to the resistance of the series impedance, and we will consider only this:

$$\begin{aligned} R &= R_{22} - R_{ab} + R_{11}/4 \\ &= R_{aa}^{(3)} + R_{bb}^{(2)} - R_{ab} + \frac{R_{aa}^{(2)}}{4} + \frac{R_{bb}^{(1)}}{4}. \end{aligned}$$

Here,  $R_{aa}^{(3)}$  is the resistance in ohms per meter of length of the outer conductor;  $R_{bb}^{(2)}$  and  $R_{aa}^{(2)}$  are the surface resistances along the outer and inner surfaces of the intermediate tube;  $R_{ab}$  is the transfer resistance of this tube and  $R_{bb}^{(1)}$  is the surface resistance of the inner solid conductor.

Because the intermediate tube is electrically thin for the frequencies of interest,  $R_{bb}^{(2)}$  and  $R_{ab}$  are quite flat as functions of frequency and very nearly cancel each other. Eventually,  $R_{bb}^{(2)}$  begins to increase and  $R_{ab}$  to decrease with frequency. Until this frequency is reached, the re-

sistance of the central conductor of the equivalent two-conductor coaxial is given very closely by

$$R_{c3} = \frac{1}{4}[R_{aa}^{(2)} + R_{bb}^{(1)}].$$

A physical picture of the hypothetical center conductor which agrees with this expression is shown in Fig. 9 for a line  $n$  meters long. This has a real correspondence to the actual transposed line in that each of the two inner conductors consists of alternate sections of intermediate and inner conductors having the resistances per meter of the two terms above, and each carries approximately the same value of current. Of course, the transposition interval is not necessarily one meter, as indicated in the figure. Fig. 9 also shows a representation of the central solid conductor of the reference two-conductor coaxial. It is assumed here that the intermediate tube and its inner insulation are very thin, so that their combined diameters are essentially the same as the diameter of the solid reference conductor. Its resistance per meter is then  $R_{c2} = R_{bb}^{(1)}$ .

Formulae for calculating the surface impedances are given in Section VI. The first terms of each of the approximations (38) are suitable for

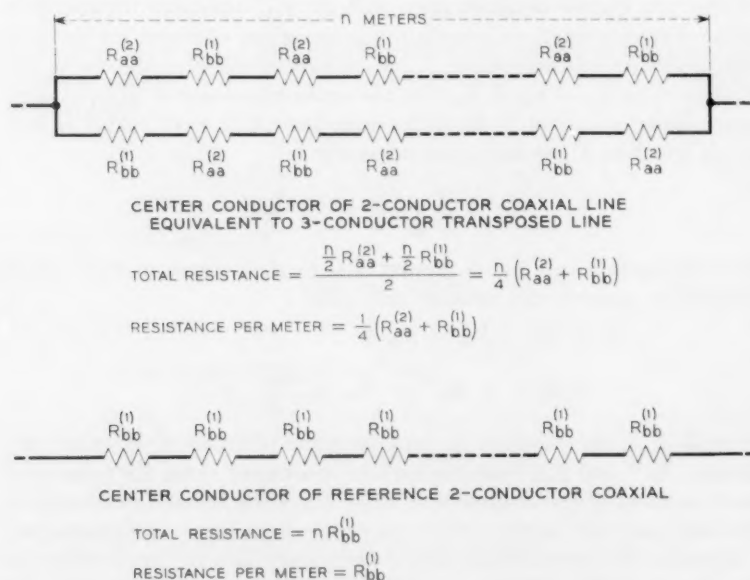


Fig. 9 — Low-frequency representation of inner and intermediate conductors in three-conductor transposed line.

present purposes and are reliable even at low frequencies for a thin-walled tube. Thus

$$Z_{aa}^{(2)} = \frac{\eta}{2\pi a_2} \frac{1}{\sigma t} = R_{aa}^{(2)} = \frac{1}{2\pi a_2 g t},$$

$$R_{bb}^{(1)} = \frac{1}{2b_1} \sqrt{\frac{\mu f}{\pi g}},$$

using (37) also. If, in addition,  $b_2$ ,  $a_2$  and  $b_1$  are approximately equal,

$$\frac{R_{aa}^{(2)}}{R_{bb}^{(1)}} = \frac{\delta}{t},$$

where

$$\delta = \sqrt{\frac{1}{\pi \mu g f}}$$

is the skin depth and  $t$  is the thickness of the intermediate conductor. Then, the ratio of center conductor resistance in the three-conductor transposed line to that of the two conductor reference line is

$$K = \frac{R_{c3}}{R_{c2}} = \frac{1}{4} \left( \frac{\delta}{t} + 1 \right).$$

At the frequency for which skin depth equals intermediate conductor thickness, the resistance is cut in half. If 78 per cent of the cable loss occurs in the center conductor, a 39 per cent reduction of attenuation would result. This is quite a bit more than was found experimentally. The difference is that, even for  $\delta/t = 1$ ,  $R_{ab}$  does not cancel  $R_{bb}^{(2)}$  exactly. If the third terms in  $\coth \sigma t$  and  $\operatorname{csch} \sigma t$  (the second terms give reactance only) are added to the above simple approximations, we find

$$K = \frac{R_{c3}}{R_{c2}} = \frac{1}{4} \left( \frac{\delta}{t} + 1 \right) + \frac{1}{6} \left( \frac{t}{\delta} \right)^3.$$

Now, when  $\delta/t$  is 1,  $K$  equals 0.667 and a 33 per cent reduction of resistance or 25.8 per cent reduction of attenuation is obtained. This is very close to the value computed from the whole expression for one-mil polyethylene (Fig. 18). When the cubic term is appreciable, the simple picture of Fig. 9 is no longer sufficient.

We find  $K$  equals one for  $\delta/t = 3$  and  $\delta/t = 0.66$ . The first is the lower-frequency crossover point (0.54 mc) and the second is the higher crossover point (11.1 mc) where the three-conductor transposed line has the same loss as the reference two-conductor line. These values agree quite

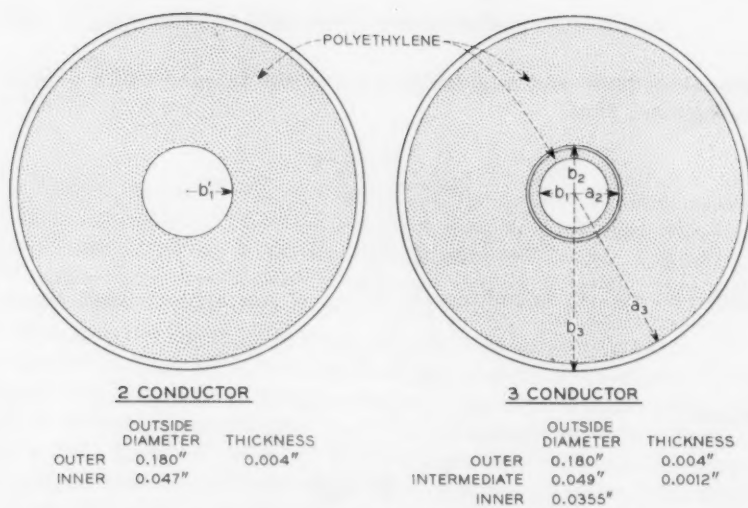


Fig. 10 — Cross sections of two-conductor and three-conductor coaxial lines used in experiment.

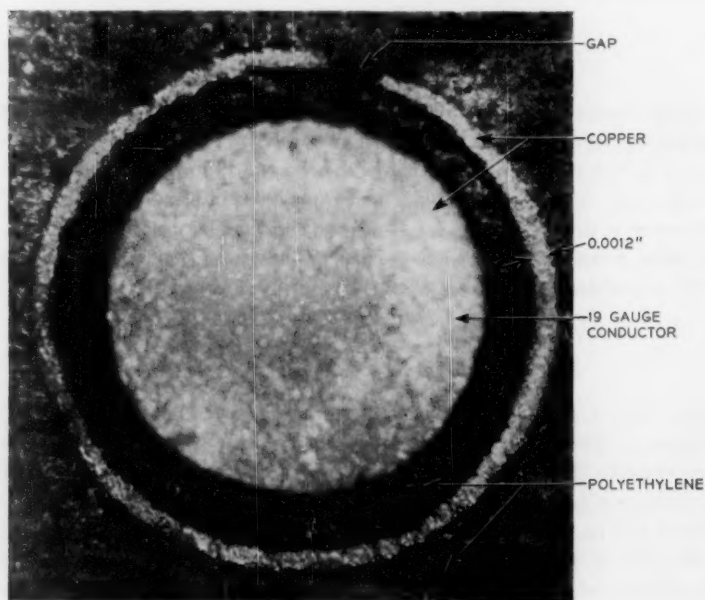


Fig. 11 — Photomicrograph of cross section of the inner conductors of the three-conductor coaxial line.

well with those calculated from the full expression for attenuation and plotted on Fig. 18.

The above simple expression for center conductor resistance reduction thus gives a good description of three-conductor transposed line performance, provided the radii of the two conductors are nearly the same.

If two thin shells surround an inner conductor to make a four-conductor transposed line, the simple picture of Fig. 9 may be generalized to give

$$K = \frac{R_{c4}}{R_{c2}} = \frac{1}{9} \left( 2 \frac{\delta}{t} + 1 \right)$$

for low frequencies. At  $\delta/t = 1$ , this would yield a 67 per cent resistance reduction or 52 per cent attenuation reduction. Naturally the cubic term is bigger than for the three-conductor line, and its effect would be felt at lower frequencies.

#### V. EXPERIMENT AND COMPARISON WITH THEORY

As mentioned above, it was predicted that there would be a reduction of attenuation in a coaxial line whose center conductor was laminated, with the laminations transposed periodically along the line. Confirmation of this prediction by resistance measurements of a three-foot length of such a line led to the decision to test the idea more fully by transmission measurements on a long section of line.

##### 5.1 *Making the Cable*

This required the manufacture of about a mile of three-conductor coaxial cable of unusual design. A design and a method of fabrication were worked out in cooperation with members of the Western Electric Company. Fig. 10 shows a cross section of the finished cable and its dimensions. The inner conductor is 19-gauge copper wire over which polyethylene was extruded to a thickness of 5 mils. Using a special die, the intermediate conductor was made by forming a copper tape about 1 mil thick and about 150 mils wide over the insulated wire, leaving a longitudinal seam. Ordinarily such a seam must be held closed with a helical wrapping of some kind, but this was found unnecessary when the second and comparatively thick layer of polyethylene dielectric was extruded over this intermediate conductor immediately after it had been formed by the die. One factor contributing to the success of this operation was the leaving of a small gap in the seam rather than an overlap. Microscopic examination of cross sections (see Fig. 11) showed the gap to be

about 5 mils or less. Capacitance measurements also indicated the presence of a slight air gap a few tenths of a mil thick between the inner and intermediate conductors. The final operation consisted of forming the outer conductor, using a copper tape 4 mils thick by 0.600 in. wide and a special forming tool. In this case, there is a small overlap at the longitudinal seam, which is held closed by a helical wrapping of paper tape, 5 mils by 0.750 in., applied 20 wraps per foot of cable. The effective air gap between the intermediate and outer conductors is about 1 mil, as determined by capacitance measurements.

At the same time this cable was made, a two-conductor coaxial cable was also made for comparison purposes. The central conductor of this cable is a solid copper wire of 0.0470-in. diameter, which is just a little less than the outside diameter of the intermediate conductor of the other cable. For both cables, the polyethylene dielectric was extruded through the same die and the outer conductor was made from the same batch of copper and applied in the same way. A cross section with dimensions for this cable is shown in Fig. 10. Sections of both cables are shown in Fig. 12.

The use of a reference cable made in the way described makes it unnecessary for the testing of the attenuation reduction idea to depend on

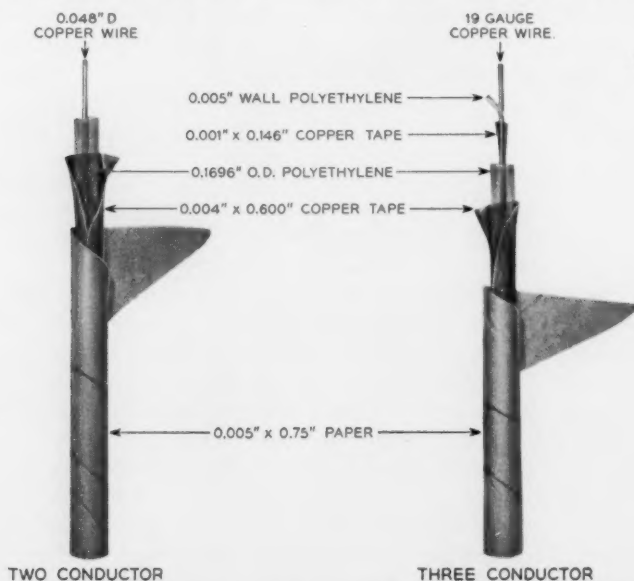


Fig. 12 — Photographs of two-conductor and three-conductor coaxial lines used in experiment.



a comparison of measurement with calculation. Rather, it depends on the comparison of the measured attenuations of two similar real cables, one having a solid central conductor, the other having a laminated central conductor in which the laminations are transposed regularly.

Open and short-circuit impedance measurements showed that the characteristic impedance of the three-conductor cable is very near 50 ohms. According to the estimates of Section II, the frequency at which maximum reduction of attenuation occurs is determined by the thickness of the intermediate conductor. For the cable described above, this is about 4 mc.

Because of the way in which they are made, the intermediate and outer conductors will buckle or even break if the cable is bent with too small a radius. To insure further against possible buckling or breaking, it was planned to handle the cable as little as possible. Hence, it was decided to re-reel the cable in a single layer onto suitable drums as the transpositions were made, so that access to any part of the cable would be possible without additional unreeling and re-reeling.

### 5.2 *Making the First Transpositions*

After the cable was fabricated as described above, the major part of the laboratory work consisted of devising and making satisfactory transpositions between the inner and intermediate conductors at regular intervals. At a point where a transposition was desired, the cable was cut and conductors and dielectric were stripped back so that all three conductors were laid bare at both sides of the cut. By means of special jacks and a plug, the center conductor on the left side of the cut was connected to the intermediate conductor on the right side of the cut and the intermediate conductor on the left side was connected to the center conductor on the right side. The two outer conductors were then connected together. Fig. 13 shows the cable ends connected to the jacks.

Because of the fragile nature of the intermediate conductor and its supporting insulation, considerable care had to be exercised in making the transpositions. Ragged edges on the 1-mil copper had to be guarded against to avoid puncturing the 5-mil polyethylene. Damage to the insulation from excessive heat was avoided by using low-melting-point solder for making electrical connection to the intermediate conductor.

### 5.3 *First Measurements, Showing the Effect of Too Long a Transposition Interval*

At the two ends of the cable, the inner and intermediate conductors were connected together to serve as one input and output terminal. Fifty-



ohm terminations were used. The results of the transmission measurements are plotted on Fig. 14, along with those for the reference two-conductor coaxial. These were disappointing because, in the frequency region where a reduction of loss was expected, two large peaks of increase were found. Measurements made after changing all the patching plugs for straight-through connection gave results very nearly the same and very nearly as smooth as those obtained from a continuous piece of cable of the same length. Apparently the transpositions and not the discontinuity at the section junctions were responsible for the peaks. With only one transposition at the center of the 1180-foot section, there were  $\pm 0.2$ -db ripples in the loss curve. The effects of reflection at the uniformly spaced transpositions accumulated, with the results already seen. Investigation showed the transposition interval to be one-quarter wavelength at the first peak and three-quarters of a wavelength at the second. Spacing the transpositions twice as far apart lowered the frequencies of the peaks by a factor of two. If there was indeed a reduction of attenuation between 1 and 10 mc, it was covered up by the reflection effects.

At this point, a thorough calculation of transmission loss was begun to help understand the phenomenon. Further experimental work was undertaken at the same time. Since no peaks appeared at frequencies below that corresponding to an interval of one-quarter wavelength, it seemed reasonable to expect the looked-for reduction of attenuation if the transposition interval was shortened so that the frequency for which it was one-quarter wavelength was outside the desired frequency region. Using our previous experience as a guide, a spacing of about 9 feet was chosen. With this spacing, the first peak should have been at around 20 mc.

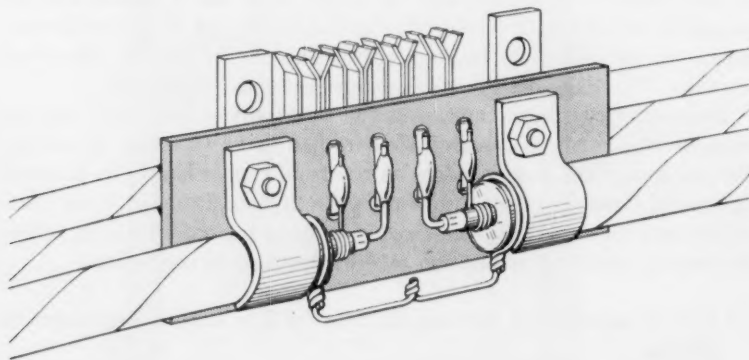


Fig. 13 — Technique for making cable connections at a plug-in transposition point.

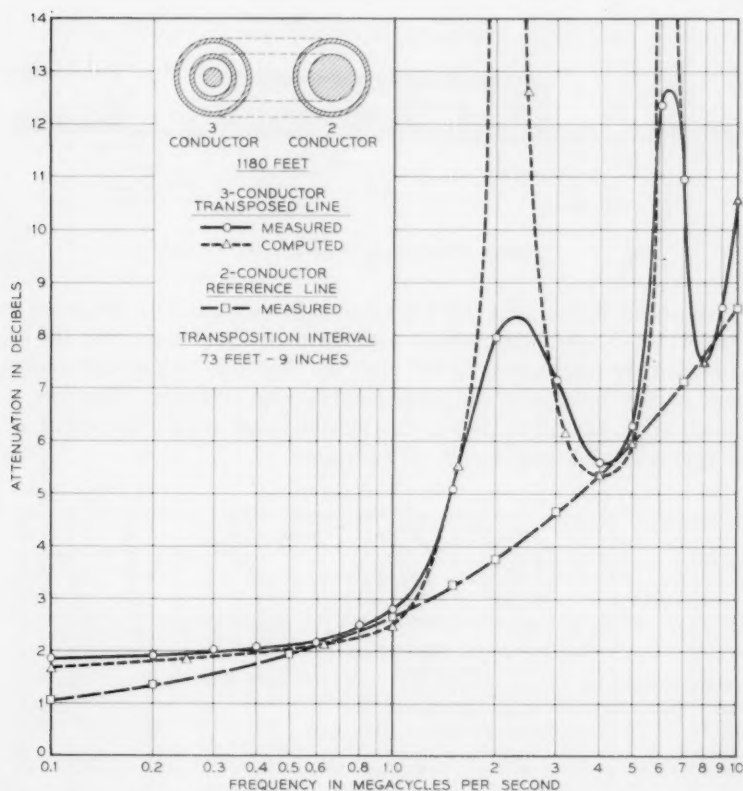


Fig. 14 — Attenuation of line with 75-foot transposition spacing (approx.) compared with that of reference two-conductor line and with computations.

#### 5.4 Final Measurement and Comparison with Theory

The plug-in transposition in Fig. 13 was too elaborate to be used in such large numbers, and not too satisfactory. Therefore, a permanent transposition, shown in Fig. 15, was devised. A continuous cable having 113 sound transpositions and 114 sections in a total length of 1057 feet was made ready for test. This time, after transmission measurements had been made and compared with those for the two-conductor reference line, the expected reduction of attenuation was found, as shown in Fig. 16. The reduction at 4 mc in the center of the region is 17 per cent.

While the rough estimate of reduction made in Section II was 27 per cent, it should be pointed out that this depended on the assumption that

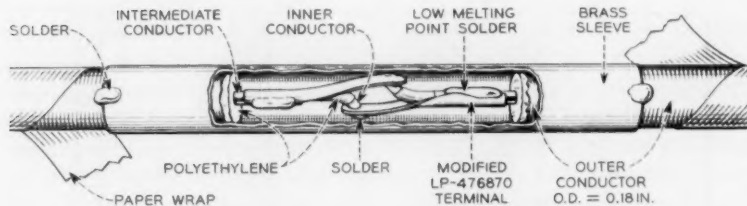


Fig. 15 — Cutaway illustration of permanent transposition.

the diameter of the solid inner conductor be substantially the same as that of the tubular intermediate conductor. In the actual cable, the diameter of the solid core is 28 per cent less than that of the surrounding tube, mainly because of the 5-mil polyethylene insulator. Therefore, a reduction of only 15 or 20 per cent should be expected. The actual reduction is right in the middle of this range.

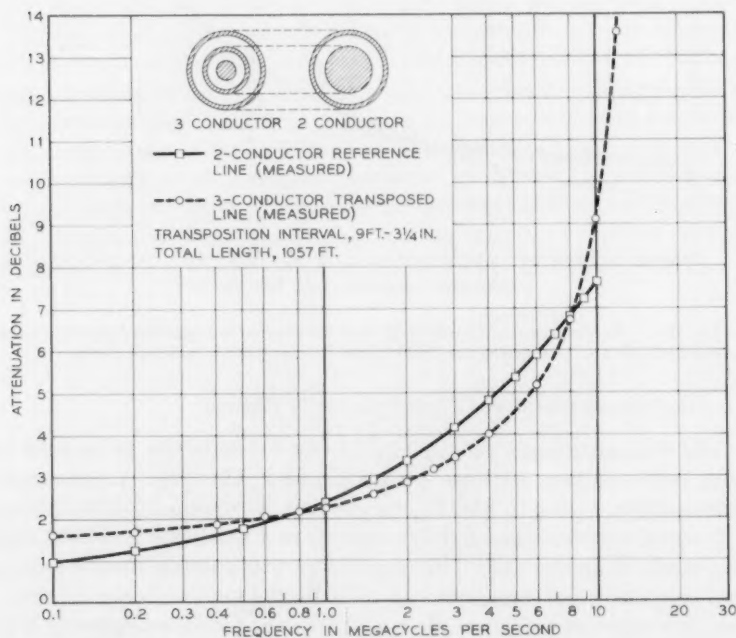


Fig. 16 — Attenuation of line with 9-foot transposition spacing (approx.) compared with that of the reference two-conductor line.

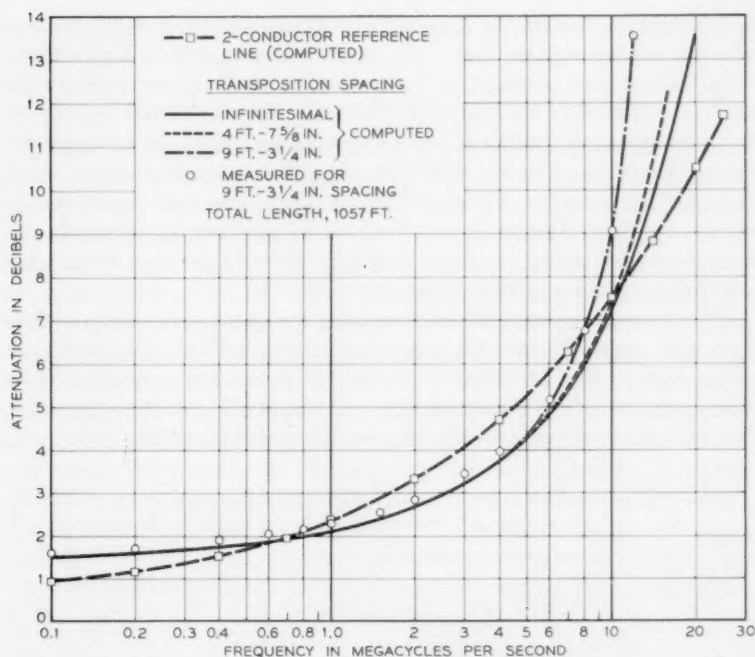


Fig. 17 — Calculation of attenuation with transpositions at approx. 9 feet, approx. 4½ feet and very small intervals; comparison with measurements where available.

The calculation of transmission loss described in Section IV was finished after the measurements. The results are plotted on Fig. 17 and show very good agreement with the measured data.

The greater attenuation at very low frequencies is caused mainly by the transpositions and not by the fact that the central conductor cross section is 38 per cent less in the three-conductor cable than it is in the two-conductor one. The central conductor of the transposed line at dc consists of two like structures in parallel. Each of these is a conductor of many series sections, with inner and intermediate sections alternating. Thus, the considerably higher-resistance intermediate sections dominate the situation. At very low frequencies, the attenuation ratio is approximately 2, which is slightly greater than the value 1.6 shown at 100 kc.

### 5.5 Transposition Interval

In the calculation it was very easy to shorten the transposition interval. Two such cases are plotted in Fig. 17. When the spacing is just one-

half as long as before, the loss curve is nearly the same, but it crosses over the reference cable loss at about 10 mc instead of at 8 mc. Thus, the reflection peak at about 20 mc (not shown on the figure) pulls up the loss curve a little at the high end. The other case calculated was for infinitesimally small spacing of transpositions, and this gave substantially the same loss curve as the  $4\frac{1}{2}$ -foot spacing. We conclude that the reflection peak at 40 mc has a negligible effect on the loss curve in the region of improvement. Also, it is seen that the 17 per cent improvement observed experimentally would be raised to 18 or 19 per cent by spacing the transpositions at about 4-foot intervals.

The attenuation was calculated also for the cable with transpositions 75 ft 9 in. apart. The results, in good agreement with the measurements, are plotted on Fig. 14. While a random longer spacing of transpositions would greatly reduce the sharp peaks of loss in Fig. 14, the way to get the smoothest loss curve with the greatest reduction of loss is to make

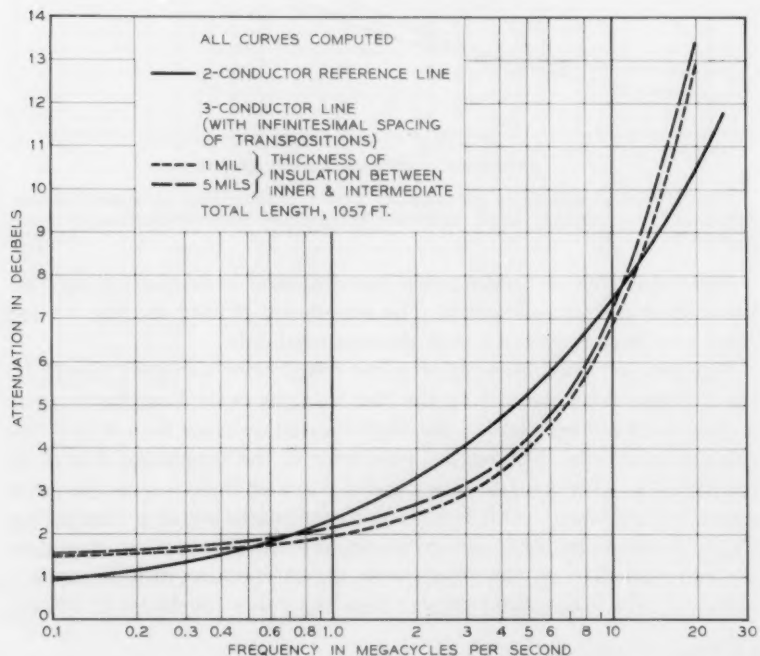


Fig. 18 — Calculated attenuation of a transposed line similar to that used in experiments, but with 1-mil dielectric thickness between innermost conductors.

the spacing small enough so that the first peak is well beyond the desired operating region.

#### 5.6 *Effect of Spacing Between Inner and Intermediate Conductors*

Another result should be of interest here even though it was not obtained experimentally. A calculation for loss was made for a line in which the inner conductor was enlarged so that the polyethylene separating it from the intermediate conductor was only 1 mil thick instead of 5 mils. The results are plotted on Fig. 18. All curves are calculated so that they are on the same basis. At 4 mc, the transposed three-conductor with 5-mil polyethylene shows an improvement of 21.2 per cent, and the transposed three-conductor with 1-mil polyethylene shows an improvement of 26.9 per cent.

The latter case approximates the original assumption of equal diameters much more closely than does the former, and shows an improvement very nearly the same as the 27 per cent prediction of Section II. It was realized in the beginning that the dielectric separating the inner and intermediate conductors should be as thin as possible, but 5 mils was a much more practical figure both for fabrication of the cable and for the transpositions. These results serve to point the way to further improvements.

#### 5.7 *Conclusions*

The experiments have compared the transmission loss of two coaxial cables which are the same except that the center conductor of one is solid while that of the other consists of a shell surrounding and insulated from a center core. It has been shown that the transmission loss is less, over a certain frequency band, for the cable with the laminated center conductor, provided the laminations are transposed at sufficiently frequent intervals. Also, calculations of transmission loss show very good quantitative agreement with measured values, thus tying the theory to the practice. Further, the results show that, if the insulating space between intermediate and inner conductors can be reduced to a thickness negligible compared to its radius, the reduction of loss can be greater and will apply over a greater frequency band.

### VI. NUMERICAL CALCULATION

#### 6.1 *Surface Impedances and Propagation Constants for Uniform Line*

The conductor surface impedances referred to in Sections II and III may be calculated from formulae given in Schelkunoff's paper.<sup>2</sup>



When the calculations were started, no attenuation reduction had been found experimentally, even though measurements had been made. Hence, we wanted to make the calculations as exact as possible in order that no small effect in the uniform line properties, which might have a large effect in the transposed line, would be overlooked. Therefore, the exact expressions for the surface impedances [equations (75) in Ref. 2] were used as far as possible. Expressed in terms of modified Bessel functions of the first and second kind,  $I_n$  and  $K_n$ , respectively, the results are:

$$\begin{aligned} Z_{bb}^{(1)} &= \frac{\eta}{2\pi b_1} \frac{I_0(\sigma b_1)}{I_1(\sigma b_1)}, \\ Z_{aa}^{(2)} &= \frac{\eta}{2\pi a_2} \frac{I_0(\sigma a_2)K_1(\sigma b_2) + K_0(\sigma a_2)I_1(\sigma b_2)}{I_1(\sigma b_2)K_1(\sigma a_2) - I_1(\sigma a_2)K_1(\sigma b_2)}, \\ Z_{bb}^{(2)} &= \frac{\eta}{2\pi b_2} \frac{I_0(\sigma b_2)K_1(\sigma a_2) + K_0(\sigma b_2)I_1(\sigma a_2)}{I_1(\sigma b_2)K_1(\sigma a_2) - I_1(\sigma a_2)K_1(\sigma b_2)}, \\ Z_{ab}^{(2)} &= \frac{1}{2\pi g a_2 b_2} \frac{1}{I_1(\sigma b_2)K_1(\sigma a_2) - I_1(\sigma a_2)K_1(\sigma b_2)}, \\ Z_{aa}^{(3)} &= \frac{\eta}{2\pi a_3} \frac{I_0(\sigma a_3)K_1(\sigma b_3) + K_0(\sigma a_3)I_1(\sigma b_3)}{I_1(\sigma b_3)K_1(\sigma a_3) - I_1(\sigma a_3)K_1(\sigma b_3)}. \end{aligned} \quad (36)$$

In these expressions, the  $b$ 's and  $a$ 's are the radii of the various conductor surfaces as shown on Fig. 1, and  $\eta$  and  $\sigma$  are the intrinsic impedance and the propagation constant of the conductor material. They are

$$\begin{aligned} \eta &= (1 + i) \sqrt{\frac{\pi f \mu}{g}}, \\ \sigma &= (1 + i) \sqrt{\pi f \mu g}, \\ i &= \sqrt{-1}. \end{aligned}$$

The dimensions of the cables as supplied by Western Electric are:

$$\begin{aligned} b_1 &= 0.0178 \text{ in.} = 4.52 \times 10^{-4} \text{ meter,} \\ a_2 &= 0.0234 \text{ in.} = 5.95 \times 10^{-4} \text{ meter,} \\ b_2 &= 0.0246 \text{ in.} = 6.25 \times 10^{-4} \text{ meter,} \\ a_3 &= 0.0862 \text{ in.} = 2.19 \times 10^{-3} \text{ meter,} \\ b_3 &= 0.0902 \text{ in.} = 2.29 \times 10^{-3} \text{ meter.} \end{aligned}$$

For the two-conductor reference line,  $a_3$  and  $b_3$  are the same as above and

$$b_2' = 0.0235 \text{ in.} = 5.97 \times 10^{-4} \text{ meter.}$$



The cable material constants as supplied by the makers of the cable are

$$\mu = \mu_0 = 4\pi \times 10^{-7} \text{ henry/meter}$$

$$\epsilon = 2.2\epsilon_0 = \frac{2.2}{36\pi} \times 10^{-9} \text{ farad/meter}$$

$$g = 5.858 \times 10^7 \text{ mho/meters}$$

(at 68°F this is 101 per cent IACS).

These impedances were calculated by means of the IBM 650 computer from 100 kc to several megacycles at points uniformly spaced on a logarithmic frequency scale. Each frequency point is higher than the one preceding it by a factor of  $10^{0.1}$ . In the main program, the libraries used for computing the modified Bessel functions at each point were prepared by Miss M. C. Gray.

For sufficiently high frequencies, approximate formulas for the surface impedances are satisfactory. These are:

$$\begin{aligned} Z_{bb}^{(1)} &= \frac{\eta}{2\pi b_1} \left[ 1 + \frac{1}{2\sigma b_1} \right], \\ Z_{aa}^{(2)} &= \frac{\eta}{2\pi a_2} \left[ \coth \sigma(b_2 - a_2) - \frac{1}{8\sigma} \left( \frac{1}{a_2} + \frac{3}{b_2} \right) \right. \\ &\quad \left. - \frac{3}{8\sigma} \left( \frac{1}{a_2} - \frac{1}{b_2} \right) \coth^2 \sigma(b_2 - a_2) \right], \\ Z_{bb}^{(2)} &= \frac{\eta}{2\pi b_2} \left[ \coth \sigma(b_2 - a_2) + \frac{1}{8\sigma} \left( \frac{3}{a_2} + \frac{1}{b_2} \right) \right. \\ &\quad \left. - \frac{3}{8\sigma} \left( \frac{1}{a_2} - \frac{1}{b_2} \right) \coth^2 \sigma(b_2 - a_2) \right], \\ Z_{ab} &= \frac{\eta}{2\pi \sqrt{a_2 b_2}} \frac{\left[ 1 - \frac{3}{8\sigma} \left( \frac{1}{a_2} - \frac{1}{b_2} \right) \coth \sigma(b_2 - a_2) \right]}{\sinh \sigma(b_2 - a_2)}, \\ Z_{aa}^{(3)} &= \frac{\eta}{2\pi a_3} \left[ \coth \sigma(b_3 - a_3) - \frac{1}{8\sigma} \left( \frac{1}{a_3} + \frac{3}{b_3} \right) \right. \\ &\quad \left. - \frac{3}{8\sigma} \left( \frac{1}{a_3} - \frac{1}{b_3} \right) \coth^2 \sigma(b_3 - a_3) \right]. \end{aligned} \quad (38)$$

The higher-order correction terms are not the same as the ones given by Schelkunoff's paper<sup>2</sup> which, as pointed out by Miss Gray, are incorrect. These also were computed using the IBM 650 machine. However, they went through much faster than the exact ones, and so all the fre-

quency points (25) from 100 kc to 25 mc were computed. As it turned out, the approximations were very close to the exact values of impedance except at the lowest few frequency points, and the greatest differences were in the reactances.

The resistance and reactance of  $Z_{bb}^{(1)}$  (surface impedance of the inner conductor) are fairly close to one another, increasing about as  $\sqrt{f}$  and having values of 0.1 ohm near 1 mc. The three resistances  $R_{aa}^{(2)}$ ,  $R_{bb}^{(2)}$  and  $R_{ab}$  of the intermediate conductor are nearly the same and constant at about 0.15 ohm up to about 3 mc, where the first two begin to increase and  $R_{ab}$  begins to decrease. The corresponding reactances vary linearly with frequency over most of the range, the first two being positive and equal to the resistance at about 0.7 mc, and  $X_{ab}$  being negative and equal to  $R_{ab}$  at about 1.5 mc. The resistance  $R_{aa}^{(3)}$  begins to increase from 0.015 ohms around 0.4 mc. All these values are per meter of length.

In the third calculation using the IBM 650, the inductive reactances  $X_{a1}$  and  $X_{a2}$  (5) of the space between conductors were computed and combined with the proper values of surface impedances at each of the 25 frequency points (exact as far as they went and approximate beyond) to give the series impedances  $Z_{11}$  and  $Z_{22}$ , (8) and (9). The dielectric admittances  $Y_1$  and  $Y_2$  (6) and the transfer impedance  $Z_{ab}$  were then combined with these to form the coefficients of the characteristic equation (22). The four roots (two distinct) of this equation are the propagation constants of the uniform three-conductor coaxial line. Voltage and current ratios were computed at each mode, using (20). These quantities are shown in Table I.

The numbers tabulated in Table I contain eight significant digits, just as they came from the IBM 650 computer. This precision would not be justified by the primary data if these were final results. But they are intermediate results which were used as input data to the computer for the transposed line calculation.

## 6.2 Transposed Line

From the characteristic equation (32) for the transposed line section of length  $2l$  having one transposition at its center, the four roots  $\nu_i$  were found and, from these, the four (two distinct) propagation constants  $\gamma_{Ti}$  were calculated. This was done for the transposition interval  $2l = 73$  ft 9 in. of the first experiment and the interval  $2l = 9$  ft  $3\frac{1}{4}$  in. of the second experiment, and for an interval of 4 ft  $7\frac{5}{8}$  in. not done experimentally. Only the  $\lambda_i$  vary with transposition interval  $2l$ , since the  $Q$ 's depend only on current and voltage ratios of the natural travelling waves. These quantities are shown in Table II.

TABLE I — UNIFORM THREE-CONDUCTOR LINE —  $\gamma_1 = \alpha_1 + j\beta_1$ 

Frequency, mc	$10^3\alpha_1$ nepers/meter	$10^3\beta_1$ radians/meter
0.10000000	3.4688831	0.33348735
0.15848935	4.0799877	0.52214634
0.25118873	4.8395041	0.81834244
0.39810738	5.7671483	1.2854328
0.63095778	6.9660247	2.0228904
1.00000008	8.5580372	3.1876156
1.5848947	10.693456	5.0275308
2.5118893	13.462726	7.9349729
3.9810768	16.887865	12.532983
6.3095828	21.135279	19.809733
10.000016	26.526402	31.329134
15.848960	33.384128	49.567992
25.118912	42.047592	78.451609
Frequency, mc	$10^3\alpha_2$ nepers/meter	$10^3\beta_2$ radians/meter
0.10000000	4.7318826	0.62320343
0.15848935	5.6942080	0.84536090
0.25118873	6.7525699	1.1723877
0.39810738	7.8427964	1.6701939
0.63095778	8.9337375	2.4480157
1.00000008	10.044322	3.6761608
1.5848947	11.241957	5.6192649
2.5118893	12.643512	8.6900187
3.9810768	14.433451	13.536061
6.3095828	16.928777	21.174433
10.000016	20.664341	33.195442
15.848960	26.361051	52.069905
25.118912	34.329361	81.679447
Frequency, mc	$i_{12}/i_{11}$ (r.p.)	$i_{12}/i_{11}$ (i.p.)
0.10000000	0.18362010	0.16630834
0.15848935	0.22474330	0.22944720
0.25118873	0.27695130	0.30501473
0.39810738	0.33751280	0.40492969
0.63095778	0.40881000	0.54361980
1.00000008	0.48911890	0.73916345
1.5848947	0.56956110	1.0221795
2.5118893	0.62801670	1.4417420
3.9810768	0.60888470	2.0726476
6.3095828	0.37242140	3.0234415
10.000016	-0.41964610	4.4235045
15.848960	-2.5566098	6.2815904
25.118912	-7.7731939	7.8207114
Frequency, mc	$i_{22}/i_{11}$ (r.p.)	$i_{22}/i_{11}$ (i.p.)
0.10000000	-1.1816245	0.025519684
0.15848935	-1.1729224	0.032395813
0.25118873	-1.1624073	0.038792862
0.39810738	-1.1501389	0.045454252
0.63095778	-1.1354390	0.052262004
1.00000008	-1.1181120	0.058627941
1.5848947	-1.0980730	0.063870189
2.5118893	-1.0754678	0.066832765
3.9810768	-1.0512315	0.065599039
6.3095828	-1.0272895	0.060118625
10.000016	-1.0063910	0.048717882
15.848960	-0.99185120	0.032878953
25.118912	-0.98612750	0.016017054

TABLE I — *Concluded*

Frequency, mc	$v_{12}/v_{11}$ (r.p.)	$v_{12}/v_{11}$ (i.p.)
0.10000000	0.84589800	0.018268992
0.15848935	0.85192153	0.023529840
0.25118873	0.85932664	0.026878194
0.39810738	0.86810431	0.034308091
0.63095778	0.87885470	0.040451987
1.00000008	0.89191254	0.046767278
1.5848947	0.90761553	0.052792147
2.5118893	0.92625098	0.057560082
3.9810768	0.94753039	0.059488464
6.3095828	0.97011293	0.056772712
10.000016	0.99132599	0.047989710
15.848960	1.0071079	0.033385241
25.118912	1.0137993	0.016466337
Frequency, mc	$v_{22}/v_{21}$ (r.p.)	$v_{22}/v_{21}$ (i.p.)
0.10000000	-2.9917880	2.7097173
0.15848935	-2.1786147	2.2242917
0.25118873	-1.6316601	1.7969975
0.39810738	-1.2145871	1.4571936
0.63095778	-0.88363188	1.1750175
1.00000008	-0.62260636	0.94088943
1.5848947	-0.41596602	0.74652410
2.5118893	-0.25394751	0.58298677
3.9810768	-0.13047707	0.44414391
6.3095828	-0.040132660	0.32580464
10.000016	0.021255900	0.22404223
15.848960	0.055588468	0.13656873
25.118912	0.063935269	0.064322522
Frequency, mc	$v_{11}/i_{11}$ (r.p.), ohms	$v_{11}/i_{11}$ (i.p.), ohms
0.10000000	-77.329377	-1.1101280
0.15848935	-78.639675	-6.2732360
0.25118873	-80.548062	-11.518517
0.39810738	-83.030268	-17.666091
0.63095778	-86.205314	-25.523024
1.00000008	-89.947652	-36.084481
1.5848947	-93.776202	-50.973284
2.5118893	-96.541720	-72.748214
3.9810768	-95.405167	-105.27411
6.3095828	-83.247510	-154.12323
10.000016	-42.817517	-225.93510
15.848960	66.135311	-321.23818
25.118912	332.08865	-400.61598
Frequency, mc	$v_{21}/i_{21}$ (r.p.), ohms	$v_{21}/i_{21}$ (i.p.), ohms
0.10000000	-5.7971713	0.30779950
0.15848935	-5.9324594	-0.10551400
0.25118873	-6.0322898	-0.46269910
0.39810738	-6.1941820	-0.89163540
0.63095778	-6.5156971	-1.3739212
1.00000008	-7.0303966	-1.8609257
1.5848947	-7.7530091	-2.2944494
2.5118893	-8.6694443	-2.5937969
3.9810768	-9.7168424	-2.6696293
6.3095828	-10.780327	-2.4534229
10.000016	-11.699977	-1.9224920
15.848960	-12.286170	-1.1462743
25.118912	-12.411509	-0.33026606

TABLE II — TRANSPOSED THREE-CONDUCTOR COAXIAL LINE

$$\gamma_{Ti} = \alpha_{Ti} + j\beta_{Ti}$$

Transposition Interval  $2l = 73$  ft 9 in.

Frequency, mc	$10^3\alpha_{Ti}2l$ nepers	$\beta_{Ti}2l$ radians	Total Attenuation, db/1180 ft.
0.1000	1.204	0.07565	1.674
0.1585	1.257	0.1187	1.747
0.2512	1.320	0.1871	1.834
0.3981	1.399	0.2955	1.944
0.6310	1.519	0.4679	2.111
1.0000	1.776	0.7471	2.468
1.585	4.018	1.209	5.584
1.995	15.56	1.475	21.63
2.512	9.072	1.415	12.61
3.162	4.387	0.9181	6.097
3.981	3.831	0.3169	5.325
5.012	4.253	0.4368	5.991
6.310	14.52	1.367	20.17
7.943	5.346	0.6606	7.429
10.00	7.610	0.8457	10.58
12.60	7.044	0.5103	9.789
15.85	10.51	1.0378	14.61

Transposition Interval  $2l = 4$  ft  $7\frac{1}{8}$  in.

Frequency, mc	$10^3\alpha_{Ti}2l$ nepers	$\beta_{Ti}2l$ radian	Total Attenuation, db/1057 ft.
1.000	1.214	0.04610	2.404
1.585	1.322	0.07292	2.618
2.512	1.545	0.1153	3.059
3.981	1.867	0.1825	3.698
6.310	2.543	0.2890	5.035
10.00	3.770	0.4579	7.467
12.60	4.767	0.5767	9.440
15.85	6.185	0.7273	12.25

Transposition Interval  $2l = 9$  ft  $3\frac{1}{2}$  in.

Frequency, mc	$10^3\alpha_{Ti}2l$ nepers	$\beta_{Ti}2l$ radians	Total Attenuation, db/1057 ft.
0.1000	1.506	0.009458	1.491
0.1585	1.574	0.01486	1.558
0.2512	1.655	0.02337	1.638
0.3981	1.756	0.03690	1.739
0.6310	1.900	0.05830	1.882
1.000	2.124	0.09221	2.103
1.585	2.464	0.1459	2.440
2.512	2.990	0.2308	2.961
3.981	3.804	0.3655	3.767
6.310	5.301	0.5798	5.249
10.00	9.102	0.9258	9.012
12.60	16.45	1.185	16.29

TABLE II — *Concluded*

Frequency, mc	$10^3\alpha_{T1}2l$ nepers	$\beta_{T1}2l$ radians	
0.1000	1.2450	0.01740	
0.1585	1.4960	0.02391	
0.2512	1.776	0.03354	
0.3981	2.072	0.04826	
0.6310	2.381	0.07121	
1.000	2.715	0.1073	
1.585	3.092	0.1640	
2.512	3.546	0.2535	
3.981	4.126	0.3947	
6.310	4.932	0.6180	
10.00	6.214	0.9763	
12.60	7.533	1.243	

$$\gamma_{T1} = \alpha_{T1} + j\beta_{T1}$$

Transposition Interval — Infinitesimal

5-mil Dielectric

Frequency, mc	$10^3\alpha_{T1}$ nepers/meter	$\beta_{T1}$ radian/meter	Total Attenuation, db/1057 ft.
0.1000	0.5329	0.003347	1.419
0.1585	0.5569	0.005521	1.558
0.2512	0.5856	0.008271	1.638
0.3981	0.6215	0.01306	1.739
0.6310	0.6725	0.02063	1.882
1.000	0.7504	0.03263	2.100
1.585	0.8716	0.05161	2.439
2.512	1.053	0.08163	2.947
3.981	1.326	0.1291	3.711
6.310	1.780	0.2043	4.980
10.00	2.586	0.3233	7.234
15.85	3.944	0.5113	11.04
19.95	4.842	0.6430	13.55

1-mil Dielectric

Frequency, mc	$10^3\alpha_{T1}$ nepers/meter	$\beta_{T1}$ radian/meter	Total Attenuation, db/1057 ft.
0.1000	0.5109	0.003331	1.429
0.1585	0.5330	0.005232	1.491
0.2512	0.5565	0.008248	1.557
0.3981	0.5867	0.01303	1.642
0.6310	0.6308	0.02060	1.765
1.000	0.6999	0.03258	1.958
1.585	0.8098	0.05155	2.266
2.512	0.9770	0.08156	2.734
3.981	1.232	0.1290	3.447
6.310	1.663	0.2042	4.652
10.00	2.439	0.3232	6.825
15.85	3.762	0.5112	10.53
19.95	4.368	0.6428	12.98

TABLE III — TWO-CONDUCTOR LINE —  $\gamma = \alpha + j\beta$ 

Frequency, mc	$10^3\alpha$ nepers/meter	$\beta$ radian/meter	Total Attenuation, db/1057 ft.
0.1000	0.3350	0.003342	0.9373
0.2000	0.4252	0.006549	1.190
0.4000	0.5547	0.01292	1.552
0.7000	0.7055	0.02242	1.974
1.000	0.8344	0.03188	2.335
2.000	1.186	0.06332	3.320
4.000	1.687	0.1259	4.721
7.000	2.227	0.2197	6.232
10.00	2.659	0.3133	7.441
14.00	3.145	0.4380	8.799
20.00	3.756	0.6250	10.51
25.00	4.198	0.7808	11.75

In the case of infinitesimal spacing of transpositions, the propagation constant  $\gamma_{T1}$  for the low-loss mode was computed from (35) for both the actual cable and a hypothetical one in which the intermediate conductor was separated from the inner conductor by only 1 mil instead of 5 mils. These quantities appear at the end of Table II.

In order to have a calculated curve to compare these two results with, the propagation constant of the two-conductor reference cable was also computed by modifying the process used for the uniform line. These quantities are shown in Table III.

The numbers delivered by the computer were rounded off to four significant digits in Tables II and III. In the table of results for the 9 ft  $3\frac{1}{4}$  in. interval, the values for infinitesimal spacing were used up to 1 mc because the eight-digit precision of the computer was not sufficient to calculate the roots of (32) at these frequencies. At 1 mc the two methods give answers differing by about 0.1 per cent.

#### VII. ACKNOWLEDGMENT

The project described in this paper involved the efforts of so many people over such a long period of time that individual mention of their contributions is impossible. Certain individuals have been named at appropriate places in the text. In addition, we owe a debt to W. H. Doherty, R. K. Potter and R. L. Wallace, who stimulated this project in its early stages; to C. V. LoBianco, who made many contributions to the fabrication, measurement and computations; to P. H. Smith and J. M. Olsen; and to the members and former members of the Transmission Research, Outside Plant Development and Mathematical Research Departments of Bell Telephone Laboratories, without whose cooperation



and assistance this project could not have been carried to a successful conclusion.

## REFERENCES

1. Carson, J. R. and Gilbert, J. J., Transmission Characteristics of the Submarine Cable, B.S.T.J., **1**, July 1922, pp. 89-115.
2. Schelkunoff, S. A., The Electromagnetic Theory of Coaxial Transmission Lines and Cylindrical Shields, B.S.T.J., **13**, October 1934, pp. 532-579.
3. Terman, H. E., *Radio Engineer's Handbook*, McGraw-Hill, New York, 1943, p. 37.
4. Green, E. I., Liebe, F. A. and Curtis, H. E., The Proportioning of Shielded Circuits for Minimum High-Frequency Attenuation, B.S.T.J., **15**, April 1936, pp. 248-283.
5. Butterworth, S., Eddy-Current Losses in Cylindrical Conductors, Trans. Roy. Soc. (London), **222**, May 1922, pp. 57-100.
6. Beckenbach, E. F., ed., *Modern Mathematics for the Engineer*, McGraw-Hill, New York, 1956, pp. 307-345. (Author of this section is L. A. Pipes.)
7. Guillemin, E. A., *The Mathematics of Circuit Analysis*, Wiley, New York, 1949.

# Synthesis of Series-Parallel Network Switching Functions

By WARREN SEMON\*

(Manuscript received February 13, 1958)

*From the switching functions of  $n$  variables, those which correspond to networks are abstracted and called network functions. Properties of those network functions corresponding to series-parallel networks are studied and a method for synthesis is developed.*

## I. INTRODUCTION

It is known that one may establish a mathematical model in which Boolean polynomials explicitly represent two terminal single-impulse series-parallel contact networks. The conventions used in this paper are Boolean plus, symbolized by  $\oplus$ , to represent parallel connection; Boolean times, symbolized by  $\cdot$  or by juxtaposition, to represent series connection; zero, to represent an open circuit; and one, to represent a closed circuit. The symbol  $'$  is used to represent Boolean negation, also called "inversion" or "complementation." Whenever  $f$  represents an open circuit,  $f'$  represents a closed circuit and conversely. This is a conductance analogue, the dual of that used by Shannon.<sup>1</sup> If  $f(x_1, x_2, \dots, x_n)$  is a switching function it may be represented in tabular form<sup>2</sup> as a "canonical-form matrix" whose rows consist of those configurations of the variables for which  $f = 1$ , as shown below for the function

$$f = x_1'(x_2' \oplus x_3') = x_1'x_2'x_3' \oplus x_1'x_2'x_3 \oplus x_1'x_3x_3'.$$

$x_1$	$x_2$	$x_3$
0	0	0
0	0	1
0	1	0

\* The Computation Laboratory of Harvard University, Cambridge, Mass.

*Definition 1*

A "series-parallel" network is a series or parallel combination of two series-parallel networks; a single element is a series-parallel network.<sup>3</sup>

*Definition 2*

A "network" function is a switching function of  $n$  variables, having no vacuous variables, which can be realized by a network containing  $n$  switches.

As an example:  $f(x_1, x_2, x_3, x_4) = x_1x_2' \oplus x_3'x_4$  is a network function. A four-switch realization is shown in Fig. 1.

*Definition 3*

A "series-parallel network function" is a network function at least one of whose  $n$ -switch realizations is a series-parallel network.

The network of Fig. 1 is series-parallel, hence the corresponding function is a series-parallel network (SPN) function.

In what follows we will be concerned with the characterization of SPN functions and the synthesis of the networks to which they correspond. It should be noted that, although series-parallel networks comprise a small subclass of the class of all relay contact networks,<sup>3</sup> there are other types of switching elements for which they represent the only electrically useful networks.

## II. GENERAL THEORY

*Theorem 1*

*The inverse of any SPN function is also an SPN function.*

*Proof:* A Boolean expression may be derived which corresponds explicitly



Fig. 1 — Four-switch realization.

to the series-parallel realization of the function.<sup>4</sup> DeMorgan's law, when applied to this expression, yields a Boolean expression which exactly corresponds to a series-parallel  $n$ -switch realization of the inverse function.

Theorem 1 may be extended to cover all network functions whose  $n$ -switch realizations are planar.<sup>5</sup>

#### Theorem 2

*A minimum generating set\* of network functions of  $n$  variables may be put into a one-to-one correspondence with the distinct† networks of  $n$  elements. A proof of this theorem has been given by Ashenurst.<sup>6</sup> Some implications should be noted explicitly: (a) the  $n$ -switch realization of a network function is unique, and (b) only network functions correspond to networks.*

#### Theorem 3

*Suppose that  $f(x_1, x_2, \dots, x_n)$  is an SPN function. Then  $f$  can be expressed as an SPN function of the variables  $\alpha_1, \alpha_2, \dots, \alpha_k$ , where each  $\alpha$  is itself an SPN function of the variables in one of  $k$  nonoverlapping subsets of the variables  $x_1, x_2, \dots, x_n$ .*

*Proof:* This is obvious from the definitions of SPN function and series-parallel network.

#### Theorem 4

*Let  $f(x_1, x_2, \dots, x_n)$  be an SPN function which in canonical form has  $m$  terms. Let  $f$  be expressed as an SPN function  $F(\alpha_1, \alpha_2, \dots, \alpha_k)$ ,  $k \leq n$ , where each  $\alpha_i$  is itself an SPN function of  $S_i$  variables with  $m_i$  terms in its canonical form (as a function of its  $S_i$  variables only). In the canonical form of  $F(\alpha_i)$ , replace each  $\alpha_i$  by  $m_i$ , each  $\alpha_i'$  by  $m_i' = 2^{S_i} - m_i$ , each Boolean  $\oplus$  by algebraic  $+$  and each Boolean  $\cdot$  by algebraic  $\cdot$ ; then the result is  $m$ .*

*Proof:* It is only necessary to prove the theorem for two variables, since Definition 1 and Theorem 3 may then be used to complete an inductive proof. Suppose  $f$  equals  $\alpha_1 \alpha_2$ .‡ Each term of the canonical form of  $f$  may be formed by selecting one of the  $m_1$  terms of  $\alpha_1$  and one of the  $m_2$  terms

\* The group of variable transformations (permutations and inversions of the variables) divides any class of switching functions into  $N$  nonoverlapping subsets, called equivalence classes; a set of  $N$  functions, one from each equivalence class, is called a "minimum generating set."

† Two networks are "distinct" if one is not derivable from the other by transformations consisting of the reversal of two-terminal subnetworks.

‡ Such a function is said to be "essentially series."

of  $\alpha_2$ . All such terms must appear, and no others can. Hence  $m$  equals  $m_1 m_2$ .

Now suppose  $f$  equals  $\alpha_1 \oplus \alpha_2$ .<sup>\*</sup> For each of the  $m_1$  terms of  $\alpha_1$  there are  $2^{s_2}$  configurations of the variables of  $\alpha_2$  which appear in the canonical form of  $f$ ; similarly,  $2^{s_1}$  configurations of the variables of  $\alpha_1$  are associated with each of the  $m_2$  terms of  $\alpha_2$ . This gives  $2^{s_1} m_2 + 2^{s_2} m_1$  terms. Of these,  $m_1 m_2$  are duplicates. Hence

$$\begin{aligned} m &= 2^{s_1} m_2 + 2^{s_2} m_1 - m_1 m_2, \\ &= m_1 m_2' + m_1' m_2 + m_1 m_2. \end{aligned}$$

#### Theorem 5

If  $f(x_1, \dots, x_n)$  is any SPN function, and  $m$  is the number of terms in its canonical form, then  $m$  is odd.

*Proof:* By induction on  $n$ . The theorem may be verified by inspection for the cases  $n = 1$  and  $n = 2$ .

Now assume the theorem true for all  $k < n$ . Consider an arbitrary SPN function of  $n$  variables. It can be expressed either as  $\alpha_1 \alpha_2$  or as  $\alpha_1 \oplus \alpha_2$ , where  $\alpha_1$  and  $\alpha_2$  are SPN functions of fewer than  $n$  variables. Again let  $m_1$  be the number of terms of  $\alpha_1$  and  $m_2$  the number of terms of  $\alpha_2$ . Then

$$m = m_1 \cdot m_2$$

is odd, or

$$m = 2^{s_2} m_1 + 2^{s_1} m_2 - m_1 m_2$$

is odd, since  $m_1$  and  $m_2$  are odd by the inductive hypothesis. This proves the theorem.

#### Corollary

It follows immediately that any network function for which  $m$  is even has only a bridge circuit realization.

As an example, consider the function  $f(x_1, x_2, x_3, x_4, x_5)$ , whose canonical-form matrix is given in Fig. 2 ( $m = 16$ ). It has the five-switch realization shown, but no series-parallel five-switch realization.<sup>†</sup>

It is reasonable to ask whether an odd number of terms in the canonical form of a network function implies that its realization is series-parallel. This is not so, as may be seen from the following example.

<sup>\*</sup> Such a function is said to be "essentially parallel."

<sup>†</sup> Note that Theorem 2 asserts that there is no other five-switch realization of this function.

The function  $F(x_1, x_2, x_3, x_4, x_5, x_6, x_7)$ , whose canonical-form matrix and seven-switch realization are shown in Fig. 3, has  $m = 59$  but the network is not series-parallel.

*Theorem 6<sup>7, 8</sup>*

The function  $f(x_1, x_2, \dots, x_n)$  defined by  $f_i = 1, i = 0, 1, \dots, m-1$  and  $f_i = 0$  for  $i \geq m$  is an SPN function for  $m$  odd.

$x_1$	$x_2$	$x_3$	$x_4$	$x_5$
0	0	0	0	0
0	0	0	0	1
0	0	0	1	0
0	0	0	1	1
0	0	1	0	0
0	0	1	0	1
0	0	1	1	0
0	0	1	1	1
0	1	0	0	0
0	1	0	0	1
0	1	0	1	0
1	0	0	0	0
1	0	0	0	1
1	0	1	0	0
1	1	0	0	0
1	1	0	0	1

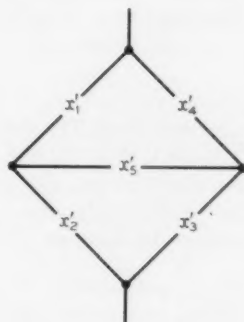


Fig. 2 — Five-switch realization.

#### Definition 4

The SPN function defined by  $f_i = 1, i = 0, 1, \dots, m-1$  and  $f_i = 0$  for  $i \geq m, m$  odd, is called a "canonical-form network function."

All SPN functions of one, two and three variables are, to within a variable transformation, canonical-form network functions. The first SPN functions which are not canonical-form network functions appear in four variables. Such functions may be characterized by the following discussion.

Consider the Boolean expression for an SPN function which explicitly represents<sup>4</sup> the  $n$ -switch series-parallel network for the function. Then

- i. There may exist a variable  $x$  such that  $f = xg$ , with  $g$  an SPN function.

\* Here,  $f_i$  is the value of the function for the configuration of the variables which would represent the integer  $i$  in the dyadic number system.

- ii. There may exist a variable  $x$  such that  $f = x \oplus g$ , with  $g$  an SPN function.
- iii. The function may be such that no  $x$  exists which satisfies either i or ii.

In cases i and ii the function is said to be "reducible"; in case iii, "irreducible."

If a function is reducible, then the "residue" function  $g$  may be examined for reducibility. For any SPN function such reduction will ultimately lead to a residue function which is (a) a single variable, or (b) irreducible and a function of more than one variable. An SPN function whose ultimate residue function is a single variable is said to be "completely reducible."

#### Theorem 7

*An SPN function is, to within a variable transformation, a canonical-form network function if and only if it is completely reducible.*

*Proof:* By induction on  $n$ , the number of variables. For  $n = 1$  and  $n = 2$  the theorem is obviously true.

Now assume the theorem true for all  $k < n$ . Suppose  $f$  to be an SPN

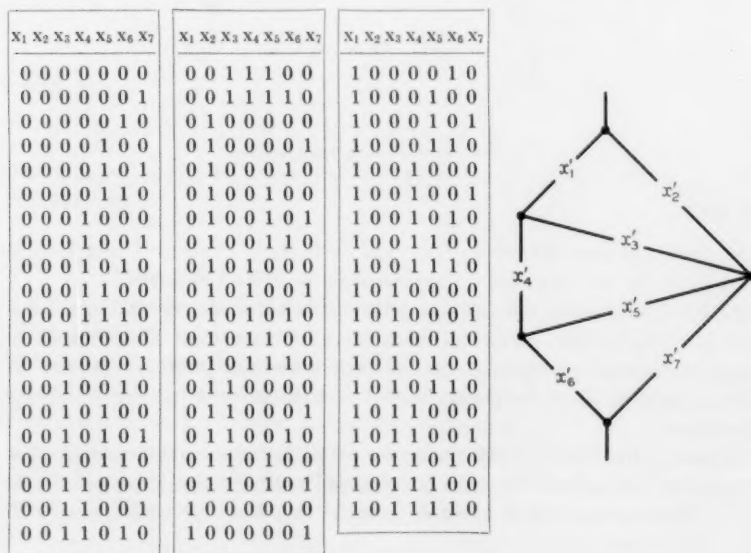


Fig. 3 — Seven-switch realization.



function of  $n$  variables which is completely reducible. Then either  $f = x'g$  or  $f = x' \oplus g$ , and  $g$  is a completely reducible SPN function of  $n - 1$  variables. The inductive hypothesis then guarantees that  $f$  is a canonical-form network function.

Suppose now that  $f$  is a canonical-form network function of  $m$  terms.

- (a) If  $m < 2^{n-1}$ , then  $f$  equals  $x_n'g(x_1, \dots, x_{n-1})$ , where  $g$  is a canonical-form network function.
- (b) If  $m > 2^{n-1}$ , then  $f$  equals  $x_n' \oplus g(x_1, \dots, x_{n-1})$ , where  $g$  is a canonical-form network function.

In both cases, the inductive hypothesis guarantees that  $g$  is completely reducible, hence so is  $f$ . This proves the theorem.

The irreducible SPN functions of  $n$  variables are a set of some interest. One question occurs immediately: How many such functions are there? This may be answered as follows.

Let  $S_n$  be the number of functions in a minimum generating set of SPN functions of  $n$  variables. Since, by Theorem 2, the correspondence between functions and networks is one-to-one,  $S_n$  is the number of series-parallel networks of  $n$  elements.\* Let  $i_n$  be the number of functions in a minimum generating set of irreducible SPN functions of  $n$  variables.

#### Theorem 8

$$i_{n+1} = S_{n+1} - 2S_n.$$

*Proof:*  $S_n$  is the number of series-parallel networks of  $n$  elements, and  $i_n$  is the number of series-parallel networks of  $n$  elements which have no single elements in series or in parallel with the entire network. Form networks of  $n + 1$  elements by adding a single element in series to each of the  $S_n$  networks of  $n$  elements; form the corresponding set by adding one element in parallel. There are  $2S_n$  such  $n + 1$  element networks. None of these corresponds to an irreducible function. If the networks corresponding to all the irreducible functions are now adjoined, giving  $2S_n + i_{n+1}$ , this includes all the SPN functions of  $n + 1$  variables, since any reducible function is included in the set of  $2S_n$  functions, and all irreducible functions are included in the set of  $i_{n+1}$  functions. Hence  $S_{n+1} = 2S_n + i_{n+1}$ . It is obvious that there are  $2^{n-1}$  completely reducible SPN functions of  $n$  variables since they are canonical-form network functions, and these correspond to the odd integers  $m$ ,  $1 \leq m \leq 2^n$ . The remaining SPN functions of  $n$  variables are each either irreducible or reducible to some irreducible function. Theorem 9 exhibits this division.

\* These numbers are discussed in Ref. 3.

## Theorem 9

$$S_n = 2^{n-1} + i_n + \sum_{j=1}^{n-2} i_{j+1} 2^{n-j-1}.$$

- (a) The term  $2^{n-1}$  represents the canonical-form network functions of  $n$  variables.  
 (b) The term  $i_n$  represents the irreducible SPN functions of  $n$  variables.  
 (c) The remaining terms

$$\sum_{j=1}^{n-2} i_{j+1} 2^{n-j-1}$$

represent the SPN functions which are reducible to irreducible functions of more than one variable. To prove Theorem 9, it is only necessary to solve<sup>9</sup> the difference equation,  $S_{n+1} - 2S_n = i_{n+1}$ . Table I shows the numbers of interest for  $n = 1(1)10$ .

Let  $f(x_i)$  be a function of  $n$  variables, represented by a canonical-form matrix of zeros and ones ( $n$  columns,  $m$  rows), as in Section I. Let  $m_{i0}$  and  $m_{i1} = m - m_{i0}$  be equal to the number of zeros and ones respectively in the  $x_i$  column of the matrix.

## Theorem 10

If  $f(x_i)$  is an SPN function, it is a function of  $x_j'$  or  $x_j$  according as  $m_{i1}$  or  $m_{i0}$  is the lesser.

TABLE I

$n$	$S_n$	$i_n$	$r_n = \sum_{j=1}^{n-2} i_{j+1} 2^{n-j-1}$	$C_n$
1	1	0	0	1
2	2	0	0	2
3	4	0	0	4
4	10	2	0	8
5	24	4	4	16
6	66	18	16	32
7	180	48	68	64
8	522	162	232	128
9	1532	488	788	256
10	4624	1560	2552	512

$S_n$  = total number (taken from Ref. 3) of SPN functions in a minimum generating set.

$i_n$  = number of irreducible SPN functions in a minimum generating set.

$r_n$  = number of reducible but not completely reducible SPN functions in a minimum generating set.

$C_n$  = number of completely reducible SPN functions in a minimum generating set.

*Proof:* By hypothesis,  $f$  can be written as  $f = x_j^* A \oplus B$ , where (a)  $x_j^*$  is either  $x_j$  or  $x_j'$ ; (b)  $A$  and  $B$  are functions of the remaining variables only. Then

$$\begin{aligned} f &= x_j^* A \oplus x_j^* B \oplus x_j^{*'} B \\ &= x_j^* (A \oplus B) \oplus x_j^{*'} B. \end{aligned}$$

Since  $B \leq A \oplus B$ , the number of terms in  $B$  is equal to or less than the number of terms in  $A \oplus B$ . Now suppose that  $x_j^*$  be equal to  $x_j$ , then  $f = x_j(A \oplus B) \oplus x_j' B$ . But the number of terms in  $B$  is  $m_{j0}$ , and the number of terms in  $(A \oplus B)$  expanded as a function of all  $n - 1$  variables is  $m_{j1}$ , hence  $m_{j0} \leq m_{j1}$ . But  $m = m_{j0} + m_{j1}$  is odd, hence  $m_{j0} < m_{j1}$ .

Similarly, if  $x_j^* = x_j'$ ,  $m_{j0}$  is the number of terms in  $(A \oplus B)$  and  $m_{j1}$  is the number of terms in  $B$ , so that  $m_{j1} \leq m_{j0}$ . Again, the equality is impossible, so that  $m_{j1} < m_{j0}$ . This completes the proof.

As an example, consider the series-parallel network shown in Fig. 4. The corresponding function is

$$f(x) = x_1'(x_4 \oplus x_2'x_3),$$

and the canonical-form matrix for  $f$  is:

$x_1$	$x_2$	$x_3$	$x_4$
0	0	0	1
0	0	1	0
0	0	1	1
0	1	0	1
0	1	1	1

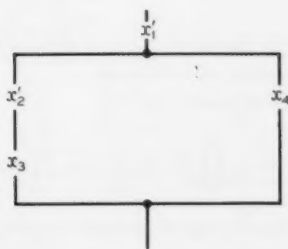


Fig. 4 — Network for  $f(x) = x_1'(x_4 \oplus x_2'x_3)$ .

The counts for each element are:

$j$	$m_{j0}$	$m_{j1}$
1	5	0
2	3	2
3	2	3
4	1	4

By Theorem 10,  $f$  is a function of  $x_1', x_2', x_3$  and  $x_4$ , and this is clearly true.

Consider any element  $x_j$  in a series-parallel network. Let  $A_1$  represent all of that part of the network which is in parallel with  $x_j$ . Let  $B_1$  represent all of that part of the network which is in series with the parallel combination of  $A_1$  and  $x_j$ . Let  $g_1$  be equal to  $B_1(A_1 \oplus x_j)$ . In general, let  $A_i$  be that part of the network which is in parallel with  $g_{i-1}$ , and  $B_i$  be that part of the network which is in series with the parallel combination of  $A_i$  and  $g_{i-1}$ . Then an SPN function  $f$  may be expressed as:

$$f = x_j \prod_{i=1}^N B_i \oplus \sum_{k=1}^N A_k \prod_{i=k}^N B_i,*$$

where  $A_i$  and  $B_i$  are SPN functions of distinct variables (see Fig. 5);  $A_1$  may be the trivial function 0, while  $B_N$  may be the trivial function 1.

#### Definition 5

$x_j$  is said to be a "series" element if and only if  $A_1 \equiv 0$ , and  $x_j$  is said to be a "parallel" element if and only if  $A_1 \neq 0$ .

#### Theorem 11

In the circuit for an SPN function,  $x_j$  is a series (parallel) element if and only if the lesser of  $m_{j0}$  and  $m_{j1}$  is even (odd).

*Proof:* Suppose that  $f$  is expressed as:

$$f = x_j \prod_{i=1}^N B_i \oplus \sum_{k=1}^N A_k \prod_{i=k}^N B_i,$$

with  $A_i$  and  $B_i$  SPN functions of nonoverlapping subsets of the vari-

\* Henceforth the symbol  $\Sigma$  will be used to signify extended application of the operation  $\oplus$ .

ables. Then

$$\begin{aligned} f(x_j = 1, A_i, B_i) &= \prod_{i=1}^N B_i \oplus \sum_{k=1}^N A_k \prod_{i=k}^N B_i \\ &= \prod_{i=1}^N B_i \oplus A_1 \prod_{i=1}^N B_i \oplus \sum_{k=2}^N A_k \prod_{i=k}^N B_i. \end{aligned}$$

Clearly  $A_1$  is a vacuous variable in this function, and wherever  $A_1 P$  appears in the canonical form  $A_1' P$  appears also ( $P$  is a product involving  $A_2, \dots, A_N, B_1, \dots, B_N$  and their primes). Hence, if  $m_{A_1}$  is the number of terms in  $A_1$  and  $A_1$  is a function of  $S_{A_1}$  variables, then, by Theorem 4,  $m_{A_1} + m_{A_1}' = 2^{S_{A_1}}$  is a factor of  $m_{j1}$ . If  $A_1 \neq 0$ , then  $S_{A_1} \neq 0$ , hence  $m_{j1}$  is even and  $m_{j0}$  odd.

Now suppose  $A_1$  is identically equal to 0, then

$$\begin{aligned} f(x_j = 0, A_i, B_i) &= \sum_{k=1}^N A_k \prod_{i=k}^N B_i \\ &= A_1 \prod_{i=1}^N B_i \oplus \sum_{k=2}^N A_k \prod_{i=k}^N B_i \\ &= \sum_{k=2}^N A_k \prod_{i=k}^N B_i, \end{aligned}$$

and clearly  $B_1$  is vacuous. Hence,  $m_{B_1} + m_{B_1}' = 2^{S_{B_1}}$  is a factor of  $m_{j0}$ ,

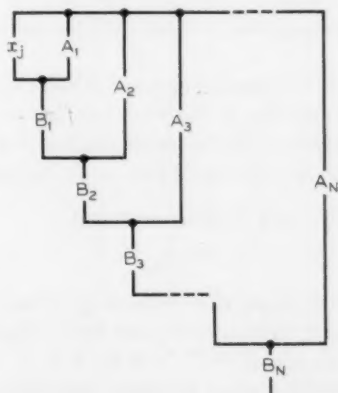


Fig. 5 — Network for  $f = x_j \prod_{i=1}^N B_i \oplus \sum_{k=1}^N A_k \prod_{i=k}^N B_i$

and  $m_{j0}$  is even,  $m_{j1}$  odd. (Note that  $S_{A_1} = S_{B_1} = 0$  implies  $f \equiv 0$ ; this case need not be considered.)

### Theorem 12

If two elements  $x_j$  and  $x_k$  are in series or in parallel, then  $m_{j0}$  equals  $m_{k0}$  and  $m_{j1}$  equals  $m_{k1}$ .

*Proof:* If the function is expanded as

$$f = x_j x_k \prod_{i=1}^N B_i \oplus \sum_{k=1}^N A_k \prod_{i=k}^N B_i$$

or as

$$f = (x_j \oplus x_k) \prod_{i=1}^N B_i \oplus \sum_{k=1}^N A_k \prod_{i=k}^N B_i,$$

and Theorem 4 is applied, the result follows immediately.

It should be noted that the converse is not true; that is,  $m_{j0} = m_{k0}$  and  $m_{j1} = m_{k1}$  does not necessarily imply that  $x_j$  and  $x_k$  are in series or in parallel. This will be seen in one of the examples which will be given.

### Theorem 13

One of  $m_{j0}$  and  $m_{j1}$  is even; call this  $\bar{m}$ . Let  $k$  be the largest integer such that  $2^k \mid \bar{m}$ .<sup>\*</sup> Then  $k$  is the number of switches in the subnetwork which is in series or in parallel with  $x_j$ .

*Proof:* Suppose that  $f$  is a function of  $x_j$  (not of  $x_j'$ ). This assumption is irrelevant in the argument, and is made only for the sake of definiteness. Then  $m_{j0} < m_{j1}$ .

*Case 1:* Suppose that  $x_j$  is a parallel element. Then  $m_{j0}$  is odd, by Theorem 11, hence  $\bar{m} = m_{j1}$ . Clearly, in the function  $f(x_j = 1, A_i, B_i)$ ,  $A_1$  is a vacuous variable. Therefore, in the canonical form of  $f(x_j = 1, A_i, B_i)$  wherever  $A_1'P$  appears so does  $A_1P$ . Hence, by Theorem 4,

$$\begin{aligned} m_{j1} &= (m_{A_1} + m_{A_1'})C \\ &= 2^{S_{A_1}}C. \end{aligned}$$

But  $C$  is odd (if it were even, then removing the subfunction  $A_1$  would make  $x_j$  a series element, with  $m_{j0}$  odd, and this is impossible by Theorem 11). Therefore  $2^{S_{A_1}} \mid \bar{m}$ , and  $2^{(S_{A_1} + k)} \nmid \bar{m}$  for  $k = 1, 2, \dots$ .

*Case 2:* If  $x_j$  is supposed a series element, then clearly  $\bar{m} = m_{j0}$ . Also  $B_1$  is vacuous in  $f(x_j = 0, A_i, B_i)$ . (Note that  $A_1 \equiv 0$  by hypoth-

<sup>\*</sup> $a \mid b$  as usual means "a divides b";  $a \nmid b$  means "a does not divide b."

esis.) A similar argument shows that  $2^{s_{B_1}} \mid \bar{m}$ , while  $2^{(s_{B_1}+k)} \nmid \bar{m}$  for  $k = 1, 2, \dots$ . This proves the theorem.

#### Theorem 14

Consider an SPN function  $f$ . Of  $f$  and  $f'$ , one is essentially series, say  $f$ . Then  $f$  may be expressed as  $f = \alpha \cdot \beta$ , where  $\alpha, \beta$  are SPN functions of nonoverlapping subsets of the variables. If  $\alpha$  equals  $\alpha(x_j)$ , then  $m_\beta \mid m_{j0}$  and  $m_\beta \mid m_{j1}$ ; if  $\beta$  equals  $\beta(x_j)$ , then  $m_\alpha \mid m_{j0}$  and  $m_\alpha \mid m_{j1}$ .

*Proof:* If  $\alpha$  equals  $\alpha(x_j)$  then  $m_\beta \mid m_{j0}$  and  $m_\beta \mid m_{j1}$ , since every term in the canonical form of  $\alpha$  (as a function of its subset of the variables) is repeated in the canonical form of  $f$  exactly  $m_\beta$  times.

### III. SYNTHESIS

Consider the function defined by the canonical-form matrix:

$x_1$	$x_2$	$x_3$	$x_4$	$x_5$
0	1	0	1	1
0	1	1	0	0
0	1	1	0	1
0	1	1	1	0
0	1	1	1	1
1	0	0	1	1
1	0	1	0	0
1	0	1	0	1
1	0	1	1	0
1	0	1	1	1
1	1	0	1	1
1	1	1	0	0
1	1	1	0	1
1	1	1	1	0
1	1	1	1	1

Suppose it is given that this function is an SPN function, and it is required to find the network.

Table II shows the counts for each variable and the information which is derived from these counts by application of Theorems 10 through 14.



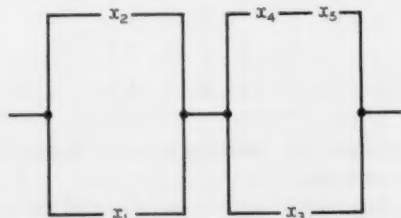
TABLE II

$j$	$m_{j0}$	$m_{j1}$	Variable	Series or Parallel	$k$	Prime Factorization of	
						$m_{j0}$	$m_{j1}$
1	5	10	$x_1$	P	1	5	2, 5
2	5	10	$x_2$	P	1	5	2, 5
3	3	12	$x_3$	P	2	3	3, $2^2$
4	6	9	$x_4$	S	1	2, 3	$3^2$
5	6	9	$x_5$	S	1	2, 3	$3^2$

The column headed "variable" is filled in by applying Theorem 10. Since in every case  $m_{j0} < m_{j1}$ , only unprimed variables occur. The column headed "series or parallel" is filled in by applying Theorem 11. Since  $m_{10}$ ,  $m_{20}$  and  $m_{30}$  are odd,  $x_1$ ,  $x_2$  and  $x_3$  are parallel elements;  $x_4$  and  $x_5$  are series elements, since  $m_{40}$  and  $m_{50}$  are even. The column headed " $k$ " is filled in for use in applying Theorem 13. Since  $2 \mid 10$  and  $4 \nmid 10$ , the values for  $x_1$  and  $x_2$  are 1. Also  $4 \mid 12$  and  $8 \nmid 12$  gives  $k = 2$  for  $x_3$ . Similarly for  $x_4$  and  $x_5$  the values are 1. The last two columns give the prime factors of  $m_{j0}$  and  $m_{j1}$ . Since  $m_{11} = m_{21} = 10$  and each of  $x_1$  and  $x_2$  is in parallel with a single switch and since no other  $m_{j1}$  equals 10,  $x_1$  and  $x_2$  are in parallel, i.e.,  $(x_1 \oplus x_2)$  represents a component of the network. Similarly  $(x_4 \cdot x_5)$  represents a component. Since  $x_3$  is in parallel with a two-switch network but not in parallel with  $x_1$  (by Theorem 12), it must be in parallel with  $x_4 \cdot x_5$ . Hence  $(x_3 \oplus x_4 x_5)$  represents a component. Since  $x_3$  cannot be in parallel with  $x_1$ , these two components must be in series, therefore  $f = (x_1 \oplus x_2)(x_3 \oplus x_4 x_5)$  and the network is as shown in Fig. 6. Note that if  $\alpha$  equals  $(x_1 \oplus x_2)$  and  $\beta$  equals  $(x_3 \oplus x_4 x_5)$ , then  $m_\alpha = 3$ ,  $m_\beta = 5$  and

$$\begin{array}{cccccc} m_\beta \mid m_{10}, & m_\beta \mid m_{11}, & m_\beta \mid m_{20}, & m_\beta \mid m_{21}, & m_\beta \mid m_{30}, \\ m_\alpha \mid m_{31}, & m_\alpha \mid m_{40}, & m_\alpha \mid m_{41}, & m_\alpha \mid m_{50}, & m_\alpha \mid m_{51}, \end{array}$$

as required by Theorem 14. If Theorems 10 through 14 are to be applied mechanically, the following fact should be noted. Once it has been deter-

Fig. 6 — Network for  $f = (x_1 \oplus x_2)(x_3 \oplus x_4 x_5)$ .

mined that  $(x_1 \oplus x_2)$  and  $x_4x_5$  represent components, these combinations may be treated as single elements; the canonical form may then be modified and the count repeated. For example, let  $A$  equal  $(x_1 \oplus x_2)$  and  $B$  equal  $x_4x_5$ . Then the original canonical form may be rewritten (in two steps) as

$A$	$x_3$	$x_4$	$x_5$
1	0	1	1
1	1	0	0
1	1	0	1
1	1	1	0
1	1	1	1

and this function is obviously  $A(x_3 \oplus B)$ .

Consider the canonical-form matrix:

[illegible]

TABLE III

$j$	$m_{j0}$	$m_{j1}$	Variable	S or P	$k$	Prime Factorization of	
						$m_{j0}$	$m_{j1}$
1	30	75	$x_1$	S	1	2, 3, 5	3, 5 <sup>2</sup>
2	75	30	$x_2'$	S	1	3, 5 <sup>2</sup>	2, 3, 5
3	30	75	$x_3$	S	1	2, 3, 5	3, 5 <sup>2</sup>
4	30	75	$x_4'$	S	1	2, 3, 5	3, 5 <sup>2</sup>
5	63	42	$x_5'$	S	1	3 <sup>2</sup> , 7	2, 3, 7
6	63	42	$x_6'$	S	1	3 <sup>2</sup> , 7	2, 3, 7
7	21	84	$x_7$	P	2	3, 7	2 <sup>2</sup> , 3, 7
8	70	35	$x_8'$	P	1	2, 5, 7	5, 7
9	35	70	$x_9$	P	1	5, 7	2, 5, 7

This gives Table III. It is evident that

- i. one of  $x_1x_2'$ ,  $x_1x_3$ ,  $x_1x_4$  appears in the network;
- ii.  $x_5'x_6'$  appears in the network;
- iii.  $x_8' \oplus x_9$  appears in the network.

In order to select the correct one of  $x_1x_2'$ ,  $x_1x_3$ ,  $x_1x_4$ , Table IV is constructed. Note that if  $xy$  is to be a component it must be possible to substitute  $A$  for  $xy$  in the canonical form. Then a count can be made of  $m_{A0}$  and  $m_{A1}$ . But  $A$  equals zero implies three terms as shown:

$$A = 1$$

$xy$
11

$$A = 0$$

$xy$
00
01
10

Therefore, the number of occurrences of  $xy = 00$ ,  $xy = 01$  and  $xy = 10$  must all be equal. Clearly, in the example only the combination  $x_1x_2'$  satisfied this requirement. This implies that  $x_1x_2'$  and  $x_3x_4$  represent

TABLE IV

	00	01	10	11
$x_1x_2$	15	15	60	15
$x_1x_3$	0	30	30	45
$x_1x_4$	0	30	30	45

components. Reducing the canonical form in terms of the new variables

$$y_1 = x_1 x_2'$$

$$y_2 = x_3 x_4$$

$$y_3 = x_5' x_6'$$

$$y_4 = x_7$$

$$y_5 = x_8' \oplus x_9$$

gives the following matrix:

$y_1$	$y_2$	$y_3$	$y_4$	$y_5$
0	1	0	1	1
0	1	1	0	1
0	1	1	1	1
1	0	0	1	1
1	0	1	0	1
1	0	1	1	1
1	1	0	1	1
1	1	1	0	1
1	1	1	1	1

Analysis of the counts for this matrix is shown in Table V. A count for  $y_1 y_2$ ,  $y_1 y_3$ ,  $y_1 y_4$  yields Table VI. Therefore  $z_1 = x_1 x_2' \oplus x_3 x_4$ ,  $z_2 = x_5' x_6' \oplus x_7$ , and  $z_3 = x_8' \oplus x_9$  represent components. Again reducing the canonical-form matrix leads to

$z_1$	$z_2$	$z_3$
1	1	1

Hence the function is

$$f = (x_1 x_2' \oplus x_3 x_4) (x_5' x_6' \oplus x_7) (x_8' \oplus x_9)$$

and the network is as shown in Fig. 7.

It should be noted that an attempt to apply Theorems 10 through 14 to a non-SPN function will lead to a contradiction. For example, the function whose canonical-form matrix and bridge network are shown in

TABLE V

$j$	$m_{j0}$	$m_{j1}$	Variable	S or P	$k$	Prime Factorization of	
						$m_{j0}$	$m_{j1}$
1	3	6	$y_1$	P	1	3	3, 2
2	3	6	$y_2$	P	1	3	3, 2
3	3	6	$y_3$	P	1	3	3, 2
4	3	6	$y_4$	P	1	3	3, 2
5	0	9	$y_5$	S	—	—	$3^2$

TABLE VI

	00	01	10	11
$y_1 y_2$	0	3	3	3
$y_1 y_3$	1	2	2	4
$y_1 y_4$	1	2	2	4

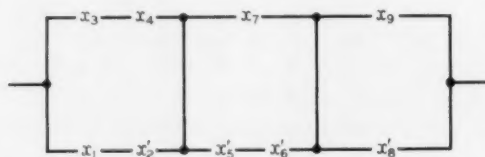
Fig. 7 — Network for  $f = (x_1 x_2' \oplus x_3 x_4) (x_5' x_6' \oplus x_7) (x_8' \oplus x_9)$ .

TABLE VII

$j$	$m_{j0}$	$m_{j1}$	Variable	S or P	$k$
1	38	21	$x_1'$	P	1
2	43	16	$x_2'$	S	4
3	33	26	$x_3'$	S	1
4	34	25	$x_4'$	P	1
5	33	26	$x_5'$	S	1
6	38	21	$x_6'$	P	1
7	43	16	$x_7'$	S	4

Fig. 3 yields Table VII. If this function is to be an SPN function,  $x_4'$  must be in parallel with a one-element subnetwork. But no other element exists with the number pair (34,25) as  $(m_{j0}, m_{j1})$ , and this contradicts Theorem 12.

The results produced thus far by this investigation suggest many intriguing possibilities. For example, if a function is not an SPN function because it requires both  $x_j$  and  $x_j'$  contacts, can rules be derived for

augmenting the canonical form of the given function so as to produce the canonical form of a new function which (a) is an SPN function of  $n + 1$  variables and (b) reduces to the given function when the new variable is replaced by  $x_i'$ ? Obviously this notion can be extended to cover all functions by introducing a large enough number of new variables. That this is not a trivial question is shown by the following example:

Let  $f(x_1, x_2, x_3, x_4)$  be defined by the canonical-form matrix

$x_1$	$x_2$	$x_3$	$x_4$
0	0	0	0
0	0	0	1
0	0	1	0
0	0	1	1
0	1	0	0
1	1	0	0

(1)

Since  $m = 6$ , it is clear that this function cannot be an SPN function. Let us assume however, that it can be realized using five switches including both an  $x_2$  and an  $x_2'$ , and attempt to form a function  $g(x_1, x_2, x_3, x_4, a)$  such that (i)  $g$  is an SPN function, and (ii)  $g(x_1, x_2, x_3, x_4, a = x_2')$  equals  $f(x_1, x_2, x_3, x_4)$ . We proceed as follows:

1. Copy the canonical form matrix of  $f$ , adding a column headed  $a$ . This column is the inverse of the column headed  $x_2$ .

$x_1$	$x_2$	$x_3$	$x_4$	$a$
0	0	0	0	1
0	0	0	1	1
0	0	1	0	1
0	0	1	1	1
0	1	0	0	0
1	1	0	0	0

(2)

Condition (ii) requires that these terms appear in the function  $g$ .

2. The canonical form matrix for  $f'$  is similarly augmented, giving

$x_1$	$x_2$	$x_3$	$x_4$	$a$
0	1	0	1	0
0	1	1	0	0
0	1	1	1	0
1	0	0	0	1
1	0	0	1	1
1	0	1	0	1
1	0	1	1	1
1	1	0	1	0
1	1	1	0	0
1	1	1	1	0

(3)

and condition (ii) requires that these terms appear in  $g'$ .

3. List the remaining possible terms of  $g$ . (These will include all combinations for which  $a = x_2$ .)

$x_1$	$x_2$	$x_3$	$x_4$	$a$
0	0	0	0	0
0	0	0	1	0
0	0	1	0	0
0	0	1	1	0
0	1	0	0	1
0	1	0	1	1
0	1	1	0	1
0	1	1	1	1
1	0	0	0	0
1	0	0	1	0
1	0	1	0	0
1	0	1	1	0
1	1	0	0	1
1	1	0	1	1
1	1	1	0	1
1	1	1	1	1

(4)

Since these terms will vanish when  $a$  is set equal to  $x_2'$ , any of them may appear in the function  $g$ . Assuming that  $g$  is to be an SPN function of primed variables only, it follows that

- (a) whenever, in the function  $g$ , the combinations  $x_1 0 x_3 x_4 1$  or  $x_1 1 x_3 x_4 0$  appear, so must  $x_1 0 x_3 x_4 0$ , and
- (b) the combination  $x_1 1 x_3 x_4 1$  may appear in  $g$  only if  $x_1 0 x_3 x_4 0$ ,  $x_1 0 x_3 x_4 1$  and  $x_1 1 x_3 x_4 0$  all appear as well.

4. By the application of these rules the terms in (4) may be divided into three sets: (a) those which must appear in  $g$ , (b) those which must appear in  $g'$  and (c) those which these rules do not determine. For this



case, these sets are

appear in  $g$

$x_1$	$x_2$	$x_3$	$x_4$	$a$
0	0	0	0	0
0	0	0	1	0
0	0	1	0	0
0	0	1	1	0
1	0	0	0	0

appear in  $g'$

$x_1$	$x_2$	$x_3$	$x_4$	$a$
0	1	0	1	1
0	1	1	0	1
0	1	1	1	1
1	1	0	0	1
1	1	0	1	1
1	1	1	0	1
1	1	1	1	1

not determined

$x_1$	$x_2$	$x_3$	$x_4$	$a$
0	1	0	0	1
1	0	0	1	0
1	0	1	0	0
1	0	1	1	0

5. Combining these with the known terms of  $g$  and  $g'$  gives

appear in  $g$

$x_1$	$x_2$	$x_3$	$x_4$	$a$
0	0	0	0	0
0	0	0	0	1
0	0	0	1	0
0	0	0	1	1
0	0	1	0	0
0	0	1	0	1
0	0	1	1	0
0	0	1	1	1
0	1	0	0	0
1	0	0	0	0
1	1	0	0	0

appear in  $g'$

$x_1$	$x_2$	$x_3$	$x_4$	$a$
0	1	0	1	0
0	1	0	1	1
0	1	1	0	0
0	1	1	0	1
0	1	1	1	0
0	1	1	1	1
1	0	0	0	1
1	0	0	1	1
1	0	1	0	1
1	0	1	1	1
1	1	0	0	1
1	1	0	1	0
1	1	0	1	1
1	1	1	0	0
1	1	1	0	1
1	1	1	1	0
1	1	1	1	1

not determined

$x_1$	$x_2$	$x_3$	$x_4$	$a$
0	1	0	0	1
1	0	0	1	0
1	0	1	0	0
1	0	1	1	0

The terms presently given as appearing in  $g$  form an SPN function

$$g = x_1'x_2' \oplus x_3'x_4'a'$$

and

$$g(x_1, x_2, x_3, x_4, a = x_2') = x_1'x_2' \oplus x_3'x_4'a' = f(x_1, x_2, x_3, x_4).$$

However, note that if all the terms listed as "not determined" are adjoined to those which "appear in  $g$ ," a canonical form for the SPN function

$$g(x_1, x_2, x_3, x_4, a) = (x_1' \oplus a')(x_2' \oplus x_3'x_4')$$

is produced, and

$$\begin{aligned} g(x_1, x_2, x_3, x_4, a = x_2') &= (x_1' \oplus x_2')(x_2' \oplus x_3'x_4') \\ &= f(x_1, x_2, x_3, x_4). \end{aligned}$$

From this example, it is clear that the requirement that  $g$  be an SPN function, with  $g(x_1, x_2, x_3, x_4, a = x_2') = f(x_1, x_2, x_3, x_4)$  does not specify  $g$  uniquely.

#### IV. CONCLUSIONS

Clearly the derivation of the circuit for an SPN function is a process which can be mechanized. If a method for augmenting the canonical form of a non-network function can be formulated, then a purely mechanical process could be set up for deriving the minimum series-parallel networks for an arbitrary function.

#### REFERENCES

1. Shannon, C. E., A Symbolic Analysis of Relay and Switching Circuits, Trans. A.I.E.E., **57**, December 1938, pp. 713-723.
2. Staff of the Computation Laboratory, Synthesis of Electronic Computing and Control Circuits, Annals Harvard Comp. Lab., **27**, 1951.
3. Riordan, J. and Shannon, C. E., The Number of Two-Terminal Series-Parallel Networks, J. Math. Phys., **21**, August 1942, pp. 83-93.
4. Semon, W. L., The Application of Matrix Methods in the Theory of Switching, Harvard Comp. Lab., Theory of Switching, Report BL-6, May 1954, pp. I-6-I-16.
5. Keister, W., Ritchie, A. E. and Washburn, S. H., *The Design of Switching Circuits*, D. Van Nostrand Co., New York, 1951, pp. 95-99.
6. Ashenurst, R. L., A Uniqueness Theorem for Abstract Two-Terminal Switching Circuits, Harvard Comp. Lab., Theory of Switching, Report BL-10, March 1955, Sec. VI.
7. Quine, W. V., Two Theorems About Truth Functions, Bol. Soc. Math. Mexicana, **10**, 1953, pp. 64-70.
8. Semon, W. L., Adding Transformations, Harvard Comp. Lab., Theory of Switching, Report BL-4, July 1953, Sec. I.
9. Milne-Thomson, L. M., *The Calculus of Finite Differences*, Macmillan, London, 1933.

# Circular Waveguide Taper of Improved Design

By HANS-GEORG UNGER

(Manuscript received August 22, 1957)

*Transitions between round waveguides of different sizes for  $TE_{01}$  transmission are required to be free of mode conversion. Conical tapers with a gradual change of cone angle transform cylindrical waves in the round waveguide into spherical waves in the transition region. They thus cause very little power conversion to spurious modes. Optimal tapers and almost optimal tapers are found. An improved taper connecting  $\frac{1}{8}$  in. to 2 in. I.D. waveguide must be 3 ft long to keep the spurious mode level below -50 db for frequencies up to 75 kmc. A taper of constant cone angle would have to be 58 ft long to obtain the same spurious mode level.*

## I. INTRODUCTION

In long-distance waveguide transmission, multimode waveguides of large diameter must be used to exploit the low-loss properties of the circular electric wave. Multiplexing of a series of frequency bands into one pipe is, however, most easily done at certain smaller diameters. Likewise, sharp intentional bends can be negotiated more easily at small diameters. Therefore, transitions between different diameters must be made quite frequently in a waveguide system.

If these transitions are built in the form of a conical taper which matches the waveguide sizes of both sides, they tend to excite higher circular electric waves. Since no simple means are known to suppress higher circular electric waves without affecting the lowest circular electric wave, mode conversion-reconversion distortion can only be avoided by keeping power in all the higher circular electric waves at an extremely low level. Transitions are therefore required which will introduce very little conversion to higher circular electric modes. Conical transitions with a constant cone angle, unless they are made very long, generally excite too high a level of these spurious modes.

Wave propagation in the conical taper is most easily explained in terms

of normal modes. The normal modes of the circular electric wave family — the only family of interest here — are, in the cylindrical guide, cylindrical circular waves with plane equiphase surfaces and, in the conical guide, spherical circular waves with spherical equiphase surfaces. At the junction of a cylindrical guide to a conical guide — such as occurs twice in a conical transition — a cylindrical wave from the cylindrical guide excites a series of spherical waves in the conical guide. For instance, an incident  $TE_{01}$  wave will excite all the  $TE_{0m}$  waves, thus causing a rather high spurious mode level.

To avoid this mode conversion, a transition which transforms the cylindrical wave into the spherical wave must be introduced at the junction. S. P. Morgan<sup>1</sup> has suggested and worked out the design of dielectric inserts placed near the junction which, acting as quasi-optical lenses, transform the cylindrical waves into the spherical waves. However, because of the dispersive character of the lenses and of the waveguide, good broadband performance is difficult to achieve.

Another way of making a transition from cylindrical waves to spherical waves — at least approximately — is to taper the cone angle from zero at the cylindrical guide to the finite value of the conical guide. If this is done gradually enough, nearly all the power incident in the cylindrical wave will be transformed into the spherical wave, with a very low spurious mode level. Although this is only an approximate solution to the problem, it does have good broadband characteristics.

## II. WAVE PROPAGATION IN A TAPERED WAVEGUIDE

In a tapered circular waveguide such as the one shown in Fig. 1, the radius  $a$  is related to the distance  $z$  along the taper by a function which is assumed only to be smooth and to have a zero first derivative at both ends.

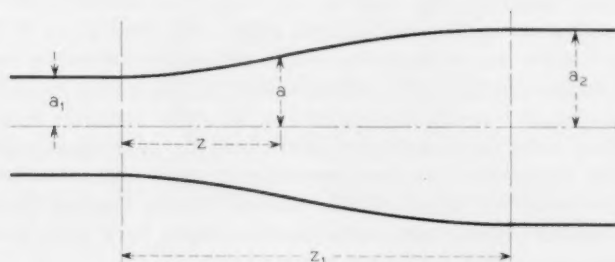


Fig. 1 — Tapered waveguide transition.

The field excited in any cross section by an incident  $TE_{01}$  wave can be expressed as the sum of the  $TE_{0m}$  waves of a cylindrical guide having the same radius as that of the cross section. With this representation, the tapered waveguide appears to be an infinite set of mutually coupled transmission lines, each line representing one of the cylindrical  $TE_{0m}$  waves. The wave propagation is described by an infinite set of first-order differential equations. If we assume the taper to be gradual enough, the power in all  $TE_{0m}$  terms with  $m$  greater than 1 will be small compared to the power in the  $TE_{01}$  term. We may then consider only coupling between  $TE_{01}$  and one of the  $TE_{0m}$  terms at a time. Furthermore, we need consider only the forward travelling waves, since the relative power coupled from the forward waves to the backward waves is quite small. Thus, the infinite system is reduced to the well-known coupled line equations:<sup>2</sup>

$$\frac{dA_1}{dz} = -j\beta_1 A_1 + k_{21} A_2, \quad \frac{dA_2}{dz} = -j\beta_2 A_2 + k_{12} A_1, \quad (1)$$

in which  $A_{1,2}$  are the complex amplitudes of the cylindrical  $TE_{01}$  and  $TE_{0m}$  respectively,  $\beta_{1,2}$  are the phase constants of these cylindrical modes and  $k_{21}$ ,  $k_{12}$  are the coupling coefficients. The coupling coefficients are calculated in the Appendix by converting Maxwell's equations into generalized telegraphist's equations. Both the phase constants and the coupling coefficients are functions of the distance along the taper. Power conservation requires

$$\begin{aligned} |k_{12}| &= k = |k_{21}| \\ k_{12}k_{21} &= -k^2. \end{aligned} \quad (2)$$

Coupled line equations with varying coupling coefficient and varying phase constant have been treated by Louisell.<sup>3</sup>

In order to solve (1), local normal modes must be introduced. Normal modes are waveforms in a uniform waveguide which propagate without change of field configuration or, in terms of the coupled line description, do not couple mutually. Analogously, local normal modes in a non-uniform waveguide are waveforms of a local cross section which would propagate without change of field configuration in a waveguide which is uniform with respect to that local cross section. For example, local normal modes in the waveguide taper are the spherical waves of a conical waveguide with a cone angle corresponding to the local cone angle in the taper. They would propagate in the conical waveguide without mutual coupling.

For the system of equations (1) local normal modes are defined by

$$\begin{aligned} A_1 &= \left( W_1 \cos \frac{1}{2} \xi - W_2 \sin \frac{1}{2} \xi \right) \exp \left( -j \int_0^z \beta \, dz \right), \\ A_2 &= -\sqrt{\frac{k_{12}}{k_{21}}} \left( W_1 \sin \frac{1}{2} \xi + W_2 \cos \frac{1}{2} \xi \right) \exp \left( -j \int_0^z \beta \, dz \right), \end{aligned} \quad (3)$$

in which

$$\beta = \frac{1}{2} (\beta_1 + \beta_2), \quad \tan \xi = 2 \frac{k}{\beta_1 - \beta_2} = 2 \frac{k}{\Delta \beta}. \quad (4)$$

Upon substituting (3) into equations (1), the local normal modes must satisfy

$$\frac{dW_1}{dz} + j\Gamma W_1 = \frac{1}{2} \frac{d\xi}{dz} W_2, \quad \frac{dW_2}{dz} - j\Gamma W_2 = -\frac{1}{2} \frac{d\xi}{dz} W_1, \quad (5)$$

where

$$\Gamma(z) = \frac{1}{2} \sqrt{\Delta \beta^2 + 4k^2}.$$

Equations (5) are coupled only through the terms proportional to  $d\xi/dz$ . If  $\xi$  is constant, they reduce to uncoupled equations for  $W_1$  and  $W_2$ . For a gentle change in taper angle, with

$$\left| \frac{1}{2\Gamma} \frac{d\xi}{dz} \right| \ll 1, \quad (6)$$

approximate solutions of (5) which proceed essentially in powers of  $d\xi/dz$  can be written down:

$$\begin{aligned} W_1(z) &= e^{-j\rho(z)} \left[ W_1(0) + \frac{1}{2} W_2(0) \int_0^z \frac{d\xi}{dz'} e^{2j\rho(z')} \, dz' \right. \\ &\quad \left. - \frac{1}{4} W_1(0) \int_0^z \frac{d\xi}{dz'} e^{2j\rho(z')} \int_0^{z'} \frac{d\xi}{dz''} e^{-2j\rho(z'')} \, dz'' \, dz' \right], \\ W_2(z) &= e^{j\rho(z)} \left[ W_2(0) - \frac{1}{2} W_1(0) \int_0^z \frac{d\xi}{dz'} e^{-2j\rho(z')} \, dz' \right. \\ &\quad \left. - \frac{1}{4} W_2(0) \int_0^z \frac{d\xi}{dz'} e^{-2j\rho(z')} \int_0^{z'} \frac{d\xi}{dz''} e^{2j\rho(z'')} \, dz'' \, dz' \right], \end{aligned} \quad (7)$$

in which

$$\rho(z) = \int_0^z \Gamma(z') \, dz'. \quad (8)$$

The initial conditions in the taper are  $A_1(0) = 1$  and  $A_2(0) = 0$ . The taper begins with zero cone angle; hence, from (3),

$$W_1(0) = 1 \quad W_2(0) = 0,$$

in which  $W_1$  corresponds to the  $TE_{01}$  wave and is the wanted local normal mode, while  $W_2$  corresponds to one of the  $TE_{0n}$  waves with  $n \neq 1$  and is an unwanted mode. At the end  $z_1$  of the taper, the unwanted mode amplitude is

$$|W_2(z_1)| = \frac{1}{2} \left| \int_0^{z_1} \frac{d\xi}{dz} e^{-2j\rho(z)} dz \right|. \quad (9)$$

At the taper end the cone angle is again zero,  $(\xi(z_1) = 0)$ . Therefore  $|W_2(z_1)|$  equals  $|A_2(z_1)|$ . Equation (9) integrated by parts becomes

$$|W_2(z_1)| = \left| \int_0^{z_1} \Gamma \xi e^{-2j\rho(z)} dz \right|. \quad (10)$$

The mode conversion in a smooth but otherwise arbitrary taper can be calculated with (9) or (10).

### III. DESIGN OF A TAPER

A waveguide taper can always be built to have as low a mode conversion as is wanted in a certain frequency band merely by making it long enough. However, an optimally designed taper has the smallest possible length for a given difference in diameters at its two ends and for a specified unwanted mode level in a given frequency band.

Some analogies between this problem and the problem of a transmission line taper of optimum design are evident. The transmission line taper for matching impedances is nothing but a tapered waveguide in which only one mode is propagating. Power can only be converted into reflected waves, and it is this reflected power which is kept small in a properly designed transmission line taper. If more than one mode is propagating, power will be scattered not only into the reflected wave but also into the other propagating modes. In fact, the power scattered into backward traveling waves is quite small compared to the power scattered into forward traveling waves, and only the latter need be considered in a multimode waveguide taper. Therefore, the mode conversion in the waveguide transition corresponds to the reflection in the transmission line taper.

It has been shown that a transition between transmission lines of different characteristic impedances is optimally made by a series of steps



spaced about a quarter wavelength apart.<sup>4</sup> The magnitude of these steps is chosen to give an input reflection described in its frequency dependence by a Tschebycheff polynomial. Similarly, a conical waveguide transition is expected to perform optimally when it is composed of a number of sections with different cone angles, as in Fig. 2. The lengths of these sections should be chosen so that the converted energy from adjacent joints of sections is 180 degrees out of phase, and the changes of angles from section to section should be chosen so that the over-all conversion pattern corresponds to a Tschebycheff polynomial. However, since there is more than one mode to which power is converted and since the phase constants change along the transition, the design of such a multisection transition will be very difficult, if not impossible.

If the number of sections in the line transition is allowed to increase indefinitely for a fixed over-all length, a continuous transmission line taper is formed. The results of the multistep transition of optimum design have been extended to this case.<sup>5</sup> The input reflection of the continuous taper of optimum design is described in its frequency dependence by a Tschebycheff polynomial of infinite degree. The taper curve itself is given essentially by the Fourier transform of this Tschebycheff polynomial. The frequency band of constant low reflection now extends from a certain lowest frequency to infinity.

The transmission line taper of optimum design does not have a continuous reflection distribution, but it has reflection impulses at both ends. Assuming a completely continuous reflection distribution, an almost optimum design has been found.<sup>6</sup> The raised cosine function is a reflection distribution which, in practical cases, closely approximates in its frequency dependence the input reflection of the continuous taper of almost optimum design.

If the integration in (9) for the mode conversion in the waveguide

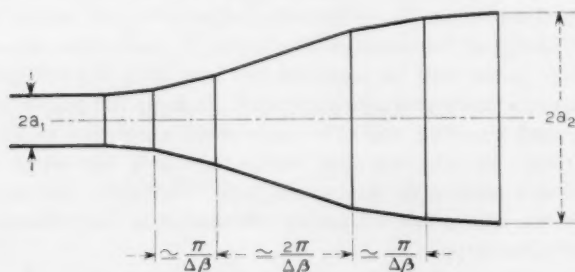


Fig. 2 — Multisection waveguide transition.

taper is extended over the parameter  $\rho$ ,

$$|W_2(\rho_1)| = \left| \int_0^{\rho_1} \xi(\rho) e^{-2j\rho} d\rho \right|, \quad (11)$$

the relationship of the mode conversion in the multimode waveguide taper to the input reflection of the transmission line taper becomes evident. In (11)  $\rho$  corresponds to the longitudinal coordinate and  $\xi(\rho)$  to the reflection distribution of the transmission line taper.

The reflection distribution for an almost optimally designed line taper can be substituted for  $\xi(\rho)$  to give the almost optimally designed waveguide taper. Even the optimum design can be found when some care is exercised in using steps in the waveguide taper to simulate the impulse functions in the reflection distribution.

Once  $\xi(\rho)$  is given, we can find the waveguide radius  $a(\rho)$  and the axial distance  $z(\rho)$  from (4), (5) and (8). The coupling coefficient can be written

$$k = c(a) \frac{da}{dz} \equiv \Gamma c(a) \frac{da}{d\rho}. \quad (12)$$

Therefore,

$$c(a) \frac{da}{d\rho} = \frac{\tan \xi(\rho)}{\sqrt{1 + \tan^2 \xi(\rho)}}, \quad (13)$$

which can readily be integrated by separation of variables to give  $a(\rho)$ . With  $a$  known,  $\Gamma$  is also known as a function of  $\rho$ , and the axial distance can be calculated:

$$z = \int_0^\rho \frac{d\rho}{\Gamma(\rho)}. \quad (14)$$

Some restricting remarks must be made in concluding this outline of the taper design.

Only one of the coupled higher-order modes has been considered here. This is adequate as long as the cone angle changes only gradually. Since all other higher order modes are weaker in coupling and farther removed in phase constant, the conversion to these modes will always be much smaller than the conversion to the  $TE_{02}$  wave. If, however, there are abrupt changes in cone angle or even if the diameter of the guide changes in steps, as in the waveguide taper of optimum design, the power conversion to higher modes must be checked.

The design procedure outlined here works only as long as the coupled mode does not go through cutoff within the transition. Power converted to backward travelling waves has been neglected, since the coupling

to these waves is smaller and they are much more removed in phase constant than are the forward travelling waves. In the vicinity of cutoff, this is no longer true. Here, the propagation is more suitably described by the original generalized telegraphist's equations (35) and (36) of the Appendix. They are, however, not easily solved in the cutoff region of a mode.

Since the coupling coefficients in (35) and (36) do not change with frequency, and since the difference in propagation constants of the coupled waves does not increase with decreasing frequency, the power conversion does not increase when the frequency is lowered to bring a coupled mode to cutoff within the taper. Consequently, the waveguide taper can be designed for a frequency high enough to keep the lowest coupled mode propagating throughout the taper. It will then work properly at all lower frequencies.

#### IV. THE RAISED COSINE TAPER

As a characteristic example, we will design a taper whose conversion distribution follows the raised cosine function

$$\xi(\rho) = \frac{2C}{\rho_1} \sin^2 \pi \frac{\rho}{\rho_1}, \quad (15)$$

in which  $C$  is yet to be determined from the radii  $a_1$  and  $a_2$ . According to (11) the over-all conversion will then be given by the Fourier transform of the raised cosine function

$$\frac{|W_2(\rho_1)|}{C} = \frac{|1 - e^{-2j\rho_1}|}{2\rho_1 \left(1 - \frac{\rho_1^2}{\pi^2}\right)}. \quad (16)$$

Equation (16) is plotted in Fig. 3.

We assume the  $TE_{01}$  and  $TE_{02}$  modes to be far enough from cutoff so that

$$\left(\frac{\lambda}{\lambda_c}\right)^2 \ll 1 \quad (17)$$

for both modes throughout the taper. Furthermore, we assume the taper to be gentle enough so that

$$\xi^2 \ll 1. \quad (18)$$

These assumptions will enable us to carry out the integrations analytically.

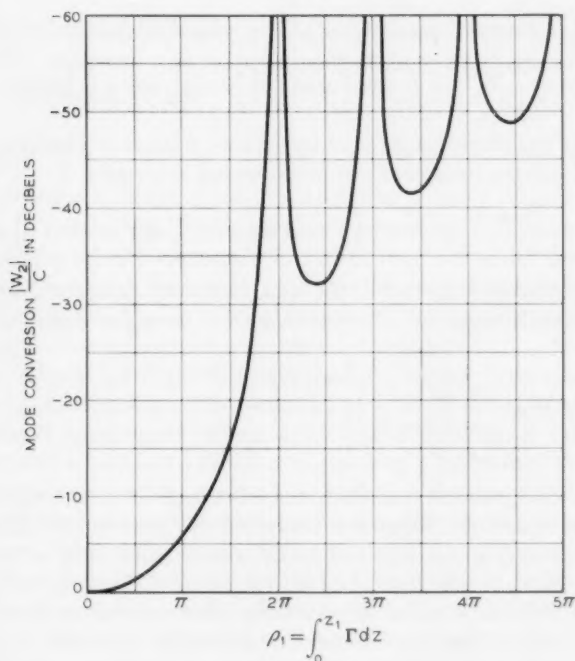


Fig. 3 — Mode conversion in the raised cosine taper.

Integrating (13) with

$$c = \frac{2k_1k_2}{k_2^2 - k_1^2} \frac{1}{a}$$

[from (42) and (12)] and  $\xi(\rho)$  from (15) we get

$$\ln \frac{a}{a_1} = \ln \frac{a_2}{a_1} \left( \frac{\rho}{\rho_1} - \frac{1}{2\pi} \sin 2\pi \frac{\rho}{\rho_1} \right), \quad (19)$$

where  $C$  has been eliminated by the boundary conditions  $a(0) = a_1$  and  $a(\rho_1) = a_2$ :

$$C = \frac{2k_1k_2}{k_2^2 - k_1^2} \ln \frac{a_2}{a_1}. \quad (20)$$

Because of (17) and (18)

$$\Gamma = \frac{k_2^2 - k_1^2}{2\beta_0 a^2}. \quad (21)$$

The axial distance is found from (14) by substituting (19) for  $a$  in (21):

$$z = \frac{4\beta_0 a_1^2}{k_2^2 - k_1^2} \int_0^{\rho} \exp \left[ 2 \ln \frac{a_2}{a_1} \left( \frac{\rho}{\rho_1} - \frac{1}{2\pi} \sin \frac{2\rho}{\pi \rho_1} \right) \right] d\rho, \quad (22)$$

where  $\beta_0$  is the phase constant of free space. With  $\alpha = 1/\pi \ln a_2/a_1$  and  $x = 2\pi(\rho/\rho_1)$ , the integrand can be expanded in a series

$$z = \frac{2\beta_0 a_1^2 \rho_1}{\pi(k_2^2 - k_1^2)} \int_0^{\pi} e^{\alpha x} \left( 1 - \alpha \sin x + \frac{\alpha^2}{2} \sin^2 x \mp \dots \right) dx \quad (23)$$

and, for moderate values of  $\alpha$ , the axial distance  $z$  can be calculated by term-by-term integration. The total length of the taper is approximately

$$z_1 \cong \rho_1 \frac{2\beta_0}{\ln \frac{a_2}{a_1} k_2^2 - k_1^2} \left[ \frac{\pi^2 + 2 \ln^2 \frac{a_2}{a_1}}{\pi^2 + \ln^2 \frac{a_2}{a_1}} + \frac{\ln^2 \frac{a_2}{a_1}}{4\pi^2 + \ln^2 \frac{a_2}{a_1}} \right]. \quad (24)$$

A numerical example will show the advantage of a properly tapered waveguide transition. Suppose a transition designed for the  $TE_{01}$  wave and connecting  $\frac{7}{8}$  in. I.D. pipe to 2 in. I.D. pipe is required to have a spurious mode level of less than -50 db for all frequencies up to 75 kmc. The most seriously coupled wave is  $TE_{02}$ . For a raised cosine taper we get, from (20),  $C$  equal to 1.28 and consequently, from Fig. 3,  $\rho_1$  equal to 14.8. Hence, from (24), the required taper length is  $z_1$  equal to 3 ft. The taper curve is plotted in Fig. 4. This curve has been calculated from (19) and (23), using  $\rho$  as a parameter. A taper of constant cone angle satisfying the same requirements would have to be 58 ft. long.<sup>1</sup>

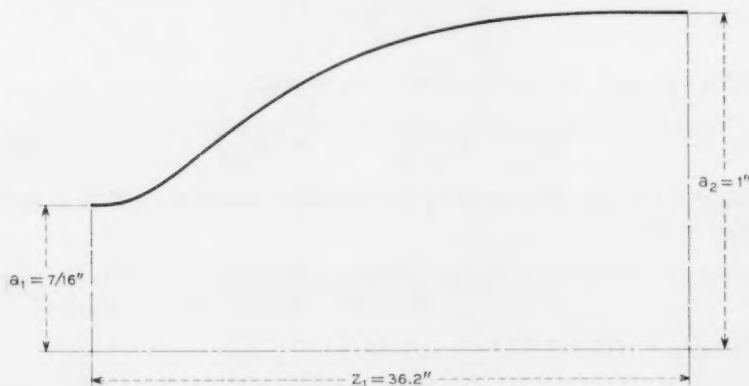


Fig. 4 — Raised cosine taper.

Circular waveguide tapers have been built according to Fig. 4. Their  $TE_{01}$ - $TE_{02}$  conversion loss was measured at frequencies near 55 kmc and found to be higher than 50 db.

#### V. SUMMARY

The power conversion from  $TE_{01}$  to higher circular electric waves occurring in conical transitions of round waveguide can be reduced by changing the cone angle gradually rather than abruptly. Instead of a taper with constant cone angle, a transition with changing cone angle, which transforms the cylindrical waves of the round waveguide into spherical waves in the transition region, is suggested.

Upon converting Maxwell's equations into generalized telegraphist's equations, the transition is represented as a set of nonuniform transmission lines, nonuniformly coupled. With proper choice of the coupling distribution — and hence the cone angle — as a function of the distance along the transition, we can find an optimum design which minimizes the length of the transition for a specified frequency range and spurious mode level. In a transition of optimum design the mode conversion is given by a Tschebycheff polynomial of infinite degree in its frequency dependence, and the geometry of the transition is found from the Fourier transform of this Tschebycheff polynomial. A simpler design, but still a good one, has a transition geometry given essentially by a raised cosine function.

#### APPENDIX

##### *Generalized Telegraphist's Equations of the Circular Electric Waveguide Taper*

A very convenient mathematical formulation of the electromagnetic problem in the waveguide transition is provided by S. A. Schelkunoff's generalized telegraphist's equations for waveguides.<sup>7</sup> Maxwell's equations for transverse electric and circular symmetric waves are, in cylindrical coordinates:

$$\frac{\partial E_\phi}{\partial z} = j\omega\mu H_r, \quad (25)$$

$$\frac{\partial H_r}{\partial z} = j\omega\epsilon E_\phi + \frac{\partial H_z}{\partial r}, \quad (26)$$

$$\frac{\partial}{\partial r}(rE_\phi) = -j\omega\mu r H_z, \quad (27)$$

where  $E_\varphi$ ,  $H_z$  and  $H_r$  are the only nonvanishing components of the field,  $\epsilon$  is the dielectric permittivity,  $\mu$  the magnetic permeability and  $\omega$  the angular pulsation. The exponential dependence of time is understood.

The boundary conditions of the waveguide taper are, at  $r$  equal to  $a$ :

$$E_\varphi = 0 \quad (28)$$

$$H_r = \frac{da}{dz} H_z. \quad (29)$$

The field at any cross section of the paper is represented as a superposition of the fields of the normal modes in a cylindrical guide of the same cross section:

$$E_\varphi = \sum_m V_m \frac{J_1\left(k_m \frac{r}{a}\right)}{\sqrt{\pi a J_0(k_m)}}, \quad (30)$$

$$H_r = -\sum_m I_m \frac{J_1\left(k_m \frac{r}{a}\right)}{\sqrt{\pi a J_0(k_m)}}, \quad (31)$$

$$H_z = \sum_m i_m \frac{J_0\left(k_m \frac{r}{a}\right)}{\sqrt{\pi a J_0(k_m)}}, \quad (32)$$

where  $J_0$  and  $J_1$  are Bessel functions of the first kind and  $k_m$  is the  $m$ th zero of  $J_1$ . The  $V_m$ ,  $I_m$  and  $i_m$  have the dimensions of voltages and currents. The factors of  $V_m$  and  $I_m$  are normalized so that  $P_m = 1/2(V_m I_m^*)$  is the complex power flow in each normal mode. It has to be kept in mind that  $a$  is a function of  $z$ .

The boundary condition (28) is satisfied by the individual terms of the series for  $E_\varphi$ . Hence, this series converges uniformly. Not so the series for  $H_r$ : (31) is a representation for  $H_r$  only in the open interval  $0 \leq r < a$ , since the individual terms vanish at  $r = a$  but, according to (29),  $H_r$  does not. In the closed interval, the series (31) represents a discontinuous function and therefore does not converge uniformly. Term-by-term differentiation will make the series diverge.

The relationship between  $i_m$  and  $V_m$  is found by substituting in (27) the series (30) for  $E_\varphi$  and the series (32) for  $H_z$ , and comparing coefficients

$$i_m = j \frac{k_m}{\omega \mu a} V_m. \quad (33)$$



Using this relation and substituting the series (30) for  $E_\phi$  in (25) at  $r = a$ , we find that the boundary condition (29) is satisfied.

To convert Maxwell's equations into generalized telegraphist's equations, we introduce (30) and (31) into (25) and (26), multiply both sides of both equations by  $J_1[k_n(r/a)]$  and integrate over the cross section. Since the series for  $H_r$  does not converge uniformly, we write for the left-hand side of (26)

$$rJ_1\left(k_n \frac{r}{a}\right) \frac{\partial H_r}{\partial z} = -rH_r \frac{\partial}{\partial z} \left[ J_1\left(k_n \frac{r}{a}\right) \right] + \frac{\partial}{\partial z} \left[ rJ_1\left(k_n \frac{r}{a}\right) H_r \right] \quad (34)$$

and invert integration and differentiation in the second term of this expression.

The generalized telegraphist's equations have the following form:

$$\frac{dV_n}{dz} = -j\omega\mu I_n + \frac{1}{a} \frac{da}{dz} \sum_m \frac{2k_n k_m}{k_m^2 - k_n^2} V_m, \quad (35)$$

$$\frac{dI_n}{dz} = -j \frac{\beta_n^2}{\omega\mu} V_n + \frac{1}{a} \frac{da}{dz} \sum_m \frac{2k_n k_m}{k_m^2 - k_n^2} I_m. \quad (36)$$

The summations are extended over all  $m$  except  $m = n$ . The quantity  $\beta_n$  is the phase constant of the  $n$ th mode in a cylindrical guide of the particular cross section;  $\beta_n$  is a function of  $a$  and therefore of  $z$ .

The generalized telegraphist's equations represent an infinite set of coupled nonuniform transmission lines. For our purpose, it is convenient to write the transmission-line equations not in terms of currents and voltages, but in terms of the amplitudes of forward and backward traveling waves. Thus, let  $A$  and  $B$  be the amplitudes of the forward and backward waves of a typical mode at a certain cross section. The mode current and voltages are related to the wave amplitudes by

$$V = \sqrt{K} (A + B), \quad (37)$$

$$I = \frac{1}{\sqrt{K}} (A - B), \quad (38)$$

where  $K$  is the wave impedance

$$K_n = \frac{\omega\mu}{\beta_n}. \quad (39)$$

If the currents and voltages in the generalized telegraphist's equations (35) and (36) are represented in terms of the traveling-wave amplitudes, after some obvious additions and subtractions, the following equations

for coupled traveling waves are obtained:

$$\frac{dA_n}{dz} = -j\beta_n A_n - \frac{1}{2} \frac{K_n'}{K_n} B_n + \sum_m (k_{nm}^+ A_m + k_{nm}^- B_m) \quad (40)$$

$$\frac{dB_n}{dz} = j\beta_n B_n - \frac{1}{2} \frac{K_n'}{K_n} A_n + \sum_m (k_{nm}^+ B_m - k_{nm}^- A_m). \quad (41)$$

The  $k$ 's are coupling coefficients defined by:

$$k_{nm}^{\pm} = \frac{k_n k_m}{k_m^2 - k_n^2} \left( \sqrt{\frac{K_n}{K_m}} \pm \sqrt{\frac{K_m}{K_n}} \right) \frac{1}{a} \frac{da}{dz} \quad (42)$$

and

$$K_n' = \frac{dK_n}{dz}.$$

For a cylindrical guide,  $da/dz$  is equal to zero and (40) and (41) reduce to uncoupled transmission-line equations.

#### REFERENCES

1. Morgan, S. P., Control of Spurious Modes in Multimode Waveguides by Use of Foam Dielectric Inserts, presented orally at the May 1956 Joint Meeting of U.R.S.I. and I.R.E.
2. Miller, S. E., Coupled Wave Theory and Waveguide Applications, B.S.T.J., **33**, May 1954, pp. 661-719.
3. Louisell, W. H., Analysis of the Single Tapered Mode Coupler, B.S.T.J., **34**, July 1955, pp. 853-870.
4. Burkhardtmaier, W., Widerstandstransformation mit Leitungen, Funk und Ton, March 1949, pp. 151-157, and April 1949, pp. 202-213; Collin, R. E., The Theory and Design of Wideband Multisection Quarter-Wave Transformers, Proc. I.R.E., **43**, February 1955, pp. 179-185.
5. Klopfenstein, R. W., A Transmission Line Taper of Improved Design, Proc. I.R.E., **44**, January 1956, pp. 31-35.
6. Collin, R. E., The Optimum Tapered Transmission Line Matching Section, Proc. I.R.E., **44**, April 1956, pp. 539-548.
7. Schelkunoff, S. A., Conversion of Maxwell's Equations into Generalized Telegraphist's Equations, B.S.T.J., **34**, September 1955, pp. 995-1043.

# The Nonuniform Transmission Line as a Broadband Termination

By IRA JACOBS

(Manuscript received December 17, 1957)

*The problem of obtaining a broadband microwave termination is considered from the point of view of nonuniform transmission line theory. Attention is restricted to lines in which only the distributed shunt admittance may be varied. An optimization argument is presented which leads to the consideration of a line in which the fractional increase in admittance per wavelength in the line is constant. The nonuniform transmission line equations are solved exactly for this case, and the results are expressed in terms of readily interpretable elementary functions. It is shown that a fixed geometrical length of line can lead to an arbitrarily large effective length without destroying the match at the input. The introduction of a small loss term makes the line almost totally absorbing regardless of its termination.*

*The line has a long-wavelength cutoff given by  $4\pi$  times the actual length of the line. If the line is short-circuited at its far end, a return loss of greater than 11.4 db is obtained at all frequencies above twice the cutoff frequency. The effect of certain practical limitations on the performance of this line is also discussed.*

## I. INTRODUCTION

Classical transmission line analysis leads to the propagation of a wave in which neither the electric nor magnetic fields have components in the direction of propagation.<sup>1</sup> These transverse electromagnetic (TEM) waves are characteristic not only of the usual transmission line structures such as parallel wires and coaxial cable; they are also characteristic of plane-wave propagation in isotropic media.

It is often convenient, when dealing with TEM-wave propagation, to make use of results of classical transmission line analysis. Some care must be exercised, however, in applying these results at microwave frequencies. Consider, for example, the problem of terminating a lossless line. Classical analysis tells us that, if the line is terminated in its charac-

teristic impedance (which is a pure resistance for a lossless line), the termination will be reflectionless. Two difficulties arise at microwave frequencies, where the physical dimensions are no longer small compared to the wavelength. First, as the frequency increases, the concept of a lumped circuit element becomes less meaningful. For example, a resistive disc termination for a coaxial line will have an effective impedance which is strongly influenced by the geometry and has very little correlation with the dc resistance of the disc.<sup>2</sup> The second difficulty is that, even if the appropriate effective lumped impedance is obtained, the analysis assumes that this impedance is connected across an open circuit. An open-ended line at high frequencies is by no means an electrical open circuit. There is a true open circuit, however, one-quarter wavelength in front of a short circuit. Therefore, if the line is short-circuited by a metallic surface, and the appropriate characteristic impedance is placed one-quarter wavelength in front of the short, the termination will be reflectionless. However, if the frequency is changed the quarter-wave condition is destroyed, so that the termination is not broadband.

The purpose of this paper is to consider analytically the use of a nonuniform transmission line as a broadband termination. If this structure is to be finite, it too must be terminated. To make the results independent of what is beyond the nonuniform line and still maintain physical realizability, it will be assumed that the nonuniform line is terminated by a short circuit. The problem, then, is to match from a given characteristic impedance,  $Z_0$ , to a short circuit by means of an appropriate nonuniform transmission line.

There is extensive literature<sup>3</sup> on the use of nonuniform transmission lines for impedance matching. Optimum matching procedures have been discussed<sup>4</sup> for matching two uniform lossless lines to one another by means of a lossless nonuniform line. In addition to the assumption of no loss, it is assumed that the magnitude of the reflection coefficient is much less than unity at all points along the line. Both of these assumptions, however, are not applicable for matching to a short circuit. Since the object here is to absorb all incident energy, the line cannot be lossless. Also, the magnitude of the reflection coefficient is unity at the short circuit. Thus, the matched-termination problem must be considered apart from the usual matching problem.

In order to define the problem more precisely, it is necessary to consider the transmission line equations which determine the voltage  $V$  and current  $I$  along the line:

$$\frac{dV}{dx} = -Z(x)I, \quad (1)$$

$$\frac{dI}{dx} = -Y(x)V, \quad (2)$$

where  $Z(x)$  is the distributed series impedance per unit length and  $Y(x)$  is the distributed shunt admittance per unit length. The line is said to be uniform if both these quantities are constant.

A uniform line may be used to match from an impedance of  $Z_0$  to a short circuit if  $Z$  and  $Y$  are both large complex constants (so that the wavelength in the line is small and the losses are large) and if, in addition,  $\sqrt{Z/Y}$  equals  $Z_0$ . Thus, in principle, a fixed length of uniform line can be made electrically long and extremely lossy, and yet it may have the same characteristic impedance  $Z_0$  as does the line it is desired to terminate. In practice, however, this may be difficult to accomplish.

Consider, for example, the problem of finding a microwave-absorbing material for anechoic chambers. Using the above principle it would be necessary to find a material with large complex relative permeability and relative dielectric constant, but such that the ratio of these two quantities was unity. It is not too difficult to obtain high dielectric constants at microwave frequencies,<sup>5</sup> but it is difficult in general to obtain equally large permeabilities.<sup>6</sup> It is of interest, then, to consider a medium with a permeability equal to that of free space, and to attempt to match this medium to a short circuit by increasing the dielectric constant as the termination is approached. In the analogous transmission line problem, the distributed series impedance,  $Z(x)$ , is a fixed constant, and only the distributed shunt admittance,  $Y(x)$ , is at our disposal.

The following problem is thus suggested. A uniform lossless line, characterized by a distributed series impedance per unit length of  $j\omega L_1$  and a distributed shunt admittance per unit length of  $j\omega C_1$ , is to be terminated by a nonuniform line of length  $s$  (see Fig. 1). The nonuniform line has a constant distributed series impedance per unit length of  $j\omega L_1$ , but the distributed shunt admittance per unit length,  $Y(x)$ , is as yet unspecified. This line is, in turn, terminated in a short circuit at  $x = s$ . It is desired to find that function  $Y(x)$  which minimizes the reflection coefficient at  $x = 0$ .

The general variational problem is outside the scope of the present work. In the following sections a somewhat intuitive argument will be presented which leads to a particular form for  $Y(x)$ . An exact solution of the transmission line equations will be obtained for this particular

nonuniform line, and it will be shown that the line indeed has the properties indicated by the simpler intuitive arguments.

## II. DETERMINATION OF THE ADMITTANCE VARIATION

Approximation techniques<sup>7</sup> indicate that, if the fractional change in the properties of the line per "local wavelength over  $2\pi$ "\* is small, then reflections may be assumed to be negligible. The exact solutions of particular nonuniform transmission lines, such as the exponential line,<sup>8</sup> indicate that reflections become important when this condition is violated.

Since we are attempting to match from an admittance level  $j\omega C_1$  to an infinite admittance, it is natural to ask the following question: How large can the admittance be made at  $x = s$ , subject to the conditions

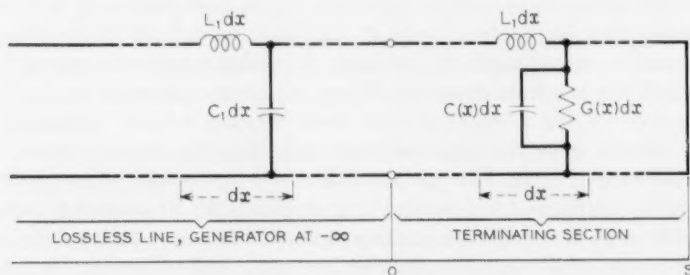


Fig. 1 — Nonuniform transmission line termination.

that it be equal to  $j\omega C_1$  at  $x = 0$  and that the fractional change in admittance per local wavelength in the line be small?

The wavelength in the uniform lossless line characterized by  $L_1$  and  $C_1$  is

$$\lambda = \frac{2\pi}{\omega \sqrt{L_1 C_1}}. \quad (3)$$

The local wavelength in the nonuniform line is given by  $\lambda/\sqrt{\epsilon(x)}$ , where

$$\epsilon(x) = \frac{Y(x)}{j\omega C_1} = \frac{C(x)}{C_1} - \frac{jG(x)}{\omega C_1}, \quad (4)$$

in which  $C(x)$  is the distributed shunt capacitance per unit length and  $G(x)$  is the distributed shunt conductance per unit length. For the pur-

\* "Local wavelength" is defined as the wavelength in a uniform line which has the same distributed constants as the line in question at the point in question.

pose of the present section, it will be assumed that the nonuniform line is lossless, so that  $G(x)$  is zero and  $\epsilon(x)$  is real. The condition that the fractional change in admittance per local wavelength over  $2\pi$  be small can then be written

$$\frac{\lambda}{2\pi} \frac{1}{\epsilon^{3/2}} \frac{d\epsilon}{dx} \leq a, \quad (5)$$

where  $a$  is an as yet unspecified small constant.

The problem to be considered is thus: Given  $s$  greater than zero, find that function  $\epsilon(x)$  which maximizes  $\epsilon(s)$ , subject to the conditions that  $\epsilon(0)$  equals 1 and that the inequality (5) is satisfied over the interval  $[0, s]$ . The solution to this problem is obtained by replacing the inequality in (5) by an equality, which leads to the result

$$\epsilon(x) = \left(1 - \frac{\pi a}{\lambda} x\right)^{-2}. \quad (6)$$

Thus, as  $x$  approaches  $\lambda/\pi a$ ,  $\epsilon(x)$  becomes infinite. It would then appear that, in a fixed length of line, an arbitrarily large change in admittance can be utilized, and consequently a large effective length obtained, without violating the slowly varying condition. The introduction of a small imaginary component (shunt conductance) to  $\epsilon(x)$  should then make the line totally absorbing regardless of termination.

In order to verify the above conjectures analytically it is necessary to solve the transmission line equations. This will be done in the following section.

### III. SOLUTION OF THE TRANSMISSION LINE EQUATIONS

For a line with uniformly distributed series impedance per unit length  $j\omega L_1$  and distributed shunt admittance per unit length  $j\omega C_1\epsilon(x)$ , the transmission line equations may be rewritten in the form

$$\frac{d^2 V}{dx^2} + \left(\frac{2\pi}{\lambda}\right)^2 \epsilon(x) V = 0, \quad (7)$$

$$\frac{d^2 I}{dx^2} - \frac{1}{\epsilon} \frac{d\epsilon}{dx} \frac{dI}{dx} + \left(\frac{2\pi}{\lambda}\right)^2 \epsilon(x) I = 0, \quad (8)$$

where  $\lambda$  is given by (3).

If  $\epsilon(x)$  is of the form  $(A + Bx)^n$ , (7) may be transformed<sup>9</sup> into Bessel's equation of order  $1/(n+2)$ . The fact that considerable simplifications result when  $n$  equals  $-2$  has been noted previously,<sup>10</sup> but the physical implications do not appear to have been discussed.



The expression for  $\epsilon(x)$ , given by (6), is real. Since we are interested in absorption, the shunt admittance must contain a conductance term in addition to the capacitance, and consequently  $\epsilon$  must be complex. In order to maintain the same functional dependance for  $\epsilon$ , it will be assumed that the ratio of shunt conductance to shunt capacitance is constant,

$$\frac{G(x)}{C(x)} = \sigma, \quad (9)$$

so that  $\epsilon(x)$  is given by

$$\epsilon(x) = \frac{1 - j\sigma/\omega}{\left(1 - \frac{\pi a}{\lambda} x\right)^2}. \quad (10)$$

If the change of variables

$$r = -\ln \left(1 - \frac{\pi a}{\lambda} x\right) \quad (11)$$

is made, (7) and (8) can be rewritten

$$\frac{d^2 V}{dr^2} + \frac{dV}{dr} + \frac{4}{a^2} (1 - j\sigma/\omega) V = 0, \quad (12)$$

$$\frac{d^2 I}{dr^2} - \frac{dI}{dr} + \frac{4}{a^2} (1 - j\sigma/\omega) I = 0, \quad (13)$$

where the expression for  $\epsilon$  as given by (10) has been used. The solutions of these equations are

$$V = e^{-r/2} [V_1 e^{-\gamma r} + V_2 e^{\gamma r}] \quad (14)$$

and

$$I = j \frac{a}{2} \sqrt{C_1/L_1} e^{r/2} \left[ -\left(\gamma + \frac{1}{2}\right) V_1 e^{-\gamma r} + \left(\gamma - \frac{1}{2}\right) V_2 e^{\gamma r} \right], \quad (15)$$

where

$$\gamma = \sqrt{\frac{1}{4} - \frac{4}{a^2} (1 - j\sigma/\omega)} \quad (16)$$

may be interpreted as an effective propagation constant and  $r$  may be interpreted as an effective length.

The lossless line ( $\sigma = 0$ ) is cut off when the effective propagation constant becomes real; that is, when  $a \geq 4$ . If the shunt capacitance,  $C(x)$ , is to be frequency-independent, it follows from the form of  $\epsilon(x)$  that  $a$

must be proportional to wavelength. A cutoff wavelength  $\lambda_0$  and cutoff frequency  $\omega_0$  may then be defined such that

$$a = \frac{4\lambda}{\lambda_0} = \frac{4\omega_0}{\omega}. \quad (17)$$

Thus,  $\gamma$  can be written as

$$\gamma = \left(\frac{1}{2}\right) \sqrt{1 - \frac{\omega^2}{\omega_0^2} + j\sigma \frac{\omega}{\omega_0^2}}. \quad (18)$$

It is interesting to note that these results are identical in form to the results that would be obtained for an exponential line,<sup>8</sup> in which the admittance and impedance vary as  $e^{ax}$  and  $e^{-ax}$  respectively, and where  $r$  is defined as  $ax$ . However, in order to obtain the same effective length,  $R$ , the actual length of the exponential line must be longer by a factor  $R/(1 - e^{-R})$ , which increases linearly with  $R$  for large effective lengths. Thus, the equivalent exponential line will, in general, be considerably longer than the line considered here.

#### IV. REFLECTION COEFFICIENT

If the boundary condition,  $V = 0$  at  $x = s$ , is substituted into (14), the following relation is obtained for the input admittance:

$$Y_i = \frac{I(x=0)}{V(x=0)} = -2j \frac{\omega_0}{\omega} \sqrt{\frac{C_1}{L_1}} \left( \frac{1}{2} + \gamma \coth \gamma R \right), \quad (19)$$

where  $R$  is the value of  $r$  corresponding to  $x = s$ ; that is,

$$R = -\ln \left( 1 - \frac{4\pi}{\lambda_0} s \right). \quad (20)$$

The complex voltage reflection coefficient,  $\rho$ , is given by

$$\rho = \frac{\sqrt{C_1/L_1} - Y_i}{\sqrt{C_1/L_1} + Y_i}. \quad (21)$$

Substitution of (19) into (21) gives

$$\rho = \frac{1 + j \frac{\omega_0}{\omega} + 2j\gamma \frac{\omega_0}{\omega} \coth \gamma R}{1 - j \frac{\omega_0}{\omega} - 2j\gamma \frac{\omega_0}{\omega} \coth \gamma R}. \quad (22)$$

For the reflection coefficient to be small over a broad frequency band, it is necessary that the transmission loss be large; that is, the real part of  $\gamma R$  must be large. For any nonzero loss,  $\sigma > 0$ , one can, in principle,

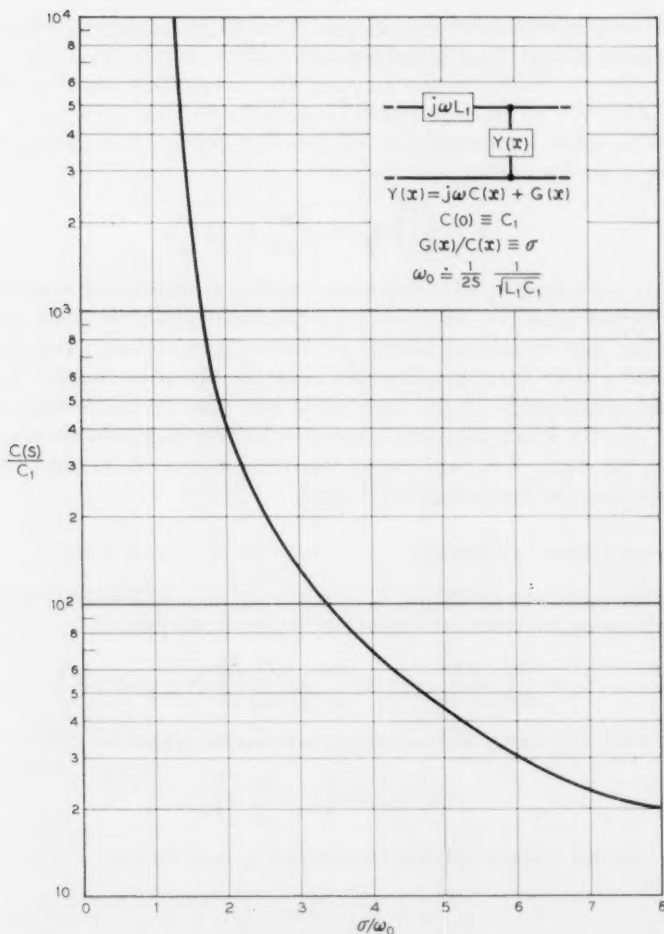


Fig. 2 — Admittance ratio required for 13-db transmission loss.

make the effective length of the line,  $R$ , sufficiently large so that the transmission loss is as large as desired. It follows from (20) that this can be accomplished in a line whose length is

$$s = \frac{\lambda_0}{4\pi} (1 - e^{-R}). \quad (23)$$

Thus, if the physical length and the desired effective length of the line are specified, the cutoff wavelength can be determined from (23). For large  $R$ , the cutoff wavelength is essentially given by  $4\pi s$ .

A large value of  $R$  is obtained by approaching the singularity in  $\epsilon(x)$ . The real part of  $\epsilon(x)$ , at  $x = s$ , is given by

$$\frac{C(s)}{C_1} = \left(1 - \frac{4\pi}{\lambda_0} s\right)^{-2} = e^{2R}, \quad (24)$$

so that exceedingly large values of distributed shunt capacitance are required to obtain moderately large effective lengths.

The above formalism may be used to calculate the distributed shunt capacitance at  $x = s$  required to ensure a given transmission loss. This result will, of course, depend on the value of the loss parameter,  $\sigma/\omega_0$ . As an example, in Fig. 2 the value of  $C(s)/C_1$  required to ensure a minimum transmission loss of 13 db for all  $\omega \geq \omega_0$  is shown as a function of  $\sigma/\omega_0$ .<sup>\*</sup> If  $\sigma/\omega_0$  is very much less than one, an astronomically large value of  $C(s)/C_1$  is required. Although this may not be realizable in practice, it gives an upper limit to the ideal behavior of the line.

If the transmission loss is sufficiently large,

$$\coth \gamma R \doteq 1. \quad (25)$$

If, in addition,  $\sigma/\omega_0$  is neglected in comparison to unity, it follows from (18) and (22) that

$$|\rho|^2 = \frac{1 - \sqrt{1 - \omega_0^2/\omega^2}}{1 + \sqrt{1 - \omega_0^2/\omega^2}}. \quad (26)$$

Equation (26) gives the intensity reflection coefficient of the ideal line. The return loss ( $-10 \log_{10} |\rho|^2$ ) is plotted as a function of frequency in Fig. 3. The return loss is zero at the cutoff frequency, but increases rapidly as the frequency is increased.<sup>†</sup>

As a more practical example, the return loss will also be calculated for  $\sigma/\omega_0 = 2$ . It follows from Fig. 2 that this requires  $C(s)/C_1$  to be 400 to ensure a 13-db transmission loss. This choice, in addition to being physically reasonable, leads to some computational simplifications. It follows from (18) that, if  $\sigma/\omega_0$  is 2, then

$$\gamma = \frac{1}{2} \left(1 + j \frac{\omega}{\omega_0}\right), \quad (27)$$

<sup>\*</sup> The 13-db transmission loss requirement is equivalent to  $|e^{-2\gamma R}| = 0.05$ . It can be shown from (18) that the real part of  $\gamma$  has a minimum,  $\alpha_m$ , given by the smaller of  $\sqrt{\sigma/8\omega_0}$  and  $\sigma/4\omega_0$ . These two results, together with (24), were used to obtain Fig. 2.

<sup>†</sup> In Section II the parameter  $a$  was introduced, and it was assumed that reflections would be small if  $a$  were small. It has since been shown [in (17)] that  $a = 4/(\omega/\omega_0)$ . Fig. 3 then gives a quantitative demonstration of the initial supposition. For  $a = 4$ , there is total reflection. As  $a$  decreases ( $\omega/\omega_0$  increases), the reflection is seen to decrease rapidly.

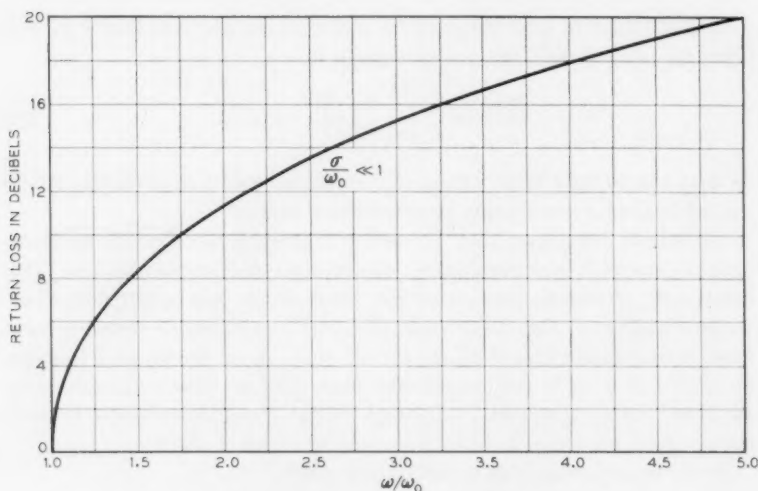


Fig. 3 — Return loss of the "ideal line".

so that the effective attenuation constant (real part of  $\gamma$ ) is frequency-independent. The effective length of this line is  $R = 3$ . For these values of  $\gamma$  and  $R$ ,  $\coth \gamma R$  varies between 0.9 and 1.1 as the frequency is changed. If, as before, it is assumed that  $\coth \gamma R = 1$  (thus assuming  $R \gg 1$ , which is equivalent to neglecting interference effects due to multiple reflections), the reflection coefficient of the line is given by

$$|\rho|^2 = \frac{1}{1 + (\omega/\omega_0)^2}. \quad (28)$$

If this approximation is not made, the exact expression for  $|\rho|^2$  is more complicated but still easily amenable to numerical evaluation. The solid curve in Fig. 4 gives the return loss as a function of frequency, as evaluated from the exact expression. The dashed curve gives the return loss, neglecting interference effects, as determined from (28). In the frequency range depicted, the exact return loss is seen to oscillate about the value obtained when interference effects are neglected. However, in the high-frequency limit ( $\omega \gg \omega_0$ ) the two curves diverge. The return loss increases without limit if the effective length of the line is infinite. However, for  $R = 3$ , the return loss at high frequencies approaches 26 db, which is just the two-way transmission loss of the line.

It is seen from Fig. 4 that there is a 3-db return loss at the cutoff frequency of the "ideal line." However, as the frequency increases, the loss increases only gradually; at  $\omega = 4\omega_0$  the return loss is 13.3 db as com-

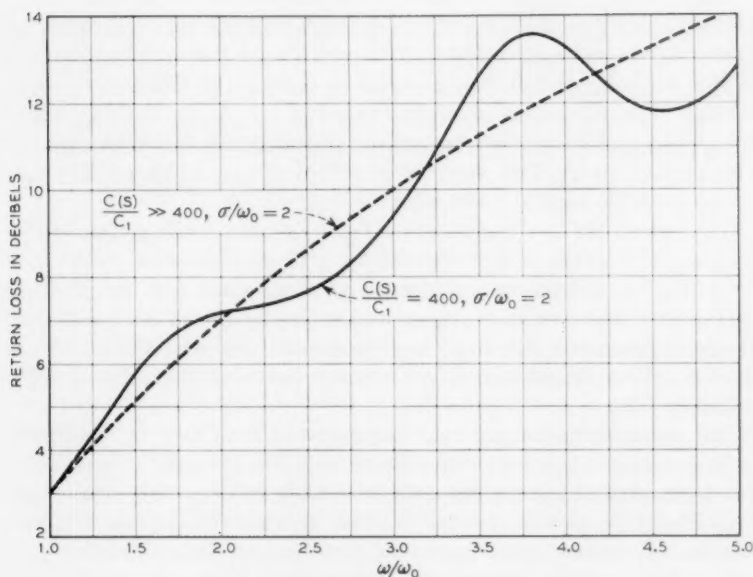


Fig. 4 — Return loss of a "practical line".

pared to 17.8 db for the ideal line. Thus, practical limitations on maximum shunt capacitance have an appreciable influence on the behavior of the line.

#### V. CONCLUSIONS

Properties of nonuniform transmission lines have led to the consideration of a line in which the fractional change in shunt admittance per wavelength in the line is constant. The transmission line equations have been solved exactly for this case. The solution indicates that a fixed length of line  $s$  can be made to have as large an effective length as desired. Hence, with the introduction of a small loss term, all energy matched into the line is essentially completely absorbed regardless of the line's termination.

It has been shown that the line has a long wavelength cutoff given essentially by  $\lambda_0 \doteq 4\pi s$ . As the frequency increases beyond cutoff frequency  $\omega_0$ , the reflected intensity from the short-circuited line diminishes rapidly, being 11.4 db down at  $2\omega_0$  and 17.8 db down at  $4\omega_0$ , as seen from Fig. 3.

If practical considerations limit the maximum shunt capacitance, it is necessary to use a larger shunt conductance to obtain the same trans-

mission loss. This degrades the performance of the line somewhat, as shown by the example in Fig. 4. If a return loss of 10 db is required, it is seen from Fig. 4 that the line must be operated at frequencies above  $3.1 \omega_0$ . Thus, the length of the line would be  $s = \lambda_0/4\pi = 0.25\lambda$ , where  $\lambda$  is the longest wavelength for which the return loss would be equal or greater than 10 db. This length is one-third of that which would be required with the equivalent exponential line.

The "ideal line", as indicated by Fig. 3, gives a 10-db return loss at  $1.75 \omega_0$ . The length of line required for a 10-db absorption would then be  $0.14\lambda$ . The differences between the ideal structure and the practical example become even more pronounced as greater absorption is required. However, practical structures may approach the performance of the ideal line if one considers a variation of the loss term  $\sigma$  in addition to the variation  $C(x)$ .

The nonuniform transmission line analyzed here may be considered to be a singularity of the general Bessel line. It is of analytic interest because the solutions are in the form of readily interpretable elementary functions. It is also of physical interest because the particular variation of line parameters is suggested by a common approximation procedure for analyzing nonuniform transmission lines, and because the exact solutions indicate that the line has desirable properties as a broadband termination.

#### ACKNOWLEDGMENT

The author wishes to acknowledge the many helpful discussions on this subject with W. J. Albersheim and W. H. von Aulock.

#### REFERENCES

1. Schelkunoff, S. A., *Electromagnetic Waves*, D. Van Nostrand Co., New York, 1943, Chapter 7.
2. Jackson, W., *High Frequency Transmission Lines*, Methuen & Co., London, 1945, Chapter 4.
3. Kaufman, H., Bibliography of Nonuniform Transmission Lines, Trans. IRE, AP-3, October 1955, pp. 218-220.
4. Willis, J. and Sinha, N. K., Nonuniform Transmission Lines as Impedance-Matching Sections, Proc. IRE, 43, December 1955, p. 1975.
5. Kock, W. E., Metallic Delay Lenses, B.S.T.J., 27, January 1948, pp. 58-82.
6. Bozorth, R. M., *Ferromagnetism*, D. Van Nostrand Co., New York, 1951, pp. 798-803.
7. Slater, J. C., *Microwave Transmission*, McGraw-Hill Book Co., New York, 1942, pp. 69-78.
8. Burrows, C. R., The Exponential Transmission Line, B.S.T.J., 17, October 1938, pp. 555-573.
9. McLachlan, N. W., *Bessel Functions for Engineers*, 2nd ed., Oxford Univ. Press, New York, 1955, pp. 123-132.
10. Starr, A. T., The Nonuniform Transmission Line, Proc. IRE, 20, June 1932, pp. 1052-1063.



# Using Contact Resistance to Measure Adsorption of Gases on Metals

By P. KISLIUK

(Manuscript received December 5, 1957)

*The contact resistance between electrodes of molybdenum and tungsten is used to investigate the adsorption of nitrogen and oxygen. It is found that, on clean metals, the initial period of fast adsorption gives rise to a surface resistivity of about  $4 \times 10^{-10}$  ohm-cm<sup>2</sup>, corresponding to a layer of the order of 1.6 Angstroms thick on each surface. To remove, within a minute or so, the layers resulting from adsorption beyond this initial period, temperatures near 1700°K are required for all four metal-gas combinations.*

*Some of the oxygen adsorbed at a pressure of a few torr\* at room temperature can be removed by lowering the pressure, but such an effect was not observed for nitrogen. Nitrogen or oxygen adsorbed during the initial period of fast adsorption on clean molybdenum or tungsten at a temperature of 100°K is not removed in times of the order of one hour by lowering the pressure, in disagreement with some results in the literature. The rate of migration of adsorbed oxygen into and out of the region between closed contacts is found to be much lower than that reported in an earlier experiment of the same type.*

## I. INTRODUCTION

Measurement of the contact resistance between metal electrodes can be used to study surface films of nonconducting substances such as adsorbed gases. In comparison with other techniques it has the following advantages:

1. It can be used in the presence of the gas.
2. It can be used over a wide temperature range.
3. It does not depend primarily on the change in work function, which might be small for some adsorbates.

\* Throughout this paper the unit of pressure will be the "torr", a unit widely used in Europe to designate one millimeter of mercury of pressure, i.e.,  $1.332 \times 10^3$  dynes/cm<sup>2</sup>. (See, for example, W. H. Westphal, *Physikalisches Wörterbuch*, Springer Verlag, Berlin, 1952). This avoids the awkward "millimeters of mercury of gas X."

4. Under many conditions it does not destroy the surface film.

5. Adsorption can be studied on the bulk metal, which can be degassed by vigorous heating; i.e., dispersed conditions such as powders or porous films are not required.

In general, the contact resistance arises from two effects, the constriction of the lines of current flow into a relatively small region of contact and the resistance offered by a surface film. The pioneering paper in this field is due to Holm and Meissner,<sup>1,2</sup> who resorted to low temperatures to minimize the constriction resistance and showed that, for reasonably clean metals, there remained a resistance due to the surface film of the order of  $5 \times 10^{-9}$  ohm-cm<sup>2</sup>. Although the method has been applied by a number of authors under a wide range of conditions,<sup>3 to 10</sup> only J. J. Went<sup>11</sup> attempted to obtain clean surfaces under high vacuum and then to investigate the adsorption of gases under controlled conditions. The present investigation is an attempt to extend these measurements using the improved vacua now available, and to interpret the results in terms of the advances in the knowledge of adsorption gained since that paper was published.

## II. PRINCIPLES OF THE METHOD

For a single circular contact area of diameter,  $d$ , much smaller than the dimensions of the electrodes, the "constriction" or "spreading" resistance is given by (Ref. 2, p. 16):

$$R_s = \rho/d, \quad (1)$$

where  $\rho$  is the bulk resistivity of the metal.

A surface film gives rise to an additional resistance inversely proportional to the contact area (Ref. 2, p. 79),  $A$ :

$$R_t = \sigma_t/A, \quad (2)$$

where  $\sigma_t$  is called the "surface resistivity."

Although  $R_s$  is not completely independent of  $R_t$  because of the rearrangement of the lines of current flow, the change is negligible for our purposes (Ref. 2, p. 18), and we may write:

$$R = R_s + R_t \quad (3)$$

Since  $R_s$  is proportional to  $1/d$  and  $R_t$  is proportional to  $1/d^2$ , smaller diameters of the contact area lead to an increase in the ratio  $R_t/R_s$ . Thus, for sufficiently small contact forces and hard metals it is not necessary to go to extremely low temperatures to measure  $R_t$ . In this

manner Went<sup>11</sup> was able to perform some of his experiments on molybdenum at room temperature.

The theory accounting for the resistance  $R_t$  for films less than about 20 Angstroms thick, valid for small potential drops (less than a few tenths of a volt), is based on a model in which the adsorbed gas is regarded as simply a spacer holding the metal contacts apart. The electrons flow by means of quantum mechanical penetration of the potential barrier. The result of calculations based on the potential barrier illustrated in Fig. 1, is:<sup>2,12,13,14</sup>

$$\begin{aligned}\sigma_t &= \frac{h^2 l}{e^2 \sqrt{2m\phi}} \exp\left(\frac{4\pi l}{h} \sqrt{2m\phi}\right) \text{ statohm-cm}^2 \\ &= 3 \times 10^{-11} (l/\sqrt{\phi}) \exp(l\sqrt{\phi}) \text{ ohm-cm}^2,\end{aligned}\quad (4)$$

where  $h$ ,  $e$ , and  $m$  have their usual significance,  $l$  is the thickness of the film and  $\phi$  the work function of the metal. The second form of the expression is valid for  $\phi$  in volts and  $l$  in Angstrom units.

This resistance is ohmic (i.e., current proportional to voltage) according to both theory and experiment.<sup>1,2</sup> A further refinement involves the inclusion of the electron image forces,<sup>2,14</sup> and the result of this calculation is plotted in Fig. 2. It may be seen from (4) that the exponential factor is dominant so long as  $l\sqrt{\phi}$  is greater than one and that, under this condition, the resistance is extremely sensitive to  $l$  and slightly less sensitive to  $\phi$ . This is the case for all practically attainable values of  $l$  and  $\phi$ .

To interpret the data one must have some knowledge of the dimensions of the contact area. For perfectly smooth electrodes under most of the experimental conditions, the contact force could, in principle, be supported elastically. Because of the roughness of practical surfaces,

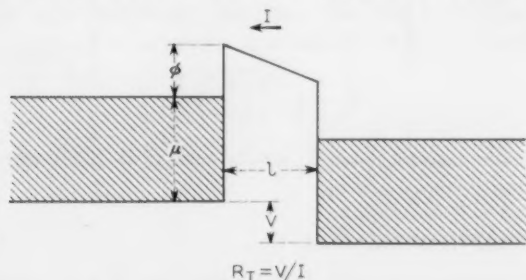


Fig. 1 — Potential diagram illustrating the model used in the derivation of equation (4).

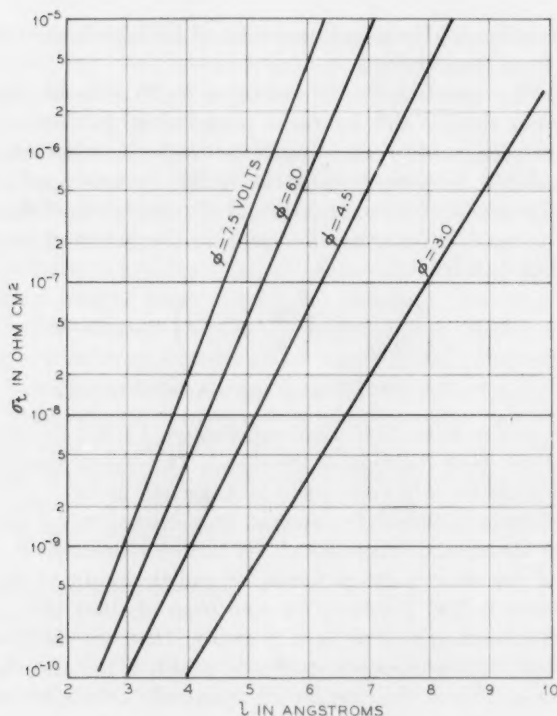


Fig. 2 — Contact resistivity,  $\sigma_c$ , versus film thickness for various values of the work function. The electron image force has been taken into account, modifying the potential barrier illustrated in Fig. 1.

however, the load is in fact supported by squashing a small contact region inelastically. Under this condition the contact area can be calculated approximately if the hardness of the metal is known:

$$d = \sqrt{\left(\frac{4}{10^8\pi}\right) \frac{P}{H}}, \quad (5)$$

where  $P$  is the contact load in grams and  $H$  is the hardness on the Vickers scale.

### III. EXPERIMENTAL APPARATUS

The apparatus used in these experiments (Fig. 3) consisted essentially of two mechanically polished crossed wires (diameter  $15 \times 10^{-3}$  in.)

mounted on flat molybdenum springs. The lower of these was connected to a quartz yoke which could be pulled up by a micrometer screw operating through a sylphon bellows. The force constant of the spring on which the upper wire was mounted was measured both before mounting and after dismantling, and the constancy of the force constant as the spring was cycled between room and liquid nitrogen temperature was verified in a separate experiment. The motion of the upper spring as a function of the micrometer setting was calibrated with a cathetometer.

The tube was mounted in a vacuum system (mercury diffusion pump and liquid nitrogen trap) capable of reducing pressure to the order of  $10^{-10}$  torr as measured on an ionization gauge. A gas-handling manifold was provided and isolated from the system by a Westinghouse-type

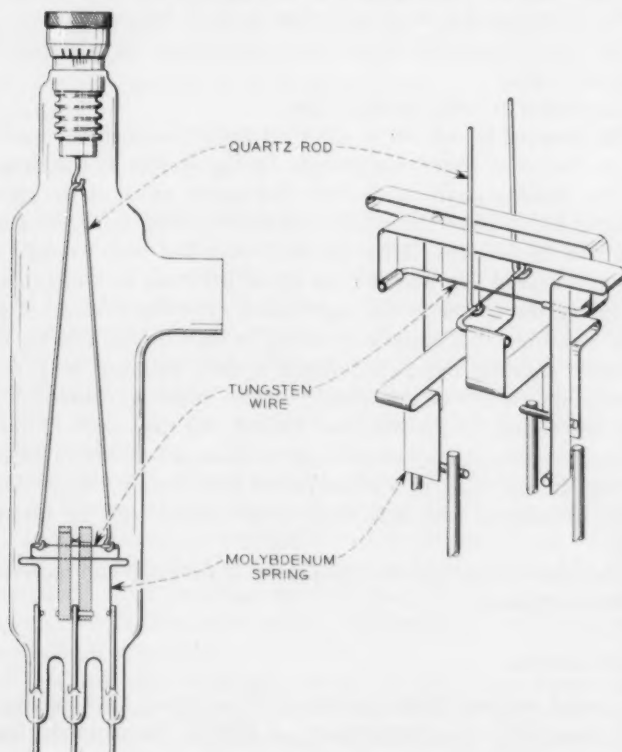


Fig. 3 — The tube in which these experiments were performed.

vacuum valve.<sup>15</sup> The gases were of spectroscopic grade supplied by the Air Reduction Company. The test wires could be flashed by conduction.

The contact resistance was measured in the region near 50 milliamperes and one millivolt by a four-terminal method using a milliammeter and microvoltmeter, exactly as described by Went.<sup>11</sup>

#### IV. EXPERIMENTAL RESULTS

Experiments were performed on tungsten and molybdenum electrodes using nitrogen and oxygen as adsorbates. The behavior of the two metals is very similar, and that of the two gases differs only at relatively high pressures. The experiments are subdivided as follows:

1. The behavior of clean metals.
2. The resistance due to gas adsorbed at room temperature.
3. The temperature of flash necessary to remove the adsorbed film in a reasonable time.
4. Adsorption at lower temperature.
5. The creeping in and out of adsorbed gas between closed contacts.

One is limited in these experiments by the scatter in the data. In a run of ten closures at the same force the largest value of the resistance was usually about twice the smallest, and the average deviation from the mean about 20 per cent. After the electrodes had been exposed to the same conditions of gas pressure for equal intervals at widely different times during the course of the experiment even the average of ten resistance measurements sometimes varied by as much as a factor of two. This scatter is partly due to differences in local hardness because of the polycrystalline nature of the wires, but also could be caused by differences in annealing, as the wire was flashed and then work-hardened in the contact region. It may also be due to local differences in adsorptive properties. In any case, as a consequence little weight can be attached to small differences and only fairly gross effects can be interpreted reliably.

Some of the relevant physical properties of tungsten and molybdenum are given in Table I.

##### 4.1 *Clean Surfaces*

The metal surfaces were presumed to be clean after having been flashed repeatedly at a temperature of 2000°K for molybdenum, and at a somewhat higher temperature for tungsten, in a measured residual gas pressure of about  $2 \times 10^{-10}$  torr. By measuring the increase in the maximum pressure during a flash as a function of the cold interval, it

TABLE I—PROPERTIES OF MOLYBDENUM AND TUNGSTEN

		Present Work*	Other References
Resistivity, $\rho$ , 300°K.	Mo W	— —	$5.9 \times 10^{-6}$ ohm-cm† $5.85 \times 10^{-6}$ ohm-cm†
Ratio of Resistivity, $\frac{\rho_{300^\circ\text{K}}}{\rho_{78^\circ\text{K}}}$	Mo W	10.2 9.3	9.3‡ 8.4‡
Hardness, $H$ , 300°K	Mo W	230 480	160–225§ 290–488§
Ratio of Hardness, $\frac{H_{300^\circ\text{K}}}{H_{78^\circ\text{K}}}$	Mo W	0.53 0.62	— —

\* Measured resistivity ratios are for wires after outgassing in high vacuum. The hardnesses were measured on larger pieces from different samples. In the case of tungsten, the hardness samples had also been vacuum annealed, but the molybdenum hardness sample was not so treated.

† Ref. 16, pp. 2357–2363

‡ Refs. 17 and 18

§ Ref. 19, pp. 1140, 1144

was verified that about five hours were required to reach a constant value. The experiments to be reported in this section were performed within a period less than one-half hour after the flash.

For a force of 1 gm ( $\pm 5$  per cent) the contact resistance averaged between 10 and 16 milliohms for molybdenum and between 14.5 and 28 milliohms for tungsten. This range of values is for different samples and for measurements taken at different times during the course of these experiments. If the values of the hardness and resistivity listed in Table I are used in equations (1) and (5), one computes 22 and 36 milliohms for the two metals. Considering that the load is supported elastically to some extent and that the contact region may not be exactly circular, this agreement is satisfactory. It is assumed in latter portions of this paper that contact areas obtained from the measured resistivities under these conditions are more reliable than those computed from the hardness.

The contact resistance between clean metal electrodes, according to (1) and (5), should vary as the inverse square root of the force, and it does so within the limits of experimental error, as can be seen in one of the curves of Fig. 4.\* However, to obtain this result it is necessary to

\* For the opposite extreme, when  $R_t \gg R_s$  rather than  $R_s \gg R_t$ , one would expect  $R$  to vary as the inverse first power of the force if the load is supported by plastic deformation. The other curve of Fig. 4, obtained for the thickest film observed during the course of these experiments, shows that this is also verified experimentally.



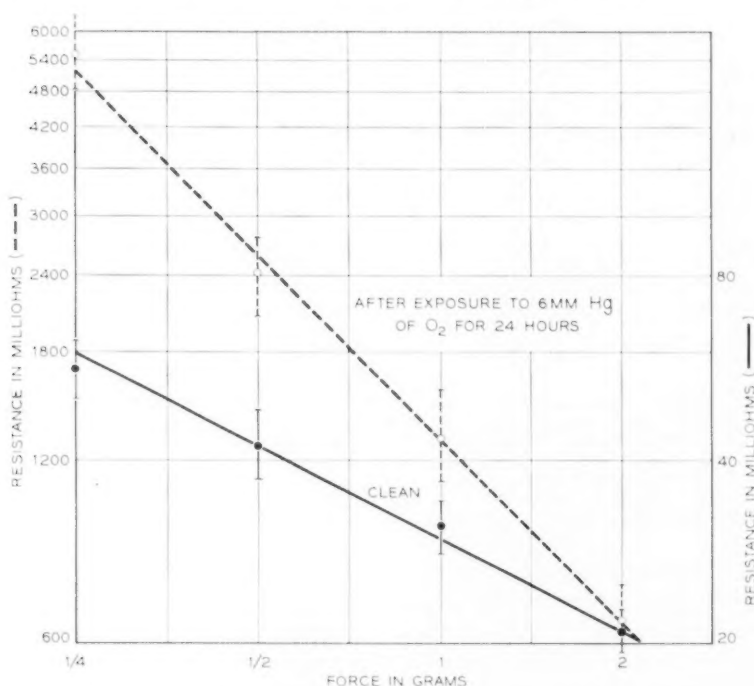


Fig. 4 — Contact resistance versus contact force for clean tungsten electrodes and for electrodes which have been exposed to 6.5 torr of oxygen for 24 hours. Each point is the average for five closures.

increase the force to its final value and not to overshoot and come back. The effect of cycling is shown in Fig. 5. There is also a relatively slow increase in contact area with time and a typical curve of the resulting decrease in resistance is shown in Fig. 6.

The assumption that the load is supported on regions formed, for the most part, by plastic flow is thus confirmed by the following observations:

1. The approximate agreement of the measured value of  $R_c$  with that computed on this assumption. The contact resistances computed for an elastically supported load are considerably smaller than those found experimentally.
2. The slopes in Fig. 4, which are 0.5 clean and 1.0 with a thick film, as expected for plastic deformation, rather than 0.3 and 0.7, as would be expected for purely elastic deformation.

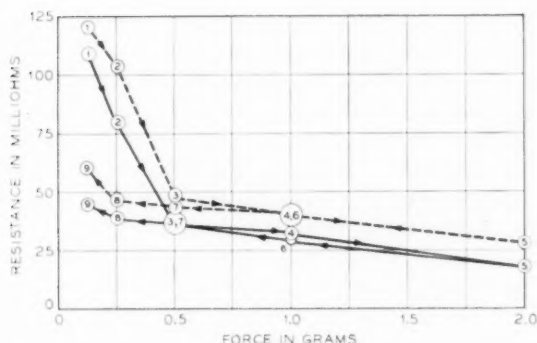


Fig. 5 — The contact resistance of clean tungsten with increasing and decreasing contact force. The numbers on the experimental points give the sequence of the measurements.

3. The irreversibility exhibited in Fig. 5.

4. The slow changes shown in Fig. 6.

The second point also shows that any surface film still present on the nominally clean surface contributes very little to the measured resistance.

The results of attempts to check the effect of lowering the temperature on the contact resistance of clean metals were inconclusive because:

1. The long time (about one-half hour) required for the contacts to cool down to liquid nitrogen temperature after flashing made the vacuum requirements much more severe.

2. Inadequate radiation shielding made the actual temperature of the contacts uncertain.

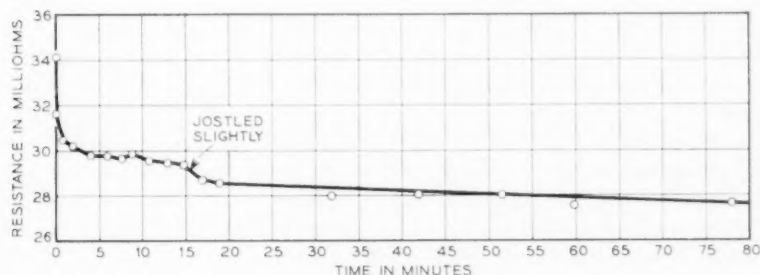


Fig. 6 — The contact resistance between closed clean tungsten contacts (force = 1 gm) as a function of time. The tube was jostled slightly by passing footsteps at the time indicated.

For both metals, the contact resistances measured when the contacts were closed with the tube immersed in a liquid nitrogen bath were lower by a factor of about four than the contact resistances measured at room temperature with the same contact force. The resistivity and hardness ratios of Table I, however, would lead one to expect a factor of about seven.\*

In summary, the results of these experiments are consistent with the behavior expected for clean metals plastically deformed by the contact load. The contact areas for a force of 1 gm at room temperature are about  $2 \times 10^{-7}$  cm<sup>2</sup> for molybdenum and  $5 \times 10^{-8}$  cm<sup>2</sup> for tungsten.

#### 4.2 *The Contact Resistance Due to Gases Adsorbed at Room Temperature*

A series of experiments in which the contact resistance was measured after tungsten contacts were exposed to nitrogen and oxygen at various pressures and for various intervals is reported in Appendices A and B and summarized in Figs. 11 and 12. The gas was usually admitted by opening a metal valve very slightly and allowing the gas to leak in while the system was continuously being pumped. Because of the pumping action of the ion gauge and the glass walls, which decreased as they became saturated, the pressure showed a steady increase with time. However, for nitrogen, except at the lowest pressures, the effect was small, so that the rate of change in pressure could be ignored in computing the pressure-time product, here called the "exposure". For oxygen, on the other hand, the effect was quite large and had to be taken into account. The corresponding desorption during the interval of pumping out the gas resulted in higher pressures after a given time with oxygen than with nitrogen.

To interpret these results, it is helpful to review some of the results of measurements obtained by other methods. When nitrogen (and perhaps oxygen) molecules strike a clean molybdenum or tungsten surface at room temperature, the sticking probability,  $s$ , is relatively constant and of the order of tenths until a coverage of roughly  $1.7 \times 10^{14}$  molecules per cm<sup>2</sup> is attained, at which point it falls off rather sharply to a much lower value.<sup>20, 21, 22</sup> Thus, after a few seconds at  $10^{-6}$  torr or a few minutes at  $10^{-8}$  torr, this coverage is attained, after which the coverage changes relatively slowly. The sticking probability continues to fall off with increasing coverage until, after a considerably longer time (of the order of 15 minutes for nitrogen at  $10^{-6}$  torr, when the coverage is above  $3.5 \times 10^{14}$  molecules per cm<sup>2</sup>), the sticking probability remains relatively constant at a value of roughly  $10^{-4}$ . When the coverage reaches approxi-

\* Went<sup>11</sup> reports a factor of only 2.3.

mately  $5.5 \times 10^{14}$  molecules per  $\text{cm}^2$ , the sticking probability for nitrogen falls off to an immeasurably small value.<sup>21</sup> The "exposure" for the first step of rapid adsorption is, for nitrogen, approximately  $3 \times 10^{-8}$  torr-min, and exposure needed for a relatively constant low value of  $s$  is approximately  $10^{-5}$  torr-min. To attain the immeasurably low sticking probability the exposure is roughly  $10^{-3}$  torr-min.\*

The results given in Appendix A and Fig. 11 for nitrogen on tungsten may be summarized as follows: Exposures corresponding to the completion of the critical period of rapid chemisorption give rise to a surface resistivity of  $3.5 \times 10^{-10}$  ohm-cm<sup>2</sup>, while exposures corresponding to the attainment of immeasurably low sticking probability give rise to a surface resistivity of  $12 \times 10^{-10}$  ohm-cm<sup>2</sup>. Higher values of the surface resistivity observed for much greater exposures may be due to impurities in the gas. No appreciable part of the adsorbed layer giving rise to the observed values of  $\sigma_t$  could be removed at room temperature by pumping out the nitrogen.

The results given in Appendix B and Fig. 12 for oxygen on tungsten yield  $\sigma_t = 5 \times 10^{-10}$  ohm-cm<sup>2</sup> at the completion of the initial period of rapid absorption, and  $\sigma_t \approx 10 \times 10^{-10}$  ohm-cm<sup>2</sup> for exposures roughly ten times as great. However, at pressures above  $10^{-5}$  torr the resistance continues to increase at a measurable rate up to the longest times observed (24 hours) and eventually exceeds any of the values observed for nitrogen on tungsten. This is attributed to the formation of one of the stable oxides of tungsten (perhaps  $\text{WO}_3$ ). For the growth of such films a logarithmic law, the "Elovich" equation, has been widely observed,<sup>23</sup> but no attempt to follow this growth quantitatively will be made in the present paper. For the thickest film observed, resulting from the exposure to 6 torr of oxygen for 24 hours (Fig. 4),  $\sigma_t$  was equal to  $6 \times 10^{-8}$  ohm-cm<sup>2</sup>.

When the pressure has been as high as several torr of oxygen, loosely held molecules on the oxide film contribute to the contact resistance. These can, however, be pumped off at room temperature.

While the data on molybdenum are less extensive, the values of  $\sigma_t$  for the first and second steps of adsorption on the two metals are similar, as is the behavior of oxygen at a pressure of a few torr.

#### 4.3 Temperature of Flash Necessary to Remove the Adsorbed Film

In these experiments, the contacts were exposed to a few torr of the gas in question for a few minutes, and the system was then pumped

\* The sticking probability may be a function of pressure at high pressure; i.e., processes other than the arrival rate may control the rate of reaction.

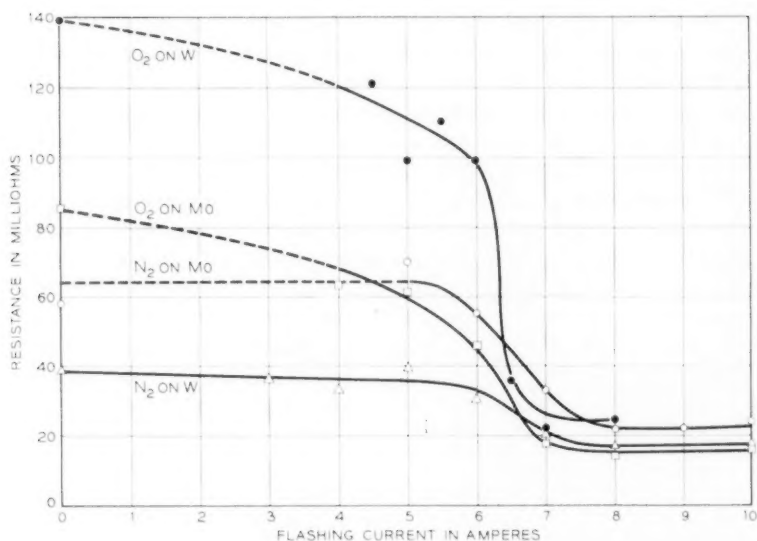


Fig. 7 — The contact resistance at room temperature (force = 1 gm) after heating for 30 sec with various currents for molybdenum and tungsten contacts which have been exposed to a few torr of oxygen or nitrogen.

down to a pressure of about  $10^{-8}$  torr before the flashing procedure\* was started.

The heating current was maintained for 30 seconds, after which 5 minutes were allowed for cooling. The results are given in Fig. 7, where each point is the average for five closings.

Flashing at about  $1000^{\circ}\text{K}$  causes some lowering of the contact resistance for oxygen on either metal, whereas for nitrogen there is no observable effect below  $1450^{\circ}\text{K}$  on molybdenum, and below a somewhat higher temperature on tungsten. For all four combinations of gas and metal there is a sharp drop in resistance after flashing at 6.5 amperes ( $1600 \pm 50^{\circ}\text{K}$  for molybdenum,  $1750 \pm 100^{\circ}\text{K}$  for tungsten) and the curve is essentially flat above about  $1725^{\circ}\text{K}$  for molybdenum, and above  $1800^{\circ}\text{K}$  for tungsten.

The molybdenum temperatures were measured with an optical pyrometer and suitably corrected for the emissivity and reflection in the glass.

\* Even at this lower pressure, a layer corresponding to the fast adsorption (first step) can be adsorbed in the few minutes necessary for the electrodes to cool, so that it was not possible to determine whether the metal had been completely cleaned, but only whether the thicker layers had been flashed off.

Unfortunately, the wall of the tube in the tungsten experiment had been coated with evaporated metal before such a temperature measurement was taken, so that these temperatures are taken from the tables of Jones and Langmuir,<sup>24</sup> with an estimated correction for cooling at the ends.

The data for oxygen on molybdenum are consistent with those of Went,<sup>11</sup> who finds some reduction in resistance after heating to 1000°K for 5 minutes and a more marked drop after heating to 1750°K. A rise in resistance observed by Went at 1400°K was not observed in the present experiment.

For oxygen on tungsten the results of field emission microscope experiments are roughly consistent with the present experiments. These results have been interpreted to be due to these successive actions: partial desorption from some crystal planes in one minute at 800°K; a temperature region (800 to 1400°K) where there is no further desorption; a resumption of desorption (perhaps of  $\text{WO}_3$ ) from all planes in the region from 1400 to 1700°K.<sup>20,25</sup>

The observation of some relatively loosely bound oxygen is also in agreement with Morrison and Roberts,<sup>26,27</sup> who suggest that these molecules are adsorbed on isolated empty sites for the chemisorption of an atom, where the molecule is prevented from dissociating by the lack of an adjacent empty site.

For nitrogen on tungsten the present result differs from that of Becker and Hartman,<sup>28</sup> in that we do not observe a decrease in contact resistance after 30 seconds at temperatures in the neighborhood of 1100°K even when, in their notation,  $\theta \approx 2$  (second step of adsorption complete), under which condition they observe a measurable rate of desorption. However, there is rough agreement as to the temperature necessary to clean the metal surface.

#### 4.4 Adsorption at Lower Temperature

Went<sup>11</sup> and de Boer and Kraak<sup>29</sup> present evidence that oxygen is only physisorbed and may be pumped off when it is admitted to a nominally clean molybdenum surface at a temperature near 100°K. On the other hand, Gomer<sup>25,30</sup> has shown that, even at 40°K, oxygen is rapidly chemisorbed on a clean tungsten surface. One is tempted to conclude that the vacuum techniques at the time of the experiments of Went and de Boer and Kraak were not adequate to maintain a clean surface during preparations necessary before oxygen was admitted (cooling down after flashing, in the case of Went, and pre-sintering the evaporated film, in

the case of de Boer and Kraak). The reversible adsorption they observe may thus apply to surfaces already covered with chemisorbed atoms. The arguments presented by Went to show that his surface was essentially clean can be shown to be inconclusive. One possible exception may be the high temperature required to recover his "clean" state, but the evidence that the surfaces remained clean while cooling down to liquid oxygen temperature is unconvincing.

The present experiments were performed in a liquid nitrogen bath for oxygen on tungsten, nitrogen on tungsten and nitrogen on molybdenum. The results of these experiments are tabulated in Appendix C. In no case was the initial state of cleanliness recovered by pumping at the low temperature. In the case of nitrogen on tungsten, there was an increase in resistance during the pumping interval, possibly due to the accumulation of impurity gases on the surface.

The temperature of the contacts in these experiments was somewhat above that of the liquid nitrogen bath, because of inadequate radiation shielding. With all exposed parts of the tube packed with dry ice to reduce thermal radiation, the resistance of one of the tungsten wires was used as a thermometer. Using this procedure, the temperature in the above experiments was estimated to be  $95 \pm 10^\circ\text{K}$ .

In summary, the bulk of the nitrogen and oxygen taken up during the initial period of fast adsorption at  $95^\circ\text{K}$  cannot be removed in a few hours by merely reducing the gas pressure to a much lower value. This is in disagreement with some early results,<sup>11,29</sup> but is in agreement with more recent experiments.<sup>25,30</sup>

#### 4.5 *The Creeping in and out of Adsorbed Gas Between Closed Contacts*

Went (Ref. 11, Fig. 10) reports that physisorbed layers of oxygen at room temperature can migrate in and out of the region between contacts of molybdenum. He presents arguments to show that this is possible. In the present experiments the observed effects were smaller by at least one order of magnitude.

After the sequence of measurements of Fig. 6, where the fall in contact resistance with time on clean metal is attributed to a slow increase in area, 5 torr of oxygen were admitted to the closed tungsten contacts. The contact resistance as a function of time is shown in Fig. 8(a). The increase in resistance in 100 minutes is small and occurs in a single jump, and so may be due to a jarring of the apparatus.

If the contacts are closed in the presence of the gas, the resistance between the contacts decreases with time [Fig. 8(b)]. This is not necessarily due to the squeezing out of gas, as it is of the order to be expected



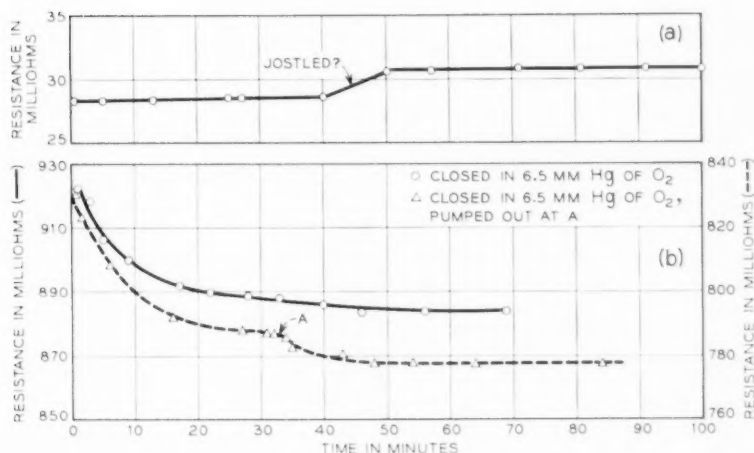


Fig. 8 — (a) The resistance between closed tungsten contacts (force = 1 gm) as a function of time when 5 torr of oxygen are admitted at  $t = 0$ . This sequence actually follows that of Fig. 6. While no actual disturbance was noted at the time marked "jostled?" the flatness of the curve for earlier and later times indicates that this is very likely the reason for the sudden small increase in resistance during this interval. (b) The resistance between closed tungsten contacts as a function of time after exposure to 6.5 torr of oxygen. At the point marked "A" on one of the curves the gas was pumped out without disturbing the closed contacts.

because of slowly increasing area, judging from the rate of change of the resistance between clean contacts (Fig. 6). If the gas is pumped out during such a sequence, a small discontinuity sometimes results [Fig. 8(b)] which may be due to gas molecules migrating out of a small region near the edge of the contact area.

A similar sequence for oxygen on molybdenum is shown in Fig. 9. However, this is for a somewhat lower pressure and smaller time of exposure before closing than that used by Went<sup>11</sup> (2.7 torr rather than 10 torr and two hours rather than ten hours).

#### V. INTERPRETATION AND DISCUSSION

The experiments on clean metal (Section 4.1) show that the assumptions leading to equations (1), (2), (3) and (5) are approximately valid, and give a means for measuring the contact area.

To interpret the data on films adsorbed at room temperature (Section 4.2) by means of (4) it is necessary to assign a value to the work function,  $\phi$ . The changes in contact potential during the adsorption of nitrogen or oxygen show that the work function is increased,<sup>21, 31</sup> but in

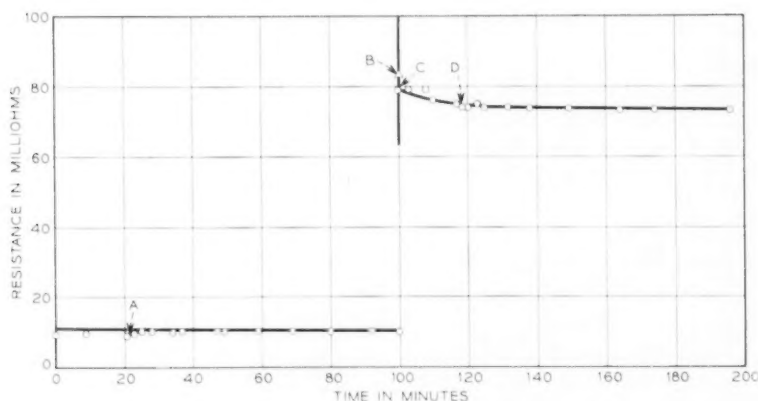


Fig. 9 — The resistance between closed, initially clean, molybdenum contacts (force = 1 gm) as a function of time at room temperature. At point A, 2.7 torr of oxygen were admitted to the system. Point B is the average resistance for ten closings in the presence of the gas. Beginning at point C the contacts were again left closed. At point D the gas was pumped out.

the presence of such an adsorbed film the potential diagram of Fig. 1 is an oversimplification and the values of  $l$  obtained by the use of (4) can have only an approximate meaning. Furthermore, the film may not be uniform over the contact area, in which case the measured values are averages heavily weighted toward a value appropriate to the thinnest film within the contact area. The values of  $l$  according to (4), using the data of Section 4.2, are given in Table II. Here,  $\phi = 5.0$  volts for nitrogen on tungsten;  $\phi = 6.0$  volts for oxygen on tungsten.

For the thickness of the layer on a single surface these values of  $l$  should be approximately halved. Thus, the entire range of thickness of the layers on each surface in these experiments is from 1.5 to 2.6 Angstroms, i.e., one or two atom diameters in thickness. The interpretation of this distance on an atomic model, however, offers considerable diffi-

TABLE II — THICKNESS OF ADSORBED FILM ON TUNGSTEN

Coverage, Molecules/cm <sup>2</sup>	Surface Resistivity Due to Film, $\sigma_f$ , ohm-cm <sup>2</sup>		Thickness of Film, $l$ , Angstrom Units	
	Nitrogen	Oxygen	Nitrogen	Oxygen
$1.7 \times 10^{14}$	$3.5 \times 10^{-10}$	$5 \times 10^{-10}$	3.3	3.1
$3.4 \times 10^{14}$	$1.2 \times 10^{-9}$	$1 \times 10^{-9}$	4.0	3.4
More than $4 \times 10^{14}$	$\sim 5 \times 10^{-9}$	up to $6 \times 10^{-8}$	4.5	up to 5.1

culty, as is illustrated diagrammatically in Fig. 10. This difficulty is connected with the problem of where to place the potential barrier (as illustrated in Fig. 1) with respect to the positions of the atoms in the surface plane<sup>32</sup>.

In Section 4.3 the range of temperatures necessary to remove these films from the surface is found to be in general agreement with that determined by other techniques. It is perhaps surprising how similar the behaviors of nitrogen on tungsten, oxygen on tungsten, nitrogen on molybdenum and oxygen on molybdenum are to one another: All require a temperature in the vicinity of 1700°K to remove a large fraction of the adsorbed gas within about 30 seconds. The heat of adsorption of the desorbing molecules is thus of the order of five electron volts.<sup>33</sup>

In Section 4.2 it was shown that some of the oxygen giving rise to the measured resistance after relatively great exposures could be pumped off at room temperature. This was not the case for nitrogen. The result reported in Section 4.3—that temperatures sufficient to remove a considerable amount of oxygen had no observable effect on the nitrogen layers—confirms the conclusion that additional oxygen is bound, though with relatively weak bonds, on top of the more firmly held layers.<sup>26,27,34</sup> Nitrogen, on the other hand, shows little tendency to stick to the completed nitrogen layers at room temperature, although some

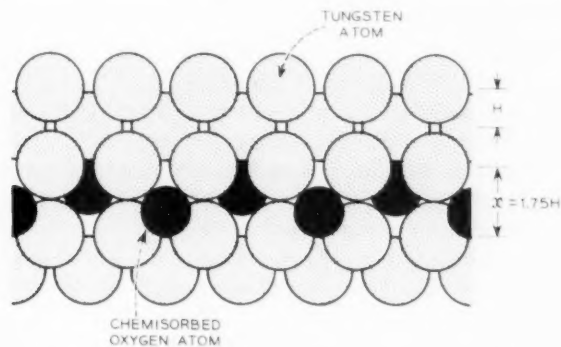


Fig. 10 — A conceivable arrangement of atoms when two (100) faces of a body centered cubic lattice are opposed, with chemisorbed gas atoms on each surface in one quarter of the lattice sites. If the coverage were twice as great, the opposing lattice planes would not necessarily be farther apart — the alternate empty positions could simply be filled in. The relative radii are approximately those appropriate to oxygen on tungsten. The distance,  $x$ , between the nearest opposed (100) planes is 1.75 times that in the normal lattice,  $H$ , i.e., about 2.8 Å. The distance  $l$  to be used in (4) should perhaps lie between this value and  $x - H$ , the increase over the normal distance, which is about 1.2 Å.

of the gas adsorbed at liquid nitrogen temperature is released as the contacts are allowed to warm up (Appendix C, Table VII).

The differences between the results of Section 4.4 on adsorption at 95°K and those reported by Went<sup>11</sup> are unexplained.

In Section 4.5 the effects of migration of adsorbed molecules between closed contacts are found to be much smaller than those observed by Went (Ref. 11, Fig. 10). This might be due to low-frequency mechanical vibration in his experiments resulting from footsteps etc., which may have rocked the contacts, allowing different regions to be exposed.<sup>7</sup> Extensive precautions against vibrations were necessary to obtain the results presented in Figs. 6, 8 and 9.

#### VI. ACKNOWLEDGMENT

The author wishes to express his thanks to G. E. Reitter for his part in the design and construction of the apparatus, to R. A. Maher for his assistance in performing the experiments, to L. H. Germer and H. D. Hagstrum for their support of the program at various stages, to the Metallurgical Research Department for the performance of the hardness tests reported in Table I and to U. B. Thomas, R. L. Barnes and G. T. Kohman for helpful criticism.

#### APPENDIX A

We interpret the values of  $\sigma_t$  for the entries in Table III numbered 2 through 6 and 12 and 13, for exposures between  $7 \times 10^{-8}$  and  $6 \times 10^{-5}$  torr-min as due to a layer corresponding approximately to the completion of the first step of rapid chemisorption. The average value of  $\sigma_t$  is  $3.5 \times 10^{-10}$  ohm-cm<sup>2</sup> ( $\pm 30$  per cent). Entries numbered 7, 8, 15 through 21 and 23 through 27, for exposures between  $1.7 \times 10^{-4}$  and  $8 \times 10^{-1}$  torr-min, we attribute to a layer somewhere in the second or third steps of slower chemisorption. The value of  $\sigma_t$  averages  $1.2 \times 10^{-9}$  ohm-cm<sup>2</sup> ( $\pm 25$  per cent).

The higher values of  $\sigma_t$  in entries 28 through 34 corresponding to exposures from 1.0 to 85 torr-min might possibly be attributed to an impurity in the gas. Oxygen, if present in a few parts in  $10^5$ , could account for such an effect, while spectroscopically unobservable impurities might be present in concentrations of the order of a few parts in  $10^4$ . The highest value of  $\sigma_t$  observed in the presence of nominally pure nitrogen is  $\sim 5 \times 10^{-9}$  ohm-cm<sup>2</sup>.

Entries 9, 10, 20, 21, 33 and 34 show that none of the adsorbed gas

TABLE III — THE ADSORPTION OF NITROGEN ON TUNGSTEN AT ROOM TEMPERATURE (Fig. 11)

Treatment	Contact Resistance (Milliohms) Average of Five Closures Force = 1 gm	$\sigma_f$ (ohm-cm <sup>2</sup> )	Total Exposure of Electrodes to Gas Since Previous Flash (torr-min)
1. Flash repeatedly; allow to cool for 10 min in residual pressure $1.1 \times 10^{-10}$ torr	17	0, assumed	0
2. Admit $7 \times 10^{-9}$ torr of N <sub>2</sub> ; wait 10 min	22	$5 \times 10^{-10}$	$7 \times 10^{-8}$
3. Wait 35 min	21	$4 \times 10^{-10}$	$3 \times 10^{-7}$
4. Wait 35 min	20	$3 \times 10^{-10}$	$5.5 \times 10^{-7}$
5. Admit $2 \times 10^{-7}$ torr of N <sub>2</sub> ; wait 5 min	20	$3 \times 10^{-10}$	$1.5 \times 10^{-6}$
6. Wait 50 min	21	$4 \times 10^{-10}$	$1 \times 10^{-8}$
7. Admit $8 \times 10^{-5}$ torr of N <sub>2</sub> ; wait 5 min	30	$1.3 \times 10^{-9}$	$4 \times 10^{-4}$
8. Wait 30 min	37	$1.9 \times 10^{-9}$	$3 \times 10^{-3}$
9. Close leak from N <sub>2</sub> source; pump for 5 min, pressure down to $5 \times 10^{-7}$ torr	36	$1.8 \times 10^{-9}$	—
10. Pump for 16 hours, pressure down to $8 \times 10^{-9}$ torr	40	$2.2 \times 10^{-9}$	—
11. Flash repeatedly, pressure falls to $1 \times 10^{-9}$ ; wait 10 min	17.5	0, assumed	0
12. Admit $4.5 \times 10^{-6}$ torr of N <sub>2</sub> ; wait 3 min	20	$2 \times 10^{-10}$	$1.3 \times 10^{-8}$
13. Wait 10 min	22.5	$4.5 \times 10^{-10}$	$6 \times 10^{-8}$
14. Wait 10 min	25	$7 \times 10^{-10}$	$1.0 \times 10^{-4}$
15. Wait 15 min	33	$1.4 \times 10^{-9}$	$1.7 \times 10^{-4}$
16. Wait 10 min	31	$1.2 \times 10^{-9}$	$2.2 \times 10^{-4}$
17. Wait 15 min	33	$1.4 \times 10^{-9}$	$2.8 \times 10^{-4}$
18. Wait 40 min	35	$1.6 \times 10^{-9}$	$4.6 \times 10^{-4}$
19. Wait 50 min	31	$1.2 \times 10^{-9}$	$6.9 \times 10^{-4}$
20. Close leak from source; pump for 5 min, pressure down to $1 \times 10^{-7}$ torr	30	$1.1 \times 10^{-9}$	—
21. Pump for 16 hours, pressure down to $3 \times 10^{-9}$ torr	31	$1.2 \times 10^{-9}$	—
22. Flash repeatedly, residual pressure down to $1 \times 10^{-9}$ torr; wait 10 min	14.5	0, assumed	0
23. Admit $4 \times 10^{-3}$ torr of N <sub>2</sub> ; wait 5 min	19	$6 \times 10^{-10}$	$2 \times 10^{-2}$
24. Wait one hour	21	$8.5 \times 10^{-10}$	$2.6 \times 10^{-1}$
25. Wait one hour	22	$1.0 \times 10^{-9}$	$5 \times 10^{-1}$
26. Admit $1.4 \times 10^{-2}$ torr of N <sub>2</sub> ; wait 5 min	21	$8.5 \times 10^{-10}$	$6 \times 10^{-1}$
27. Admit $3 \times 10^{-2}$ torr of N <sub>2</sub> ; wait 5 min	23	$1.1 \times 10^{-9}$	$8 \times 10^{-1}$
28. Admit $1.5 \times 10^{-1}$ torr of N <sub>2</sub> ; wait 2 min	33	$2.4 \times 10^{-9}$	1.0
29. Wait 30 min	28	$1.8 \times 10^{-9}$	5.5
30. Admit $9 \times 10^{-1}$ torr of N <sub>2</sub> ; wait 5 min	26	$1.5 \times 10^{-9}$	10
31. Admit 3.3 torr of N <sub>2</sub> ; wait 3 min	58	$5.7 \times 10^{-9}$	20
32. Wait 20 min	42	$3.7 \times 10^{-9}$	85
33. Open valve to pumps; in 5 min, pressure down to $3 \times 10^{-7}$ torr	51	$4.8 \times 10^{-9}$	—
34. Wait 30 min, pressure down to $2.5 \times 10^{-8}$ torr	53	$5.0 \times 10^{-9}$	—

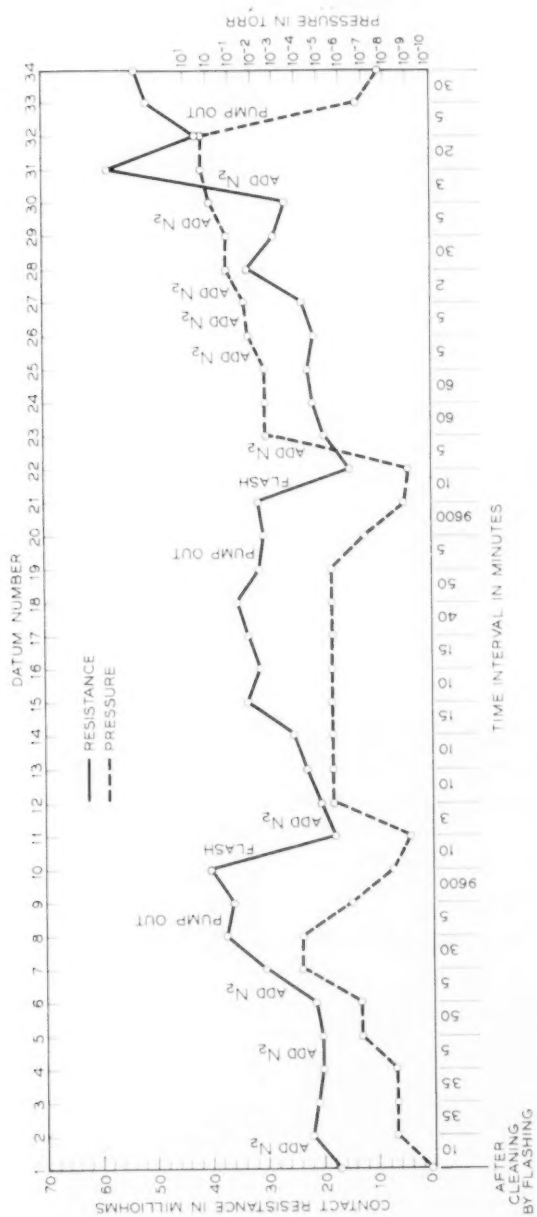


Fig. 11 — Nitrogen on tungsten, at room temperature.

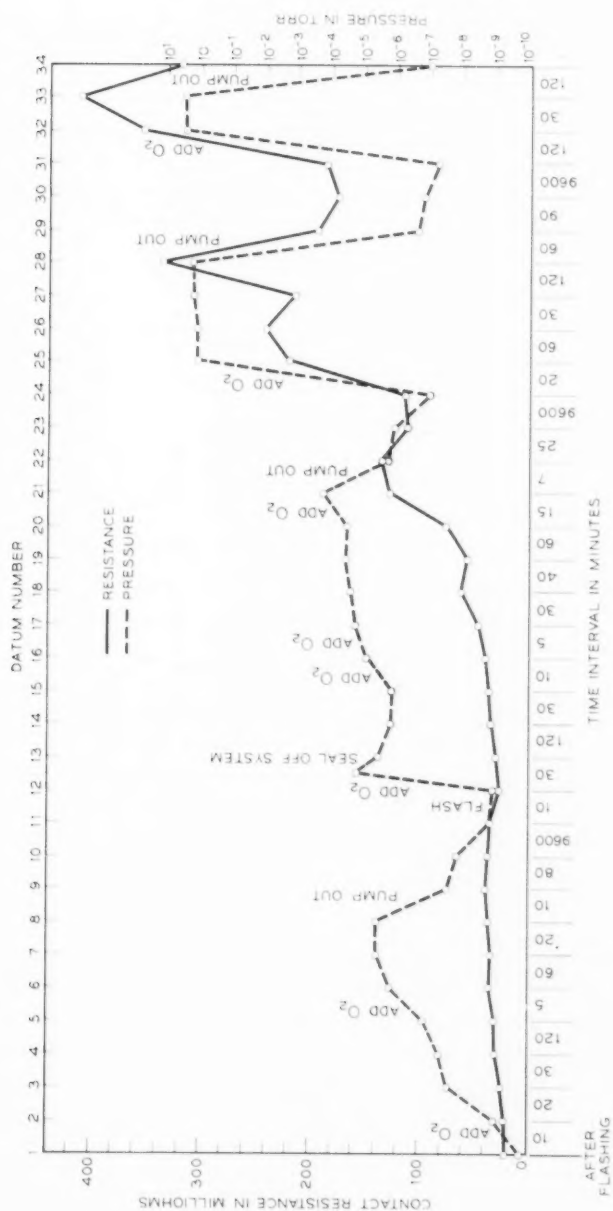


Fig. 12 — Oxygen on tungsten, at room temperature.



TABLE IV — THE ADSORPTION OF OXYGEN ON TUNGSTEN AT ROOM TEMPERATURE (Fig. 12)

Treatment	Contact Resistance (Milliohms) Average of Five Closures Force = 1 gm	$\sigma_t$ (ohm-cm <sup>2</sup> )	Total Exposure of Electrodes to Gas Since Previous Flash (torr-min)
1. Flash repeatedly in residual pressure $2 \times 10^{-10}$ torr; wait 10 min	20	0, assumed	0
2. Flash in presence of $1 \times 10^{-9}$ torr of O <sub>2</sub> ; wait 10 min, during which pressure rises to $2.5 \times 10^{-9}$ torr	20	0	$2 \times 10^{-8}$
3. Wait 20 min, during which pressure rises to $3.5 \times 10^{-8}$ torr of O <sub>2</sub>	23	$2 \times 10^{-10}$	$4 \times 10^{-7}$
4. Wait 30 min, pressure up to $6.5 \times 10^{-8}$ torr	29	$6 \times 10^{-10}$	$2 \times 10^{-6}$
5. Wait 2 hours, pressure up to $2.7 \times 10^{-7}$ torr	30	$7 \times 10^{-10}$	$2 \times 10^{-5}$
6. Reduce pumping speed, pressure rises to $2 \times 10^{-6}$ torr; wait 5 min	33.5	$9.5 \times 10^{-10}$	$3 \times 10^{-5}$
7. Wait 1 hour, pressure up to $5 \times 10^{-6}$ torr	33	$9.9 \times 10^{-10}$	$2 \times 10^{-4}$
8. Wait 20 min, pressure up to $6 \times 10^{-6}$ torr	34.5	$1.0 \times 10^{-9}$	$3.2 \times 10^{-4}$
9. Close valve to O <sub>2</sub> source; increase pump speed; wait 10 min, pressure down to $5 \times 10^{-8}$ torr	37	$1.2 \times 10^{-9}$	—
10. Pump for 80 min, pressure down to $1.5 \times 10^{-8}$ torr	35	$1.1 \times 10^{-9}$	—
11. Pump for 16 hours, pressure down to $2 \times 10^{-9}$ torr	35	$1.1 \times 10^{-9}$	—
12. Flash repeatedly, pressure falls to $1.3 \times 10^{-9}$ torr; wait 10 min	25	$3 \times 10^{-10}$	$1.3 \times 10^{-8}$
13. Admit O <sub>2</sub> to closed system at $\sim 2 \times 10^{-8}$ torr; wait 30 min, pressure falls to $5 \times 10^{-8}$ torr	28	$6 \times 10^{-10}$	$\sim 3 \times 10^{-4}$
14. Wait two hours, pressure down to $1.8 \times 10^{-6}$ torr	33	$9 \times 10^{-10}$	$\sim 10^{-3}$
15. Wait 30 min, pressure down to $1.6 \times 10^{-6}$ torr	35	$1.1 \times 10^{-9}$	$\sim 10^{-3}$
16. Admit O <sub>2</sub> to pressure $9 \times 10^{-6}$ torr; wait 10 min	39	$1.3 \times 10^{-9}$	$\sim 10^{-3}$
17. Admit O <sub>2</sub> to pressure $3 \times 10^{-5}$ torr; wait 5 min	46	$1.8 \times 10^{-9}$	$\sim 10^{-3}$
18. Wait 30 min, pressure $4 \times 10^{-5}$ torr	61	$2.8 \times 10^{-9}$	$\sim 2 \times 10^{-3}$
19. Wait 40 min, pressure $5 \times 10^{-5}$ torr	55.5	$2.5 \times 10^{-9}$	$\sim 3 \times 10^{-3}$
20. Wait one hour, pressure $5 \times 10^{-5}$ torr	74.5	$3.8 \times 10^{-9}$	$\sim 10^{-2}$
21. Increase pressure to $3 \times 10^{-4}$ torr, wait 15 min	127	$7.5 \times 10^{-9}$	$\sim 10^{-2}$

TABLE IV — *Continued*

Treatment	Contact Resistance (Milliohms) Average of Five Closures Force = 1 gm	$\sigma_t$ (ohm-cm <sup>2</sup> )	Total Exposure of Electrodes to Gas Since Previous Flash (torr-min)
22. Close O <sub>2</sub> leak; increase pumping speed; wait 7 min, pressure down to $2.5 \times 10^{-6}$ torr	132	$7.7 \times 10^{-9}$	—
23. Wait 25 min, pressure $1.2 \times 10^{-6}$	110	$6.3 \times 10^{-9}$	—
24. Pump for 16 hours, pressure $1.1 \times 10^{-7}$ torr	111	$6.4 \times 10^{-9}$	—
25. Admit O <sub>2</sub> to pressure 1.4 torr; wait 20 min	219	$1.4 \times 10^{-8}$	~30
26. Wait one hour	240	$1.5 \times 10^{-8}$	100
27. Increase pressure to 2.1 torr; wait 30 min	215	$1.4 \times 10^{-8}$	175
28. Wait 2 hours	335	$2.2 \times 10^{-8}$	400
29. Open valve to pumps; wait one hour, pressure $5 \times 10^{-7}$ torr	193	$1.2 \times 10^{-8}$	—
30. Pump for 1½ hours, pressure $2.5 \times 10^{-7}$ torr	175	$1.1 \times 10^{-8}$	—
31. Pump for 16 hours, pressure $7 \times 10^{-8}$ torr	184	$1.1 \times 10^{-8}$	—
32. Admit 5.5 torr of O <sub>2</sub> ; wait 2 hours	354	$2.3 \times 10^{-8}$	~1,000
33. Wait 30 min	410 (2 unusually large readings not included in average ~1400)	$2.7 \times 10^{-8}$ (~ $1.0 \times 10^{-7}$ )	~1,000
34. Open valve to pump; wait 2 hours, pressure down to $1 \times 10^{-7}$ torr	319	$2.0 \times 10^{-8}$	—

giving rise to the measured resistance pumps off at room temperature even after the nitrogen pressure has been as high as 3 torr.

## APPENDIX B

We attribute entries in Table IV numbered 3 through 6 for exposures from  $4 \times 10^{-7}$  to  $3 \times 10^{-6}$  torr-min to the first step of fast adsorption, with  $\sigma_t \approx 5 \times 10^{-10}$  ohm-cm<sup>2</sup>. Entries 7 through 11, 14 and 15, for exposures from  $2 \times 10^{-4}$  to about  $10^{-3}$  torr-min, are attributed to the completion of the second step, with  $\sigma_t \approx 1.0 \times 10^{-9}$  ohm-cm<sup>2</sup>. For pressures of oxygen above  $\sim 10^{-5}$  mm of mercury, the resistance continues to increase at an observable rate (entries 16 through 33).

Entries 28 through 31, 33 and 34 show that, after exposure to a few torr, a considerable decrease in resistance occurs on pumping out the gas.

## APPENDIX C

*Adsorption and Desorption at Low Temperatures*

TABLE V — OXYGEN ON TUNGSTEN

Treatment	Contact Resistance (Milliohms)
1. Expose to $10^{-6}$ torr of $O_2$ at room temperature for a few minutes; measure resistance with force = 1 gm.....	50
2. Close contacts with force = 2 gm.....	37
3. Apply liquid $N_2$ and wait 30 min with contacts remaining closed.....	17
4. Increase $O_2$ pressure to $10^{-6}$ torr; allow contacts to stand open 15 min; measure resistance with force = 1 gm.....	140
5. Wait 2 hours.....	160
6. Open valve to pumps, wait 1 hour until pressure is $10^{-7}$ torr; measure resistance with force = 1 gm.....	160
7. Remove liquid $N_2$ ; allow system to warm 10 minutes, pressure = $2 \times 10^{-7}$ torr (force = 1 gm).....	120
8. Pump 16 hours at room temperature, pressure = $10^{-8}$ torr (force = 1 gm).....	90

TABLE VI — NITROGEN ON MOLYBDENUM

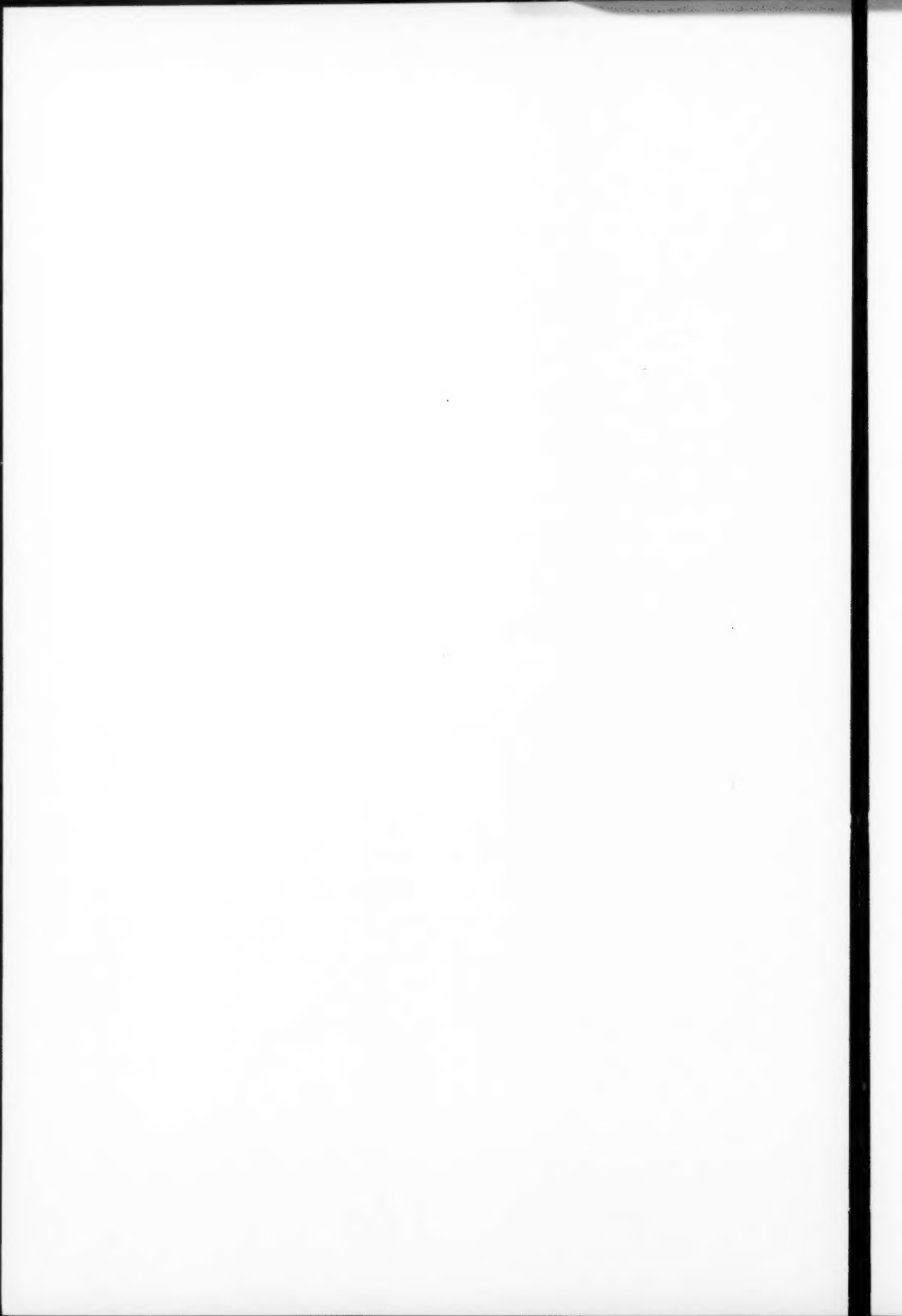
Treatment	Contact Resistance (Milliohms) Force = 1 gm
1. Flash contacts in liquid $N_2$ bath; allow 30 min to cool, pressure = $7 \times 10^{-11}$ torr.....	6
2. Admit $N_2$ , pressure = $5 \times 10^{-6}$ torr; wait 10 min.....	22
3. Open valve to pumps; wait 1 hour, pressure = $1 \times 10^{-9}$ torr.....	23
4. Admit nitrogen, pressure 6.0 torr; wait 10 min.....	41
5. Open valve to pumps; wait 10 min, pressure = $10^{-6}$ torr.....	41

TABLE VII — NITROGEN ON TUNGSTEN

Treatment	Contact Resistance (Milliohms) Force = 1 gm
1. Flash in liquid $N_2$ bath; wait 30 min, pressure $2 \times 10^{-10}$ torr.....	8
2. Admit 1.0 torr of $N_2$ ; wait 40 min.....	85
3. Open valve to pumps; wait 5 min, pressure down to $3 \times 10^{-6}$ torr.....	124
4. Wait 1 hour, pressure $3 \times 10^{-7}$ torr.....	150
5. Remove liquid $N_2$ ; wait 15 min to allow system to come to room temperature, pressure = $10^{-8}$ torr.....	60

## REFERENCES

1. Holm, R. and Meissner, Z. Physik, **74**, 1932, p. 715.
2. Holm, R., *Electrical Contacts*, H. Gebers, Stockholm, 1946. (Modernized version: *Electrical Contacts Handbook*, Springer, Berlin, 1958).
3. Twigg, G. H., Trans. Faraday Soc., **42**, 1946, p. 657.
4. Kappler, Ruchardt and Schlater, Z. Ang. Phys., **8**, 1950, p. 313.
5. Little, C. W. and Kouvenhoven, W. B., Trans. AIEE, Part 2, **72**, 1953, p. 314.
6. Savage, R. H., and Flom, D. G., Ann. N. Y. Acad. Sci., **58**, No. 6, 1954, p. 949.
7. Cocks, M., Proc. Phys. Soc. (London), **B67**, 1955, p. 238.
8. Wilson, R. W., Proc. Phys. Soc. (London), **B68**, 1956, p. 625.
9. Millian, K. and Rieder, W., Z. Ang. Phys., **8**, 1956, p. 28.
10. Ittner, W. B. and Magill, P. J., I.B.M. J. of Res. and Dev., **1**, 1957, p. 44.
11. Went, J. J., Physica, **8**, 1941, p. 233; see also Philips Tech. J., **4**, 1939, p. 332 and **5**, 1940, p. 238.
12. Frenkel, J., Phys. Rev., **36**, 1931, p. 1604.
13. Sommerfeld, A. and Bethe, H., *Handbuch der Physik*, Vol. 24, Part 2, Springer, Berlin, 1937, p. 450.
14. Holm, R. and Kirschstein, B., Physik. Z., **36**, 1935, p. 882.
15. Alpert, D., J. Appl. Phys., **24**, 1953, p. 860; Bayard, R. T. and Alpert, D., Rev. Sci. Instr., **21**, 1950, p. 571.
16. *Handbook of Chemistry and Physics*, 37th Ed., Chemical Publishing Co., Cleveland, 1955-6.
17. Kannuliuk, W. G., Proc. Roy. Soc. (London), **A141**, 1933, p. 159.
18. Kaye, G. W. C. and Laby, T. H., *Physical and Chemical Constants*, Longmans Green, New York, 1956, p. 90.
19. *Metals Handbook*, American Society for Metals, Cleveland, 1948, p. 95.
20. Becker, J. A., *Advances in Catalysis*, Vol. VII, Academic Press, New York, 1955, and private communication.
21. Eisinger, J. T., J. Chem. Phys., **28**, 1958, p. 165.
22. Ehrlich, G., J. Phys. Chem., **60**, 1956, p. 1388.
23. Taylor, H. A. and Thon, N., J. Am. Chem. Soc., **74**, 1952, p. 4169, and **75**, 1953, p. 2747.
24. Jones, H. A. and Langmuir, I., Gen. Elec. Rev., **30**, 1927, p. 310.
25. Gomer, R., *Advances in Catalysis*, Vol. VII, Academic Press, New York, 1955.
26. Morrison, J. L. and Roberts, J. W., Proc. Roy. Soc. (London), **A173**, 1939, pp. 1, 13.
27. Miller, A. R., *The Adsorption of Gases on Solids*, Cambridge Univ. Press, Cambridge, 1949.
28. Becker, J. A. and Hartman, J. Phys. Chem., **57**, 1953, p. 157, Fig. 9.
29. de Boer, J. H. and Kraak, H. H., Rec. Trav. Chem. Pays-Bas, **56**, 1937, p. 1103.
30. Gomer, R. and Hulm, J. K., J. Am. Chem. Soc., **75**, 1953, p. 4114.
31. Mignolet, J. C. P., Rec. Trav. Chem. Pays-Bas, **74**, 1955, p. 685.
32. Herring, C., *Metal Interfaces*, American Society for Metals, Cleveland, 1952, pp. 1-20.
33. de Boer, J. H., *The Dynamical Character of Adsorption*, Oxford Press, Oxford, 1953.
34. Morrison, J. L. and Grummit, W. E., J. Chem. Phys., **21**, 1953, p. 654.



# Shot Noise in p-n Junction Frequency Converters\*

By A. UHLIR, JR.

(Manuscript received January 22, 1958)

*General equations are derived for the noise figure of a frequency converter using a p-n junction diode with arbitrary minority-carrier storage. A p-n junction with a purely capacitive nonlinear admittance permits, theoretically, noiseless amplification. Structures are suggested for approximating this ideal. A diffused silicon junction diode gave 9 db of gain with a 2-db noise figure in converting 460 to 9375 mc and gave a 3-db noise figure as a 6000-mc negative-resistance amplifier. Nonlinear-resistance diodes cannot amplify but can give low-noise frequency conversion if the local-oscillator drive produces a sharply pulsed current waveform in the diode.*

## I. INTRODUCTION

The shot noise output of any p-n junction device in any circuit can be calculated by enumerating the possible hole and electron motions and summing the noise energies delivered to the load. This method of analysis will be illustrated by applying it to the de-biased p-n junction (Section IX). A more complicated example, and the principle topic of this paper, is the general p-n junction frequency converter (Section XI).

The technological significance of two kinds of semiconductor diodes used as frequency converters will be discussed briefly. Section II will explain how this theory of shot noise stimulated the recent development of low-noise microwave amplifiers using the nonlinear capacitance of p-n junctions. Section III mentions the nonlinear resistor, for which shot noise appears to be a vital problem.

The "particle-method" formulation of p-n junction theory in terms of the statistics of individual carrier motions (Section VI) is an alternative to the diffusion equations ordinarily used in the analysis of p-n junctions. Either approach leads directly to the impedance of the junction

\* Supported in part by the U. S. Army Signal Corps under contract DA 36-039 sc-5589. Preliminary reports of this work were given at the Microwave Crystal Rectifier Symposium, Fort Monmouth, N. J., February 1956, and the I.R.E.-A.I.E.E. Semiconductor Device Research Conference, Boulder, Colo., July, 1957.

(Sections VII and VIII) and to the small-signal transmission properties of frequency converters (Section X). However, the particle method is the most direct way to calculate shot noise.

After the general equations for noise figure are derived in Section XI, the consequences for nonlinear capacitors and nonlinear resistors are discussed in Sections XII and XIII. One of the virtues of the analysis is the possibility of relating impedances and noise without regard to the structure of the p-n junction. However, a few examples of nonlinear-capacitor structures are given in Section XII.

As explained in Sections IV and V, the particle method and the diffusion equation method deal with just one aspect of p-n junction phenomena: minority-carrier effects, which have varying importance, depending upon the device and its use. Minority carrier effects are nowhere more important than in p-n junction transistors. Thus, the particle method is an excellent way to calculate the shot noise in transistors, although such a calculation will not be given in this article.\*

## II. NONLINEAR-CAPACITANCE AMPLIFIERS

A time-varying capacitor is an active device that can be used as a linear amplifier of small signals, usually, but not necessarily, with a shift in signal frequency. The power required for the amplification is supplied by the motor, of whatever kind, that varies the capacitance. This principle is used in vibrating-reed electrometers for amplifying very low frequencies.<sup>1,2</sup>

To obtain microwave amplification, one needs a capacitance that varies at microwave or higher frequencies. Such a time-varying capacitance can be obtained by applying a microwave voltage to the voltage-dependent capacitance of a p-n junction diode. Remarkably general gain and power relations can be derived for circuits of this type.<sup>3</sup>

Amplifying diode-frequency converters are not new. During World War II, welded-contact germanium diodes were found to give conversion gain when used in superheterodyne receivers of the type then undergoing extensive development for radar use.<sup>4</sup> With the then-existing technology, it was found that these diodes were not as good as point-contact silicon diodes in the over-all system noise figure that could be obtained. As a result of this observation, point-contact silicon diodes took over the entire radar field until recently, and the manufacture of welded-contact diodes was discontinued.

\* For such a calculation see van der Ziel, A. and Becking, A. G. J., Theory of Junction Diode and Junction Transistor Noise, *Proc. I.R.E.* **46**, March 1958, pp. 589-594.



These results, though entirely empirical, may very well have led to a belief that amplification by diodes was a freak effect and necessarily noisy. In the years following World War II, casual experiments on diode amplification were performed in many laboratories, but low noise was not found, nor was it intensively sought. The amplification effect was put to practical use in transmitting modulators, where noise would not be important.<sup>5</sup>

At this point, the shot-noise theory of p-n junction frequency converters was developed. It provided one logically complete example of how a diode could amplify with arbitrarily low noise. It was recognized that the minority-carrier mechanism assumed in the analysis was probably not as important, at high frequencies, as the depletion-layer capacitance; at the same time, the understanding acquired from the shot-noise theory suggested that the depletion-layer capacitance would also be noiseless.

Subsequent efforts to make improved nonlinear capacitance diodes<sup>6</sup> and to give them a fair circuit evaluation have been extremely well rewarded. A diffused-junction silicon diode has given 9 db of gain with a 2-db noise figure in converting 460 mc to 9375 mc.<sup>7</sup> Also, such a diode has given 35 db of negative-resistance gain at 6000 mc with a 3-db noise figure (for double sideband input).<sup>7</sup>

In view of the large variety of possible frequency relations, to say nothing of the circuits involving combinations of diodes, it is fortunate that it can be deduced that an ideal nonlinear capacitor is noiseless in any circuit. By p-n junction techniques it is possible to make nonlinear capacitors that are practically ideal, except for a series resistance. Working theories of nonlinear capacitors will therefore be concerned with the noise from this series resistance.<sup>8</sup>

### III. NONLINEAR RESISTORS

Point-contact crystal rectifiers are in widespread practical use in microwave superheterodyne receivers. It has long been believed that the useful action of these devices results from nonlinear resistance and, as yet, there is no reason to doubt that this is true.

As far as noise is concerned, there is no difference between the mathematical results for the p-n junction type of nonlinear resistance and the results that would have been obtained from earlier ideas of metal-semiconductor contacts. But the older theory was not carried very far for the calculation of noise figure. Therefore, it seems worthwhile to point out the importance of the local-oscillator waveform.

In the past, most analyses have been made on the assumption of short-circuited harmonics. This rather arbitrary postulation of a waveform is not realizable in practice, but it does give rise to some simple relations between conversion loss and noise figure. Another case, open-circuited harmonics, will be found to have an entirely different relation between conversion loss and noise figure. Thus, the analysis of nonlinear resistors will show, by example, that no general relation between gain and noise figure is true.

In contrast to the nonlinear resistor, a nonlinear capacitor gives low noise for any local-oscillator waveform.

#### IV. p-n JUNCTION THEORY

As shown in Fig. 1, there are two important methods of analyzing p-n junctions, each complementing the other. The pseudo-equilibrium method is an accurate means of calculating the capacitance-voltage characteristic of a p-n junction if one knows, from other considerations, that it is a nonlinear capacitor. However, this method gives no information about frequency dependence and noise.

The kinetic method begins with an approximate separation of physical mechanisms, as discussed in Section V. This separation makes it relatively easy to calculate the frequency-dependent admittance and noise. The kinetic method can be applied not only to nonlinear resistors and nonlinear capacitors but also to the host of intermediate types of p-n

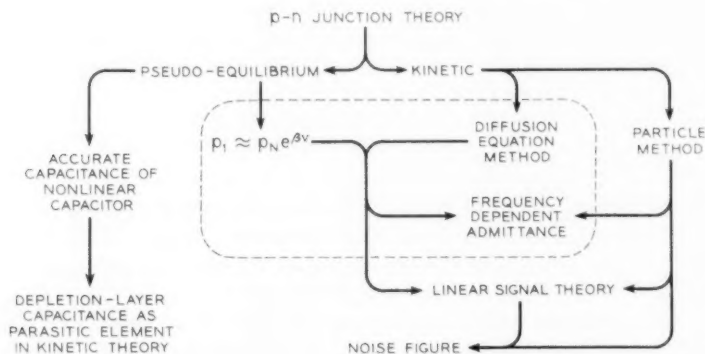


Fig. 1 — Structure of p-n junction theory involved in or related to the calculation of noise figure. The encircled elements constitute the "classical" kinetic theory of p-n junctions.

junctions (including the so-called "simple" p-n junction between homogeneous semi-infinite p and n regions).

The usual mathematical approach in the kinetic method involves solving the diffusion equation, a differential equation for the average motion of carriers. This approach, which will be referred to as "classical" p-n junction theory, is satisfactory for calculating junction admittance. In calculating noise, it seems to be much easier first to calculate the noise due to individual carrier motions and then to sum them. This second procedure will be referred to as "the particle method," since the individuality of the carriers is preserved to a later stage in the calculation.

The particle method gives relations between small-signal junction admittances and the noise figure of frequency converters. The train of reasoning to be used is indicated by the arrows in Fig. 1. However, the connecting lines in Fig. 1 may be followed in any direction. For example, the small-signal admittances may be calculated from the diffusion equation or measured experimentally and used to calculate gain and noise figure.

#### V. APPROXIMATE SEPARATION OF PHYSICAL MECHANISMS

The equivalent circuit of Fig. 2 denotes the principal physical mechanisms of p-n junction action. The p-n junction is considered to be divided into essentially neutral p and n regions and an intervening space-charge region known as the depletion layer.

The capacitance of the depletion layer may be analyzed by pseudo-equilibrium methods under the approximation that the depletion layer is free of carriers.<sup>9</sup> This capacitance varies with voltage, and amplifying frequency converters can be built that rely on it alone. It is reasonably certain that the depletion-layer capacitance will be very important in all high-frequency nonlinear-capacitance diodes. Nevertheless, we will ignore the depletion-layer capacitance entirely in the following theory of gain and shot noise, except for qualitative remarks. This theory will be developed around the motion of carriers *across* the depletion layer.

The theory of noise thus obtained will illustrate the fact that at least one conceptual type of nonlinear capacitance amplifier is noiseless. It will then perhaps be easy to believe that the depletion-layer capacitance also should not be a source of noise. The analysis should be directly applicable to practical nonlinear resistors, for these must have relatively small values of depletion-layer capacitance for satisfactory operation.

The inescapable importance of the depletion-layer capacitance is con-

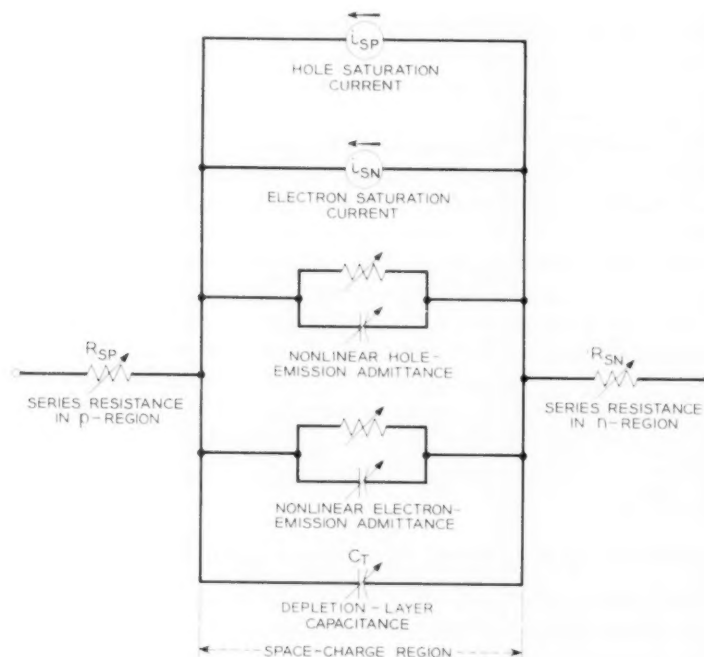


Fig. 2 — Equivalent circuit of p-n junction. In general, the nonlinear resistors and capacitors may be frequency-dependent.

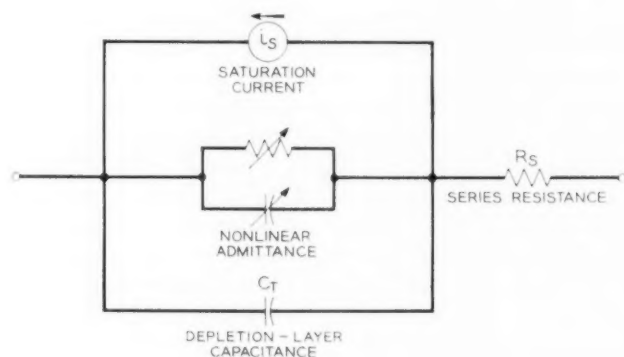


Fig. 3 — Simplified equivalent circuit in which constant parasitic elements are assumed and hole and electron admittances are combined.

nected with the fact that there is series resistance  $R_s$  between the junction and the metallic contacts, as indicated in Fig. 2. For many diodes, the series resistance is found to be reasonably constant as bias is varied, giving the equivalent circuit in Fig. 3. This observation is consistent with (but does not prove) the conjecture that the series resistance exhibits thermal noise. If this conjecture is true, the noise figure will depend upon the frequencies involved and upon the product  $R_s C_{\min}$ , where  $C_{\min}$  is the value of the depletion layer capacitance at the maximum reverse voltage. But the immediate problem is to calculate shot noise due to minority carriers (i.e., due to carriers that cross the space-charge region), and  $R_s$  and the depletion-layer capacitance will both be neglected. That is, the analysis will be carried out for the equivalent circuit of Fig. 4. It should be noted that this neglect corresponds to the usual first approximation made in analyzing junction transistors.<sup>10</sup>

#### VI. STATISTICAL DESCRIPTION OF MINORITY-CARRIER MOTION

Each minority carrier — a hole in an n region or an electron in a p region — can be thought of as an individual. A hole may begin its existence as a minority carrier by surmounting the barrier potential of the depletion layer and entering the n region, or by being spontaneously (thermally) generated in the n region. Its existence may end by recombination in the n region or by return to the p region. The situation for electrons is analogous.

One need consider only the holes and electrons that cross the barrier. The life-histories of these carriers, which are the elementary events of the theory, fall into the three classes shown in Fig. 5. Their meandering paths indicate that the motion of a carrier is governed by statistical rules. These rules depend upon the detailed structure of the junction, but it is in keeping with classical p-n junction theory to assume that they do not depend upon the bias applied to the junction.

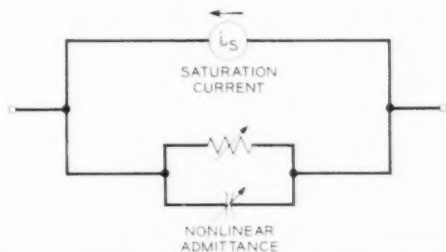


Fig. 4 — Equivalent circuit of p-n junction with negligible parasitics.

Of the three classes of elementary events, the reverse carriers will, throughout the analysis, be the simplest to deal with because they are assumed to occur entirely at random. Holes thermally generated in the neutral region of a p-n junction move about according to statistical rules, and some of them come in contact with the depletion layer. The electric field in the depletion layer is in such a direction as to move these holes across to the p region (forward bias decreases this field but ordinarily does not change its direction). Similarly, some of the electrons generated in the p region cross to the n region. These "saturation currents" are represented by current generators  $i_{sp}$  and  $i_{sn}$  in Fig. 2. They are direct-current generators and do not enter physically in the ac admittance of the junction, although their values can be introduced, by mathematical manipulation, into expressions for the ac admittance. But the saturation currents do produce shot noise. The sum of  $i_{sp}$  and  $i_{sn}$  is the saturation current, which may be determined experimentally by measuring the current at a moderate reverse voltage.

Of the many holes in the p region, a few will overcome the potential barrier of the space-charge region and be emitted into the n region. The rate of emission will be assumed to be a nonlinear function of the potential across the space-charge region. This function will be written  $\mathcal{R}(v)$ , where  $v$  is the deviation (in the forward direction) from the equilibrium potential. "Classical" p-n junction theory, to be considered in Section VIII, involves assumptions equivalent to taking

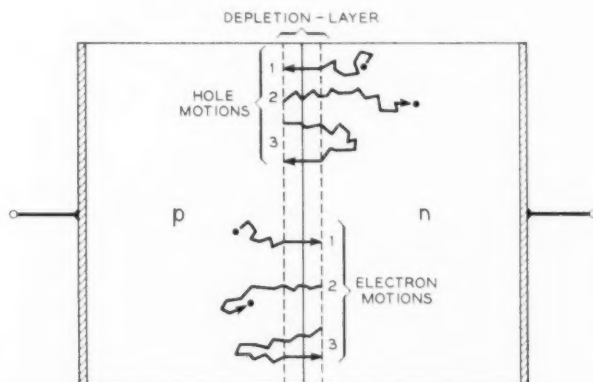


Fig. 5 — The three classes of hole and electron motions ("elementary events"): (1) reverse carrier from spontaneous generation; (2) forward carrier — emission followed by recombinations; (3) forward-and-back carrier — emission and return.

$$\mathfrak{R}(v) = \text{constant} \times e^{\beta v} \quad \beta \equiv q/kT, \quad (1)$$

where  $q$  is the electronic charge,  $k$  is Boltzman's constant, and  $T$  is absolute temperature. The constant of proportionality is not specified. The conversion and noise analyses will be carried out with an arbitrary function  $\mathfrak{R}(v)$ , to accommodate refinements in p-n junction theory that may specify an emission relation differing from (1).

The probability of an emitted carrier *not* returning will be denoted  $P_0$ . Carriers with such a fate lead to a nonlinear conductance in the equivalent circuit. The probability of an emitted carrier returning at time  $t'$  after emission will be  $P(t')$ . Forward-and-back carriers result, in general, in a nonlinear conductance and a nonlinear capacitance whose values and frequency dependence can be calculated from  $P(t')$ . Since an emitted carrier must either return or not return,

$$1 = P_0 + \int_0^\infty P(t') dt'. \quad (2)$$

It is consistent with the usual approximations of p-n junction analysis to assume that  $P_0$  is a constant and that  $P(t')$  depends only upon  $t'$ . These assumptions will permit the noise analysis to be carried out rather simply. However, the effect of high current densities upon  $P_0$  and  $P(t')$  may be an important feature of point-contact diodes.

All that has been said about the emission of holes from the p side applies to the emission of electrons from the n side. Of course,  $\mathfrak{R}(v)$ ,  $P_0$  and  $P(t')$  may be quite different for the electrons. In general, one must perform analyses for the holes and electrons and then add the currents. However, if (1) holds,  $\mathfrak{R}$  for electrons is proportional to  $\mathfrak{R}$  for holes, for all values of  $v$ . Then one can define suitable  $\mathfrak{R}$ ,  $P_0$  and  $P(t')$  to apply to holes and electrons taken together. To simplify the presentation, it will be assumed that this has been done.

In assuming a certain probability for recombination of an emitted carrier, we are, in effect, assuming linear recombination. The assumption that the probability of return depends only on the time after emission is equivalent to the assumption of a linear diffusion equation including, possibly, drift in a steady electric field. These are, of course, usual assumptions which are made in analyzing p-n junction devices. It is not necessarily assumed that the recombination occurs uniformly throughout the volume. Surface recombination or recombination at localized centers is consistent with the assumptions as long as the recombination is linear. Also, we are not restricted to simple diffusion; drift in a steady electric field is permitted.

The currents for the three types of carrier events are illustrated in



Fig. 6. The reverse carrier gives a single negative pulse with an area equal to one electronic charge; the forward carrier gives a positive pulse with an area of one electronic charge. The detailed shape of the pulses might differ from one to the next and, furthermore, the average shape of the forward pulses might be somewhat different from the average shape of the reverse pulses. However, it will be assumed in most of the analysis that the entire pulse is of such short duration that the exact shape is of no consequence at the frequencies of interest. The third type of event — forward emission followed by the return of the same carrier — leads to a current whose integral is zero net charge. The forward pulse part of this single event should be similar to the forward pulse of a carrier that is emitted and does not return. Likewise, the reverse pulse part should be similar to the reverse pulses of the thermally generated carriers. However, the fact that the two pulses correspond to a single event is statistically important.

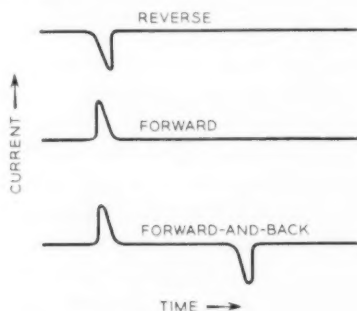


Fig. 6 — Current pulses for the three types of minority carrier events.

#### VII. SMALL-SIGNAL ADMITTANCE

The small-signal admittance of the p-n junction will be calculated from  $\alpha$ ,  $P_0$  and  $P(t')$ . The calculation introduces some relationships needed in the main analysis. To avoid the introduction of a large number of symbols, a time function and its Fourier coefficients or spectrum will be denoted by the same symbol, for example,  $i(t)$  and  $i(\omega)$ ;  $P(\omega)$  is an exception with a special definition to be given in (10).

In general, the current is equal to the difference between the current of forward carriers and the current of reverse carriers. For instantaneous forward and reverse transits, this means

$$i(t) = -i_s + q\alpha[v(t)] - q \int_0^\infty dt' \alpha[v(t-t')]P(t'). \quad (3)$$

The spectrum of  $i$  may be found from

$$i(\omega) = \frac{1}{2\pi} \int_{-\infty}^{\infty} i(t) e^{-j\omega t} dt. \quad (4)$$

This normalization of the spectrum will be adhered to in the calculation of noise. The small-signal admittance (also, the conversion matrix discussed in Section X) is a ratio of current to voltage, so any consistent normalization may be used. Consider, then a voltage of the form

$$v(t) = v_0 + \text{Re } v(\omega) e^{j\omega t}, \quad (5)$$

where  $v(\omega)$  is the complex amplitude of a vanishingly small ac voltage of angular frequency  $\omega$ . The expected solution is

$$i(t) = i_0 + \text{Re } i(\omega) e^{j\omega t}, \quad (6)$$

$$i(\omega) = Y(\omega) v(\omega). \quad (7)$$

The problem is to find  $Y(\omega)$  and  $i_0$ .

Because  $v(\omega)$  is vanishingly small,

$$\Re[v(t)] = \Re(v_0) + \Re'(v_0) \text{Re } v(\omega) e^{j\omega t}. \quad (8)$$

Inserting this expression in (3), and performing the integration indicated in (4), one finds that

$$Y(\omega) = q\Re'(v_0)P(\omega), \quad (9)$$

where

$$P(\omega) = 1 - \int_0^{\infty} e^{-j\omega t'} P(t') dt'. \quad (10)$$

Also,

$$i_0 = -i_s + q\Re(v_0)P_0 \quad (11)$$

after (2) is used.

### VIII. CLASSICAL p-n JUNCTION ANALYSIS

The analysis given thus far will be developed later into ways of relating conversion gain and noise to the small-signal admittances of a junction. Classical p-n junction analysis provides a way of predicting the small-signal admittances of postulated structures, although it does not give unique values for  $\Re(v)$ ,  $P_0$  and  $P(t')$ . Instead, it gives the products  $\Re(v)P_0$  and  $\Re(v)P(t')$ , which suffice for the desired calculations.

The basic assumption of the classical theory is that the hole concentration  $p_1$  on the n-side of the depletion layer is given by<sup>9</sup>

$$p_1 = p_N e^{\beta v} \quad (12)$$

where  $p_N$  is the equilibrium value of  $p_1$ . Equation (12) is a boundary condition for the diffusive flow of holes in the neutral n-region. The

generalized diffusion equation (including recombination and drift) is

$$\frac{\partial p}{\partial t} = -\frac{p - p_N}{\tau} + D\nabla^2 p - \mu\nabla \cdot (p\mathbf{E}). \quad (13)$$

The hole concentration  $p$  is a function of time and of position within the neutral  $n$  region;  $D$ ,  $\mu$  and  $\tau$  are diffusion constant, mobility and life-time for holes in the  $n$  region. The equilibrium hole concentration  $p_N$  will vary with position in the  $n$  region if the donor concentration is not uniform. For the formal analysis,  $\tau$  and the electric field  $\mathbf{E}$  will be assumed to be independent of  $p$  and  $t$ , so that (13) is a linear partial differential equation.

The hole current density can be calculated from

$$\mathbf{J} = -qD\nabla p + q\mu p\mathbf{E}. \quad (14)$$

If the voltage,  $v$ , is composed of a number of sinusoidal components' the hole concentration will be composed of sinusoidal components. Because (12) is nonlinear, the set of frequencies involved in  $p_1$  will not, in general, be the same as the set of frequencies in  $v$ . Even so, the relation between  $p_1$  and  $J$  is linear and may conveniently be expressed in the form

$$i(\omega) = \frac{AqD p_1(\omega)}{L_\omega}, \quad (15)$$

where  $A$  is the junction area and  $L_\omega$  is the "effective ac diffusion length" for the structure in question. In other words,  $L_\omega$  is simply a quantity that makes (6) and (15) give the right answer for  $i(t)$ . This right answer is the current obtained by solving (13), applying (14) and integrating over the junction area; this procedure will be used in Section XII in the calculation of  $L_\omega$  for a particular nonlinear-capacitor structure.

The small-signal hole admittance can be found by considering in (12) a voltage of the form given in (5). Then

$$Y(\omega) = \frac{\beta A q D p_N e^{\beta v_0}}{L_\omega}. \quad (16)$$

The electron admittance is calculated similarly, usually with a quite different value of  $L_\omega$ .

A comparison with the statistical description can now be made using (9) and (16). One finds

$$\Re'(v_0)P(\omega) = \frac{\beta A D p_N e^{\beta v_0}}{L_\omega}, \quad (17)$$

or

$$\Re(v_0)P(\omega) = \frac{ADp_N e^{\beta v_0}}{L_\omega}, \quad (18)$$

since  $\Re'$  equals  $\beta\Re$ , from (1), which is the form of  $\Re$  that must be assumed to effect a comparison of the particle theory with the classical theory. Also, if (1) is assumed, (9) can be written

$$Y(\omega) = q\beta\Re(v_0)P(\omega). \quad (19)$$

In the analysis of conversion and noise, it will be found that all important quantities can be expressed in products of  $\Re P(\omega)$  or  $\Re' P(\omega)$ . Classical p-n junction theory therefore gives a *complete* solution of the problem. Separately defined values of  $\Re$  and  $P(\omega)$  are not needed because a carrier that goes across and then comes back in an infinitesimal time might just as well not have been emitted in the first place.

The noise analysis will be carried through for an arbitrary emission function,  $\Re(v)$ , in case the classical theory is not a satisfactory one for some situations.

#### IX. SHOT NOISE FOR dc BIAS

The application of the above principles to the calculation of shot noise in dc-biased p-n junctions has been published.<sup>11</sup> For this simple case, many of the steps in the calculation combined so obviously that explicit mention of each step was not necessary. Here, a step-by-step derivation of the dc results will be given as a model for more complicated cases.

The calculation of shot noise will be based on the following general principle: Each elementary event delivers a certain amount of noise energy to the load. The noise power is the rate at which noise energy is delivered to the load.

At a given terminal pair of a linear circuit, the noise can be represented by a mean-square current generator  $\langle i^2 \rangle$ , since the noise power delivered to a load connected to the terminals can readily be calculated from such a generator, the load admittance and the output admittance of the terminals. Representation by a current generator seems particularly appropriate for shot noise, where the elementary events are represented by current generators.

In p-n junctions, the elementary events are the three classes of minority-carrier histories: reverse, forward and forward-and-back. Associated with each carrier event is a small-signal current generator  $g(t)$ , as illustrated in Fig. 6, with Fourier transform  $g(\omega)$ .

Suppose that  $g(\omega)$  is observed for an infinitesimally small frequency band  $B$ . Then the transform back to the time domain of this selected

element of the spectrum is a current generator

$$\hat{g}(t) = \int_B d\omega g(\omega) e^{j\omega t} + \text{complex conjugate}, \quad (20)$$

where the indicated integration is over the values of  $\omega$  that lie within the selected band.

If one writes

$$\hat{g}(t) = A + A^*, \quad (21)$$

then  $\hat{g}^2(t)$ , which is proportional to the instantaneous input power, is

$$\hat{g}^2(t) = 2AA^* + A^2 + (A^*)^2. \quad (22)$$

Integration over total time (to obtain a quantity proportional to the energy) can be shown to drop out the latter terms, so that

$$\int \hat{g}^2(t) dt = 2 \int AA^* dt. \quad (23)$$

Now,  $AA^*$  can be written as the double integral

$$AA^* = \int_B d\omega \int_B d\omega' g(\omega) g^*(\omega') e^{j(\omega - \omega')t}. \quad (24)$$

Integrating with respect to time gives

$$\begin{aligned} \int AA^* dt &= \int_B d\omega \int_B d\omega' g(\omega) g^*(\omega') [2\pi\delta(\omega - \omega')] \\ &= 2\pi \int_B d\omega |g(\omega)|^2, \end{aligned} \quad (25)$$

so that

$$\int \hat{g}^2(t) dt = 8\pi^2 B |g(\omega)|^2. \quad (26)$$

If the carrier transits are instantaneous, a forward or reverse transit at time  $t_0$  gives a current generator

$$g(t) = \pm q\delta(t - t_0), \quad (27)$$

where the impulse function  $\delta(t)$  has negligible width in time, but its integral over time is unity.

The spectrum of (27) is

$$g(\omega) = \frac{1}{2\pi} \int_{-\infty}^{\infty} \pm q\delta(t - t_0) e^{-j\omega t} dt = \pm \frac{q}{2\pi} e^{-j\omega t_0}. \quad (28)$$

For either a forward or a reverse transit, (26) becomes

$$\int \hat{g}^2(t) dt = 2q^2 B. \quad (29)$$

The development thus far could be used only to treat the nonlinear-resistor type of p-n junction. For the general p-n junction, forward-and-back events must be considered. A forward pulse at  $t_0$ , followed by a reverse pulse at  $t_0 + t'$ , gives a current generator

$$g(t) = q\delta(t - t_0) - q\delta(t - t_0 - t'), \quad (30)$$

$$g(\omega) = \frac{q}{2\pi} [e^{-j\omega t_0} - e^{-j\omega(t_0 + t')}] \quad (31)$$

For this case, (26) gives

$$\int \hat{g}^2(t) dt = 2q^2 B(2 - 2 \cos \omega t'). \quad (32)$$

The shot noise for each class of carrier event is found by multiplying the appropriate integral in (32) by the rate of occurrence of such carrier events. Thus,

$$\langle i^2 \rangle_{\text{reverse}} = 2q^2 B \frac{i_s}{q} = 2qBi_s, \quad (33)$$

$$\langle i^2 \rangle_{\text{forward}} = 2q^2 B \Re(v_0) P_0, \quad (34)$$

$$\begin{aligned} \langle i^2 \rangle_{\text{forward-and-back}} &= 2q^2 B \Re(v_0) \int_0^\infty (2 - 2 \cos \omega t') P(t') dt' \\ &= 2q^2 B \Re(v_0) [P(\omega) + P(\omega)^* - 2P_0]. \end{aligned} \quad (35)$$

The total shot noise is the sum of (33), (34) and (36):

$$\langle i^2 \rangle_{\text{total}} = 2qB \{ i_s + q \Re(v_0) [P(\omega) + P(\omega)^* - P_0] \}. \quad (36)$$

For the important special case of classical p-n junction theory, (36) can be transformed through use of (11) and (19) into

$$\langle i^2 \rangle_{\text{total}} = 4kTBG(\omega) - 2qi_0B, \quad (37)$$

where  $G(\omega)$  is the real part of  $Y(\omega)$ . This result is easy to remember because it has the form "thermal noise minus shot noise". However, it is evident from the derivation that no subtraction of one noise from another is actually involved.

A previous derivation of (37) was given under less general assumptions,<sup>12</sup> and the equation was compared with experimental results for

element of the spectrum is a current generator

$$\hat{g}(t) = \int_B d\omega g(\omega) e^{j\omega t} + \text{complex conjugate}, \quad (20)$$

where the indicated integration is over the values of  $\omega$  that lie within the selected band.

If one writes

$$\hat{g}(t) = A + A^*, \quad (21)$$

then  $\hat{g}^2(t)$ , which is proportional to the instantaneous input power, is

$$\hat{g}^2(t) = 2AA^* + A^2 + (A^*)^2. \quad (22)$$

Integration over total time (to obtain a quantity proportional to the energy) can be shown to drop out the latter terms, so that

$$\int \hat{g}^2(t) dt = 2 \int AA^* dt. \quad (23)$$

Now,  $AA^*$  can be written as the double integral

$$AA^* = \int_B d\omega \int_B d\omega' g(\omega) g^*(\omega') e^{j(\omega - \omega')t}. \quad (24)$$

Integrating with respect to time gives

$$\begin{aligned} \int AA^* dt &= \int_B d\omega \int_B d\omega' g(\omega) g^*(\omega') [2\pi \delta(\omega - \omega')] \\ &= 2\pi \int_B d\omega |g(\omega)|^2, \end{aligned} \quad (25)$$

so that

$$\int \hat{g}^2(t) dt = 8\pi^2 B |g(\omega)|^2. \quad (26)$$

If the carrier transits are instantaneous, a forward or reverse transit at time  $t_0$  gives a current generator

$$g(t) = \pm q\delta(t - t_0), \quad (27)$$

where the impulse function  $\delta(t)$  has negligible width in time, but its integral over time is unity.

The spectrum of (27) is

$$g(\omega) = \frac{1}{2\pi} \int_{-\infty}^{\infty} \pm q\delta(t - t_0) e^{-j\omega t} dt = \pm \frac{q}{2\pi} e^{-j\omega t_0}. \quad (28)$$



For either a forward or a reverse transit, (26) becomes

$$\int \dot{g}^2(t) dt = 2q^2 B. \quad (29)$$

The development thus far could be used only to treat the nonlinear-resistor type of p-n junction. For the general p-n junction, forward-and-back events must be considered. A forward pulse at  $t_0$ , followed by a reverse pulse at  $t_0 + t'$ , gives a current generator

$$g(t) = q\delta(t - t_0) - q\delta(t - t_0 - t'), \quad (30)$$

$$g(\omega) = \frac{q}{2\pi} [e^{-j\omega t_0} - e^{-j\omega(t_0+t')}] \quad (31)$$

For this case, (26) gives

$$\int \dot{g}^2(t) dt = 2q^2 B(2 - 2 \cos \omega t'). \quad (32)$$

The shot noise for each class of carrier event is found by multiplying the appropriate integral in (32) by the rate of occurrence of such carrier events. Thus,

$$\langle \dot{i}^2 \rangle_{\text{reverse}} = 2q^2 B \frac{i_s}{q} = 2qBi_s, \quad (33)$$

$$\langle \dot{i}^2 \rangle_{\text{forward}} = 2q^2 B \Re(v_0) P_0, \quad (34)$$

$$\begin{aligned} \langle \dot{i}^2 \rangle_{\text{forward-and-back}} &= 2q^2 B \Re(v_0) \int_0^\infty (2 - 2 \cos \omega t') P(t') dt' \\ &= 2q^2 B \Re(v_0) [P(\omega) + P(\omega)^* - 2P_0]. \end{aligned} \quad (35)$$

The total shot noise is the sum of (33), (34) and (36):

$$\langle \dot{i}^2 \rangle_{\text{total}} = 2qB \{ i_s + q \Re(v_0) [P(\omega) + P(\omega)^* - P_0] \}. \quad (36)$$

For the important special case of classical p-n junction theory, (36) can be transformed through use of (11) and (19) into

$$\langle \dot{i}^2 \rangle_{\text{total}} = 4kTBG(\omega) - 2qi_0B, \quad (37)$$

where  $G(\omega)$  is the real part of  $Y(\omega)$ . This result is easy to remember because it has the form "thermal noise minus shot noise". However, it is evident from the derivation that no subtraction of one noise from another is actually involved.

A previous derivation of (37) was given under less general assumptions,<sup>12</sup> and the equation was compared with experimental results for

p-n junctions.<sup>13,14</sup> The good agreement with experiment suggests that it is worthwhile to analyze the noise of a p-n junction frequency converter.

#### X. SIGNAL TRANSMISSION IN LINEAR FREQUENCY CONVERTERS

In a linear frequency converter, the output signal voltage and current are linearly related to the input signal voltage and current.

Of course, frequency conversion by a nonlinear device requires a finite local-oscillator voltage. The local-oscillator interaction with the device is quite nonlinear. Since the local-oscillator drive is regarded as a power supply, not an intelligence-bearing signal, a linear frequency converter can be made with a nonlinear device. Linear behavior is obtained when the signal voltages are assumed to be arbitrarily small.

The analysis of signal transmission in the linear frequency converter will be made on the assumption that the local-oscillator waveform is periodic, with a fundamental frequency  $b/2\pi$ . This assumption is not trivial, for nonlinear capacitors can be tuned to oscillate at frequencies incommensurate with the driving-oscillator frequency, as well as at subharmonics of this frequency. The formal results could be generalized to cover the nonperiodic case, but most practical situations involve periodic waveforms.

The frequency components of the emission rate  $\mathcal{R}(v)$  must be related to the frequency components of the voltage,  $v(t)$ , applied to the junction. The voltage will be given in the form

$$v(t) = v_{LO}(t) + v_{SIG}(t), \quad (38)$$

where  $v_{LO}(t)$  is the large, periodic local-oscillator voltage (plus any dc voltage) and  $v_{SIG}(t)$ , which will be regarded as arbitrarily small, is the sum of all the signal voltages. Here the word "signal" includes the input and output signals and the image-frequency signals, all of which are linearly related. The method of calculating these linear relationships will next be given. The local-oscillator voltage, whatever its waveform, may be written

$$v_{LO}(t) = \sum_m v_{LO}(m) e^{jmbt}, \quad (39)$$

where  $m$  takes on all positive and negative integer values including zero.

Most frequency-conversion problems can be treated by proper identification of  $s$  in the following representation for  $v_{SIG}$ :

$$v_{SIG}(t) = \text{Re} \sum_m v(mb + s) e^{j(mb+s)t}. \quad (40)$$

For example,  $s/2\pi$  could be the intermediate frequency (output) of a superheterodyne receiver (Figs. 7 and 8), or the input frequency of a transmitting modulator (Fig. 9). All of these circuits and many others can be obtained by suitable connections to the multiterminal "black box" indicated in Fig. 10. Negative frequencies are included in the set  $(mb + s)/2\pi$ ; they are the "lower sidebands". For the sake of obtaining noise-figure expressions, it will be assumed that the input and output are at two distinct frequencies  $(m_1b + s)/2\pi$  and  $(m_2b + s)/2\pi$ , as indicated in Fig. 11. In case the input and output are at the same frequency, as in a negative-resistance amplifier, the noise-figure expressions will not be applicable, but (65) will give the shot-noise current at the frequency of interest.

Any information-bearing signal will contain a number of frequencies (in general, a continuous spectrum). The linear nature of the small-signal problem enables one to analyze for each frequency separately.

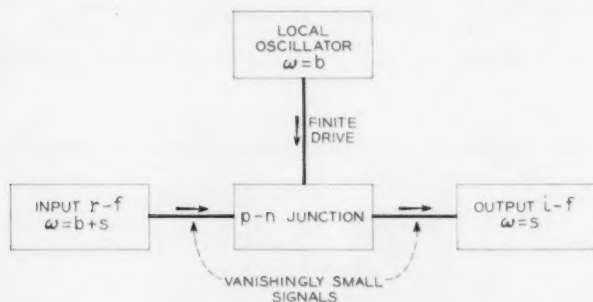


Fig. 7 — Upper-sideband superheterodyne receiver (down-converter).

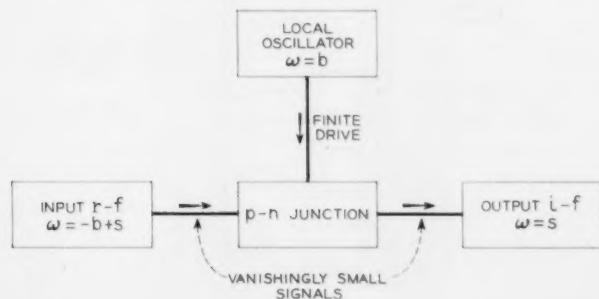


Fig. 8 — Lower-sideband superheterodyne receiver (down-converter).

Since  $v_{SIG}$  is arbitrarily small, one can write

$$\mathcal{R}[v(t)] = \mathcal{R}[v_{LO}(t)] + \mathcal{R}'[v_{LO}(t)]v_{SIG}. \quad (41)$$

The dc and large-signal dc components of  $\mathcal{R}$  are given by the Fourier expansion of  $\mathcal{R}[v_{LO}(t)]$ . The Fourier expansion of  $\mathcal{R}'[v_{LO}(t)]$  is required for the signal transmission, that is, for calculating the conversion matrix. Both expansions are necessary to calculate the noise figure.

Assume that the required Fourier coefficients have been calculated,

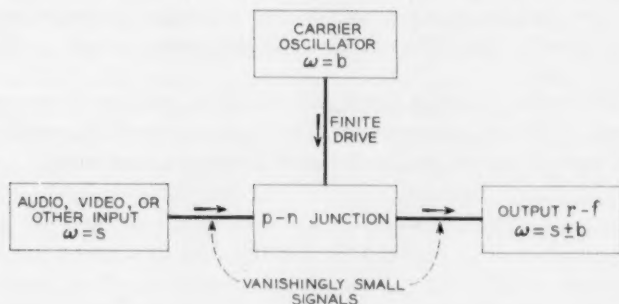


Fig. 9 — Double-sideband transmitting modulator (up-converter).

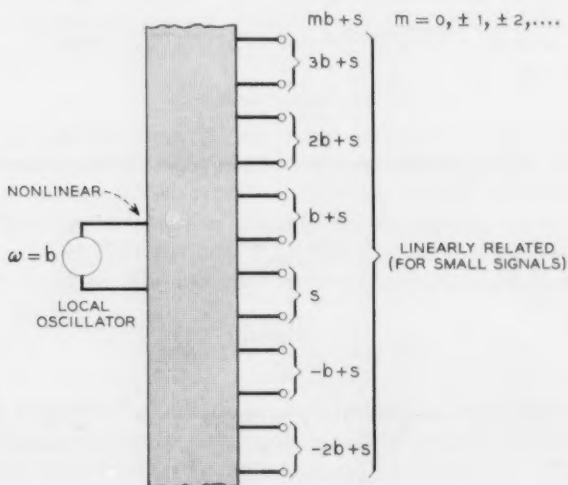


Fig. 10 — "Black box" representation of a linear frequency converter.

so that one can write

$$\Re[v_{LO}(t)] = \sum_m \Re(mb) e^{jmbt}, \quad (42)$$

and

$$\Re'[v_{LO}(t)] = \sum_m \Re'(mb) e^{jmbt}. \quad (43)$$

Then, one can say that  $\Re$  is made up of a large periodic part with Fourier components  $\Re(mb)$  and a vanishingly-small signal part with Fourier components

$$\Re(mb + s) = \sum_n R'[(m - n)b] v(nb + s). \quad (44)$$

The complex amplitudes of the alternating currents, both large and small, can be calculated by multiplying  $qP(\omega)$ . First, the large-signal current will be called  $i_{LO}$ , with Fourier components

$$i_{LO}(mb) = qP(mb)\Re(mb). \quad (45)$$

It should be noted that  $i_{LO}(0)$  differs from the net direct current,  $i_0$ , by

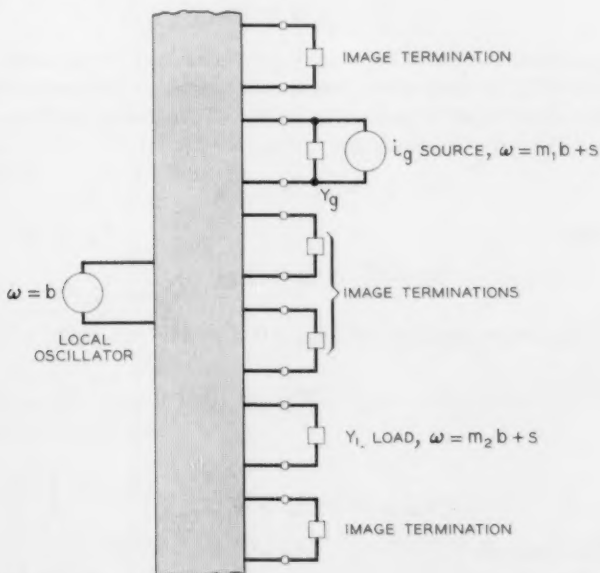


Fig. 11 — Linear frequency converter used as an active four-pole network.

the saturation current,  $i_s$  :

$$i_{Lo}(0) = i_0 + i_s. \quad (46)$$

Second, a complete specification of the small-signal transmission of the frequency converter is given by

$$i_{sIG}(t) = \operatorname{Re} \sum_m i(mb + s) e^{j(mb+s)t}, \quad (47)$$

with

$$i(mb + s) = qP(mb + s) \sum_n \mathcal{R}'[(m - n)b]v(nb + s). \quad (48)$$

Equation (48) can be written in the form

$$i(mb + s) = \sum_n Y(m, n; s) v(nb + s), \quad (49)$$

where

$$Y(m, n; s) = qP(mb + s) \mathcal{R}'[(m - n)b]. \quad (50)$$

The array  $Y(m, n; s)$  is called the conversion matrix. For brevity,

$$Y(m, n; s) \equiv Y_{mn}. \quad (51)$$

In operation, the linear frequency converter will be terminated with admittances  $Y_m$  at each of the "terminals"  $mb + s$ . A system of current generators  $\mathcal{G}_m$  at each of these terminals will produce currents and voltages that obey the relationship

$$\mathcal{G}_m = i_m + v_m Y_m. \quad (52)$$

Therefore,

$$\mathcal{G}_m = \sum_n (Y_{mn} + Y_m \delta_{mn}) v_n, \quad (53)$$

where  $\delta_{mn}$  is 1 if  $m$  equals  $n$  and  $\delta_{mn}$  is 0 if  $m$  does not equal  $n$ . One can also write

$$v_m = \sum_n \lambda_{mn} \mathcal{G}_n, \quad (54)$$

where

$$\| \lambda_{mn} \| = \| Y_{mn} + Y_m \delta_{mn} \|^{-1} \quad (55)$$

in matrix notation.

The effect at terminal  $m$  of a current generator  $\mathcal{G}_n$  at terminal  $n$  can be duplicated by a fictitious current generator  $\eta_{mn} \mathcal{G}_n$  placed at terminal

$m$ , where

$$\eta_{mn} = \frac{\lambda_{mn}}{\lambda_{nm}} \quad (56)$$

does not depend on  $Y_m$  (Thévenin-Norton theorem). This property makes  $\eta_{mn}$  a desirable quantity to use in the analysis so that a necessary characteristic of the noise figure — that it be independent of the load admittance — will appear quickly and naturally.

#### XI. NOISE IN THE GENERAL p-n JUNCTION FREQUENCY CONVERTER

Suppose that the appropriate value of  $g(\omega)$  for a carrier event is applied to each terminal of the linear frequency converter. Then the equivalent current generator at the output  $mb + s$  will be

$$\sum_n \eta_{m2n} g(nb + s). \quad (57)$$

This sum can be substituted for  $g(\omega)$  in (26). For either a forward or a reverse transit, (26) and (57) give

$$\int \hat{g}^2(t) dt = 2q^2 B \sum_{n,n'} \eta_{m2n} \eta_{m2n'}^* e^{j(n'-n)b t_0}. \quad (58)$$

The development thus far could be used to treat the nonlinear-resistor type of p-n junction. For the general p-n junction, forward and back events must also be considered. A forward pulse at  $t_0$  followed by a reverse pulse at  $t_0 + t'$  gives

$$\begin{aligned} \int \hat{g}^2(t, t') dt = & 2q^2 B \sum_{n,n'} \eta_{m2n} \eta_{m2n'}^* e^{j(n'-n)t_0} [1 - e^{-j(nb+s)t'} - e^{j(n'b+s)t'} \\ & + e^{j(n'-n)bt'}]. \end{aligned} \quad (59)$$

In all applications of (59), the weighted sum over all possible values of  $t'$  will be required:

$$\begin{aligned} \int_0^\infty dt' P(t') \int \hat{g}^2(t', t) dt = & 2q^2 B \sum_{n,n'} \eta_{m2n} \eta_{m2n'}^* e^{j(n'-n)t_0} [P(nb + s) \\ & + P^*(n'b + s) - P(nb - n'b) - P_0]. \end{aligned} \quad (60)$$



11.1 *Reverse Carriers*

The thermally generated reverse carriers occur at random but at a steady average rate  $i_s/q$ . Multiplying (58) by this rate gives

$$\langle i^2 \rangle_{\text{reverse}} = 2qBi_s \sum_n |\eta_{m_2 n}|^2, \quad (61)$$

since the terms in (58) for which  $n$  does not equal  $n'$  are oscillatory and give no contribution to the noise power when averaged for a steady rate.

Equation (61) may be interpreted as simple shot noise applied to each terminal and independently converted to the output (except the term for  $n = m_2$ , which represents the direct shot noise at the output).

11.2 *Forward Carriers*

The rate of emission  $[P_0 \Re(t_0)]$  of forward carriers varies periodically, so that an average of (58) over the local-oscillator cycle is required:

$$\langle i^2 \rangle_{\text{forward}} = \frac{b}{2\pi} \int_{-\pi/b}^{\pi/b} dt_0 P_0 \Re(t_0) \left[ 2q^2 B \sum_{n, n'} \eta_{m_2 n} \eta_{m_2 n'}^* e^{j(n' - n)bt_0} \right]. \quad (62)$$

The Fourier expansion, (42), of  $\Re(t_0)$  may be inserted in (62). One then finds

$$\langle i^2 \rangle_{\text{forward}} = 2q^2 B P_0 \sum_{n, n'} \Re(nb - n'b) \eta_{m_2 n} \eta_{m_2 n'}^*. \quad (63)$$

11.3 *Forward-and-Back Carriers*

In similar fashion, one can average (60) over the local-oscillator cycle to obtain the mean-square output current generator for all classes of forward-and-return carriers:

$$\begin{aligned} \langle i^2 \rangle_{\text{forward-and-back}} = 2q^2 B \sum_{n, n'} \Re(nb - n'b) \eta_{m_2 n} \eta_{m_2 n'}^* [P(nb + s) \\ + P^*(n'b + s) - P(nb - n'b) - P_0]. \end{aligned} \quad (64)$$

11.4 *Total Shot Noise*

The sum of (61), (63) and (64) is

$$\begin{aligned} \langle i^2 \rangle_{\text{total}} = 2qB \left\{ i_s \sum_n |\eta_{m_2 n}|^2 \right. \\ + q \sum_{n, n'} \Re(nb - n'b) \eta_{m_2 n} \eta_{m_2 n'}^* [P(nb + s) + P^*(n'b + s) \\ \left. - P(nb - n'b)] \right\}. \end{aligned} \quad (65)$$

### 11.5 Image Conversion Noise

The frequency converter is supposed to be terminated at the frequencies  $(mb + s)/2\pi$  with specified admittances which may or may not generate noise. What noise is generated will be transmitted to the output according to the coefficients  $\eta_{m_2 m}$ .

The input and output terminations  $m_1 b + s$  and  $m_2 b + s$  are in a class apart, because noise generated in these terminations is chargeable to the transducers that precede or follow the frequency converter. The other terminations  $mb + s$ , with  $m_1 \neq m \neq m_2$ , will be called images. The frequency converter (but not the diode) must be held responsible for output noise originating in the image terminations.

The properties of the image terminations as noise generators depend upon the physical nature of the terminations and are not uniquely determined by their impedances. For example, the conductance  $G_m$  for each of the image terminations  $mb + s$  might consist of a resistor at temperature  $T_m$ . Then the image termination noise at the output would be

$$\langle i^2 \rangle_{\text{image terminations}} = 4kB \sum_m' T_m G_m |\eta_{m_2 m}|^2, \quad (66)$$

where the symbol  $\sum'$  indicates that terms in  $m = m_1$  or  $m = m_2$  are not included in the summation. The terminations may be devices that are not in thermal equilibrium. If several diodes are used in combination, so that they terminate each other at some image frequencies, the noise generated in the mutual terminations can be much greater or much less than thermal noise.

### 11.6 Noise Figure

The noise output of a linear transducer must be judged in relation to the signal output for a given input signal. As a standard value for the input signal, it is conventional to use thermal noise corresponding to an absolute temperature of 290°K, which will be denoted  $T_s$ . The thermal noise current is  $\sqrt{4kT_s G_s B}$ , where  $G_s$  is the source conductance, and an rms current of this value will be the standard input signal.

The noise figure  $F$  can be defined by

$$F - 1 = \frac{\text{output noise power due to transducer}}{\text{output signal power from standard input signal}}. \quad (67)$$

The noise figure of the input stage determines receiver sensitivity if the gain of the transducer is sufficiently high. For the frequency converter,

$$F - 1 = \frac{\text{shot noise at output} + \text{image conversion noise at output}}{\text{output signal power from the standard input signal}}. \quad (68)$$

In place of power, we may use in each case the equivalent mean-square current generator at the output, which for the standard signal is

$$\langle i^2 \rangle_{\text{standard}} = 4kT_s BG_s |\eta_{m_2 m_1}|^2. \quad (69)$$

For convenience, one may define

$$\mu_n = \frac{\eta_{m_2 n}}{\eta_{m_2 m_1}} = \frac{\lambda_{m_2 n}}{\lambda_{m_2 m_1}}. \quad (70)$$

Then the total noise figure may be written

$$F - 1 = \frac{q}{2kT_s G_s} \left\{ q \sum_{n, n'} \Re(nb - n'b) \mu_n \mu_{n'}^* [P(nb + s) + P^*(n'b + s) - P(nb - n'b)] + i_s \sum_n |\mu_n|^2 \right\} + \sum_m' \frac{G_m T_m}{G_s T_s} |\mu_m|^2. \quad (71)$$

The last term of this equation represents image conversion noise. It is an important practical problem to design the circuit to minimize image conversion noise. But, in principle, this can always be made to vanish by refrigerating the terminations, so the subsequent theoretical discussion will consider only the shot noise.

### XII. NONLINEAR CAPACITORS

A nonlinear-capacitor type of p-n junction is one in which all emitted carriers are collected within a short time after emission. If all emitted carriers are collected,  $P_0$  is zero, since it is the probability of a carrier not being collected. Hence, there are no forward-only carriers. Moreover, the reverse current  $i_s$  of the thermally generated carriers must be zero. One may show this by considering the diode in equilibrium, when the net direct current must be zero; if there are no forward-only carriers, there must be no reverse-only carriers.

Thus, the only shot noise is that due to forward-and-back carriers, governed by  $P(t')$ . The exact form of  $P(t')$  is not too important. The simple rectangular function shown in Fig. 12 will serve to illustrate the main result. The maximum storage time,  $\Delta$ , will be allowed to become very small compared to  $1/\omega$ , to approach the case of an ideal nonlinear capacitor. The function  $P(\omega)$  is, according to (10),

$$P(\omega) = 1 - \int_0^\Delta \frac{1}{\Delta} e^{-j\omega t'} dt' = \frac{1}{2} j\omega\Delta + \frac{1}{6} (\omega\Delta)^2 + \dots \quad (72)$$

The shot noise due to forward-and-back carriers is obtained when this  $P(\omega)$  is inserted in (71). Each term contains a factor

$$\begin{aligned}
 P(nb + s) + P^*(n'b + s) P(nb - n'b) = \\
 \frac{1}{2} j(nb + s)\Delta - \frac{1}{2} j(n'b + s)\Delta - \frac{1}{2} j(nb - n'b)\Delta \\
 + \frac{\Delta^2}{6} [(nb + s)^2 + (n'b + s)^2 - (nb - n'b)^2] + \dots \quad (73) \\
 = \frac{\Delta^2}{3} (nb + s)(n'b + s) + \dots
 \end{aligned}$$

The first-order terms in  $\Delta$  cancel. As  $\Delta$  goes to zero, i.e., as the frequency response of the diode is increased, the shot noise goes to zero as  $\Delta^2$ .

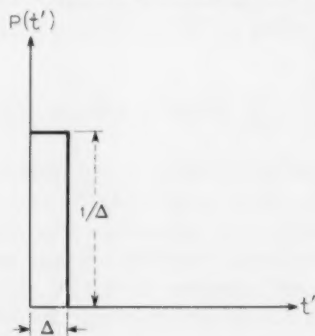


Fig. 12 — Example of a return probability distribution leading to nonlinear capacitor action.

The capacitance, for a given voltage, is proportional to  $\Delta$ . To approach an ideal nonlinear capacitor, let  $\Delta$  approach zero. At the same time, the capacitance waveform can be kept essentially unchanged if the emission rate is increased (by appropriate adjustment of the local-oscillator voltage). The shot noise then goes to zero with  $\Delta$  and we get this result: *A frequency converter using an ideal nonlinear capacitor has no shot noise output regardless of the local-oscillator waveform, the source and load admittances, and the image terminations.*

An interesting qualitative interpretation\* of this result is that, as  $\Delta$  gets smaller, an increasing number of carrier events are required to obtain a given capacitance waveform. A smoother current results from the statistical effect of having a large number of elementary events.

\* Suggested by D. Leenov.

If the nonlinear capacitance does not arise from the minority-carrier storage mechanism that has been postulated, but is wholly or partly due to depletion-layer capacitance, there is even less reason to expect noise. The depletion-layer capacitance involves widening and narrowing of the space-charge region. It requires a relatively small motion of majority carriers instead of their emission all the way across the junction, or of any subsequent existence as minority carriers. The frequency response of  $C_T$  should therefore be better than that of minority-carrier storage capacitance. Also, the elementary events are likely to be representable approximately as forward-and-back current generators, with the area under each pulse being much less than  $q$ , since the carriers do not go all the way across the junction.

The problem of finite frequency response ( $\Delta \neq 0$ ) can be studied by putting the expression given in (73) in (71), to get the leading term in the shot noise:

$$F - 1 = \frac{q^2 \Delta}{6kT_s G_s} \sum_{n,n'} \Delta \Re(nb - n'b)(nb + s)(n'b + s). \quad (74)$$

It is evident in (74) that  $F - 1$  goes to zero with  $\Delta$  if  $\Delta \Re(nb - n'b)$  is held constant. But, for a finite value of  $\Delta$ , the shot noise could be very large in the case of significant conversion from high-order harmonic images. Hence, a circuit design consideration is to make  $\mu_n$  small for all values of  $n$  such that  $nb$  is greater than  $1/\Delta$ . Short-circuiting of the harmonic images is one way of accomplishing this objective.

Apart from finite frequency response, actual diodes will fall short of ideal nonlinear-capacitor action because of the finite lifetime of minority carriers. Some minority carriers will recombine before they have a chance to return to the junction. The effect of this recombination is equivalent to that of a nonlinear resistor in parallel with a nonlinear capacitor having infinite minority-carrier lifetime. As will be shown, low-noise frequency conversion is possible with nonlinear resistors when the local-oscillator current is sharply pulsed. Therefore, low-noise frequency conversion is possible with a nonlinear capacitor suffering from recombination, but the local-oscillator waveform can no longer be arbitrary, and the conversion gain will be reduced.

### 12.1 Nonlinear Capacitor Structures

Four semiconductor structures shown in Fig. 13 exhibit nonlinear capacitance, for reasons to be discussed. The first of these can be made from a transistor, and thus is a readily available specimen for relatively low-frequency (about 10 mc) experiments with nonlinear capacitors.

However, the great promise of the nonlinear capacitor is the possibility that a diode structure can be made to work at higher frequencies than transistors. Transistors, as will be explained below, are not one-dimensional structures, a fact that aggravates the series-resistance problem. The  $p^+n-n^+$  and  $p-i-n$  and the graded  $p-n$  junction can be truly one-dimensional structures, as long as skin-effect is not important. Of

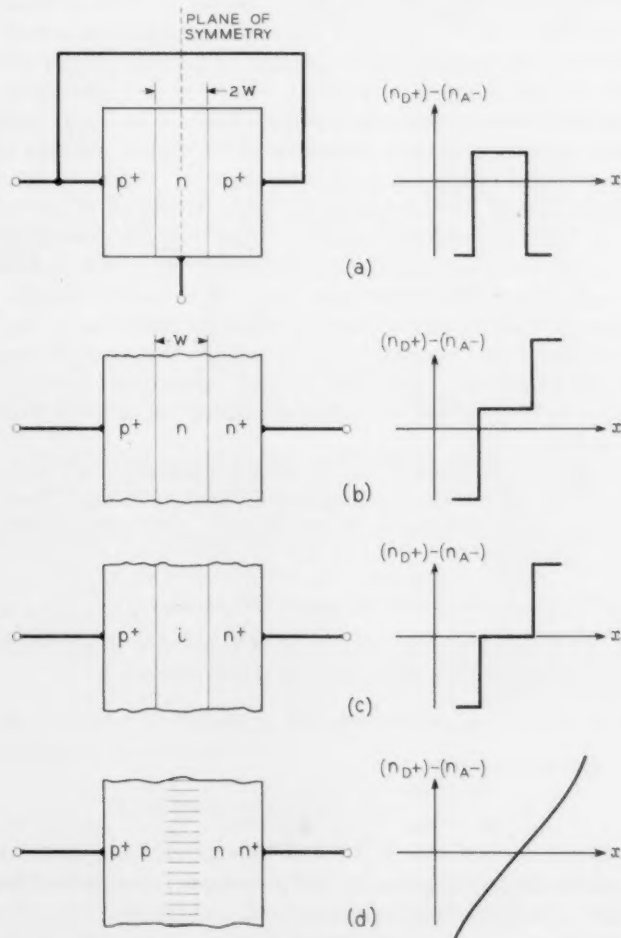


Fig. 13 — Nonlinear capacitor structures: (a)  $p^+n-p^+$ ; (b)  $p^+-n-n^+$ ; (c)  $p^+-i-n^+$ ; (d) graded  $p-n$  junction.

these, the graded p-n junction seems to be the easiest structure to fabricate by solid-state diffusion of impurities into semiconductors.

### 12.2 $p^+-n-p^+$ Structure

The  $p^+-n-p^+$  structure in Fig. 13(a) can be made by connecting the emitter and collector leads of an alloy-junction transistor. A symmetrical alloy transistor (one with emitter and collector junctions of equal size) is theoretically preferred for maximum nonlinear-capacitor action. The pains taken by the transistor manufacturer to prevent emitter-collector short circuits are, of course, completely wasted in this application.

The emitter and collector junctions thus become, in effect, one junction which almost completely surrounds the n region. Because of the high concentration of holes in the heavily doped  $p^+$  region, compared to the concentration of electrons in the n region, nearly all of the emitted carriers are holes entering the n region, rather than electrons going into the  $p^+$  regions. Holes going into the n region may recombine and become forward-only events. But if the base width  $2w$  is narrow enough, most of the holes will escape recombination, either by returning to the junction from which they were emitted or by being collected at the opposite junction. In either case, such holes become forward-and-return events with respect to the junction, consisting of emitter and collector junctions taken together.

The n region is assumed to be of uniform resistivity and thus to be field-free except for the space-charge regions at the junction. Hence, the motion of the emitted holes is simple diffusion. The diffusion equation (13) then reduces to

$$(j\omega + 1/\tau)p_w = D\nabla^2 p_w. \quad (75)$$

If one lets  $x$  equal zero at the plane of symmetry indicated in Fig. 13(a), the solution of (75) appropriate to this symmetry is

$$p_w \propto \cosh x\sqrt{(j\omega + 1/\tau)/D}. \quad (76)$$

At  $x = \pm w$ ,  $p_w$  equals  $p_{1w}$ , so

$$p_w = p_{1w} \frac{\cosh x\sqrt{(j\omega + 1/\tau)/D}}{\cosh w\sqrt{(j\omega + 1/\tau)/D}}. \quad (77)$$

The current density is given by  $qD\nabla p$  evaluated at  $x = w$ . Then, by comparison with (15), one finds that

$$1/L_w = \sqrt{(j\omega + 1/\tau)/D} \tanh w\sqrt{(j\omega + 1/\tau)/D}. \quad (78)$$

According to (18),  $1/L_w$  is proportional to  $P(\omega)$ . For comparison with



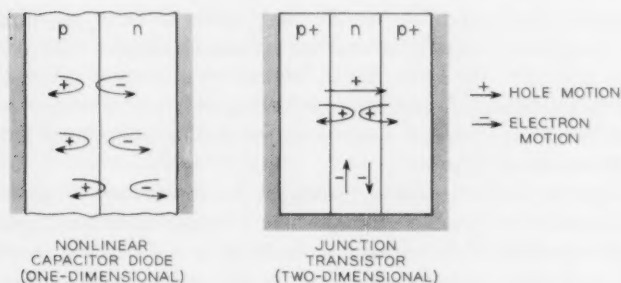


Fig. 14 — One-dimensional versus two-dimensional bipolar (hole and electron) flow patterns in junction devices.

(58), recombination may be neglected by setting  $1/\tau \approx 0$ , and (64) can then be expanded on the assumption that  $w$  is small (i.e., that the frequency response is high relative to  $\omega$ ). One finds

$$P(\omega) \propto \frac{1}{L_w} = \frac{1}{w} \left[ j \frac{\omega w^2}{D} + \frac{1}{3} \left( \frac{\omega w^2}{D} \right)^2 + \dots \right] \quad (79)$$

Hence, the leading terms are proportional to those of (72), with  $w^2/D$  playing the role of the time  $\Delta$  in which (nearly) all of the emitted carriers return.

The postulated condition of neutrality of the n region implies that, when holes are emitted into the n region, an essentially equal number of electrons must enter the n region from the base contact. A voltage drop is required to move these carriers, and this may be crudely described as a series resistance. The thinner the base layer is made for the sake of high frequency response, the higher the series resistance. This dilemma is well known in transistor design. As shown in Fig. 14, the electrons move in a direction perpendicular to the average motion of the holes; hence, two directions in space are involved. Thus, any one-dimensional analysis of the transistor is inherently an oversimplification, although sometimes a very useful approximation.

### 12.3 $p^+-n-n^+$ Structure

As an introduction to a structure that is truly one-dimensional, note that the plane of symmetry in Fig. 13(a) could be replaced by a surface that has the property of reflecting holes. A heavily doped  $n^+$  region would have this property, and this suggests the  $p^+-n-n^+$  structure shown in Fig. 13(b). Equation (78) should apply to this structure as well as to that of Fig. 13(a).

For each element of  $p^+-n$  junction area, there is a corresponding area of  $n-n^+$  junction that reflects emitted holes and also provides the electrons to neutralize the holes. Thus, the area of this structure can be increased in two dimensions without affecting its performance, except for a proportionate lowering of impedance level. This is a characteristic of a one-dimensional structure.

The depletion-layer etching technique has been used to make very thin germanium  $p^+-n-x$  structures, where  $x$  is supposed to be a region of high recombination.<sup>15</sup> The unsolved problem in making this structure is that of obtaining a satisfactory  $x$  region for nonlinear resistance action at high frequencies. No such problem exists in making a  $p^+-n-n^+$  nonlinear capacitor, since a well-understood  $n^+$  region is required in place of the little-understood  $x$  region.

#### 12.4 $p^+-i-n^+$ Structure

The  $p^+-i-n^+$  diode is another one-dimensional structure that has a carrier-storage behavior described qualitatively by (78) because the basic carrier-storage action is quite similar to that of the  $p^+-n-n^+$  structure. Thus, holes emitted from the  $p^+$  region are reflected at the  $n^+$  junction. In addition, electrons emitted from the  $n^+$  junction are reflected at the  $p^+$  junction.

An accurate analysis of the  $p^+-i-n^+$  structure requires consideration of the simultaneous motion of holes and electrons, and would represent an advance over present  $p-n$  junction theory. In the meantime, the qualitative considerations mentioned above indicate that the  $p^+-i-n^+$  structure should give nonlinear-capacitance action up to frequencies determined by the width of the  $i$  region. At much higher frequencies, the structure will just be a resistance whose value depends upon the density of carriers in the  $i$  region, which density is proportional to the forward direct current.

#### 12.5 Graded $p-n$ Junction

By drawing a smooth curve through the concentration gradients for either the  $p^+-n-n^+$  or the  $p^+-i-n^+$  structures, one obtains the graded  $p-n$  junction shown in Fig. 13(d).

The graded junction has features that recommend it as a nonlinear-capacitor structure.<sup>6</sup> The electric field associated with the impurity gradient tends to reflect emitted carriers — the steeper the gradient, the larger the field and the higher the frequency response of the capacitance. Analysis of the frequency response, based on the approximate kinetic

theory of p-n junctions, can apply (if at all) only to an intermediate region of bias where emission is significant but not so copious that the electric field is altered by the forward current.

The frequency response of the capacitance will depend on bias, being very high for reverse voltages and deteriorating gradually as the voltage approaches and enters the forward region. However, microwave experiments suggest that the series resistance will generally be a much more important source of loss and noise than any frequency limitations of the nonlinear capacitance. A steep impurity gradient makes for a series resistance that is low both in absolute value and in relation to the capacitance. However, the capacitance per unit area increases as the gradient increases.

### XIII. NONLINEAR RESISTOR NOISE

The nonlinear resistor type of p-n junction has the property that none of the emitted carriers return, except possibly some carriers that return in a time negligibly short in comparison to the frequencies under consideration. Within the frequency range of nonlinear resistor action, the admittance due to emitted carriers is real and independent of frequency.

In spite of the absence of return pulses to cancel the shot current of emission, the shot noise delivered to the load can be made very small if the local-oscillator current flows in short pulses. The plausibility of this result will be argued by representing the p-n junction as a noiseless admittance in parallel with a generator of shot current pulses. The shot current and the time variation of the admittance are governed by the local-oscillator drive. For the nonlinear resistor, the admittance is a pure conductance and the shot current to be considered is that of emitted carriers that do not return.

In a frequency converter, the nonlinear resistor is connected to a linear passive network which includes the terminations at all the signal frequencies. If practically all of the shot current flows at a time when the junction conductance is very large compared to the network admittance, the shot current will be short-circuited through the junction conductance and little noise will be delivered to the network.

Another way of describing the situation is to consider that shot noise results because one cannot predict with certainty that a carrier will be emitted in any given short time interval. When a local-oscillator voltage is applied to a junction, it is known that the sum of the carrier currents, in spite of their individual unpredictability, is very nearly equal to a definite macroscopic current waveform that can be determined from the junction characteristics. When this macroscopic current consists of short

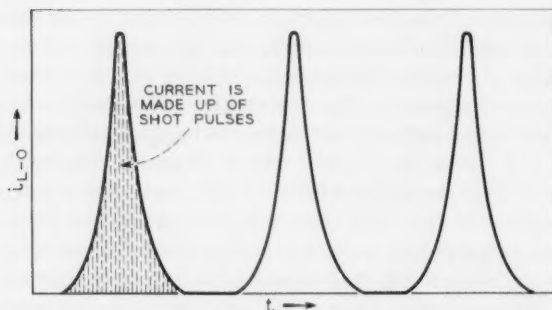


Fig. 15 — Pulsed local-oscillator current waveform giving partial reduction of shot noise.

sharp pulses, it is possible to predict that many carriers will be emitted during the pulses and practically none during other times. Unpredictability, hence shot noise, is greatly reduced for a pulsed current waveform like the one shown in Fig. 15.

The principle of using pulsed local-oscillator current can be applied in the design of nonlinear-resistance frequency converters. In a simple design, for example, it would be preferable to use shunt conductance rather than series resistance to attenuate the power from the local oscillator. More sophisticated mixers may use filters and additional diodes to shape the local-oscillator waveform.

The image terminations chosen below to illustrate the waveform effects should not be regarded as the optimum conditions for practical use. For example, the main image frequency might well be open-circuited to minimize conversion of thermal noise from the series resistance, while short-circuiting of this image will be assumed for mathematical simplicity (in the case of short-circuited harmonics).

### 13.1 Short-Circuited Harmonics

As an example of a circuit permitting low noise and good signal transmission, the mathematically simple case of short-circuited harmonics will be considered. Another way of defining this case is to say that the local-oscillator voltage waveform is purely sinusoidal (plus a dc component,  $v_0$ ). Thus,

$$v(t) = v_0 + v_b \cos bt. \quad (80)$$

The exponential emission function, (1), will be assumed, so that

$$qP_0\mathcal{R}(v) = i_s e^{\beta v} \quad (81)$$

$$= i_s e^{\beta v_0} e^{\beta v_b \cos t}. \quad (82)$$

The constant  $i_s$  is necessarily equal in magnitude to the thermally generated reverse current, so that no net external current flows when  $v$  equals zero. From (81),

$$qP_0\mathcal{R}'(v) = \beta i_s e^{\beta v} \quad (83)$$

which, with (80), gives

$$qP_0\mathcal{R}'(v) = \beta i_s e^{\beta v_0} e^{\beta v_b \cos t}. \quad (84)$$

The Fourier expansion of (84) involves modified Bessel functions of the first kind,<sup>16</sup> denoted by  $I_n$ . Thus,

$$qP_0\mathcal{R}'(nb) = \beta i_s e^{\beta v_0} I_n(\beta v_b). \quad (85)$$

From (50) and (85), one finds that the conversion matrix is

$$Y(m, n; s) = \beta i_s e^{\beta v_0} I_{m-n}(\beta v_b). \quad (86)$$

To take a specific example, conversion between two frequencies differing by  $b/2\pi$  will be considered [such as  $(b+s)/2\pi$  and  $s/2\pi$ ]. All other signal frequencies (images) will be assumed to be short-circuited. Then the conversion matrix reduces to

$$\| Y(m, n; s) \| = \beta(i_s + i_0) \begin{vmatrix} 1 & y \\ y & 1 \end{vmatrix}, \quad (87)$$

where

$$y = \frac{I_1(\beta v_b)}{I_0(\beta v_b)} \quad (88)$$

and  $i_0$ , the direct current, is introduced in view of the relation

$$i_0 = i_s [e^{\beta v_0} I_0(\beta v_b) - 1], \quad (89)$$

which may be obtained from (11).

For minimum conversion loss, the four-terminal network represented by (87) should be used with source and load admittances that simultaneously match the input and output admittances of the network. These admittances are, of course, real for a nonlinear resistor and are found, by standard methods,<sup>17</sup> to be

$$Y_{in} = Y_{out} = G_s = G_L = \beta i_s e^{\beta v_0} I_0(\beta v_b) \sqrt{1 - y^2}. \quad (90)$$

Since the images are short-circuited, all the  $\mu_n$ 's defined in (70) are zero except

$$\mu_{m_1} = 1$$

and

$$\mu_{n2} = -\frac{1 + \sqrt{1 - y^2}}{y}. \quad (91)$$

For the noise figure, algebraic manipulation that will not be detailed here gives

$$F - 1 = \frac{T}{T_s} \frac{u^2 + \theta}{u + u^2}, \quad (92)$$

where

$$u = \sqrt{1 - y^2} \quad (93)$$

and

$$\theta = \frac{i_s}{i_0 + i_s}. \quad (94)$$

Equation (90) gives the dependence of  $F_x$  upon the local-oscillator drive (represented by  $u$ ) and the direct current, represented by  $\theta$ . The quantity  $\theta$  defined in (94) is the ratio of the thermally generated current to the current carried by emitted carriers.

For any value of  $\theta$ , there is a certain value of  $u$ ,

$$u' = \sqrt{\theta^2 + \theta} - \theta, \quad (95)$$

that gives a minimum noise figure

$$F_{\min} - 1 = \frac{T}{T_s} \frac{2u'}{1 - 2u'}. \quad (96)$$

As  $\theta$  approaches zero,  $F_{\min}$  approaches unity. At the same time, the optimum value of  $u$  approaches zero. The optimum local-oscillator voltage goes to infinity and the conversion loss approaches unity (that is, no loss at all). This result shows that low noise figure and minimum conversion loss are not incompatible.

For most practical microwave diodes  $\theta$  is quite small, since  $i_s$  may be a tenth of a microampere and the direct current  $i_0$  is of the order of a milliampere. An approximate formula is therefore relevant:

$$F_{\min} \approx 1 + 2\sqrt{\theta}; \quad \theta < 0.01. \quad (97)$$

For  $\theta = 10^{-4}$ ,  $F_{\min} = 1.02 = 0.1$  db. Thus, the observed thermally generated currents would not produce much noise and probably are not

responsible for much of the observed noise figure of crystals, except possibly at elevated temperatures.

This analysis has considered only the shot noise of the emitted carriers. In actual diodes, the series resistance and the depletion-layer capacitance impair the noise figure. The depletion-layer capacitance should be essentially noiseless, but, in combination with  $R_s$ , it sets bounds on the usable impedance level of nonlinear resistance of the emitted carriers. With the impedance level thus established,  $R_s$  causes a definite signal loss and contributes thermal noise. Furthermore,  $R_s$  interferes with short-circuiting the local-oscillator harmonics or otherwise obtaining the pulsed local-oscillator current waveform essential for low shot noise.

### 13.2 Open-Circuited Harmonics

When the harmonics of the local oscillator are open-circuited, the local-oscillator current is sinusoidal (in addition to a direct current). It will be shown that this waveform is unfavorable for noise, although it permits a low conversion loss.

The emission rate and the local-oscillator current are simply related:

$$qP_0R(t) = i_{LO}(t) + i_s = (i_0 + i_s) \left( 1 + \frac{2\xi}{1 + \xi^2} \cos bt \right), \quad (98)$$

where

$$0 \leq \xi \leq 1. \quad (99)$$

The reason for introducing the quantity  $\xi$  will be apparent later. The Fourier analysis of  $P_0R(t)$  is obtained by inspection of (98):

$$\begin{aligned} qP_0R(nb) &= i_0 + i_s & \text{if } n = 0 \\ &= \frac{(i_0 + i_s)}{1 + \xi^2} & \text{if } n = \pm 1 \\ &= 0 & \text{otherwise.} \end{aligned} \quad (100)$$

Since an exponential emission rate is being considered,  $R'$  equals  $\beta R$  and, from (50),

$$\begin{aligned} Y(m, n; s) &= \beta(i_0 + i_s) & \text{if } m = n \\ &= \frac{\beta(i_0 + i_s)\xi}{1 + \xi^2} & \text{if } m = n \pm 1 \\ &= 0 & \text{otherwise.} \end{aligned} \quad (101)$$



The admittance representation of a frequency converter lends itself readily to consideration of cases where the image frequencies are short-circuited, since the elements of  $Y(m, n; s)$  corresponding to the images may then simply be omitted. One finds, however, that, with open-circuited harmonics and short-circuited images, the conversion loss is at least 3 db, quite apart from the further losses due to the parasitics. As an absolute theoretical limit, this conversion loss appears to be excessive. In seeking an escape from this limit, one naturally wonders if open-circuited images might be appropriate for open-circuited harmonics.

Indeed, open-circuited images permit unity conversion gain. To deal with open-circuited images, we may invert the infinite-dimensional matrix  $\| Y(m, n; s) \|$  to obtain the conversion matrix in impedance form:

$$Z(m, n; s) = \frac{(-\xi)^{|l-m|}}{\beta(i_0 + i_s)} \frac{1 + \xi^2}{1 - \xi^2}. \quad (102)$$

The images can now be open-circuited by considering only the  $2 \times 2$  impedance matrix pertaining to the signals. This matrix may be inverted to give the admittance matrix for open-circuited images:

$$\| Y \| = \beta(i_0 + i_s) \begin{vmatrix} 1 & \xi \\ \xi & 1 \end{vmatrix}. \quad (103)$$

For the conversion between two frequencies differing by  $b/2\pi$ , with all images open-circuited, one has, in analogy with the short-circuit case,

$$Y_{in} = Y_{out} = G_L = G_s = \beta(i_0 + i_s) \sqrt{1 - \xi^2}. \quad (104)$$

The noise figure is found to be

$$F - 1 = \frac{T}{T_s} \frac{1 + \theta(2 - z^2)}{z(1 - z)(2 - z^2)}, \quad (105)$$

where

$$z = \sqrt{1 - \xi^2}. \quad (106)$$

For any value of  $z$ , the lowest noise figure is obtained when  $\theta$  equals 0, that is, when the thermally generated current is negligible. For  $\theta = 0$ , the minimum noise figure is  $3.25 = 5.1$  db; this occurs when  $z$  equals 0.45 and the conversion loss is 4.2 db. Evidently the noise performance

with open-circuited harmonics is inferior to that obtainable with short-circuited harmonics.

#### XIV. CONCLUSIONS

The nonlinear capacitance of a p-n junction can be used in amplifiers and amplifying frequency converters. To the extent that the junction exhibits pure capacitance, it will be noiseless in any of these applications. Suitably designed p-n junctions are remarkably good nonlinear capacitors at microwave frequencies, and preliminary experiments indicate that good noise figures can be obtained.

A pulsed local-oscillator current is required for low-noise frequency conversion with nonlinear resistance p-n junctions. This requirement is a logical consequence not only of p-n junction theory, but also of earlier metal-semiconductor rectification theories that assumed emission of carriers across a barrier.

#### XV. ACKNOWLEDGMENT

The author wishes to thank H. W. Andrews for advice and assistance in setting up the first up-converter experiment to give proof of the low-noise possibilities of diffused nonlinear capacitor diodes.

#### REFERENCES

1. Palevsky, H., Swank, R. K. and Grenchik, R., Design of Dynamic Condenser Electrometer, *Rev. Sci. Instr.*, **18**, May 1947, pp. 298-314.
2. Scherbatskoy, S. A., Gilmartin, T. H. and Swift, G., The Capacitive Commutator, *Rev. Sci. Instr.*, **18**, June 1947, pp. 415-421.
3. Manley, J. M. and Rowe, H. E., Some General Properties of Nonlinear Elements, *Proc. I.R.E.*, **44**, July 1956, pp. 904-913.
4. Torrey, H. C. and Whitmer, C. A., *Crystal Rectifiers*, McGraw-Hill, New York, 1948, Chap. 13.
5. Semiconductor Diodes Yield Converter Gain, Bell Labs. Record, **35**, October 1957, p. 412.
6. Bakanowski, A. E., Cranna, N. G. and Uhler, A., Jr., Diffused Silicon and Germanium Nonlinear Capacitance Diodes, I.R.E.-A.I.E.E. Semiconductor Device Research Conference, Boulder, Colo., July 1957.
7. Herrmann, G. F., Uenohara, M. and Uhler, A., Jr., *Proc. I. R. E.*, **46**, June 1958, pp. 1301-1303.
8. Leenov, D., this issue, pp. 989-1008.
9. Shockley, W., The Theory of p-n Junctions in Semiconductors and p-n Junction Transistors, *B.S.T.J.*, **28**, July 1949, pp. 435-589.
10. Shockley, W., Sparks, M. and Teal, G. K., p-n Junction Transistors, *Phys. Rev.*, **83**, July 1951, pp. 151-162.
11. Uhler, A., Jr., High-Frequency Shot Noise in p-n Junctions, *Proc. I.R.E.*, **44**, April 1956, pp. 557-558; Nov. 1956, p. 1541.
12. van der Ziel, A., Theory of Shot Noise in Junction Diodes and Junction Transistors, *Proc. I.R.E.*, **43**, November 1955, pp. 1639-1646.

13. Anderson, R. L. and van der Ziel, A., On the Shot Effect of p-n Junctions, Trans. I.R.E., **EO-1**, November 1952, pp. 20-24.
14. Guggenbuehl, W. and Strutt, M. J. O., Theory and Experiments on Semiconductor Diodes and Transistors, Proc. I.R.E., **45**, June 1957, pp. 839-854.
15. Rediker, R. H. and Sawyer, D. E., Very Narrow Base Diode, Proc. I.R.E., **45**, July 1957, pp. 944-953.
16. McLachlan, N. W., *Bessel Functions for Engineers*, Oxford Univ. Press, London, 1955, Chap. 6.
17. Lo, A. W., Endres, R. O., Zawels, U., Waldauer, F. D. and Cheng, C. C., *Transistor Electronics*, Prentice-Hall, Englewood Cliffs, N. J., 1955, pp. 100-102.

# Gain and Noise Figure of a Variable-Capacitance Up-Converter\*

By D. LEENOV

(Manuscript received March 31, 1958)

*The performance of a p-n junction nonlinear-capacitance diode as a low-noise, amplifying frequency converter is analyzed for the case in which the output signal frequency is many times greater than the input signal frequency. The diode is represented by an equivalent circuit consisting of a time varying capacitance and a constant series resistance. Formulae for the maximum available gain and the noise figure of the circuit are obtained, and representative numerical values are given for the noise figures of systems incorporating such diodes as preamplifiers.*

## I. INTRODUCTION

Since microwave receivers frequently must operate at a very low input signal level it is important to obtain the smallest possible noise figure. One way of accomplishing this is to use a low-noise amplifier at the input of the receiver. In this article the role of a nonlinear-capacitance p-n junction diode in performing such a function is analyzed.

The performance of a variable capacitance as a frequency converter has been extensively discussed in the literature.<sup>1,2,3</sup> Theory indicates that when the variable capacitance is used for conversion between a low frequency and an upper sideband (a noninverting frequency), the maximum available gain is  $f_2/f_1$ ,  $f_1$  being the input frequency and  $f_2$  being the output frequency. Hence in up-conversion (modulation) a power gain results, with the power added to the input signal being supplied by the beat oscillator. In down-conversion a power loss results. (These statements apply when no signal power is transferred at the lower sideband or at any of the harmonic images). The situation is different when one of the two frequencies involved is a lower sideband (an inverting frequency). A negative resistance may then appear at both sets of terminals,

\* Supported in part by the U. S. Army Signal Corps under contract DA 36-039 sc-73224.

resulting in regenerative gain or stable oscillations.<sup>4</sup> Large gains may be obtained when going either up or down in frequency. The present paper, however, is restricted to a consideration of upper sideband frequency conversion. Analysis of lower sideband operation is now in progress.

In this article the frequency conversion performance of a nonlinear capacitance (N-C) diode with parasitics is analyzed. In Section V the maximum available gain (MAG) is calculated and is compared with the MAG predicted for an ideal device. In Section VI, an equation for the noise figure of an N-C diode is obtained, taking into account only the thermal noise of the series resistance. Over-all noise figures are given in Table I for three types of receivers with diode preamplifiers, operating at specified input and output frequencies.

## II. THE EQUIVALENT CIRCUIT

For the calculations to be made here, the p-n junction might be represented by the lumped-parameter equivalent circuit shown in Fig. 1. Here  $R_s$  and  $C_T$  are as defined and the "variable admittance", shown as lumped parameters, accounts for the current carried across the junction by the motion of carriers through the space charge region. A calculation of the mixing action of the diode, using Fig. 1, would involve a rather complicated formulation.<sup>3</sup> However, the silicon and germanium retarding-field diffused diodes now under investigation are fairly accurately represented by the equivalent circuit shown in Fig. 2. (The design and properties of these devices are discussed in other papers).<sup>5,6</sup> In this diagram,  $C_{\min}$  represents the smallest capacitance attainable, determined by the limitation on reverse bias voltage imposed by breakdown, and  $C_{\max}$  is the largest value, determined either by physical limitations or by choice.

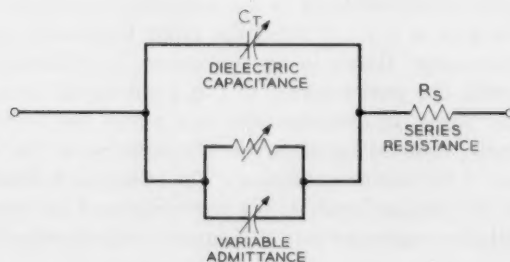


Fig. 1 — Equivalent circuit for nonlinear-capacitance diode.

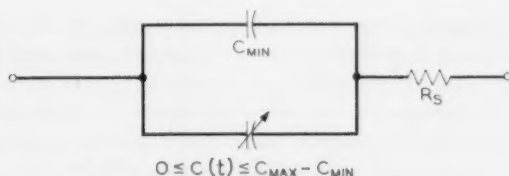


Fig. 2 — Simplified diode equivalent circuit.

## III. ASSUMPTIONS FOR CALCULATION OF GAIN AND NOISE FIGURE

In this article the gain and noise figure of an N-C diode frequency converter are calculated according to the following assumptions: (1) Upper sideband operation is assumed; that is, an input frequency  $f_1$  is converted to an output frequency  $f_2$  using a beating oscillator at the frequency  $f_2 - f_1$ . (2) The lower sideband, of frequency  $f_2 - 2f_1$ , and all the harmonic images are assumed to be open circuited, implying that no power is delivered by the frequency converter at these frequencies. (3) The equivalent circuit of Fig. 3 is used. Here, filters are indicated which restrict transmission in the left-hand branch to a narrow band about the frequency  $f_1$  and transmission in the right-hand branch to a narrow band about  $f_2$ ;  $\mathcal{E}_1$  and  $\mathcal{E}_2$  are signal voltages and  $\mathcal{E}_{N1}$  and  $\mathcal{E}_{N2}$  are noise voltages at frequencies  $f_1$  and  $f_2$  respectively. The equivalent circuit of the diode which was discussed in connection with Fig. 2 is assumed applicable over the operating range of pump voltage and frequency.

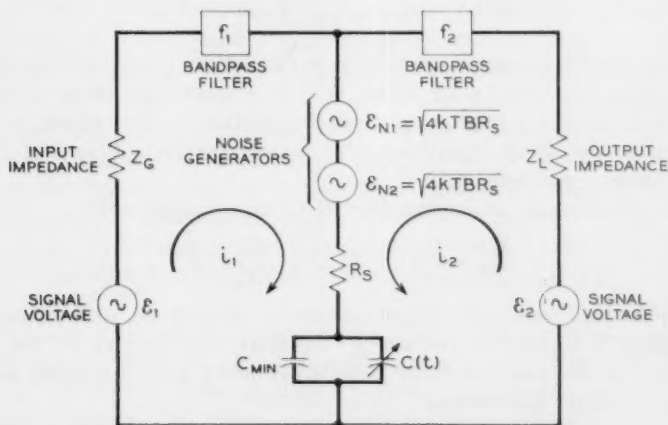


Fig. 3 — Equivalent circuit for the calculation of gain and noise figure.

Using these assumptions, results have been obtained in a simple form which can serve as a guide to diode development and application. It is not supposed that the model used here constitutes a very accurate characterization of the frequency converter operation. In particular, assumption (2) is theoretically possible, but there would be considerable practical difficulty in satisfying these conditions in a microwave circuit.

#### IV. GENERAL EQUATIONS FOR FREQUENCY CONVERSION

In subsequent sections we shall need to calculate, for the circuit shown in Fig. 3, the power delivered to the load at frequency  $f_2$  when specified signal voltages at frequencies  $f_1$  and  $f_2$  are applied. Hence, what is desired is a means of calculating the current  $i_2$  for given signal voltages. For the specific applications to be made later on, we shall obtain in this section a solution in general form for the currents  $i_1$  and  $i_2$  resulting when signal (or noise) voltages  $\mathcal{E}_1$  and  $\mathcal{E}_2$ , at frequencies  $f_1$  and  $f_2$  respectively, are applied to an N-C diode.

It is possible to express the relation between currents and voltages of a frequency converter by means of an admittance matrix; this will be done here for a nonlinear-capacitance frequency converter. Let the beat oscillator voltage be represented by  $V_0$ , and the combined signal voltages by  $\delta V$ . If noise is of any consequence, one may surely assume  $\delta V \ll V_0$ . Hence we may write (1), representing the charge on the capacitor as a function of voltage, in the form of a Taylor expansion,

$$Q(V) = Q_{V_0} + \left( \frac{\partial Q}{\partial V} \right)_{V_0} \delta V + \dots \quad (1)$$

The subscript  $V_0$  signifies that  $Q$  or its derivatives have the value determined by  $V_0$  alone, i.e.  $\delta V$  equals 0. It is assumed that terms of higher order in  $\delta V$  are negligible, so that the relations to be derived will be linear in the signal quantities. (For a more complete theory of linear frequency converters, see Ref. 6).

To evaluate (1) we expand  $(\partial Q / \partial V)_{V_0}$  in a Fourier series,

$$\frac{\partial Q}{\partial V} = C(t) + C_{\min} = \sum_{n=-\infty}^{\infty} C_n e^{jnbt}, \quad (2)$$

with the beat oscillator voltage assumed to be periodic, with pulsance (angular frequency)  $b$ . The signal voltage  $\delta V$  may involve all the harmonics of the beat oscillator pulsance mixed with the signal pulsance  $s$ . Hence it is written

$$\delta V = \sum_{m=-\infty}^{\infty} \sum_{s \pm} v_{mb+s} e^{j(mb+s)t}. \quad (3)$$



Referring to (1), it is seen that the first term on the right-hand side contains only pulsances which are harmonics of  $b$ . The second term, which we designate  $\delta Q$ , contains the various signal pulsances. It is given by

$$\delta Q = \left( \frac{\partial Q}{\partial V} \right)_{V_0} \delta V = \sum_{n,m} \sum_{s \pm} C_n v_{mb+s} e^{j[(m+n)b+s]t}. \quad (4)$$

Since we shall want to select individual pulsance terms from the right-hand side of (4), we set  $m + n = l$ . The result is

$$\delta Q = \sum_{l,m} \sum_{s \pm} C_{l-m} v_{mb+s} e^{j(lb+s)t}. \quad (5)$$

Also, being interested in the current components, we use the relation  $i_\omega = j\omega q_\omega$ , obtaining finally

$$i_{lb+s} = \sum_m j(lb + s) C_{l-m} v_{mb+s} \quad (6)$$

(we have here stopped considering the terms containing  $-s$ , because  $i_{lb-s} = i_{-lb+s}^*$ ). Equation (6) is equivalent to the matrix equation

$$i_{lb+s} = \sum_m Y_{lm} v_{mb+s}, \quad (7)$$

where the elements  $Y_{lm}$  are given by

$$Y_{lm} = j(lb + s) C_{l-m}. \quad (8)$$

The admittance representation is convenient to use when only a few signal voltages have specified values and the rest are zero (i.e. short-circuited). In the case of the equivalent circuit used here, none of the voltages can be short-circuited, because of the diode series resistance. The possibility remains, however, of presenting open circuits to all the image pulsances (all the  $mb + s$ ) except for the two involved in frequency conversion,  $s$  and  $b + s$ . This means that all the currents except  $i_s$  and  $i_{b+s}$  will be assumed to vanish. The relation between voltage and current can then be simplified when it is expressed in the impedance matrix form. Hence we must obtain the matrix inverse of  $\|Y\|$ , which is  $\|Z\| \equiv \|Y\|^{-1}$ .

There is at least one case in which this matrix inversion can be readily performed. If  $\partial Q / \partial V$  equals  $C_0 + 2C_1 \cos bt$  then only the coefficients  $C_0$  and  $C_1$  in the expansion (2) do not vanish. The matrix of (8) is now limited to elements on the diagonal and once removed from the diagonal. As a product of infinite matrices (in these arrays only the nonzero elements are indicated), it is written

$$\| Y \| = \begin{vmatrix} \dots & & & & \\ & j(-b + s) & & & \\ & & js & & \\ & & & j(b + s) & \\ & & & & j(2b + s) \\ & & & & & \dots \end{vmatrix} \begin{vmatrix} \dots & & & & \\ & C_1 & C_0 & C_1 & \\ & & C_1 & C_0 & C_1 \\ & & & C_1 & C_0 & C_1 \\ & & & & \dots \end{vmatrix}. \quad (9)$$

The second matrix on the right-hand side of (9) may be factored to obtain (10),

$$\| C_{lm} \| = C_0 \begin{vmatrix} \dots & & & & \\ & \xi & 1 & \xi & \\ & & \xi & 1 & \xi \\ & & & \xi & 1 & \xi \\ & & & & \dots \end{vmatrix}, \quad (10)$$

where  $\xi = C_1/C_0$ . Equation (9) can be written symbolically as

$$\| Y \| = \| j(lb + s) \| \| C_{lm} \|,$$

and, by a rule of matrix algebra, the impedance matrix is given by

$$\| Z \| = \| Y \|^{-1} = \| C_{lm} \|^{-1} \| j(lb + s) \|^{-1}. \quad (11)$$

The first matrix on the right-hand side of (9) is diagonal, hence its inverse is easily obtained. The inverse of the second matrix is also known.<sup>6</sup> If a matrix has the form

$$\begin{aligned} M_{ij} &= 1; & \text{if } i &= j \\ &= \frac{\xi}{1 + \xi^2}; & \text{if } i &= j \pm 1 \\ &= 0; & \text{otherwise,} \end{aligned} \quad (12a)$$

the inverse matrix is given by

$$(M^{-1})_{ij} = \frac{1 + \xi^2}{1 - \xi^2} (-\xi)^{|i-j|}. \quad (12b)$$

This result can be used to obtain  $\| C_{lm} \|^{-1}$ , if we set  $\xi \equiv \xi/(1 + \xi^2)$  [see (10)]. If it is now assumed that all pulsataces in the spectrum, other than  $b + s$  and  $s$ , are open-circuited, the impedance matrix reduces to

$$Z_c = \frac{1}{C_0} \frac{1 + \xi^2}{1 - \xi^2} \begin{vmatrix} 1 & -\xi \\ -\xi & 1 \end{vmatrix} \begin{vmatrix} \frac{1}{js} & 0 \\ 0 & \frac{1}{j(b+s)} \end{vmatrix}. \quad (13)$$

To simplify future work, we shall use the abbreviated representation

$$Z_c = \begin{vmatrix} Z_{11} & Z_{12} \\ Z_{21} & Z_{22} \end{vmatrix}. \quad (14)$$

The matrix  $Z_c$  represents the capacitive impedance of the diode. The total impedance  $Z$  must include the series resistance  $R$ ; it is given by

$$Z = \begin{vmatrix} Z_{11} + R & Z_{12} \\ Z_{21} & Z_{22} + R \end{vmatrix}. \quad (15)$$

By the definition of an impedance matrix we have

$$\begin{vmatrix} v_1 \\ v_2 \end{vmatrix} = \begin{vmatrix} Z_{11} + R & Z_{12} \\ Z_{21} & Z_{22} + R \end{vmatrix} \begin{vmatrix} i_1 \\ i_2 \end{vmatrix}. \quad (16)$$

Here  $v_1$  and  $v_2$  are the voltages across the diode terminals at the input and output frequencies, respectively, and  $i_1$  and  $i_2$  are the corresponding currents. It follows from Fig. 3 that these two voltages are given by

$$\begin{aligned} v_1 &= \varepsilon_1 - i_1 Z_G \\ v_2 &= \varepsilon_2 - i_2 Z_L \end{aligned} \quad (17)$$

Substituting (17) into (16), and rearranging, we obtain

$$\begin{vmatrix} \varepsilon_1 \\ \varepsilon_2 \end{vmatrix} = \begin{vmatrix} Z_{11} + R + Z_G & Z_{12} \\ Z_{21} & Z_{22} + R + Z_L \end{vmatrix} \begin{vmatrix} i_1 \\ i_2 \end{vmatrix}. \quad (18)$$

The solution for the currents is written in matrix form

$$\begin{vmatrix} i_1 \\ i_2 \end{vmatrix} = \begin{vmatrix} Z_{11} + R + Z_G & Z_{12} \\ Z_{21} & Z_{22} + R + Z_L \end{vmatrix}^{-1} \begin{vmatrix} \varepsilon_1 \\ \varepsilon_2 \end{vmatrix}, \quad (19)$$

where the reciprocal matrix is given by

$$\begin{aligned} & \left\| \begin{array}{cc} Z_{11} + R + Z_g & Z_{12} \\ Z_{21} & Z_{22} + R + Z_L \end{array} \right\|^{-1} \\ &= \frac{1}{D} \left\| \begin{array}{cc} Z_{22} + R + Z_L & -Z_{12} \\ -Z_{21} & Z_{11} + R + Z_g \end{array} \right\|, \end{aligned} \quad (20)$$

and  $D$  is the determinant of the matrix:

$$D = (Z_{11} + R + Z_g)(Z_{22} + R + Z_L) - Z_{12}Z_{21}. \quad (21)$$

The output current, and hence the output power, may be determined from (19) when the voltages  $\mathcal{E}_1$  and  $\mathcal{E}_2$  are specified. This equation will be used as a starting point for calculations of gain and noise figure.

#### V. GENERAL EQUATIONS FOR MAXIMUM AVAILABLE GAIN

We shall calculate the gain of the frequency converter by using the condition

$$\begin{aligned} \mathcal{E}_1 &= \mathcal{E}, \\ \mathcal{E}_2 &= 0, \end{aligned} \quad (22)$$

where  $\mathcal{E}$  is the signal voltage. The gain  $G$  is defined by

$$G = \frac{\text{power absorbed in } Z_L}{\text{power available at input}} = \frac{|i_2|^2 \operatorname{Re} Z_L}{|\mathcal{E}|^2/4 \operatorname{Re} Z_g}. \quad (23)$$

We shall calculate  $G$  with the aid of (19), (20) and (22), and then determine the values of  $Z_g$  and  $Z_L$  leading to a maximum  $G$ , designated by  $G_{\max}$ .

We first solve for  $i_2$  by substituting the conditions of (22) into (19) and obtain

$$i_2 = -\frac{1}{D} Z_{21} \mathcal{E}. \quad (24)$$

Hence, for the gain we have

$$\frac{|Z_{21}|^2 |\mathcal{E}|^2 \operatorname{Re} Z_L / |D|^2}{|\mathcal{E}|^2 / 4 \operatorname{Re} Z_g} = 4 \operatorname{Re} Z_g \operatorname{Re} Z_L \frac{|Z_{21}|^2}{|D|^2} \quad (25)$$

which, with the aid of (21) becomes

$$G = \frac{4 \operatorname{Re} Z_g \operatorname{Re} Z_L |Z_{21}|^2}{|(Z_{11} + R + Z_g)(Z_{22} + R + Z_L) - Z_{12}Z_{21}|^2}. \quad (26)$$

To maximize  $G$ , we first impose the tuning conditions

$$j \operatorname{Im} Z_g = -Z_{11}, \quad j \operatorname{Im} Z_L = -Z_{22}.$$

[Note that, according to (13), the quantities  $Z_{11}$  and  $Z_{22}$  are pure imaginary numbers]. As a result, we obtain

$$G = \frac{4R_o R_L |Z_{21}|^2}{[(R + R_o)(R + R_L) - Z_{12}Z_{21}]^2}. \quad (27)$$

Here  $R_o$  is  $\text{Re } Z_o$ ,  $R_L$  is  $\text{Re } Z_L$ , and  $Z_{12}Z_{21}$  is a real number (since it is the product of two imaginary numbers), and we may dispense with the absolute magnitude sign in the denominator.

To obtain  $G_{\max}$  we must maximize the right hand side of (27) with respect to  $R_o$  and  $R_L$ . The values of  $R_o$  and  $R_L$  satisfying this condition are the matching values, and will be designated by  $R_o'$  and  $R_L'$ . They may be obtained by solving the pair of equations

$$\begin{aligned} \frac{\partial G}{\partial R_o} &= 0, \\ \frac{\partial G}{\partial R_L} &= 0. \end{aligned} \quad (28)$$

On solving these we obtain

$$\begin{aligned} R_o &= \frac{R^2 K^2 + R R_L}{R + R_L}, \\ R_L &= \frac{R^2 K^2 + R R_o}{R + R_o}, \end{aligned} \quad (29)$$

where  $K = \sqrt{1 - Z_{12}Z_{21}/R^2}$ . These equations give the value of  $R_o$  which maximizes  $G$  for any selected value of  $R_L$ , and correspondingly for  $R_L$ . The matching values  $R_o'$  and  $R_L'$  satisfy (29) simultaneously. They are

$$R_o' = R_L' = KR. \quad (30)$$

The equality of the input and output matching resistors could have been predicted from the form of (27) for  $G$ , which is completely symmetrical in  $R_o$  and  $R_L$ ; i.e. an interchange of  $R_o$  and  $R_L$ , whatever their values, does not alter the value of  $G$ . Thus, let us suppose that we determine  $R_o'$  and  $R_L'$  experimentally by trial and error, and assume that they are a unique pair. Interchanging them must leave  $G$  a maximum, hence  $R_o'$  equals  $R_L'$ .

An expression for  $G_{\max}$  may now be obtained by substituting (30) into (27). We find, noting that  $Z_{12}Z_{21}$  equals  $-R^2(K^2 - 1)$ ,

$$G_{\max} = \frac{4K^2 R^2 |Z_{21}|^2}{[R^2(K + 1)^2 - Z_{12}Z_{21}]^2} = \frac{|Z_{21}|^2}{R^2(K + 1)^2}. \quad (31)$$

Equation (31) expresses the maximum available gain as a function of

the diode parameters  $R$  and  $C_{\min}$ , and of the time variation of the diode capacitance, through the quantities  $C_0$  and  $C_1$ . For a given diode the first two quantities are assumed fixed, while the last two may be varied within limits set by their status as Fourier coefficients of a real, positive, periodic function of time. In the Appendix,  $G_{\max}$  is evaluated explicitly in terms of  $R$  and  $C_{\min}$  for the case that  $Z_c$  is given by (13). The result is

$$G_{\max} = \frac{f_2}{f_1} \frac{1}{(x + \sqrt{1 + x^2})^2}, \quad (32)$$

where  $\sqrt{1 + 1/x^2} = K$  as introduced in (29), and

$$x = \lambda \bar{\omega} C_{\min} R,$$

with  $\lambda$  a numerical factor depending upon  $C_0$  and  $C_1$ , and

$$\bar{\omega} = \sqrt{\omega_1 \omega_2} = \sqrt{s(b + s)}.$$

To simplify future analysis, we write

$$x = \lambda \frac{\tilde{f}}{f_c}, \quad (33)$$

where

$$\tilde{f} = \sqrt{f_1 f_2}$$

and

$$f_c = \frac{1}{2\pi R_s C_{\min}} = \text{a figure of merit for the diode.}$$

The expression for  $x$  in (33) is convenient for evaluating  $G_{\max}$  from (32). We shall first consider low-frequency operation, where  $\tilde{f}$  is very much less than  $f_c/\lambda$ . Then  $x$  is very much less than 1, and

$$G_{\max} \approx f_2/f_1.$$

As  $x$  increases,  $G_{\max}/(f_2/f_1)$  monotonically decreases from its asymptotic value of 1. This is shown graphically in Fig. 4. Since  $x = \lambda \tilde{f} 2\pi R_s C_{\min}$ , the best operation is obtained for minimum values of  $R_s$ ,  $C_{\min}$  and  $\lambda$ , or a maximum value of  $f_c/\lambda$ . In the Appendix it is shown that, for the type of operation under consideration, the minimum attainable value of  $\lambda$  is 5.83.

We next consider high-frequency operation, characterized by

$\bar{f} \gg f_c/\lambda$  or  $x \gg 1$ . It is then convenient to rewrite (32) in the following form:

$$G_{\max} = \frac{f_2}{f_1 x^2} \frac{1}{\left(1 + \sqrt{1 + \frac{1}{x^2}}\right)^2} = \frac{f_2}{f_1 x^2} \frac{1}{(1 + K)^2}. \quad (34)$$

As  $x$  approaches  $\infty$ , (34) becomes

$$\lim_{x \rightarrow \infty} G_{\max} \rightarrow G_{\lim} = \frac{f_2}{4 f_1 x^2} = \left(\frac{f_c}{2 \lambda f_1}\right)^2. \quad (35)$$

Since we would like to have  $G_{\lim}$  as large as possible, it is evident that  $f_c/\lambda$  should be large, or, correspondingly, that  $R_s$ ,  $C_{\min}$  and  $\lambda$  should be small, as was true for the low-frequency limit of operation.

Equation (35) indicates that, for a given input frequency  $f_1$ , the gain should approach a limiting value as  $f_2$  approaches  $\infty$ . This behavior is shown graphically in Fig. 5. It is noteworthy that  $G_{\lim}$  decreases with increasing  $f_1$ , and in particular that, for  $f_1 \geq f_c/2\lambda$ ,  $G_{\lim} \leq 1$ . This places a fundamental upper limit on the input frequency, if power gain is to be obtained.

The above results show how the maximum available gain of a diode amplifier is affected by parasitics. Of greater significance in characteriz-

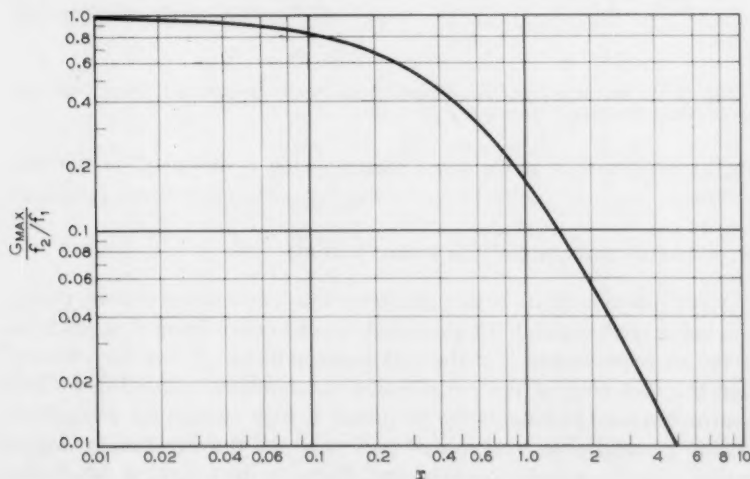


Fig. 4 — Ratio of MAG of a diode with parasites to the MAG of an ideal variable capacitance, plotted against the parameter  $x$ .



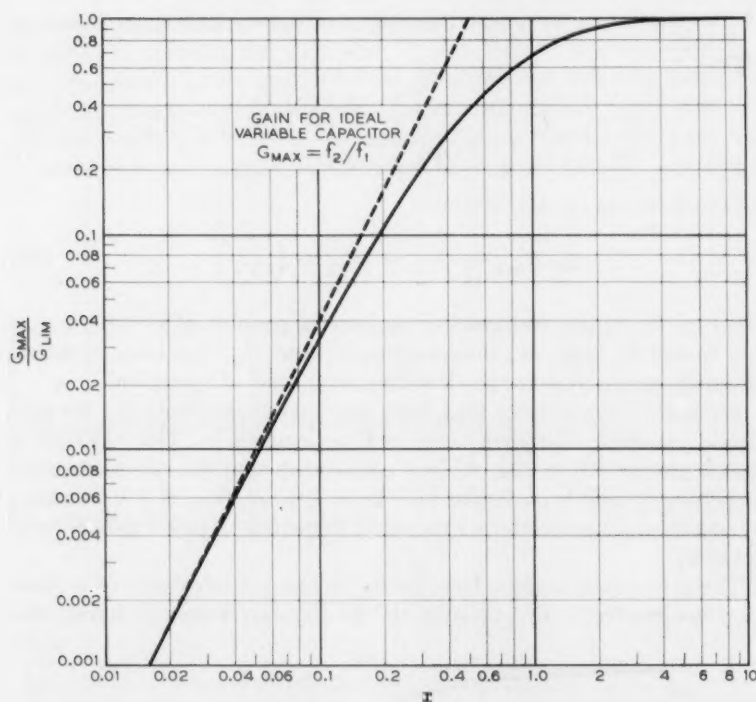


Fig. 5 — The ratio  $G_{max}/G_{lim}$  versus  $x$ , the input frequency  $f_1$  being kept constant while the output frequency  $f_2$  varies.

ing its performance is the noise figure, which is discussed in the next section.

#### VI. GENERAL EQUATIONS FOR NOISE FIGURE

A p-n junction diode is thought to contain two sources of noise power, one being shot noise at the p-n junction, the other being thermal noise in the series resistance  $R$  of the bulk semiconductor. It has been shown<sup>6</sup> that the shot noise of the p-n junction of a nonlinear-capacitance diode approaches zero so long as the frequency is high enough for recombination to be negligible, and not so high that the p-n junction no longer exhibits purely capacitive behavior. Hence in the following calculation of noise figure only the contribution of the thermal noise of  $R$  is considered.

The noise figure of an N-C diode frequency converter is calculated using the equivalent circuit of Fig. 3 and the assumptions of Section III, together with the additional assumption that the noise generators at the frequencies  $f_1$  and  $f_2$  are uncorrelated.

The noise figure is calculated in accordance with

$$F - 1 = \frac{\text{noise output originating in thermal noise of } R}{\text{noise output due to thermal noise at } 290^\circ\text{K in source resistance}} \quad (36)$$

Thus, as a "standard signal", one uses the thermal noise output of the source resistance, assumed to be at a temperature of  $290^\circ\text{K}$ . The noise output of the diode is assumed to arise from two components of the thermal noise of  $R$ . One of these, the thermal noise emf  $\varepsilon_{N1}$ , sets up a current of frequency  $f_1$  in the left-hand loop of Fig. 3, which, by the frequency-converting action of the diode, is partly converted into a current  $i_2$ , of frequency  $f_2$ ; this then passes into the right-hand loop and introduces noise power into the load. The other component,  $\varepsilon_{N2}$ , also causes a current  $i_2$ , of frequency  $f_2$ , to flow through the load. The noise power received by the load is determined by these two currents, which are assumed to be uncorrelated.

The noise power can be readily calculated from (19) and (20). The current  $i_2$  due to  $\varepsilon_{N1}$  is given by solving

$$\begin{bmatrix} i_1 \\ i_2 \end{bmatrix} = \frac{1}{D} \begin{bmatrix} Z_{22} + R + Z_L & -Z_{12} \\ -Z_{21} & Z_{11} + R + Z_G \end{bmatrix} \begin{bmatrix} \varepsilon_{N1} \\ 0 \end{bmatrix} \quad (37a)$$

Similarly, the current  $i_2$  due to  $\varepsilon_{N2}$  is obtained from

$$\begin{bmatrix} i_1 \\ i_2 \end{bmatrix} = \frac{1}{D} \begin{bmatrix} Z_{22} + R + Z_L & -Z_{12} \\ -Z_{21} & Z_{11} + R + Z_G \end{bmatrix} \begin{bmatrix} 0 \\ \varepsilon_{N2} \end{bmatrix} \quad (37b)$$

Solving these, we obtain

$$\varepsilon_{N1} \neq 0: \quad i_2 = -\frac{1}{D} Z_{21} \varepsilon_{N1}, \quad (38a)$$

$$\varepsilon_{N2} \neq 0: \quad i_2 = \frac{1}{D} (Z_{11} + R + Z_G) \varepsilon_{N2}. \quad (38b)$$

The noise power delivered to the load is then:

$$\langle i_2^2 \rangle R_L = \frac{4kTBRR_L}{|D|^2} (|Z_{11} + R + Z_o|^2 + |Z_{21}|^2), \quad (39)$$

in accordance with the assumption that the currents in (38) are uncorrelated. Following (36), the noise figure is given by

$$F - 1 = \frac{\langle i_2^2 \rangle R_L}{290kBG}, \quad (40)$$

where  $290kB$  is the available thermal noise of the source resistance and  $G$  is the gain of the network under the same conditions, defined by (23). The gain was calculated in Section V, with the result in (25), given here by

$$G = 4R_oR_L \frac{|Z_{21}|^2}{|D|^2}. \quad (41)$$

Combining this with (39) and (40), we obtain

$$F - 1 = \frac{R}{R_o} \frac{|Z_{11} + R + Z_o|^2 + |Z_{21}|^2}{|Z_{21}|^2} \frac{T}{290}. \quad (42)$$

The noise figure here depends upon the diode structure, through  $R$ ,  $Z_{11}$  and  $Z_{21}$ ; upon the beat frequency oscillator waveform and the operating frequencies, through  $Z_{11}$  and  $Z_{21}$ ; and upon the input termination, through  $Z_o$ . (Note that  $F$  is independent of the load impedance.) Even if all the other quantities are fixed, considerable variation in performance can be obtained by varying  $Z_o$ . In this presentation, the noise figure is calculated for the value of  $Z_o$  which gives maximum available gain, and for the value giving minimum noise figure.

The noise figure corresponding to the condition of maximum available gain is obtained by inserting the appropriate value of  $Z_o$  into (42). In Section V this was shown to be  $Z_o = KR - Z_{11}$ . Equation (42) then gives

$$F - 1 = \frac{1}{K} \frac{R^2(K+1)^2 + |Z_{21}|^2}{|Z_{21}|^2} \frac{T}{290}. \quad (43)$$

On the other hand, from (31) we have

$$G_{\max} = \frac{|Z_{21}|^2}{R^2(K+1)^2}.$$

Hence, (43) may be written

$$F - 1 = \frac{1}{K} \left( 1 + \frac{1}{G_{\max}} \right) \frac{T}{290}. \quad (44)$$

Before proceeding further, it is interesting to note that (44) can be obtained by a simple intuitive analysis, making use of (36) directly. We assume that the diode series resistance  $R$  generates noise emfs equal to  $\sqrt{4kTBR}$  at the two frequencies  $f_1$  and  $f_2$ . Due to the emf at frequency  $f_2$ , the load receives noise power proportional to  $R$ . The noise power generated at frequency  $f_1$  is also proportional to  $R$ ; it is converted to frequency  $f_2$  with a gain  $G$ , so that the load receives additional noise power proportional to  $GR$ , making the total noise power from the diode proportional to  $(G + 1)RT$ . This is to be compared with the noise received at the load due to a matching resistance at the input. This matching resistance  $R_G = KR$ , and the corresponding noise power received is proportional to  $290GKR$ . Hence, according to (36),

$$F - 1 = \frac{(G + 1)RT}{290GKR} = \frac{1}{K} \left( 1 + \frac{1}{G_{\max}} \right) \frac{T}{290}.$$

Equation (44) can be expressed in a more useful form by substituting an equivalent expression for  $K$ . From (34) and (35) it follows that

$$G_{\max} = G_{\lim} \frac{4}{(1 + K)^2}. \quad (45)$$

Hence

$$K = 2 \left( \frac{G_{\lim}}{G_{\max}} \right)^{1/2} - 1. \quad (46)$$

Substituting this into (44) gives

$$F = 1 + \frac{1}{2 \left( \frac{G_{\lim}}{G_{\max}} \right)^{1/2} - 1} \left( 1 + \frac{1}{G_{\max}} \right) \frac{T}{290}. \quad (47)$$

This is the noise figure corresponding to a matching input impedance. In using (47),  $G_{\max}$  and  $G_{\lim}$  may be determined for any set of operating conditions, with the help of (34) and (35). Two limiting expressions obtained from (47) are of interest:

$$G_{\max} \ll G_{\lim}: F \cong 1 + \frac{1}{2} \left( \frac{G_{\max}}{G_{\lim}} \right)^{1/2} \left( 1 + \frac{1}{G_{\max}} \right) \frac{T}{290}, \quad (48a)$$

$$G_{\max} \cong G_{\lim}: F \cong 1 + \left( 1 + \frac{1}{G_{\max}} \right) \frac{T}{290}. \quad (48b)$$

Hence, when  $G_{\max}$  is very much less than  $G_{\lim}$ ,  $F$  is not much greater than 1. When  $G_{\max}$  approaches  $G_{\lim}$ ,  $F$  becomes approximately equal to 2. Thus, even under the most unfavorable conditions, the theoretical

noise figure will not be much more than 3 db if there is a significant amount of gain.

The minimum noise figure may also be found from (42), and applying first the tuning condition  $jX_a = -Z_{11}$ , we obtain

$$F - 1 = \frac{R}{R_a} \frac{(R + R_a)^2 + |Z_{21}|^2}{|Z_{21}|^2} \frac{T}{290}. \quad (49)$$

The value of  $R_a$  making  $F$  a minimum can be found from (49) by the standard procedures of differential calculus. The appropriate value of  $R_a$ , represented by  $R_a''$ , is

$$R_a'' = (|Z_{21}|^2 + R^2)^{1/2}. \quad (50)$$

Here  $G_{\max}$  is, as before, the maximum available gain, obtained with the matching value of  $R_a$ . On comparing (31) and (45), one determines that

$$|Z_{21}|^2 = 4R^2 G_{\lim}. \quad (51)$$

Substituting (50) and (51) into (49) gives

$$\begin{aligned} F_{\min} &= 1 + \frac{(4G_{\lim} + 1)^{1/2} + 1}{2G_{\lim}} \frac{T}{290} \\ &\cong 1 + \frac{T}{290} \left( \frac{1}{\sqrt{G_{\lim}}} + \frac{1}{2G_{\lim}} + \dots \right). \end{aligned} \quad (52)$$

The approximate form is valid when  $G_{\lim} \gg 1$ . Equation (52) indicates that a noise figure of close to zero db is theoretically attainable.

It is also important to determine the maximum gain  $G_N$  attainable under the conditions leading to minimum noise figure, as  $G_N$  may be needed to calculate the over-all noise figure of a system using a diode preamplifier. To obtain  $G_N$ , we substitute into (27) the value  $R_a = R_a''$  given by (50), together with the value of  $R_L$  that makes  $G$  a maximum. This quantity, represented by  $R_L''$ , is found from (29). In the present case it is:

$$R_L'' = \frac{R^2 K^2 + R R_a''}{R + R_a''}. \quad (53)$$

Substituting (53) and (50) into (27) gives  $G_N$ . Making use of the definition  $K = \sqrt{1 - Z_{12}Z_{21}/R^2}$  and  $|Z_{21}|^2 = 4R^2 G_{\lim}$  given in (51), we find

$$G_N = \frac{4}{1 + R/R_a''} \frac{G_{\lim}}{R_a''/R + K^2}. \quad (54)$$

Using the relation  $K = 2(G_{lim}/G_{max})^{1/2} - 1$  given in (46), equation (50) and the assumption  $G_{lim} \gg 1$ , we obtain the approximate expression:

$$G_N \cong \left\{ \frac{4G_{lim}}{2\sqrt{G_{lim}} + \left[ 2\left(\frac{G_{lim}}{G_{max}}\right)^{1/2} - 1 \right]^2} \right\} \left( \frac{1}{1 + \frac{1}{2\sqrt{G_{lim}}}} \right). \quad (55)$$

We now consider two special cases. For  $G_{max}$  sufficiently small,

$$\left(\frac{G_{lim}}{G_{max}}\right)^{1/2} \gg 1, \quad \text{and} \quad \frac{G_{lim}}{G_{max}} \gg \sqrt{G_{lim}}.$$

Therefore

$$G_N \cong G_{max}. \quad (56a)$$

For  $G_{max} \cong G_{lim}$

$$G_N \cong 2\sqrt{G_{lim}}. \quad (56b)$$

The equations obtained for the noise figure have been evaluated for certain receiver systems, and the results are given in Table I. The examples include, respectively, an N-C diode up-converter followed by (1) a travelling-wave tube amplifier operating at 3 kmc with a noise figure of 4.5 db; (2) a point-contact superheterodyne converter plus IF amplifier stage operating at an input frequency of 10 kmc with a noise figure of 7.0 db; (3) a system similar to (2) operating at an input frequency of 55 kmc with a noise figure of 10 db (a value that may seem optimistic but is probably attainable by combining the best point-contact diodes with the best IF amplifier). Values for over-all noise figures of each system are obtained from equations (47) and (52), and compared; these corre-

TABLE I—NOISE FIGURES FOR CERTAIN RECEIVER SYSTEMS

$$f_c = 160 \text{ kmc} \quad \lambda = 6.0 \quad T = 290^\circ\text{K}$$

Receiver System	Output Frequency, $f_2$ (kmc)	Noise Figure, $F_1$ (db)	Over-all Noise Figure of System, $F_{system}$ (db)			
			Input Frequency, $f_1 = 500 \text{ mc}$		Input Frequency, $f_1 = 1000 \text{ mc}$	
			$F_A$	$F_B$	$F_A$	$F_B$
(1)	3	4.5	1.40	1.40	2.51	2.48
(2)	10	7.0	1.24	1.20	2.15	2.20
(3)	55	10.0	1.20	1.14	1.94	2.10

$F_A$  = noise figure of system corresponding to maximum available gain for diode.

$F_B$  = noise figure of system corresponding to minimum noise figure for diode.

spond to the conditions of maximum available gain and minimum noise figure, respectively. The difference between them is not significant in most cases. The calculations were made assuming  $\lambda = 6.0$ ,  $T = 290^\circ\text{K}$  and  $f_c = 160$  kmc, the latter figure being obtainable with recently produced diffused silicon diodes.

#### VII. CONCLUSIONS

Equations for the maximum available gain (MAG), and the noise figure have been obtained for a nonlinear capacitance diode containing parasitics. Because of the series resistance and minimum capacitance, the MAG reaches a limiting value as the output frequency increases without limit. The thermal noise of the series resistance is also responsible for noise output of the diode. In contrast, a perfect variable capacitance would have its MAG always equal to the ratio of output frequency to input frequency, and it would generate no noise.

The results obtained depend upon the diode cutoff frequency  $f_c$ , and upon the operating conditions through the parameter  $\lambda$ . Values of  $f_c$  up to 200 kmc have been obtained with recently prepared diffused diodes, hence the use of the value  $f_c = 160$  kmc is not overly optimistic.

#### VIII. ACKNOWLEDGMENTS

The author wishes to express his appreciation to A. Uhler, Jr., for many helpful discussions, and to the U. S. Army Signal Corps, for its support of the microwave diode program, of which this work was a part.

#### APPENDIX

##### *Derivation of the Equation for Maximum Available Gain*

In Section V the maximum available gain was obtained in the following form, from (31):

$$G_{\max} = \frac{|Z_{21}|^2}{R^2(K+1)^2}, \quad (57)$$

where  $K = \sqrt{1 - Z_{12}Z_{21}/R^2}$ . It is convenient to define the quantity  $x$  such that  $K = \sqrt{1 + 1/x^2}$ . Hence

$$x^2 = -\frac{R^2}{Z_{12}Z_{21}} \quad (58)$$

After (58) has been solved for  $R^2$ , (57) can be written

$$G_{\max} = \frac{|Z_{21}|^2}{-Z_{12}Z_{21}} \frac{1}{x^2(K+1)^2} = \frac{|Z_{21}|^2}{-Z_{12}Z_{21}} \frac{1}{(x + \sqrt{x^2 + 1})^2}. \quad (59)$$



The impedance matrix elements, obtained from (13), are

$$\begin{aligned} Z_{12} &= j \frac{1 + \xi^2}{1 - \xi^2} \frac{\xi}{b + s} \frac{1}{C_0}, \\ Z_{21} &= j \frac{1 + \xi^2}{1 - \xi^2} \frac{\xi}{s} \frac{1}{C_0}. \end{aligned} \quad (60)$$

Then

$$G_{\max} = \frac{b + s}{s} \frac{1}{(x + \sqrt{x^2 + 1})^2} = \frac{\omega_2}{\omega_1} \frac{1}{(x + \sqrt{x^2 + 1})^2}, \quad (61)$$

where

$$x = \frac{1 - \xi^2}{\xi(1 + \xi^2)} \bar{\omega} R C_0. \quad (62)$$

The quantity  $G_{\max}$  in (61) is the gain obtained with matching terminations. It depends upon the diode parameters  $R_s$  and  $C_{\min}$ , and upon the operating conditions through the operating frequencies and the Fourier amplitudes  $C_0$  and  $C_1$ . The diode parameters are fixed for a given device, of course, but  $C_0$  and  $C_1$  may be varied to further maximize  $G$ . To demonstrate this, we first express the variables  $C_0$  and  $C_1$  in terms of  $C_{\max}$  and  $C_{\min}$ , where  $C_{\min}$  is a constant, namely, the lowest value of capacitance obtainable. [From (69), below, it can be seen that, for any given value of  $C_{\max}$ , the gain increases with decreasing  $C_{\min}$ ]. We therefore need consider only  $C_{\max}$  to be variable. For convenience, in the calculation of maximum gain, below, the variable  $\mu$  is used, where  $\mu^2 = C_{\max}/C_{\min}$ .

The process of maximizing  $G$  is equivalent to minimizing  $x$ . To accomplish this we start with (62) and express the quantities  $\xi$  and  $C_0$  in terms of  $\mu$  and  $C_{\min}$ . From (12a) we have

$$\xi \equiv \frac{C_1}{C_0} = \frac{\xi}{1 + \xi^2}. \quad (63)$$

Since  $C(t)$  is a sine wave, it follows that

$$C_0 - C_{\min} = 2C_1. \quad (64)$$

Equations (63) and (64) may be used to eliminate  $C_1$ , obtaining

$$C_0 = \frac{1 + \xi^2}{(1 - \xi^2)^2} C_{\min}. \quad (65)$$

Next, we express  $\xi$  in terms of  $\mu$ . As  $C(t)$  is sinusoidal, it also follows that

$$C_{\max} = C_0 + 2C_1. \quad (66)$$

Combining (64), (65) and (66), we obtain

$$C_{\max} = \left( \frac{1 + \xi^2}{1 - \xi^2} \right)^2 C_{\min}, \quad (67a)$$

or

$$\mu^2 = \frac{C_{\max}}{C_{\min}} = \left( \frac{1 + \xi}{1 - \xi} \right)^2. \quad (67b)$$

Solving for  $\xi$ , we obtain

$$\xi = \frac{\mu - 1}{\mu + 1}. \quad (68)$$

Finally, combining (62), (65) and (68), we get

$$x = \frac{\mu(\mu + 1)}{\mu - 1} \bar{\omega} RC_{\min}, \quad (69)$$

or

$$\lambda = \frac{\mu(\mu + 1)}{\mu - 1}.$$

The minimum value of  $\lambda$  is found to be

$$\lambda = (1 + \sqrt{2})^2 = 5.83 \quad (70)$$

for

$$\mu = 1 + \sqrt{2}.$$

The corresponding value of  $C_{\max}/C_{\min}$  is

$$\frac{C_{\max}}{C_{\min}} = \mu^2 = (1 + \sqrt{2})^2 = 5.83. \quad (71)$$

Thus, the maximum gain and minimum noise figure are obtained for a variation of capacitance over a 5.8-to-1 ratio. In practice, however, the dynamic range of capacitance may be no greater than 3 to 1. This corresponds to  $\mu = \sqrt{3}$ , and  $\lambda = 6.5$ . Hence, for this limited range the performance would still not be far from optimum.

#### REFERENCES

1. Manley, J. M. and Rowe, H. E., Some General Properties of Nonlinear Elements, Part I, Proc. I.R.E., **44**, July 1956, pp. 904-913.
2. Edwards, C. F., Frequency Conversion by Means of a Nonlinear Admittance, B.S.T.J., **35**, November 1956, pp. 1403-1416.
3. Macpherson, A. C., An Analysis of the Diode Mixer Consisting of Nonlinear Capacitance and Conductance and Ohmic Spreading Resistance, N.R.L. Report 4667.
4. Hartley, R. V. L., Oscillations in Systems with Nonlinear Reactance, B.S.T.J., **15**, July 1936, pp. 424-440.
5. Bakanowski, A. E., Cranna, N. G., and Uhler, A., Jr., I.R.E.-A.I.E.E. Semiconductor Device Research Conference, Boulder, Colo., July 1957.
6. Uhler, A., Jr., this issue, pp. 951-988.

# Nonstationary Velocity Estimation

By T. M. BURFORD

(Manuscript received January 3, 1958)

A nonstationary noise may frequently be approximated by the product of a stationary noise and a deterministic function of time. From observations of the sum of such a nonstationary noise and a linear signal, an estimate of the rate of change of the signal is found. More exactly, a random function,  $x(t)$ , is assumed to be one of the following:

$$a + bt + g(t)n(t),$$

$$a + bt + g(t) \int_{-\infty}^t h(t - \tau)n(\tau) d\tau, \quad \text{or}$$

$$a + bt + \int_{-\infty}^t h(t - \tau)g(\tau)n(\tau) d\tau,$$

where  $a$  and  $b$  are constants,  $h(t)$  is the impulse response of a lumped parameter filter,  $n(t)$  is white noise and  $g(t)$  is a nonzero deterministic function. A least squares estimate of  $b$  is found as a linear operation on a finite sample of  $x(t)$ .

## I. WHITE NOISE CASE

A well-known estimation problem is that of forming a mean square estimate of the constant,  $b$ , in the random function  $x(t) = a + bt + n(t)$ , where  $n(t)$  is white noise and  $a$  and  $b$  are unknown constants. The estimate of  $b$  is required to be the linear operation

$$\hat{b} = \int_{t-T}^t K(t - \tau)\dot{x}(\tau) d\tau,$$

where  $K(z)$  vanishes outside  $(0, T)$  and  $\hat{b}$  is to equal  $b$  in the absence of noise. The solution is known<sup>1,2</sup> to be

$$\begin{aligned} K(z) &= \frac{6}{T^3} (T - 2z); & 0 \leq z \leq T \\ &= 0; & \text{elsewhere.} \end{aligned} \quad (1)$$

The above problem will be generalized here to include one type of non-stationary noise.

Let

$$x(t) = a + bt + g(t)n(t), \quad (2)$$

where  $a$  and  $b$  are unknown constants,\*  $n(t)$  is white noise of unit spectral density and  $g(t)$  is a nonzero, deterministic function. Formally, it follows that

$$E[g(t)n(t)g(t')n(t')] = g(t)g(t')\delta(t - t'). \quad (3)$$

We wish an estimate of  $b$  in the form

$$\hat{b} = \int_{t-T}^t K(t, t - \tau)x(\tau) d\tau, \quad (4)$$

where  $K(t, z)$  vanishes for  $z$  outside  $(0, T)$ . A constraint is that, in the absence of noise, (4) should give  $b$  exactly. Therefore

$$b = \int_{t-T}^t K(t, t - \tau)(a + b\tau) d\tau,$$

which implies, with a change of variable, that

$$\int_0^T K(t, z) dz = 0, \quad (5)$$

and

$$\int_0^T zK(t, z) dz = -1. \quad (6)$$

Using (3), (5) and (6) and again changing variables we find that the expected error is now

$$E(\hat{b} - b)^2 = \int_0^T K^2(t, z)g^2(t - z) dz. \quad (7)$$

The minimization of (7) is easily done by the usual variational technique, using (5) and (6) as isoperimetric constraints. The variation gives

$$2g^2(t - z)K(t, z) + \lambda + \mu z = 0.$$

Therefore

$$K(t, z) = \frac{-\lambda - \mu z}{2g^2(t - z)}, \quad (8)$$

\* The linear  $a + bt$  is used here for simplicity. The coefficients of a general polynomial may be estimated in a similar way.

where  $\lambda$  and  $\mu$  are undetermined multipliers to be fixed by (5) and (6). From (5),

$$\int_0^T K(t, z) dz = -\frac{\lambda}{2} \int_0^T \frac{dz}{g^2(t-z)} - \frac{\mu}{2} \int_0^T \frac{z dz}{g^2(t-z)} = 0,$$

and, from (6),

$$\int_0^T z K(t, z) dz = -\frac{\lambda}{2} \int_0^T \frac{z dz}{g^2(t, z)} - \frac{\mu}{2} \int_0^T \frac{z^2 dz}{g^2(t-z)} = -1.$$

Solving the preceding equations for  $\lambda$  and  $\mu$  and substituting into (8) gives

$$\begin{aligned} K(t, z) &= \frac{A_1 - zA_0}{(A_0A_2 - A_1^2)g^2(t-z)}; & 0 \leq z \leq T \\ &= 0; & \text{elsewhere,} \end{aligned} \quad (9)$$

with

$$A_i(t) = \int_0^T \frac{z^i dz}{g^2(t-z)},$$

which gives the minimized error

$$E(b - \hat{b})^2 = \frac{A_0}{A_0A_2 - A_1^2}.$$

The denominator of  $K(t, z)$  does not vanish, since  $g(t-z)$  is assumed nonzero, and

$$\int_0^T \frac{\left(z - \frac{A_1}{A_0}\right)^2}{g^2(t-z)} dz > 0,$$

$$A_2 - \frac{A_1^2}{A_0} > 0,$$

$$A_0A_2 - A_1^2 > 0.$$

In general, the  $K(t, z)$  found here defines a time variable filter over a finite time interval. However, if  $g$  is a constant, (9) reduces to (1). Another interesting special case is that in which  $g$  is assumed to be of exponential form, which implies that

$$g(t-z) = g(t)g(-z),$$

and therefore

$$A_j = \frac{1}{g^2(t)} \int_0^T \frac{z^j dz}{g^2(-z)} = \frac{B_j}{g^2(t)}.$$

Substitution into (9) gives

$$K(z) = \frac{B_1 - zB_0}{(B_0B_2 - B_1^2)g^2(-z)}; \quad 0 \leq z \leq T$$

$$= 0; \quad \text{elsewhere.}$$

Now, however, the  $B_j$ 's are constants instead of functions of  $t$ , as the  $A_j$ 's were. For an exponential  $g$ , therefore, the filter given by (9) is time-invariant.

The function  $g(t)$  is not necessarily continuous. For example, let

$$g(x) = g_1; \quad x < \beta$$

$$= g_2; \quad x > \beta.$$

Then

$$A_j = \frac{1}{g_2^2} \frac{T^{j+1}}{j+1}; \quad \beta < t - T,$$

$$= \frac{1}{g_1^2} \frac{T^{j+1}}{j+1} + \left( \frac{1}{g_2^2} - \frac{1}{g_1^2} \right) \frac{\beta^{j+1}}{j+1}; \quad t - T < \beta < t,$$

$$= \frac{1}{g_1^2} \frac{T^{j+1}}{j+1}; \quad \beta > t,$$

which implies that  $K(t, z)$  is linear but has a discontinuity in value and slope at  $z = \beta$ .

Many applications involve a linear  $g(t)$ . For this case, it is possible to plot a one-parameter family of curves which completely describe  $K(t, z)$ . If  $g(t)$  equals  $\alpha + \beta t$ , we define  $Q = -(\alpha + \beta t)/\beta t$ . Then, by a change of variable,

$$A_j = \frac{T^{j-1}}{\beta^2} \int_0^1 \frac{s^j ds}{(Q + s)^2} = \frac{T^{j-1}}{\beta^2} C_j,$$

and substitution into (9) gives

$$T^2 K(t, z) = \frac{C_1 - C_0 \left( \frac{z}{T} \right)}{(C_0 C_2 - C_1^2) \left[ Q + \left( \frac{z}{T} \right) \right]^2}.$$

All of the time dependence is now included in  $Q$ . Fig. 1 shows  $T^2 K(t, z)$  plotted against  $z/T$  for several values of  $Q$ . A positive value of  $Q$  implies that  $|g(t)|$  is decreasing with time and therefore that recent data are superior. Values of  $Q$  in  $(-1, 0)$  are not permitted, since such a  $Q$  would imply that  $g(t)$  vanished somewhere in  $(t - T, t)$ . If  $g(t)$  is constant,  $Q$  is infinite and (1) applies.

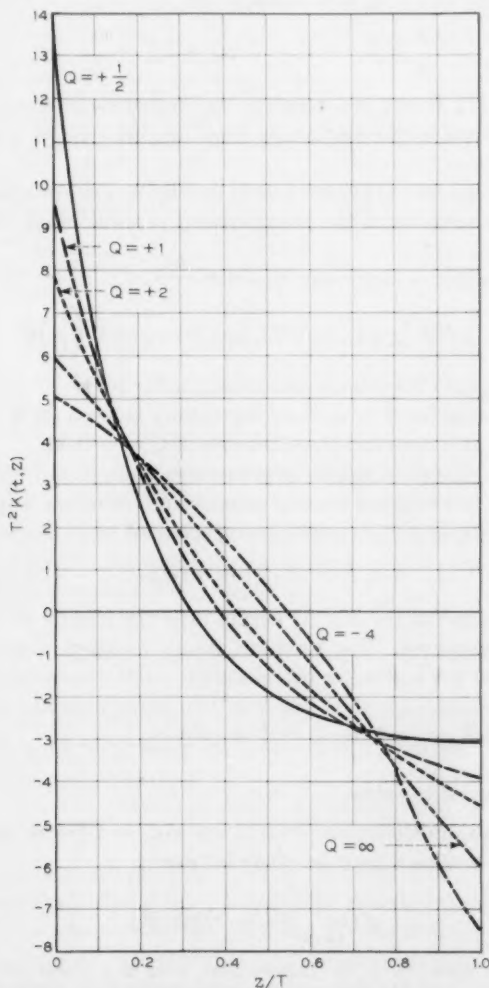


Fig. 1 — Weighting functions,  $K(t, z)$ , for linear  $g(t)$ .



The  $K(t, z)$  just found for the linear  $g(t)$  case may be substituted into (7) to give the variance of  $\hat{b}$  as a function of  $Q$ :

$$\frac{T}{\beta^2} E(\hat{b} - b)^2 = \left[ 1 - \left( \log \frac{Q+1}{Q} \right)^2 Q(Q+1) \right]^{-1}. \quad (10)$$

An interesting comparison may be made with the variance resulting from using  $K(z)$  of (1) in (7), which gives

$$\frac{T}{\beta^2} E(\hat{b} - b)^2 = 3(2Q+1)^2 + \frac{9}{5}. \quad (11)$$

Equation (11) shows the error to be expected from using a  $K(z)$ , which is optimum in the stationary case, on this type of nonstationary data.

Equations (10) and (11) are plotted in Fig. 2. The difference between the curves is a measure of the improvement possible\* with time-variable smoothing.

As  $Q$  approaches  $\infty$ , (10) may be written

$$\frac{T}{\beta^2} E(\hat{b} - b)^2 = 3(2Q+1)^2 - \frac{7}{5} + O\left(\frac{1}{Q}\right);$$

therefore (10) and (11) will asymptotically differ by  $16/5$ .

Fig. 2 is plotted for  $Q > 0$ ; however, it may be used for  $Q < -1$  since both (10) and (11) are even on either side of  $Q = -0.50$ .

Fig. 1 also suggests a simple approximate realization for  $K(t, z)$ . The several curves have approximately common intersections near  $z/T = 0.2$  and  $0.8$ . Therefore,  $K(t, z)$  might be represented as

$$K(t, z) = K_1(z) + f(Q)K_2(z),$$

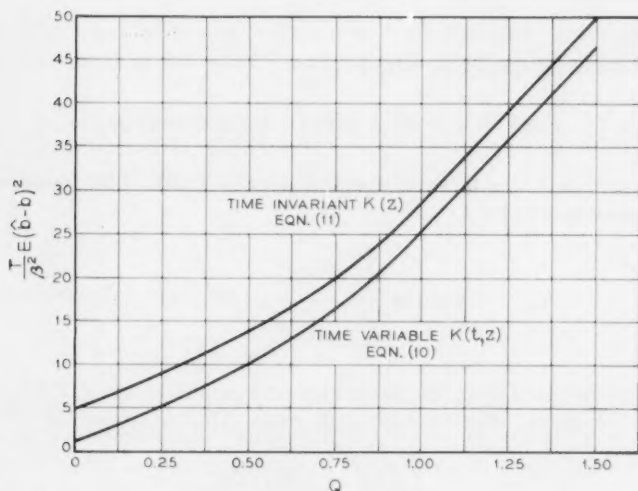
where  $K_1(z)$  is one of the  $K(t, z)$  curves near the middle of the range of  $Q$ 's to be considered. The function  $K_2(z)$  vanishes near the points  $z/T = 0.2$  and  $0.8$  and takes on relatively small values elsewhere. This approximate realization thus involves two time-invariant filters and a multiplier which depends on  $Q$  and thereby on  $t$ .

## II. PRE-FILTERING OF NOISE

Filtering and multiplication by  $g(t)$  are not, in general, commutative operations, so a choice must be made between

$$g(t) \int_{-\infty}^t h(t-\tau)n(\tau) d\tau \quad (12)$$

\* It has been shown by E. N. Gilbert that, even if a linear  $g(t)$  vanishes in the smoothing interval, the best possible estimate has variance  $\beta^2/T$  and, therefore, perfect estimation is not possible.

Fig. 2 — Variance for linear  $g(t)$ .

and

$$\int_{-\infty}^t h(t - \tau) g(\tau) n(\tau) d\tau \quad (13)$$

as noise functions to be added to  $a + bt$ . In certain cases, the representations (12) and (13) are virtually equivalent in the sense that, given  $h(t - \tau)$ , there exists an  $\tilde{h}(t - \tau)$  such that

$$g(t) \int_{-\infty}^t h(t - \tau) n(\tau) d\tau = \int_{-\infty}^t \tilde{h}(t - \tau) g(\tau) n(\tau) d\tau.$$

From the point-wise uncorrelation of  $n(\tau)$ , the preceding equation, if it is true at all, must be true for all values of  $\tau$ . Therefore

$$\tilde{h}(t - \tau) = \frac{g(t)}{g(\tau)} h(t - \tau),$$

which implies that  $g(t)/g(\tau)$  must be a function of  $(t - \tau)$ . The only nonconstant  $g(t)$  satisfying this condition is the exponential. If  $g(t)$  is an exponential, the choice between (12) and (13) is arbitrary. In general, however, the choice is not arbitrary and depends on physical considerations. The forms (12) and (13) will now be treated as Cases 1 and 2.

## Case 1

The observed quantity,  $x(t)$ , is

$$x(t) = a + bt + g(t) \int_{-\infty}^t h(t - \tau) n(\tau) d\tau,$$

where  $n(\tau)$  is white noise of spectral density unity. The transform of  $h(t)$  is assumed to be

$$T[h(t)] = \frac{\sum_0^m \beta_j (i\omega)^j}{\sum_0^n \alpha_j (i\omega)^j}; \quad m < n.$$

It is also assumed that the numerator and denominator of  $T[h(t)]$  have neither common factors nor multiple roots. The covariance of

$$\int_{-\infty}^t h(t - \tau) n(\tau) d\tau$$

is defined to be  $\rho(\tau)$ . A particular  $K(t, z)$  is sought such that

$$\hat{b} = \int_{t-T}^t K(t, t - \tau) x(\tau) d\tau$$

minimizes

$$E(\hat{b} - b)^2 = \int_0^T dz g(t - z) K(t, z) \int_0^T dz' g(t - z') K(t, z') \rho(z - z'). \quad (14)$$

In obtaining (14), it was assumed that, in the absence of noise,  $\hat{b}$  equals  $b$ , or

$$\int_0^T K(t, z) dz = 0 \quad \int_0^T z K(t, z) dz = -1. \quad (15)$$

Using the constraints of (15), the variation of (14) gives the integral equation\*

$$\int_0^T dz' K(t, z') g(t - z') \rho(z - z') = \frac{\lambda + \mu z}{g(t - z)}. \quad (16)$$

From the form of  $T[h(t)]$ , it is evident that

$$\rho(z - z') = \frac{1}{2\pi} \int_{-\infty}^{\infty} \frac{M(\omega^2)}{N(\omega^2)} e^{i\omega(z-z')} d\omega,$$

\* A similar equation, of somewhat different origin, has been considered by Ule.<sup>3</sup>

where  $M(\omega^2)$  and  $N(\omega^2)$  are polynomials in  $\omega^2$  of degrees  $m$  and  $n$ . Now form<sup>4</sup> the operation  $N(-d^2/dz^2)$  and apply it to (16), giving

$$\frac{1}{2\pi} \int_0^T dz' K(t, z') g(t - z') \int_{-\infty}^{\infty} M(\omega^2) \epsilon^{i\omega(z-z')} d\omega = N\left(-\frac{d^2}{dz^2}\right) \frac{\lambda + \mu z}{g(t - z)},$$

which is, formally, the same as

$$\frac{1}{2\pi} M\left(-\frac{d^2}{dz^2}\right) \int_0^T dz' K(t, z') g(t - z') \int_{-\infty}^{\infty} \epsilon^{i\omega(z-z')} d\omega = N\left(-\frac{d^2}{dz^2}\right) \frac{\lambda + \mu z}{g(t - z)},$$

or, the differential equation

$$M\left(-\frac{d^2}{dz^2}\right) K(t, z) g(t - z) = N\left(-\frac{d^2}{dz^2}\right) \frac{\lambda + \mu z}{g(t - z)}. \quad (17)$$

The general bounded solution of (17) will not necessarily satisfy (16), however. As is well known,<sup>2</sup> singularity functions up to order  $n - m - 1$  should be added at the end points of the interval in order to satisfy the boundary conditions of the integral equation (16).

Therefore, let

$$\begin{aligned} K(t, z) g(t - z) = & \sum_0^{2m-1} a_j \epsilon^{m_j z} + \int_0^T k(z - x) N\left(-\frac{d^2}{dx^2}\right) \left(\frac{\lambda + \mu x}{g(t - x)}\right) dx \\ & + \sum_0^{n-m-1} b_j \delta^{(j)}(z) + \sum_0^{n-m-1} c_j \delta^{(j)}(z - T), \end{aligned} \quad (18)$$

where  $\delta^{(0)}$  is the Dirac delta function,  $\delta^{(1)}$  its derivative, etc. The function  $k(z - x)$  is the Green's function associated with  $M(-d^2/dz^2)$  and the  $2m$  constants  $m_j$  are the roots of  $M(-X^2)$ . The  $a_j$ ,  $b_j$  and  $c_j$  comprise  $2n$  undetermined constants. They may be determined by substituting (18) into the integral equation (16) and requiring an identity in the  $2n$  exponentials of  $\rho$ . For example, assume  $h(x) = \epsilon^{-\alpha x}$ , which implies that

$$\frac{M(\omega^2)}{N(\omega^2)} = \frac{1}{a^2 + \omega^2}.$$

Then

$$K(t, z) g(t - z) = \left(a^2 - \frac{d^2}{dz^2}\right) \frac{\lambda + \mu z}{g(t - z)} + b_0 \delta(z) + c_0 \delta(z - T),$$

and substitution into (16) gives the following equations for  $b_0$  and  $c_0$ :

$$b_0 = \left(a - \frac{d}{dz}\right) \frac{\lambda + \mu z}{g(t - z)} \Big|_{z=0} \quad c_0 = \left(a + \frac{d}{dz}\right) \frac{\lambda + \mu z}{g(t - z)} \Big|_{z=T}.$$

Except for evaluating  $\lambda$  and  $\mu$  from (15), the solution is

$$K(t, z) =$$

$$\frac{1}{g(t-z)} \left[ a^2 - \frac{d^2}{dz^2} + \delta(z) \left( a - \frac{d}{dz} \right) + \delta(z-T) \left( a + \frac{d}{dz} \right) \right] \frac{\lambda + \mu z}{g(t-z)}.$$

### Case 2

The observed quantity  $x(t)$  now is

$$x(t) = a + bt + \int_{-\infty}^t h(t-\tau)g(\tau)n(\tau) d\tau.$$

We define  $\hat{b}$ ,  $K(t, z)$  and  $h(t-\tau)$  as in Case 1 and again require that in the absence of noise,  $\hat{b}$  equal  $b$ , or that the constraints (15) hold. These assumptions lead to the following integral equation:

$$\int_0^T dz' K(t, z') \Phi(t-z, t-z') = \lambda + \mu z,$$

where

$$\Phi(t-z, t-z') = \int_0^\infty h(y)h(y+z'-z)g^2(t-z'-y) dy.$$

Instead of dealing directly with the integral equation, we first rewrite  $x(t)$  as

$$x(t) = \int_{-\infty}^t h(t-\tau)[\beta + \gamma\tau + g(\tau)n(\tau)] d\tau, \quad (19)$$

where

$$\gamma = \frac{\alpha_0 b}{\beta_0},$$

and

$$\beta = \frac{\alpha_0 a}{\beta_0} + \frac{b}{\beta_0} \left( \alpha_1 - \frac{\beta_1 \alpha_0}{\beta_0} \right),$$

since it is easily shown that

$$\int_0^\infty h(x) dx = \frac{\beta_0}{\alpha_0},$$

and

$$\int_0^\infty xh(x) dx = \frac{\beta_0 \alpha_1}{\alpha_0^2} - \frac{\beta_1}{\alpha_0},$$

from the assumed form of  $T[h(t)]$ , and that

$$\int_{-\infty}^t h(t - \tau)(\beta + \gamma\tau) d\tau =$$

$$\beta \int_0^{\infty} h(x) dx + \gamma t \int_0^{\infty} h(x) dx - \gamma \int_0^{\infty} xh(x) dx = a + bt$$

when the values of  $\beta$  and  $\gamma$  are substituted from (19).

A function  $y(t)$  is now defined as

$$y(t) = \beta + \gamma t + g(t)n(t)$$

and a function  $\tilde{K}(t, z)$  is defined as the convolution of  $K(t, z)$  and  $h(z)$ , so that (14) is replaced by

$$\dot{b} = \int_{-\infty}^t \tilde{K}(t, t - \tau)y(\tau) d\tau.$$

The function  $y(t)$  is similar to  $x(t)$  as defined in (2). Therefore,  $\tilde{K}(t, z)$  may be found in a manner analogous to that used in the case in which the noise was not pre-filtered. Recalling that  $K(t, z)$  is required to vanish outside  $(0, T)$ , we may define  $\tilde{K}(t, z)$  more exactly by

$$\begin{aligned}\tilde{K}(t, z) &= \int_0^z dv K(t, v)h(z - v); & 0 < z < T \\ &= \int_0^T dv K(t, v)h(z - v); & z > T \\ &= 0; & z < 0,\end{aligned}\tag{20}$$

or the equivalent:

$$\begin{aligned}\sum_0^n \alpha_j \frac{d^j}{dz^j} \tilde{K}(t, z) &= \sum_0^m \beta_j \frac{d^j}{dz^j} K(t, z); & 0 < z < T \\ &= 0; & z > T, \quad z < 0.\end{aligned}\tag{21}$$

Since  $\tilde{K}(t, z)$  may be discontinuous at  $z = 0$  and  $T$ , these points have been excluded. While  $K(t, z)$  is constrained by (15), it follows that  $\tilde{K}(t, z)$  must satisfy

$$\begin{aligned}\int_0^{\infty} \tilde{K}(t, z) dz &= 0 \\ \int_0^{\infty} z \tilde{K}(t, z) dz &= -\frac{\beta_0}{\alpha_0}.\end{aligned}\tag{22}$$

The variance to be minimized is now

$$E(b - \hat{b})^2 = \int_0^\infty \bar{K}^2(t, z) g^2(t - z) dz.$$

From (21),

$$\bar{K}(t, z) = \sum_0^{n-1} s_j \epsilon^{\xi_j z}; \quad z > T, \quad (23)$$

where the  $s_j$  are presently unknown but will be selected to minimize  $E(\hat{b} - b)^2$  and the  $\xi_j$  are known in terms of the  $\alpha_j$ . A variation of

$$\int_0^\infty [\bar{K}^2(t, z) g^2(t - z) + \lambda \bar{K}(t, z) + \mu z \bar{K}(t, z)] dz$$

gives

$$2\bar{K}(t, z) g^2(t - z) + \lambda + \mu z = 0; \quad 0 < z < T \quad (24)$$

and a set of  $n$  equations defining the  $s_j$ :

$$2 \sum_{j=0}^{n-1} s_j \int_T^\infty \epsilon^{(\xi_j + \xi_k)z} g^2(t - z) dz + \int_T^\infty (\lambda + \mu z) \epsilon^{\xi_k z} dz = 0, \quad (25)$$

where

$$k = 0, 1, \dots, n-1.$$

Equations (23) and (24), together with the constraints (22), define  $\bar{K}(t, z)$  completely. The function  $K(t, z)$  may now be found from (21).

From the discontinuities in  $\bar{K}(t, z)$  at  $z = 0$  and  $T$ , delta functions of order as high as  $n - m - 1$  may be expected in  $K(t, z)$  at  $z = 0$  and  $T$ . For example, if  $h(x)$  equals  $\epsilon^{-ax}$ , (21) becomes

$$\begin{aligned} \frac{d\bar{K}(t, z)}{dz} + a\bar{K}(t, z) &= K(t, z); \quad 0 < z < T \\ &= 0; \quad z < 0, \quad z > T \end{aligned}$$

and

$$\bar{K}(t, z) = s \epsilon^{-az}; \quad z > T.$$

From (24),

$$\bar{K}(t, z) = \frac{-\lambda - \mu z}{2g^2(t - z)}; \quad 0 < z < T$$

and, from (25),

$$2s \int_T^\infty \epsilon^{-2az} g^2(t - z) dz + \int_T^\infty (\lambda + \mu z) \epsilon^{-az} dz = 0,$$



which defines  $s$  and therefore  $\tilde{K}(t, z)$  for  $z > T$ . Except for evaluating  $\lambda$  and  $\mu$  from (15), the solution is

$$K(t, z) = \left[ \delta(z) - \delta(z - T) + a + \frac{d}{dz} \right] \left( \frac{\lambda + \mu z}{g^2(t - z)} \right) + \frac{\lambda + \mu \left( T + \frac{1}{a} \right)}{aH(t, T)} \delta(z - T),$$

where

$$H(t, T) = e^{2at} \int_T^\infty e^{-2az} g^2(t - z) dz.$$

### III. ACKNOWLEDGMENTS

The author appreciates the helpful suggestions of S. Darlington, E. N. Gilbert, and D. Slepian.

### REFERENCES

1. Blackman, R. B., Bode, H. W. and Shannon, C. E., *Data Smoothing and Prediction in Fire-Control Systems*, NDRC Report MGC 12/1, 1948 (Confidential).
2. Zadeh, L. A. and Ragazzini, J. R., An Extension of Wiener's Theory of Prediction, *J. Appl. Phys.*, **21**, July 1950, p. 645.
3. Ule, L. A., A Theory of Weighted Smoothing, *Trans. I.R.E.*, **IT-3**, June 1957, p. 131.
4. Youla, D. C., The Use of the Method of Maximum Likelihood in Estimating Continuous-Modulated Intelligence Which Has Been Corrupted by Noise, *Trans. I.R.E.*, **PGIT-3**, March 1954, p. 90.



# Amplitude Modulation Suppression in FM Systems

By C. L. RUTHROFF

(Manuscript received January 8, 1958)

*Inadequacies of some limiter concepts are discussed and a limiter analysis in terms of low-index modulation theory is presented. The analysis of a particular circuit proves the possibility of perfect amplitude modulation suppression with small loss to the frequency modulated signal. Experimental data are presented which verify the theory and demonstrate the practicability of the device analyzed.*

## I. INTRODUCTION

Since the early days of frequency modulation (FM) it has been known that to realize the full advantage of FM with respect to signal-to-noise ratio it is necessary to suppress any amplitude modulation (AM) which may be present on the signal. Various kinds of limiters have been used for this purpose: overloaded amplifiers, grid and plate clippers and vacuum diode clippers, to mention a few. In recent years, the trend has been to use germanium or silicon diodes for this function, particularly in broadband systems such as the TD-2 and TJ microwave systems and in systems using transistors.

There is some ambiguity in the use of the word "limiter." In this discussion a limiter is a device whose function is to reduce the index of amplitude modulation of the input signal. This function is called limiting or AM suppression and the amount of limiting is the ratio of the index of AM in the output signal to the index of AM of the input signal.

The operation of limiters has been only partially understood and as a consequence the operation is not efficient either in the sense of loss to the FM signal or in the amount of amplitude modulation suppression (limiting).

If it is recognized that limiting is a modulation process, it becomes clear that modulation theory can be used to analyze limiter circuits. This is done here for a diode limiter. Theoretical and experimental curves are presented, as are equivalent circuits.

## II. GENERAL

Before launching into the modulation theory of limiters, it is first necessary to point out some of the inadequacies of some current concepts.

It might be surmised that, if the carrier output voltage is plotted as a function of the input voltage, the amount of limiting is given by the slope of this curve. In Appendix B it is shown that this is not necessarily true. In particular, it is demonstrated that the limiting characteristic can be altered without altering the carrier transfer function.

A common "clipper" limiter and its dual are shown in Figs. 1(a) and 1(b). The customary explanation of limiting by the circuit in Fig. 1(a) is accomplished with the aid of Fig. 2. The diodes are assumed ideal in the sense that the back resistance is infinite and the forward resistance is zero. The bias current  $I_0$  is assumed to come from a constant current source and to bias both diodes in the forward or low-resistance direction. The input signal voltage  $e$  shown in Fig. 2(a) is a sine-wave amplitude-modulated carrier. The output voltage across  $R_L$  follows the input voltage until the input voltage reaches the clipping level  $A$ , Fig. 2(b). At this point, diode  $D_1$  switches to its back resistance and further increase in input voltage does not appear in the output, since the back resistance of  $D_1$  is infinite. Now, when the input voltage is reduced again to value  $A$ ,  $D_1$  switches to its forward resistance and the output voltage is again a replica of the input. A similar sequence is followed on the

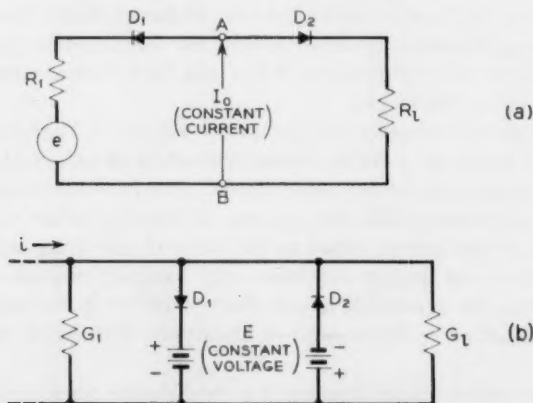


Fig. 1 — A common idealized limiter circuit (a) and its dual (b). The diodes are assumed to have zero forward resistance and infinite back resistance.

negative half of the cycle except that, in this case, it is the diode  $D_2$  that switches at level  $-A$ . The net result is an output voltage of the form of Fig. 2(c). If the clipping level  $A$  were reduced and made to approach zero, only the zero crossings of the original signal would be preserved and the amplitude modulation would be completely suppressed.

The above explanation is useful for some purposes, but it has these serious limitations:

1. It is not obvious from Fig. 2(c) that any AM remains in the signal when, in fact, there may be a considerable amount. The fact that the usual envelope structure has disappeared does not prove the absence of AM.

2. The output is as shown in Fig. 2(c) only if the limiter circuit has a bandwidth which includes many harmonics of the carrier frequency and the baseband frequencies of interest. These harmonics are not negligible in amplitude and have important effects on limiting. In most practical circuits only the fundamental is passed and the simplified explanation is not accurate enough. The effects of preventing the flow of

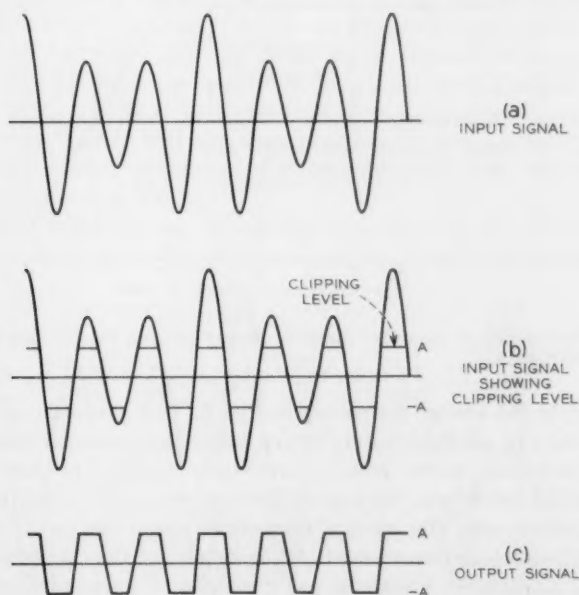


Fig. 2 — Input and output signals for the limiters of Fig. 1.

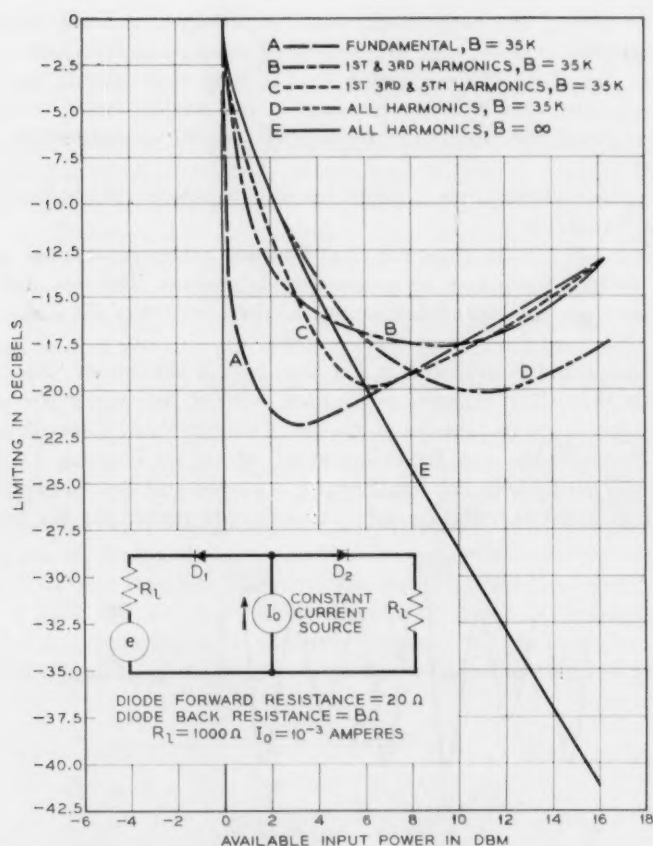


Fig. 3 — Calculated data for "clipper" limiter passing various harmonics of the carrier frequency.

harmonics of the carrier are shown in Fig. 3. This figure gives limiting as a function of available input power level. As mentioned previously, limiting is defined as the ratio of amplitude modulation index of the output signal to that in the input. Curve A shows the usual practical case, i.e., where only the band of frequencies about the carrier and the baseband frequencies are allowed. All harmonics of the carrier and sidebands are suppressed. Curves B and C include all harmonics up to the third and fifth respectively. Curve D includes all harmonics of the carrier and sidebands. Curve E is for diodes with infinite back resistance.

This is the case usually analyzed. These curves were calculated from formulae derived in Appendix A; the circuit constants used are indicated on the figure.

3. The third limitation has to do with the assumptions concerning the diodes. From Fig. 2(c) it can be seen that, if the clipping level is reduced (this is equivalent to increasing input amplitude and keeping clipping level constant), the AM suppression increases, as does the loss at the carrier frequency. In the limit, the AM suppression is perfect and the loss to the carrier is infinite. It is commonly thought that, for this reason, increasing the input level increases the AM suppression. In a practical limiter this is not true. One important reason is that the back resistance of a diode is never infinite. In Fig. 4, which is similar to Fig. 2 except that the diodes are assumed to have a finite back resistance, note that the output waveform is slightly rounded instead of being clipped sharply. The portions are rounded because, even when one diode is on its back resistance, the input voltage influences the output voltage. In fact, during the clipping interval the output waveform is simply a greatly reduced replica of the input waveform in that interval. Now, if the clipping level is reduced to zero, the output waveform is exactly the same shape as the input waveform. At every instant, one diode is on its back resistance and the other on its forward resistance or, in other words, the circuit is linear and there is no limiting whatever. The loss, however, is finite. This means that there is some one input level at which the limiting is best and that, contrary to common belief, merely increasing the input level does not necessarily improve the limiting. This is also illustrated in Fig. 3.

For these three reasons, the simple clipping picture does not give a suitable explanation of the limiting action. A more accurate description

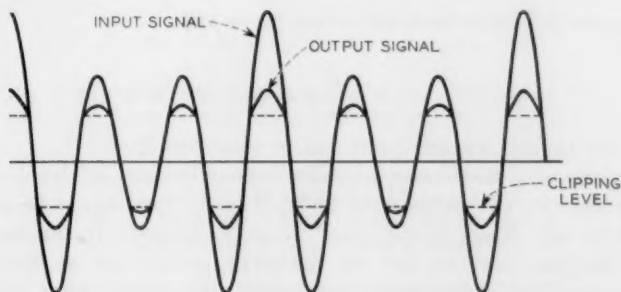


Fig. 4 — Input and output signals for a clipper limiter using diodes with finite back resistance.



is given by analyzing the circuit in terms of modulation theory. To justify the modulation theoretical approach, a simple argument can be given.

A simple example of an FM signal is a sine-wave modulated carrier with low index of modulation. If the index is sufficiently low, only the first pair of sidebands is important. The only difference between this FM wave and an AM wave modulated with the same signal is in the phase relationships between the sidebands and the carrier frequency. An AM wave can be superimposed on the FM wave so that the AM sidebands occur at exactly the same frequencies as do the FM sidebands. This situation is illustrated as follows:

$$\begin{aligned}
 \text{AM: } E(1 + k \cos pt) \cos \omega t &= E \cos \omega t \\
 &\quad + \frac{kE}{2} [\cos (\omega + p)t + \cos (\omega - p)t], \\
 \text{FM: } E \cos \left( \omega t + \frac{\Delta \omega}{p} \sin pt \right) &\approx E \cos \omega t \\
 &\quad + E \frac{\Delta \omega}{2p} [\cos (\omega + p)t - \cos (\omega - p)t], \\
 k \ll 1; \quad \frac{\Delta \omega}{p} &\ll 1,
 \end{aligned} \tag{1}$$

where  $\Delta \omega$  is the peak deviation of the carrier

$p$  is the modulating frequency

$\omega$  is the carrier frequency

$k$  is the AM index of modulation.

The composite FM signal with AM present is:

$$\begin{aligned}
 E \cos \omega t + E \frac{\Delta \omega}{2p} [\cos (\omega + p)t - \cos (\omega - p)t] \\
 + k \frac{E}{2} [\cos (\omega + p)t + \cos (\omega - p)t],
 \end{aligned} \tag{2}$$

where the AM and FM sidebands can be identified from (1).

The purpose of the limiter is to eliminate only those sidebands representing AM, i.e., the second pair in (2). Clearly this cannot be accomplished by any linear circuit, since whatever happens to the AM sidebands happens also to the FM sidebands, which are at the same frequencies. The limiter must accomplish two things. First, it must identify the AM sidebands; second, it must eliminate them. And it must do these things without interfering with the FM sidebands.

The identification can be made with an amplitude detector. Such a

detector does not interfere with an FM wave but does detect whatever AM is present. The output of the detector can then be used to generate a pair of sidebands in the output circuit similar to the original AM but opposite in phase. If care is taken to adjust the amplitude properly, these remodulated sidebands will completely cancel the original sidebands; and the output signal will be free of AM. It is important to note that neither the detection nor modulation affects the FM signal except to introduce some loss. The output of the limiter contains only the desired FM signal.

This argument, although heuristic, indicates three important results. It shows that limiting is necessarily a nonlinear process. More important, it indicates the possibility, at least theoretically, of perfect limiting using diodes with finite forward and reverse resistances and with a finite loss to the FM signal. In addition, it points the way to a mathematical approach using low-index modulation theory.

The limiter configuration of Fig. 5, based on the principles discussed above, has been analyzed and the details are included in Appendix A.

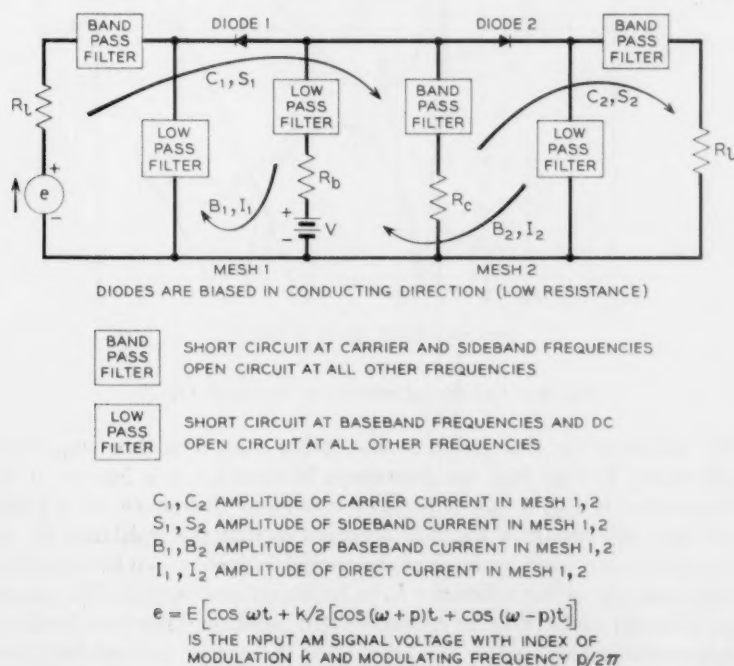


Fig. 5 — Limiter circuit with which perfect limiting can be obtained.

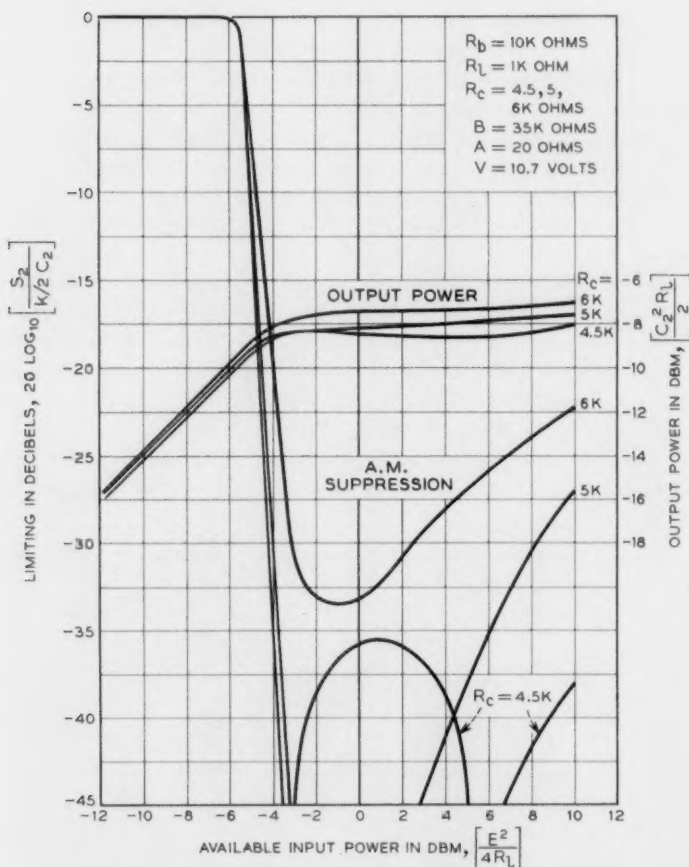


Fig. 6 — Calculated results for limiter of Fig. 5.

The limiter of Fig. 5 is similar to that of Fig. 1(a), with three important differences. In Fig. 1(a), the impedance in branch A-B is infinite at all frequencies; in Fig. 5, this impedance is finite at all frequencies of interest. Also, the circuit in Fig. 5 is arranged so that the resistance  $R_c$ , at frequencies in a band centered at the carrier frequency, can be controlled independently of the resistance  $R_b$  at baseband frequencies. (The diodes are assumed to have finite resistance.) In addition, only two bands of frequencies are allowed: a band including the carrier and sideband frequencies and another band extending from dc up to the highest baseband frequency of interest.

The resistances  $R_b$  and  $R_c$  play a vital role in the operation of the limiter. By properly proportioning these resistances, the limiting can be made theoretically perfect at one or two input levels. If good diodes are used (diodes with a high ratio of reverse to forward resistance; most germanium and silicon diodes are good by this definition) perfect limiting can be achieved when  $R_b = R_c$ . From formulae derived in Appendix

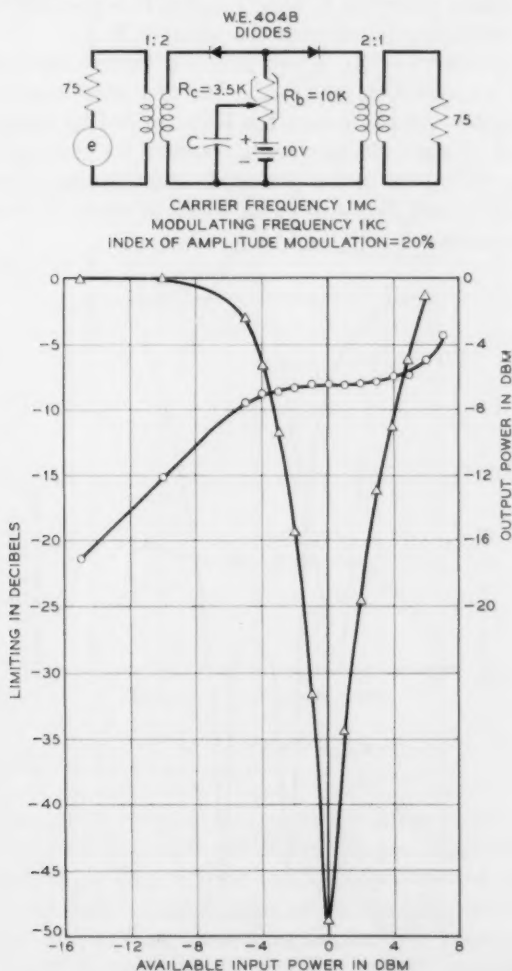


Fig. 7 — Experimental results for practical limiter based on Fig. 5, with  $R_c$  adjusted for one limiting peak.

A, several curves of limiting versus input carrier level have been calculated and are plotted in Fig. 6. For all the curves  $R_b = 10,000$  ohms, but  $R_c$  is different for each curve. For all such data, limiting is defined as the ratio of the AM index of modulation of the output to the index of modulation of the input signal. In Fig. 6, the curve for  $R_c = 4500$  ohms shows two points of perfect limiting, and this behavior is verified in experimental data presented in Figs. 7 and 8. It is possible to get either one or two peaks, depending upon the value of  $R_c$ .

The theory indicates that, if two points of perfect limiting exist, the phase of the AM sidebands reverses at the first point and again at the second. That this actually occurs has been verified by experiment.

Figs. 9 and 10 show similar results obtained for the condition  $R_b = R_c$ . Where possible, this is the preferred condition since it requires less by-passing of  $R_c$  and  $R_b$ , a problem which is especially important in broadband systems.

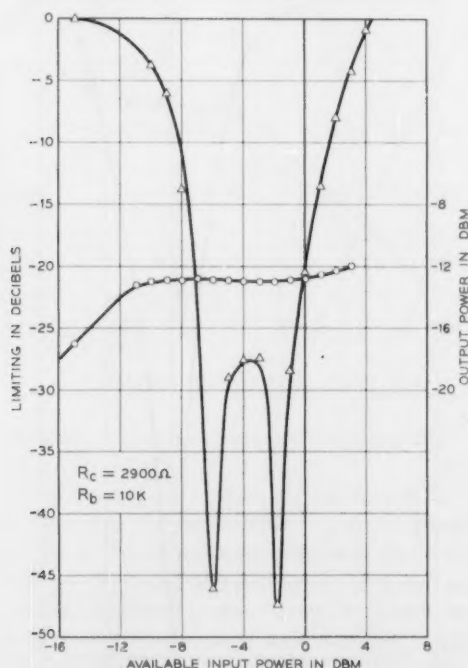


Fig. 8 — Experimental results for practical limiter based on Fig. 5, with  $R_c$  adjusted for two limiting peaks.

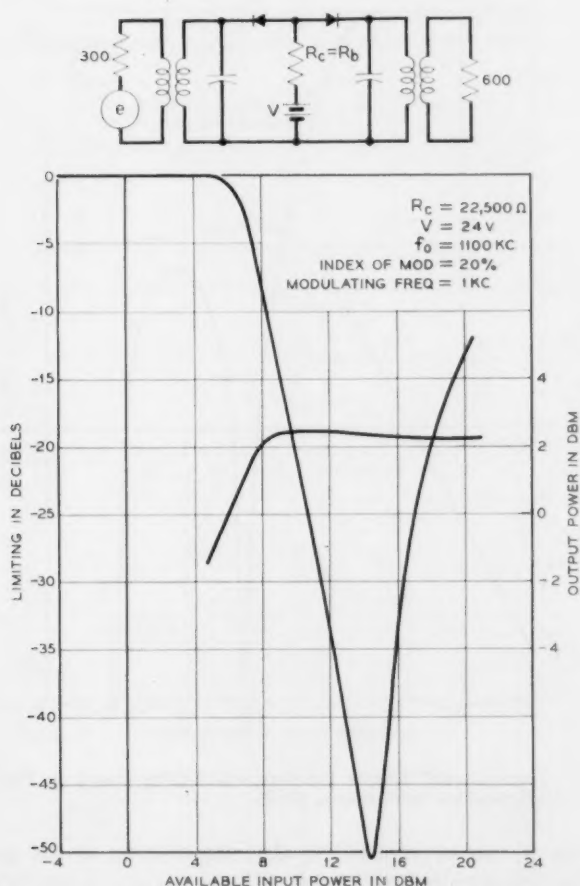


Fig. 9 — Experimental results for practical limiter based on Fig. 5, with  $R_b = R_c$  and adjusted for one limiting peak.

Figs. 6 through 10 indicate that perfect limiting occurs only at isolated values of input power for this limiter. No practical difficulty arises, however, because perfect limiting can be approximated as closely as desired over any finite range of input power levels by cascading several stages similar to Fig. 5 and arranging the limiting peaks properly. In Fig. 6 the hump between the two peaks of perfect limiting can be reduced to any desired level by increasing  $R_c$ . This will have the effect of reducing the separation of the peaks. After choosing any finite amount

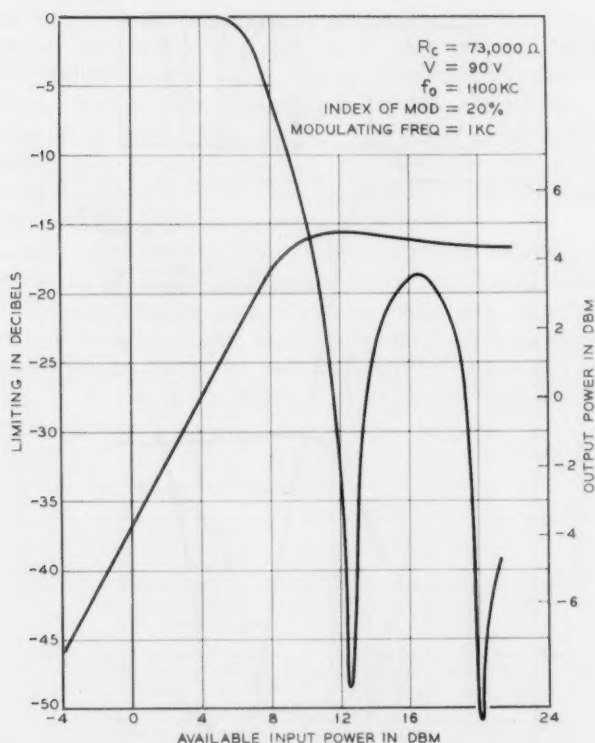
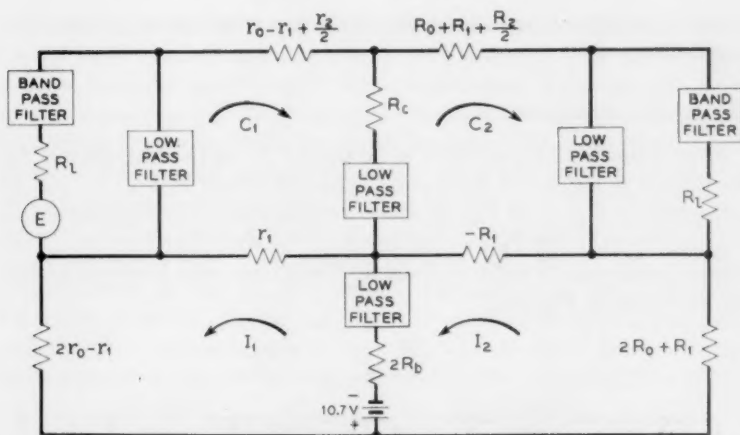


Fig. 10 — Experimental results for practical limiter based on Fig. 5, with  $R_b = R_c$  and adjusted for two limiting peaks.

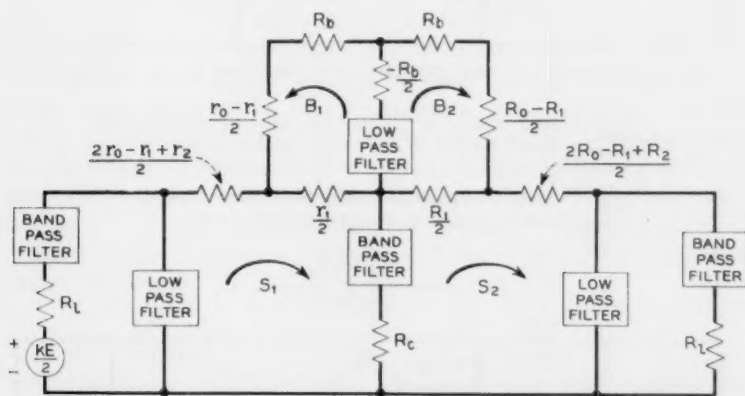
of limiting,  $R_c$  can be adjusted so that the limiting at the maximum point of the hump exceeds this value. (The minus sign is usually omitted and we say that 40 db of limiting is more than, or exceeds, 30 db, i.e., the decrease in AM index is greater for 40 db of limiting than for 30 db.) Then, for a continuous range of input levels, the limiting is more than the desired amount. Another stage can be adjusted so that its limiting peaks fall near but to the right of those of the first stage, in such a way that the limiting between the peaks always exceeds the predetermined number. Control of bias current and  $R_c$  will be required for this adjustment. If this process is continued it is evident that perfect limiting can be approximated as closely as desired over any finite range of input levels.

In many practical situations, one stage is sufficient because the AGC





(a) EQUIVALENT CIRCUIT SHOWING COUPLING BETWEEN THE CARRIER AND DC FOR THE LIMITER OF FIG. 5



(b) EQUIVALENT CIRCUIT SHOWING COUPLING BETWEEN SIDEBANDS AND BASEBAND FREQUENCIES FOR THE LIMITER OF FIG. 5

$$r_0 = (B-A) \beta_1 + A$$

$$R_0 = (B-A) \beta_2 + A$$

$$r_n = 2(B-A) \frac{\sin n\beta_1\pi}{n\pi}$$

$$R_n = 2(B-A) \frac{\sin n\beta_2\pi}{n\pi}$$

B = BACK RESISTANCE OF DIODE

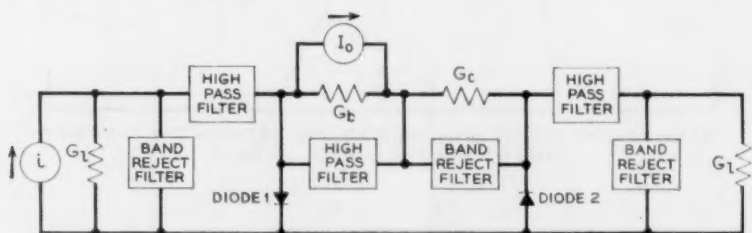
A = FORWARD RESISTANCE OF DIODE

Fig. 11 — Equivalent circuits for limiter of Fig. 5.

of the IF amplifier acts to keep the carrier input level near the value for best limiting.

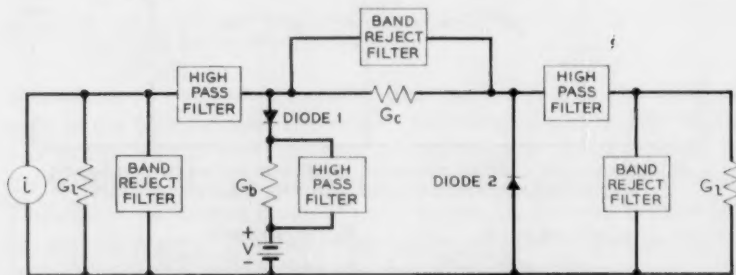
### III. EQUIVALENT CIRCUITS

From equation (13) derived in Appendix A, equivalent circuits for the limiter of Fig. 5 can be drawn. These are shown in Fig. 11. Fig. 12 is the dual of Fig. 5. In Fig. 11 all resistances with numbered subscripts are coefficients in the Fourier expansion of the resistance function of the diodes; lower case  $r$ 's indicate diode  $D_1$ . Resistances with letter subscripts are as shown in Fig. 5(a).



(a) DIODES BIASED IN NON-CONDUCTING DIRECTION [BACK RESISTANCE]

BAND REJECT FILTER	OPEN CIRCUIT AT CARRIER AND SIDEBAND FREQUENCIES SHORT CIRCUIT AT ALL OTHER FREQUENCIES
HIGH PASS FILTER	OPEN CIRCUIT AT BASEBAND FREQUENCIES AND DC SHORT CIRCUIT AT ALL OTHER FREQUENCIES



(b) SAME AS (a) EXCEPT CURRENT GENERATOR REPLACED WITH VOLTAGE GENERATOR

$i = I [\cos \omega t + k/2 [\cos(\omega + p)t + \cos(\omega - p)t]]$  IS THE INPUT AM SIGNAL CURRENT WITH INDEX OF MODULATION  $k$  AND MODULATING FREQUENCY  $p/2\pi$

Fig. 12 — Dual of limiter circuit shown in Fig. 5.

The limiting mechanism can be understood by consideration of the circuit involving AM sidebands [Fig. 11(b)]. Some AM sideband energy is coupled from the input mesh 1 to the output mesh 2 through  $R_c$ . Some of the remaining sideband energy is coupled to mesh 3 through the  $r_1/2$  where it appears at the baseband frequency. This baseband energy in mesh 3 is coupled in turn through  $-R_b/2$  into mesh 4, where it is still at the baseband frequency. From mesh 4 it is coupled through  $R_1/2$  into the output mesh 2, where it appears at the sideband frequencies in phase opposition to the energy coupled through  $R_c$ . By properly proportioning  $R_b$  and  $R_c$ , the energies coupled by  $R_c$  and  $-R_b/2$  can be made to cancel, leaving no sideband currents in the output mesh and therefore achieving perfect limiting. The FM signal behaves in the same manner as the carrier and suffers loss only in passing through the limiter.

#### APPENDIX A

The material in this section is based on Refs. 1 and 2. In Ref. 1 Caruthers develops the superposition principle for low-index modulation; i.e., he shows that circuits containing nonlinear resistive elements can be resolved into equivalent linear systems using a large carrier and small signal amplitude. In Ref. 2 it is shown that a nonlinear resistance can be represented by a Fourier series, the coefficients of which have the dimensions of resistance. If the carrier is large compared to the signal, this resistance is a function of carrier frequency and harmonics only and, to a good approximation, is independent of the signal.

Based on these ideas, the limiter circuit can be solved by usual linear circuit techniques.

##### A.1 Superposition

Any nonlinear resistance has a current voltage characteristic that can be expressed by a power series of the form:

$$e = a_1 i + a_2 i^2 + a_3 i^3 + \cdots + a_n i^n + \cdots \quad (3)$$

If a carrier and signal current are applied to this nonlinear resistance, each term after the first will produce voltages at new frequencies consisting of the intermodulation products of the carrier and signal. If finite external impedances are presented to these voltages, currents will flow at these new frequencies and produce still more new frequencies. The number of currents can be minimized by presenting infinite impedance to some of the modulation products.

If a carrier current  $C \cos ct$  and two signal currents  $S_1 \cos s_1 t$  and

$S_2 \cos s_2 t$  are applied to the nonlinear resistance the voltage due to the  $n$ th term of (3) is

$$\begin{aligned} C_n &= A_n(C \cos ct + S_1 \cos s_1 t + S_2 \cos s_2 t)^n \\ &= A_n C^n \left( \cos ct + \frac{S_1}{C} \cos s_1 t + \frac{S_2}{C} \cos s_2 t \right)^n. \end{aligned} \quad (4)$$

We now make the usual assumption of low-index modulation theory. This assumption is that  $S_1/C$  and  $S_2/C$  are small enough so that terms in the expansion of (4) containing products and powers of  $S_1/C$  and  $S_2/C$  are negligible. The expansion of (4) is then:

$$C_n \approx A_n C^n \left( \cos^n ct + n \cos^{n-1} ct \frac{S_1}{C} \cos s_1 t + n \cos^{n-1} ct \frac{S_2}{C} \cos s_2 t \right). \quad (5)$$

The first term in (5) is the dc and the harmonics of the carrier. The second and third terms contain the input signal, the output signal (usually the first order sidebands) and other unwanted modulation products. The important thing to note about (5) is that the input and output voltages (second and third terms) are the same whether the input signals are applied separately and the outputs summed or whether the inputs are applied simultaneously. Therefore, the superposition principle holds and is a direct consequence of the fact that the carrier amplitude is much greater than the signal amplitude.

#### A.2 Fourier Series Representation of Nonlinear Resistance

The power series expansion for the nonlinear resistance as a function of current can be obtained by differentiating (3) with respect to  $i$ . The nonlinear resistance is:

$$r(i) = \frac{de}{di} = a_1 + 2a_2 i + 3a_3 i^2 + \dots + nA_n i^{n-1} + \dots, \quad (6)$$

where  $r(i)$  is the nonlinear resistance.

The usual assumption made in low-index amplitude modulation theory and the one made here is that only the carrier current is significant in determining the nonlinear resistance. If the carrier current  $i = I \cos \omega t$  is substituted into (6) and the series rearranged, the result is a Fourier series. Such a series can be written as

$$r(t) = r_0 + \sum_{n=1}^{\infty} r_n \cos n\omega t. \quad (7)$$

If the current-voltage characteristics of the nonlinear element were expanded in terms of voltage instead of current, an analogous analysis

would lead to a representation of the element as a conductance:

$$g(t) = g_0 + \sum_{n=1}^{\infty} g_n \cos n\omega t. \quad (8)$$

Either (7) or (8) can be used to represent a nonlinear resistance in low-index modulation problems. The accuracy of the representation depends upon the index of modulation; the lower the index, the better the representation.

### A.3 Limiter Analysis

With superposition established and a simple expression for the nonlinear resistance, the rest of the analysis can be done by usual linear circuit techniques. The procedure is as follows:

i. An amplitude-modulated sine wave voltage is applied to the circuit of Fig. 5. No FM need be included, since it is not affected in any way by the limiter except to suffer some attenuation.

ii. A solution is assumed; i.e., currents at certain frequencies are assumed to flow in the two meshes. The magnitudes of these currents are unknown and are to be determined. Currents at all other frequencies are not allowed to flow.

iii. The mesh equations are set up and solved for pertinent currents.

With reference to Fig. 5, the input voltage  $E$  is a carrier, amplitude-modulated with a sine wave:

$$e = E \cos \omega t + \frac{k}{2} E [\cos (\omega + p)t + \cos (\omega - p)t], \quad (9)$$

where  $k$  = index of modulation

$\omega/2\pi$  = carrier frequency

$p/2\pi$  = modulating frequency.

The currents that are assumed to flow are:

$$\begin{aligned} i_1 &= C_1 \cos \omega t + S_1 [\cos (\omega + p)t + \cos (\omega - p)t] + B_1 \cos pt + I_1, \\ i_2 &= C_2 \cos \omega t + S_2 [\cos (\omega + p)t + \cos (\omega - p)t] + B_2 \cos pt + I_2. \end{aligned} \quad (10)$$

The circuit of Fig. 5 is arranged so that no other currents are allowed to flow. With these currents the  $IR$  drops across the nonlinear elements can be calculated. Let the diodes have the following expansions:

$$\begin{aligned} \text{Diode } D_1: r_1(t) &= r_0 + \sum_{n=1}^{\infty} r_n \cos n\omega t, \\ \text{Diode } D_2: r_2(t) &= R_0 + \sum_{n=1}^{\infty} (-1)^n R_n \cos n\omega t. \end{aligned} \quad (11)$$

The factor  $(-1)^n$  in  $r_2(t)$  is due to the fact that the diodes are poled in opposite directions. The voltage drops across the diodes are found by multiplying (10) and (11):

$$v_1 = i_1 r_1(t) = C_1 \left( r_0 + \frac{r_2}{2} \right) \cos \omega t \\ + \left[ r_0 S_1 + \frac{r_2}{2} S_1 + \frac{r_1}{2} B_1 \right] [\cos (\omega + p)t + \cos (\omega - p)t] \\ + (r_0 B_1 + r_1 S_1) \cos pt + \frac{r_1}{2} C_1 + I_1 r_0 + I_1 r_1 \cos \omega t, \quad (12)$$

$$v_2 = i_2 r_2(t) = C_2 \left( R_0 + \frac{R_2}{2} \right) \cos \omega t \\ + \left[ R_0 S_2 + \frac{R_2}{2} S_2 - \frac{R_1}{2} B_2 \right] [\cos (\omega + p)t + \cos (\omega - p)t] \\ + (R_0 B_2 - R_1 S_2) \cos pt - \frac{R_1}{2} C_2 + I_2 R_0 - I_2 R_1 \cos \omega t.$$

The next step is to equate the voltage drops at each frequency to the generator emf's in each mesh:

$$\left. \begin{aligned} E &= R_m C_1 - R_c C_2 + I_1 r_1 \\ 0 &= -R_c C_1 + R_s C_2 - I_2 R_1 \end{aligned} \right\} \text{carrier} \\ \left. \begin{aligned} -V &= \frac{r_1}{2} C_1 + I_1 (r_0 + R_b) - I_2 R_b \\ V &= \frac{-R_1}{2} C_2 + I_2 (R_0 + R_b) - I_1 R_b \end{aligned} \right\} \text{dc} \quad (13) \\ \left. \begin{aligned} \frac{kE}{2} &= R_m S_1 - R_c S_2 + \frac{r_1}{2} B_1 \\ 0 &= -R_c S_1 + R_s S_2 - \frac{R_1}{2} B_2 \end{aligned} \right\} \text{sidebands} \\ \left. \begin{aligned} 0 &= r_1 S_1 + (r_0 + R_b) B_1 - R_b B_2 \\ 0 &= -R_1 S_2 - R_b B_1 + (R_0 + R_b) B_2 \end{aligned} \right\} \text{baseband,}$$

where

$$R_m = r_0 + \frac{r_2}{2} + R_c + R_l$$

$$R_s = R_0 + \frac{R_2}{2} + R_c + R_l.$$

The set of equations (13) can be solved for the pertinent currents:

$$C_1 =$$

$$\frac{E \left\{ R_x [(r_0 + R_b)(R_0 + R_b) - R_b^2] - \frac{R_1^2}{2} (r_0 + R_b) \right\} + V \left( R_1 R_c r_0 + r_1 R_x R_0 - \frac{r_1 R_1^2}{2} \right)}{D},$$

$$C_2 =$$

$$\frac{E \left\{ R_c [(r_0 + R_b)(R_0 + R_b) - R_b^2] - \frac{r_1}{2} R_1 R_b \right\} + V \left( R_m R_1 r_0 + r_1 R_c R_0 - \frac{r_1^2 R_1}{2} \right)}{D}, \quad (14)$$

$$S_2 = \frac{k}{2} E \frac{\left\{ R_c [(r_0 + R_b)(R_0 + R_b) - R_b^2] - \frac{r_1 R_1 R_b}{2} \right\}}{D},$$

where

$$D = [(r_0 + R_b)(R_0 + R_b) - R_b^2](R_m R_x - R_c^2) - \frac{R_1^2}{2} R_m (r_0 + R_b) - \frac{r_1^2}{2} R_x (R_0 + R_b) + r_1 R_1 R_c R_b + \left( \frac{r_1 R_1}{2} \right)^2.$$

The insertion loss ratio is

$$\frac{P_{out}}{P_{avail}} = \frac{C_2^2 R_l}{\frac{E^2}{4R_l}} \quad (15)$$

and the limiting, or amplitude modulation suppression, is

$$\text{limiting} = \frac{S_2}{\frac{k}{2} C_2}. \quad (16)$$

Expression (16) shows that perfect limiting occurs when  $S_2 = 0$ . The numerator of  $S_2$  as given in (14) indicates the possibility of perfect limiting if  $R_c$  and  $R_b$  can be adjusted independently.

At this point it is convenient to place some further restrictions on the diode characteristics so that the calculations can be made more easily. The diodes are assumed to switch from a constant forward resistance  $A$  to a constant backward resistance  $B$ . The fraction of the carrier cycle that the diodes remain on the back resistance is designated  $\beta_1, \beta_2$ .



With these simplifications, the diode characteristics given in (3) are:

$$\begin{aligned} r_1(t) &= r_0 + \sum_{n=1}^{\infty} r_n \cos n\omega t \\ r_2(t) &= R_0 + \sum_{n=1}^{\infty} (-1)^n R_n \cos n\omega t, \end{aligned} \quad (17)$$

where

$$\begin{aligned} r_0 &= (B - A)\beta_1 + A, & R_0 &= (B - A)\beta_2 + A, \\ r_n &= \frac{2(B - A)}{n\pi} \sin n\beta_1\pi, & R_n &= \frac{2(B - A)}{n\pi} \sin n\beta_2\pi, \end{aligned}$$

$B$  = back resistance of the diode,

$A$  = forward resistance of the diode,

$\beta$  = the fraction of the cycle during which the diode is on its back resistance.

All of the currents in (14) are functions of  $E$ ,  $\beta_1$  and  $\beta_2$ , where  $E$  is the amplitude of the input carrier voltage. In order to make calculations for (14), relations among  $E$ ,  $\beta_1$  and  $\beta_2$  must be derived.

When the input to the limiter is very low, both diodes are on their forward resistances, due to the forward bias current  $I_0$ . At these low levels  $\beta_1$ ,  $\beta_2$  are both zero and, from (14),

$$\frac{C_2}{C_1} = \frac{R_c}{R_c + R_l}. \quad (18)$$

Because the circuit is resistive and because only the carrier current is involved in switching the diodes, (18) holds for all instantaneous loop currents less than  $I_0$ . From the definition of  $\beta$ , the diodes switch to their back resistances when

$$\begin{aligned} C_1 \cos(-\beta_1\pi) &= I_0, & C_1 &\geq I_0, \\ C_2 \cos(-\beta_2\pi) &= I_0, & C_2 &\geq I_0. \end{aligned} \quad (19)$$

At the switching point, both (18) and (19) hold. Therefore, by substituting (18) into (19), a relation between  $\beta_1$ ,  $\beta_2$  follows:

$$\cos \beta_1\pi = \frac{R_c}{R_c + R_l} \cos \beta_2\pi. \quad (20)$$

In a similar manner, a relation can be derived for  $E$ ,  $\beta_1$ . When  $C_1 = I_0$ ,  $\beta_1 = \beta_2 = 0$  and, from (14),

$$E_0 = I_0 \frac{(R_m R_z - R_c^2)}{R_z} \Big|_{(\beta_1 = \beta_2 = 0)}. \quad (21)$$

Now, for any  $E \geq E_0$ , diode  $D_1$  switches to its back resistance when

$$E \cos \beta_1 \pi = E_0 = I_0 \frac{[R_m R_x - R_c^2]}{R_x} \quad (\beta_1 = \beta_2 = 0), \quad (22)$$

where  $I_0$  is the bias current in each diode and is given by (13) for  $\beta_1 = \beta_2 = 0$ . Thus,

$$I_0 = \frac{V}{2R_b + A}, \quad (23)$$

where

$V$  = dc bias voltage

$A$  = forward resistance of diode.

Curves of power output and amplitude modulation suppression have been calculated and are shown in Fig. 6.

#### A.4 Circuit Simplification

A natural question to ask about the limiter is, "Can perfect limiting be obtained when  $R_b = R_c$ ?" If so, the circuit is much simpler. The answer to this question is yes, and this can be demonstrated by considering the numerator of  $S_2$ . Perfect limiting is achieved when this numerator is zero. Setting the numerator of  $S_2$  equal to zero and letting  $R_b = R_c$ , the resulting expression is solved for  $R_c$ :

$$R_c = \frac{2r_0 R_0 \left( \frac{r_1 R_1}{2r_0 2R_0} - \frac{1}{2} \right)}{r_0 + R_0}, \quad (24)$$

where

$$R_c \geq 0. \quad (25)$$

Using this fact in (24), it follows that perfect limiting can be obtained when  $R_b = R_c$  if the following inequality is satisfied:

$$\frac{r_1}{2r_0} \frac{R_1}{2R_0} \geq \frac{1}{2}. \quad (26)$$

Let us examine this further by using the idealized diode characteristics of (17). Substituting these expressions into (26), we get

$$\left( \frac{\sin \beta_1 \pi}{\beta_1 \pi} \right) \left( \frac{1}{1 + \frac{A}{2(B-A)\beta_1}} \right) \left( \frac{\sin \beta_2 \pi}{\beta_2 \pi} \right) \left( \frac{1}{1 + \frac{A}{2(B-A)\beta_2}} \right) \geq \frac{1}{2}. \quad (27)$$

This inequality can be met easily with good diodes, i.e., diodes in which  $B/A \gg 1$ .

Figs. 9 and 10 show a limiter and experimental results for the case  $R_b = R_c$ . It should be noted that, even with poor diodes, the limiting can be perfect if  $R_b$  and  $R_c$  are allowed to differ. This can be seen in the expression for  $S_2$ .

#### A.5 The "Clipper" Limiter

A well-known limiter has the configuration of Fig. 1. The behavior of such a "clipper" limiter can be examined by setting  $R_b = R_c$  and letting  $R_b$  and  $V$  increase without bound in such a way as to maintain the initial bias current  $I_0$  unchanged. This will also insure that  $\beta_1 = \beta_2$  and  $r_i = R_i$ .

If these exercises are performed on (14) and the results substituted into (16), the limiting is found to be

$$\text{limiting} = \frac{E}{E + 2r_1 I_0}, \quad (28)$$

where

$E$  = carrier voltage amplitude,

$I_0$  = constant current dc bias,

$r_1 = [2(B - A)/\pi] \sin \beta_1 \pi$ .

Several remarks can be made concerning the "clipper limiter" of (28):

i. Before the diodes begin to switch,  $r_1 = 0$  and there is no limiting. This is to be expected.

ii. If  $I_0 = 0$  there is no limiting. This too is to be expected because, with no bias, one diode has its back resistance in the circuit while the other one has its forward resistance in the circuit, and vice versa. The circuit is linear under these conditions and cannot limit.

iii. Expression (28) indicates that the larger  $r_1$ , the better will be the limiting for a given  $I_0$ . But  $r_1$  is proportional to  $(B - A)$ , so this indicates a good diode for a limiter of this type is one with a high back resistance  $B$  and a high ratio of back-to-front resistance.

iv. If the diodes have a finite back resistance, perfect limiting cannot be achieved. Furthermore, as  $\beta_1$  approaches  $1/2$ , the limiting tends to zero. The reason for this is that  $r_1$  is proportional to  $\sin \beta_1 \pi$ , which tends to a constant value as  $\beta_1$  approaches  $1/2$  while  $E$  increases without limit.

The output carrier current can be calculated in the same way as (28). It is

$$C_2 = \frac{E + 2r_1 I_0}{2r_0 + r_2 + R_l}. \quad (29)$$

Comments can also be made concerning this equation:

i. At low levels of input voltage the diodes do not switch and  $r_1 = r_2 = 0$ , and  $r_0 = A$ . The output is then  $C_2 = E/[2(R_L + A)]$ , as expected.

ii. If  $I_1 = 0$ , then  $\beta_1 = \beta_2 = 1/2$ , resulting in  $r_0 = (B + A)/2$  and  $r_2 = 0$ . In this case  $C_2 = E/(B + A + 2R_L)$  and the circuit is linear.

In the above discussion of the "clipper" limiter, all harmonics of the carrier were suppressed. Two other cases have been considered: in one case, the third harmonic was allowed and, in the other, the third and fifth harmonics were allowed (even harmonics cancel). The analysis follows the same pattern as previously demonstrated except that currents at all allowed frequencies are assumed. Only the results will be shown.

When the third harmonic is allowed, limiting is given by:

$$L = \frac{1}{1 + \frac{\cos \beta \pi}{R_L + A} \left[ r_1 - \frac{r_3(r_2 + r_4)}{2R_L + 2r_0 + r_6} \right]}. \quad (30)$$

Similarly, when the fifth harmonic is added,

$$L = \left( 1 + \frac{\cos \beta \pi}{R_L + A} \{ r_1 - r_3[(r_2 + r_4)(2R_L + 2r_0 + r_{10}) - (r_2 + r_8)(r_4 + r_6)] - r_5[(r_2 + r_4)(r_2 + r_8) - (r_4 + r_6)(2R_L + 2r_0 + r_6)] \} \right)^{-1} \quad (31)$$

Equations (30) and (31) are plotted in Fig. 3. The curve for all harmonics was calculated by a Fourier analysis of the "clipped" wave.

#### APPENDIX B

In this Appendix it will be shown that the amount of limiting is not necessarily given by the slope of the carrier transfer function.

Assume that the limiter of Fig. 5 is adjusted for perfect limiting for the carrier amplitude  $E = E_1$ . In the equivalent circuits of Fig. 11, it is noted that the output carrier current  $C_2$  depends upon the dc coupling through  $R_b$ . Note further that the sideband current  $S_2$  depends upon the baseband coupling through  $R_b$ .

By proper filtering, the dc and baseband currents can be made to flow through separate resistors without changing the behavior of the limiting or carrier transfer functions. With respect to  $R_b$ , the equivalent circuits of Fig. 11 are then completely independent. If the baseband

resistance in Fig. 11(b) is changed,  $S_2$  will clearly change. But the carrier transfer function is undisturbed, since no change was made in Fig. 11(a). Therefore, the limiting is not completely determined by the slope of the carrier transfer function.

This behavior has been verified experimentally using a limiter similar to that of Fig. 7.

#### REFERENCES

1. Caruthers, R. S., Copper Oxide Modulators in Carrier Telephone Systems, B.S.T.J., **18**, April 1939, p. 315.
2. Peterson, E. and Hussey, L. W., Equivalent Modulator Circuits, B.S.T.J., **18**, January 1939, p. 32.
3. Arguimbau, L. B. and Granlund, J., *Interference in Frequency-Modulation Reception*, Res. Lab. Elec., Mass. Inst. of Tech., Report 42, Cambridge, Mass., 1949.
4. Kahn, L. R., Analysis of a Limiter as a Variable-Gain Device, Elec. Eng., **72**, December 1953, p. 1106.
5. Tucker, D. G., Linear Rectifiers and Limiters, Wireless Engr., **29**, May 1952, p. 128.
6. Seeley, S. W. and Avins, J., The Ratio Detector, RCA Review, **8**, June 1947, p. 201.

# Oxides of the 3d Transition Metals\*

By F. J. MORIN

(Manuscript received April 16, 1958)

*The magnetic, electrical and optical properties of the 3d metal oxides are examined for clues to the energy band structure. A tentative energy band scheme is proposed for the oxides of scandium, titanium and vanadium which suggests that the nonbonding 3d orbitals of neighboring cations overlap sufficiently to form a 3d conduction band. The 3d orbitals do not overlap in the oxides of the remaining 3d metals, with the consequence that the 3d electrons are in isolated energy states and electron transport occurs by electron exchange between cation neighbors and involves an activation energy. An energy level scheme for these latter oxides is calculated from simple electrostatics, and it is shown to agree with the observed electrical properties. Conduction in these oxides includes transport of high-mobility holes in the 2p band of the oxygen lattice and of low-mobility holes and electrons in the 3d levels of the cation lattice.*

## I. INTRODUCTION

The transition metals combine with other elements to form a host of compounds which are electronic conductors and which range in chemical bonding from ionic (oxides), through covalent (sulfides, arsenides) to metallic (carbides, nitrides). This range in valence character promises a great variety of energy band structures and transport processes and offers a rich field for theoretical and experimental investigation. No detailed determination of band structure or transport has been made for any of these compounds, and so they constitute an enormous gap in our knowledge of the solid state. Indeed, except for the 3d oxides, the semiconductor properties of transition metal compounds are largely unknown. In recent years the use of these oxides in electric<sup>1</sup> and magnetic<sup>2</sup> circuit elements and in heterogeneous catalysis,<sup>3</sup> as well as their importance in corrosion<sup>4</sup> have emphasized the necessity for a fundamental understanding of their properties. Now, from our point of view, the most fundamental aspect of a solid is its energy band structure. Therefore, it will

\* This article is a chapter from *Semiconductors*, edited by N. B. Hannay, to be published by Reinhold Publishing Corp., New York, as part of the American Chemical Society Monograph Series.

be the concern of this paper to provide a tentative energy band scheme for the  $3d$  oxides. The discussion will be restricted to the simple oxides and avoid the more complicated situations to be found in the oxide compounds, such as garnets, spinels and perovskites. Because of the scarcity of reliable experimental data on single-crystal material, the proposed scheme can only be regarded as tentative. At the same time, it provides a useful frame of reference for the planning and interpretation of future experiments.

We can begin by considering a relatively simple oxide, for example, zinc oxide, which is composed of ions having a closed-shell electronic configuration. The energy bands in zinc oxide arise, to a first approximation, from the filled  $2p$  levels of the  $O^-$  and the empty  $4s$  levels of the  $Zn^{++}$  which are broadened when the ions are brought together to form the solid. The filled  $2p$  band is separated from the empty  $4s$  band by a forbidden energy region. Thus, zinc oxide is a semiconductor. In the same way, a  $2p$  band and a  $4s$  band are expected to arise in the  $3d$  oxides. However, it is not easy to see what to expect from the partially filled  $3d$  levels of the cations, and we must attempt to answer such questions as (i) whether the  $3d$  wave functions overlap sufficiently to form a  $3d$  band in any of the oxides or if they do not overlap, so that the  $3d$  levels are localized energy levels, and (ii) the location in energy relative to the  $3d$  levels (or band) of the  $2p$  band of the anion lattice and the  $4s$  band of the cation lattice.

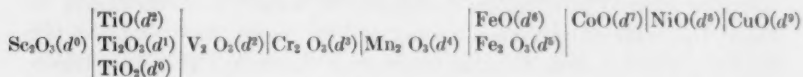
To learn something about the properties of a  $3d$  band it is instructive to consider the energy band situation in the  $3d$  metals. Energy band calculations have been made for some of these metals, using the cellular and the tight binding methods.<sup>5</sup> Usually it is found that the  $4s$  band is at least 10 ev wide and overlaps the  $3d$  band, which in nickel, for example, is about 2.8 ev wide. On the other hand, the  $3d$  band can hold ten electrons per atom, while the  $4s$  band can hold only two electrons. This difference in numbers accentuates the difference in bandwidth: per electron, the  $3d$  band in Ni is only  $\frac{1}{5}$  as wide as the  $4s$  band. The narrowness of the band means a high effective mass and low mobility for charge carriers in the band. In the metals, the electric current is carried largely by electrons in the  $4s$  band, but these have their mobility decreased by transitions to the  $3d$  band. In the  $3d$  oxides, the increased internuclear distance can be expected to reduce the  $3d$  bandwidth still further, because the overlap of the  $3d$  wave functions will be greatly reduced. This will result in a further increase in effective mass and lowering of mobility. Later in this paper it is shown that the  $4s$  band probably does not overlap



the 3d band in most of the oxides, so that electronic conduction can be entirely within the 3d band and thus involve carriers of very high effective mass and very low mobility. On the other hand, transport in a 4s or 2p band, should it occur, will probably be evidenced by the relatively high mobility of low-mass carriers in a wide band. Results of soft X-ray emission indicate the 2p band in oxides to be 10 to 20 ev wide.<sup>6</sup>

When the 3d band becomes extremely narrow it is no longer meaningful to assign a width to the band, and the 3d charge carriers can be considered to occupy energy levels localized on the cations. It was first pointed out by de Boer and Verwey<sup>7</sup> and by Mott<sup>8</sup> that this situation must exist in many oxides such as  $\text{Cr}_2\text{O}_3$ ,  $\text{Mn}_2\text{O}_3$ ,  $\text{Fe}_2\text{O}_3$ ,  $\text{CoO}$ ,  $\text{NiO}$  and  $\text{CuO}$  which are insulators when pure and stoichiometric and have room-temperature resistivities exceeding  $10^{10}$  ohm-cm. In order that conduction in the 3d levels can occur there must be present, in pure  $\text{NiO}$  for example, some  $\text{Ni}^{+++}$  and  $\text{Ni}^+$  ions (electron hole pair) which can move about by exchanging electrons with the normal  $\text{Ni}^{++}$  of the lattice. These excited states, however, can only exist at high temperatures. Nickel oxide can be made conducting at room temperature by introducing  $\text{Ni}^{+++}$  ions into the lattice, either by a departure from stoichiometry (vacant  $\text{Ni}^{++}$  sites) or by the substitution of  $\text{Li}^+$  ions for  $\text{Ni}^{++}$  ions. Wandering of the  $\text{Ni}^{+++}$  about the  $\text{Ni}^{++}$  lattice by electron exchange is possible even though the cation separation of  $3\text{\AA}$  is twice the cation diameter. Transport of this type is expected to involve an activation energy associated with self-trapping of the charge carriers. Mobility will be extremely low and increase exponentially with temperature. Such behavior is distinctly different from transport in a band where mobility decreases with increasing temperature because of lattice scattering. Semiconductors in which transport is by electron transfer do not show many of the effects which have been used for study of the band structure and transport in semiconductors like silicon or germanium. For example, no Hall effect, photoconductivity or carrier injection is observable, so that transport measurements depend primarily upon Seebeck effect and electrical conductivity.

The oxides series to be considered in this paper is the following:



The electronic configuration of the 3d shell is indicated. The 4s shell is assumed to be empty in all cases. The useful data concerning these oxides

are scant and most of them have been taken on ill-defined polycrystalline samples. However, from these data we shall try to derive a general energy band scheme for the  $3d$  oxides. Particular attention will be paid to transport and optical absorption, because these properties give an indication of  $3d$  bandwidth. Also, because the majority of the  $3d$  oxides are antiferromagnets, any correlation between their magnetic and electric properties will be considered. In Section II a brief description of their magnetic properties is given. In Section III crystal field theory is discussed in a simple way and used to explain the available absorption spectra of the  $3d$  oxides. In Section IV it is shown to be probable that a  $3d$  band having appreciable width exists in the oxides of scandium, titanium and vanadium, whereas in the remaining oxides the  $3d$  wave functions appear to be localized on the cations. In Section V the relative energies of the  $4s$ ,  $3d$  and  $2p$  levels are calculated. This energy level scheme is shown to fit fairly well the experimental results on NiO (Section VI) and  $\text{Fe}_2\text{O}_3$  (Section VII). Finally, in Section VIII, a few speculations are made concerning transport in the localized  $3d$  levels.

## II. ANTIFERROMAGNETISM<sup>9</sup>

The transition metal oxides are antiferromagnetic, a state characterized by an ordered antiparallel arrangement of electron spins. Since the electronic structure of a solid underlies its magnetic as well as its semiconducting properties, it is not surprising that experiments on oxides have shown a connection between these two properties. Two ways of explaining magnetism have been used—the energy band approach for transition metals, and the ionic approach for transition metal oxides. In transition metals, the magnetic atoms lie close together and there is an interaction between the spin moments of neighbors. This *exchange interaction* depends upon the overlap of atomic orbitals. For atoms having a partially filled  $3d$  shell the interaction may be either negative (antiparallel spins) or positive (parallel spins), depending upon interatomic distance, and changing from negative to positive with increasing distance. It is possible to divide an antiferromagnetic metal crystal into two magnetic sublattices, with each atom having nearest neighbors of opposite spins. The situation is different in transition metal oxides. In these, the magnetic cations are separated by anions. An example of this is MnO, whose sodium chloride structure is shown in Fig. 1. It is impossible for atom  $A'$  to have a spin direction antiparallel to that of all of its nearest neighbors, since one half of these  $B'$ ,  $C'$  and  $D'$  neighbors must have parallel spins to give an equal number of up and down spins in the lattice. There is one spin ordering, however, in which  $A'$  is antiparallel

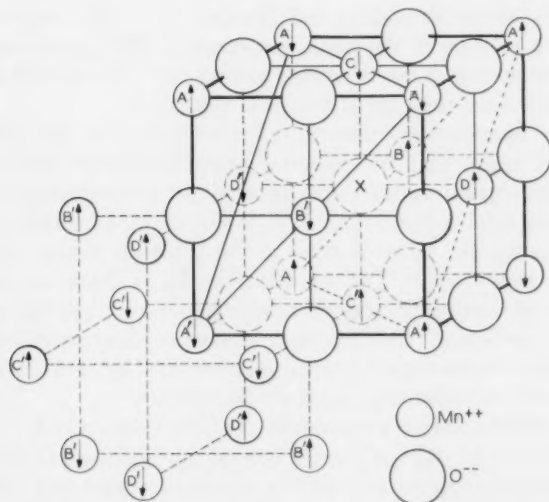


Fig. 1 — The sodium chloride structure and antiferromagnetic spin alignment in MnO. Spins in a (111) plane are parallel, with the (111) planes coupled antiparallel to each other. (After Gorter, Ref. 2.)

to all of its *next* nearest neighbors; this is shown in Fig. 1, and is the one actually found by neutron diffraction.

But now the antiparallel magnetic ions are separated by anions and the problem is to explain how exchange interaction can occur when electron orbits do not overlap. One way of approaching the problem was suggested by Slater.<sup>5</sup> Because of the exclusion principle, electrons of like spin will tend not to occupy the region between anion and cation. That is, electrons with + spin on a cation will repel electrons with + spin on the neighboring anion somewhat more than electrons with - spin. This repulsion will deform the outer electronic shell of the anion. In Fig. 1 it can be seen that anion X, for example, has three Mn<sup>++</sup> neighbors (C', B, D) in a (111) plane (dotted diagonals) and having + spin. Anion electrons with + spin will tend to collect on the side of the anion opposite from this plane of cations. This tendency will be aided if the (111) plane (solid diagonals) of cations (C, D', B') on the opposite side of X have - spins, and it may be seen in Fig. 1 that this is the case. Thus, the antiferromagnetic alignment between spins in the (111) planes represents a lower energy state than does the ferromagnetic alignment. A different quantitative description of the coupling between electron spins of two cations separated by an anion has been given by

Anderson<sup>10</sup> and by Yamashita and Kondo.<sup>11</sup> It is called *superexchange*. Since the  $p$  orbitals of the anion are directed  $180^\circ$  apart, exchange is found to be strongest when cations are on opposite sides of the anion and weakest when they are at  $90^\circ$  from the anion.

At high temperature, thermal vibrations prevent the antiparallel ordering of spins, and the material is paramagnetic. The transition temperature separating the paramagnetic and antiferromagnetic states is called the Néel temperature,  $T_N$ . A plot of  $T_N$  as a function of the number of spins per cation is given in Fig. 2 for the oxides which are of interest in this chapter. The transition at  $T_N$  is characterized by the occurrence of maxima in specific heat, magnetic susceptibility and the expansion coefficient. Electron spin resonance disappears below  $T_N$ . The direction of spin alignment can be determined by neutron diffraction and magnetic susceptibility, using single crystals.

In the rhombohedral sesquioxides  $\text{Ti}_2\text{O}_3$ ,  $\text{V}_2\text{O}_3$ ,  $\text{Cr}_2\text{O}_3$  and  $\text{Fe}_2\text{O}_3$  the cations are in pairs of closely spaced parallel layers, each pair of layers separated from the next pair by a layer of oxygen ions. The spatial arrangement of the ions projected onto a plane is shown in Fig. 3. Cation layers are represented by solid horizontal lines and anion layers by dotted horizontal lines. The heavy lines show how four cations are coordinated with each anion. Each cation participates in 18 cation-

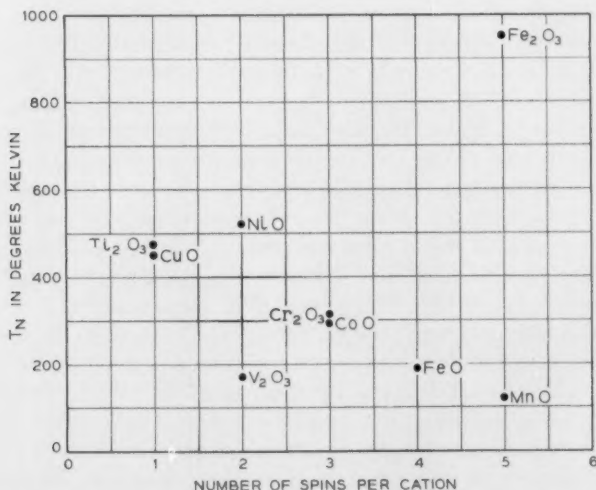


Fig. 2 — Plot of Néel temperature,  $T_N$ , against the number of spins per cation for some of the 3d oxides discussed in this paper.

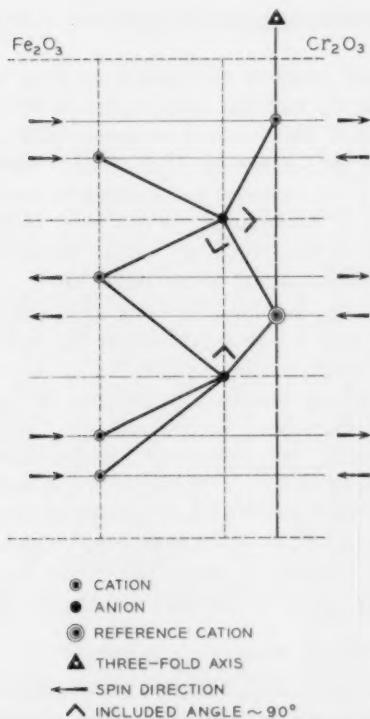


Fig. 3 — A projection onto a plane of the spatial arrangement of a group of ions in the rhombohedral sesquioxides. Cation layers are represented by solid lines and anion layers by dotted horizontal lines. The spin orientations of the cation layers are shown for  $\text{Fe}_2\text{O}_3$  and  $\text{Cr}_2\text{O}_3$ . The cation-anion-cation paths of superexchange are indicated by the heavy lines which do not include a  $90^\circ$  angle. (After Gilleo, Ref. 35.)

anion-cation configurations, one-third of which are shown in Fig. 2. Because half of the configurations include an angle of about  $90^\circ$ , only nine configurations are important in exchange interactions. The spin alignment shown in Fig. 3 was found by neutron diffraction<sup>12</sup> and by magnetic susceptibility.<sup>13</sup> Spin alignment has not been determined in  $\text{Ti}_2\text{O}_3$  and  $\text{V}_2\text{O}_3$ .

A second magnetic transformation is possible in the rhombohedral sesquioxides; that is, a change in the direction of spin alignment from perpendicular to the three-fold axis, as in Fig. 3, to parallel to this axis. According to neutron diffraction,<sup>12</sup> magnetic susceptibility<sup>14</sup> and spin

resonance,<sup>15</sup> this transformation occurs between  $-30^{\circ}\text{C}$  and  $-15^{\circ}\text{C}$  in  $\text{Fe}_2\text{O}_3$ .

Another interesting property of  $\text{Fe}_2\text{O}_3$  is its weak ferromagnetism,<sup>16</sup> which persists up to  $T_N$  and has been explained on the basis of symmetry considerations.<sup>17</sup> The internal magnetic field due to the ferromagnetism produces an anomalous Hall effect,<sup>18</sup> which depends upon the magnetization of the material and disappears above  $T_N$ . This Hall effect probably can be understood on the basis of the theory<sup>19</sup> for a similar effect found in the transition metals. It cannot be used as a measure of carrier concentration in the usual way.

Exchange interaction, besides producing spin alignment, also tends to move the ions in such a way as to increase the exchange, and thus it causes lattice deformation. The net number of antiparallel neighbors increases with decreasing temperature because the opposing effect of thermal vibration decreases; correspondingly, lattice deformation increases with decreasing temperature. At temperatures below  $T_N$ , the exchange coupling between the (111) planes of spin cause rhombohedral distortion in  $\text{MnO}$ ,  $\text{FeO}$  and  $\text{NiO}$  and tetragonal distortion in  $\text{CoO}$ .<sup>20</sup> Lattice distortion below  $T_N$  is also found in the rhombohedral sesquioxides. The exchange coupling between the cation layers contracts the lattice along the trigonal axis<sup>21</sup> but does not change the symmetry.

### III. ATOMIC ORBITALS AND THE CRYSTAL FIELD<sup>22</sup>

If the  $3d$  wave functions in an oxide do not overlap to form an energy band but remain concentrated near the cation, the cation, in effect, is isolated. It experiences, to a first approximation, only the electrostatic field due to the surrounding oxygens. Such a situation exists in the hydrated salts of the transition metals, for example the complex  $\text{Ni}(\text{H}_2\text{O})_6^{++}$ , where the cation is surrounded octahedrally by six  $\text{H}_2\text{O}$  molecules with the oxygens (the negative end of the water dipole) nearest the cation. Similarly, in  $\text{NiO}$ , which is a face-centered cubic structure, the negative oxygens are also arranged in a regular octahedron about the  $\text{Ni}^{++}$ . In fact, the optical absorption spectrum for  $\text{NiO}$  is very similar to that for the hydrated salt. Therefore, these considerations suggest that the same theories might be applied to the  $3d$  oxides as have been used in recent years to explain the optical properties of complex salts of  $3d$  ions. Conversely, this implies that, if a given oxide spectrum can be understood in this way, the  $3d$  wave functions in that oxide are concentrated near the cation and do not overlap to form a band. Accordingly, we will now see what available spectra indicate as to the possible existence of  $3d$  bands.



Three theories have been used to account for the properties of the complexes:

1. molecular orbital,<sup>23</sup>
2. valence bond,<sup>24</sup>
3. crystal field.

The advantage of the crystal field theory is that it can give information in a simple way about the excited states of the cation. Thus, it furnishes an explanation of the absorption spectra and promises to give insight into the electric and magnetic properties of the oxides.

The crystal field theory assumes a purely ionic model and considers the effect of the octahedrally coordinated negative anions on the 3d electrons of the central cation. The geometry of the cation and its surroundings is shown in Fig. 4. Suppose, at first, that the central ion has a single 3d electron with the quantum numbers  $l = 2$ ,  $s = \frac{1}{2}$ . There are five  $(2l + 1)$  d orbitals, all having the same energy in the isolated ion. The associated wave functions can be expressed as a function of radius,  $r$ , multiplied by functions with angular variation of the form  $xy/r^2$ ,  $yz/r^2$ ,  $zx/r^2$ ,  $(x^2 - y^2)/r^2$  and  $(2z^2 - x^2 - y^2)/r^2$ . These orbitals can be represented by the charge cloud distributions shown in Fig. 5. The  $xy$ ,  $yz$  and  $zx$  orbitals are designated as  $d\epsilon$  and the other orbitals as  $d\gamma$ . When negative anions are on the  $x$ ,  $y$ ,  $z$  axes, the negative charge clouds of the electrons in the  $d\gamma$  orbitals, which are directed at the anions, are

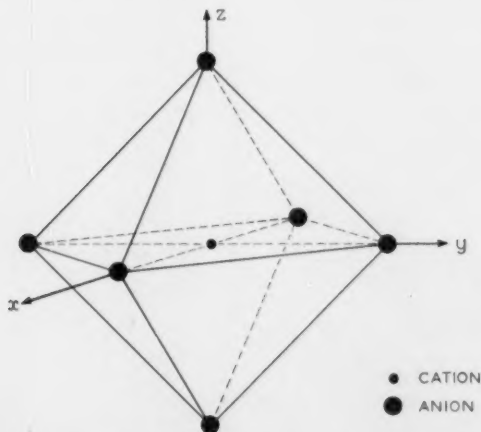


Fig. 4 — A regular octahedron of anions surrounding a central cation.



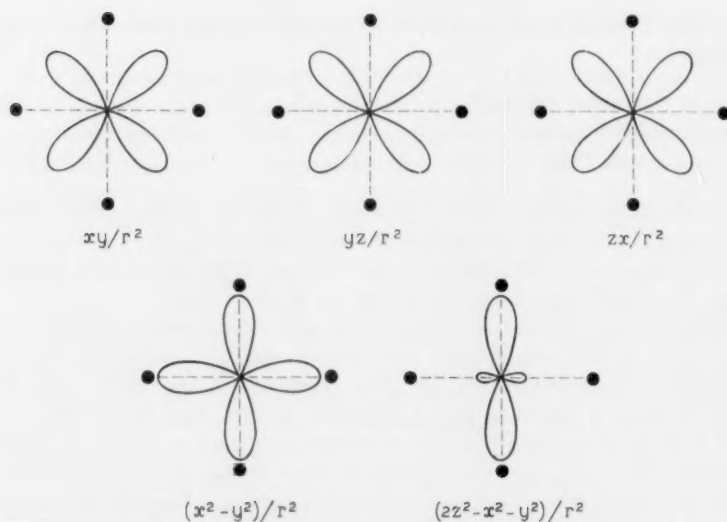


Fig. 5 — Angular distribution of the five 3d orbitals.

repulsed by the charge cloud of the anion. Thus, the  $d\gamma$  orbitals have a higher electrostatic energy than the  $d\epsilon$  orbitals, which are directed between the anions, and the ground state of the central ion is split as shown by the energy level diagram Fig. 6. This diagram is for an anion arrangement having cubic symmetry, which occurs in the rock salt oxides, and trigonal symmetry, which occurs in the rhombohedral sesquioxides. The trigonal case, since it involves a regular octahedron of anions, yields nearly the same excited states as does a cubic field, with an additional broadening of the absorption bands due to the small splitting of the  $d\epsilon$  levels shown.

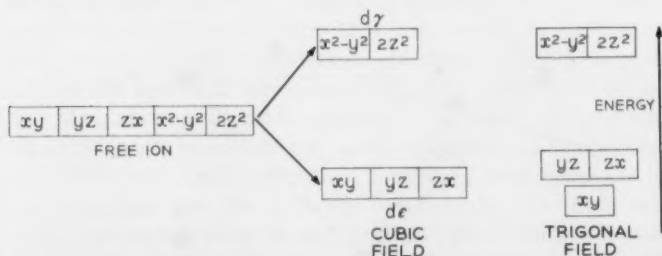


Fig. 6 — The ground state configuration of the five 3d orbitals: when in the free ion; in a crystal field of cubic symmetry (as in MnO, FeO, CoO and NiO); in a crystal field of trigonal symmetry (as in the rhombohedral sesquioxides).

An important rule concerning the splitting of these levels is that their centers of gravity in energy are not altered by the perturbation. That is,

$$3E_{\epsilon} + 2E_{\gamma} = 0. \quad (1)$$

Fixing the energy scale to be zero at the ground state of the free ion and defining  $10 Dq$  as the energy difference between the two levels which a single 3d electron can occupy when subjected to a cubic field gives, from (1)

$$E_{\epsilon} = -4Dq, \quad (2)$$

$$E_{\gamma} = +6Dq. \quad (3)$$

The relative positions of the excited states above the ground state, as determined for ions with electron configurations  $d^1$  to  $d^9$  subjected to a cubic field, are shown in Fig. 7. To the left in each diagram are shown the free ion ground states, labeled with their term symbols. In diagrams (c) and (d) are also shown the first free ion excited states having the same spin multiplicity as the ground states, and in (b) two excited levels for the free ion are depicted. To the right in each diagram are shown the ground state and excited states for the ions in the solid, as produced by a cubic crystal field of strength  $Dq$ . Configuration  $d^5$ , shown in (b), is plotted in a different way (after Orgel<sup>25</sup>) from the other configurations, because its excited states but not the ground state are split. In these diagrams, the first excited state of the ion corresponds to the excitation of an electron from the  $d_{\epsilon}$  to the  $d_{\gamma}$  levels. For example, in NiO, configuration  $d^8$ , the first excited state of the nickel ion is due to the electronic transition represented by the change in configuration  $d^6\epsilon d^2\gamma \rightarrow d^5\epsilon d^3\gamma$ , which leaves a hole in the normally filled  $d_{\epsilon}$  levels. The energy of these two states can be calculated as follows. The ground state,  $d^6\epsilon d^2\gamma$ , is located at  $(-4Dq \times 6 + 6Dq \times 2) = -12Dq$ . The excited state,  $d^5\epsilon d^3\gamma$ , is located at  $(-Dq \times 5 + 6Dq \times 3) = -2Dq$ . These energy levels are shown in Fig. 7(d). These transitions became allowed as a result of lattice vibrations<sup>26</sup> and hemihedral distortion.<sup>27</sup>

The available absorption spectra for some of the oxides are shown in Fig. 8, together with the location of the absorption maxima of a hydrated salt of the cation in aqueous solution. The close correspondence between maxima found in hydrated complex and oxide for  $\text{Fe}^{+++}$  and  $\text{Ni}^{++}$  indicates that the cation is isolated in the oxide as it is in the hydrated salt, and suggests that the 3d wave functions do not overlap in the oxides of the metals iron and nickel. The spectra of  $\text{Cr}_2\text{O}_3$ , however, show a slight shift to frequencies lower than that of the hydrated

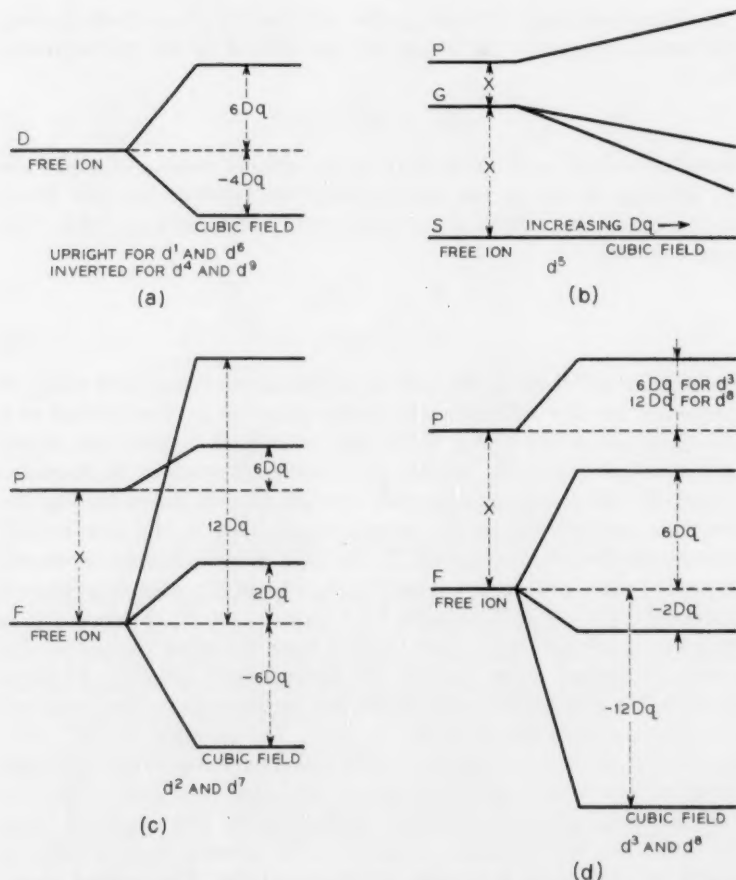


Fig. 7 — Positions of some excited states above the ground state for ions with electron configurations  $d^1$  to  $d^9$ . In each diagram the free ion is to the left and labeled with appropriate term symbols, the ion in a cubic field is to the right.

salt, indicating a slight overlap of the  $3d$  wave functions. This shift becomes very large in the spectra of  $Ti_2O_3$ , probably indicating that the cations in this oxide are not isolated as in their hydrated salts, and may be due to the overlap of  $3d$  orbitals, with the formation of a  $3d$  band.

From the spectra, the energy level diagrams of Fig. 7, and the values for the free ion excitation energies,  $X$  (from Ref. 28), the information given in Table I is obtained. The observed frequencies in the oxides,

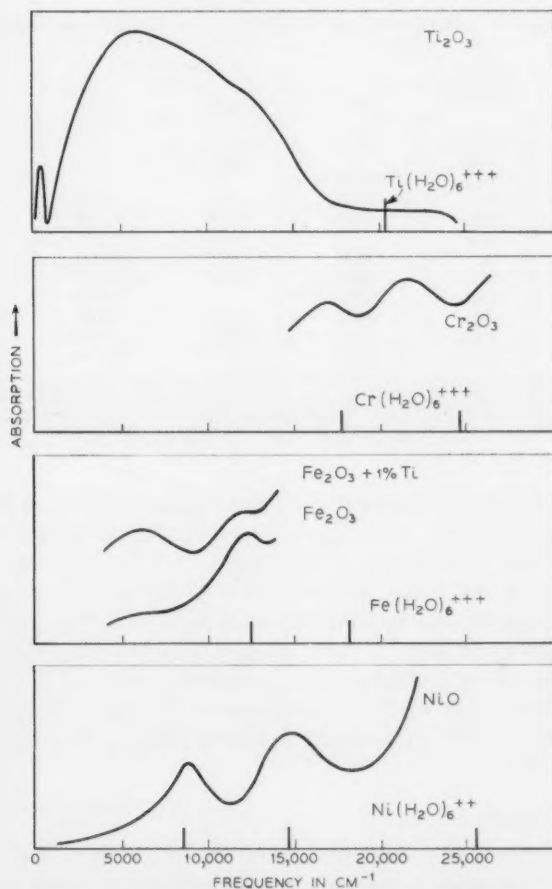


Fig. 8 — Absorption spectra for  $\text{Ti}_2\text{O}_3$ ,  $\text{Cr}_2\text{O}_3$ ,  $\text{Fe}_2\text{O}_3$  and  $\text{NiO}$  compared to the location of absorption bands for hydrated salts of the corresponding cations. ( $\text{Ti}_2\text{O}_3$  spectra after Pearson, Ref. 32;  $\text{Cr}_2\text{O}_3$  spectra after D. S. McClure, unpublished; hydrated salt spectra after Holmes and McClure, Ref. 43.)

shown in Column 3, were used to calculate the values of  $Dq$  in Column 4. In turn, these were used to obtain the calculated frequencies in the final two columns.

Another bit of information can be obtained from the absorption spectrum of  $\text{Fe}_2\text{O}_3$  containing titanium, Fig. 8, which shows an additional absorption band appearing at  $6100\text{ cm}^{-1}$  when one per cent titanium is added substitutionally. Titanium is a donor in  $\text{Fe}_2\text{O}_3$  and, in

TABLE I—SPECTRA OF OXIDES AND HYDRATED SALTS

Ion	Type of Comparison of Spectra	Frequencies			
		$\nu_1(\text{cm}^{-1})$	$Dq(\text{cm}^{-1})$	$\nu_2(\text{cm}^{-1})$	$\nu_3(\text{cm}^{-1})$
$\text{Ti}^{+++}$	exp.	6000	—	—	—
	calc.	—	600	—	—
	aq.	20300	—	—	—
$\text{V}^{+++}$	aq.	17800	—	25700	—
$\text{Cr}^{+++}$	exp.	16800	—	21300	> 27000
	calc.	—	1680	24000	30000
	aq.	17600	—	24700	—
$\text{Fe}^{+++}$	exp.	12200	—	> 15500	—
	aq.	12600	—	18200	24500
	exp.	8600	—	15400	> 22000
$\text{Ni}^{++}$	calc.	—	860	15500	26000
	aq.	8600	—	14700	25500

Comparison of spectra of oxides: exp. (measured); calc. (calculated from oxide data and diagrams Fig. 7); aq. (measured on hydrated salts). Data for the hydrated salts were taken from O. G. Holmes, and D. S. McClure.<sup>43</sup>

Note: 1 ev = 8100  $\text{cm}^{-1}$

this concentration, it is nearly all ionized to give  $\text{Ti}^{+++}$  and  $\text{Fe}^{++}$  ions. This absorption band, therefore, is probably due to the  $\text{Fe}^{++}$  ions, so that, from this information,  $Dq$  is 610  $\text{cm}^{-1}$  for the  $\text{Fe}^{++}$  environment in  $\text{Fe}_2\text{O}_3$ . Now the value of  $Dq$  for  $\text{Fe}^{++}$  in  $\text{Fe}(\text{H}_2\text{O})_6^{++}$  is 1000  $\text{cm}^{-1}$ , which can also be taken to be the value of  $Dq$  in  $\text{FeO}$ . The smaller value found for the  $Dq$  of  $\text{Fe}^{++}$  in  $\text{Fe}_2\text{O}_3$  suggests that the anions surrounding the  $\text{Fe}^{++}$  ion are at a greater distance from the  $\text{Fe}^{++}$  ion in  $\text{Fe}_2\text{O}_3$  than in  $\text{FeO}$ . This is just what one would expect to find if the conduction electron ( $\text{Fe}^{++}$ ) in  $\text{Fe}_2\text{O}_3$  polarized (repulsive polarization) the surrounding lattice.

#### IV. THE 3d BAND

The inner electronic configuration of the 3d metals is that of argon. As electrons are added to the argon core to build up the series, the nuclear charge is also increased. The electron cloud is thus subjected to an increasing nuclear charge but, on the other hand, the mutual repulsion of the electrons increases. The over-all decrease in ionic radius going from  $\text{Ca}^{++}(r = 0.99\text{\AA})$  to  $\text{Zn}^{++}(r = 0.83\text{\AA})$  indicates that nuclear attraction predominates over mutual repulsion, and the electron cloud becomes contracted. Therefore, if 3d wave functions overlap sufficiently to form a band in any 3d oxides, such band formation is to be expected at the beginning of the 3d series. Since, in fact, oxides such as  $\text{Cr}_2\text{O}_3$ ,  $\text{Fe}_2\text{O}_3$  and  $\text{NiO}$  normally are insulators, it is in the oxides of Sc, Ti and V that a 3d band might be expected. In the previous section it was sug-

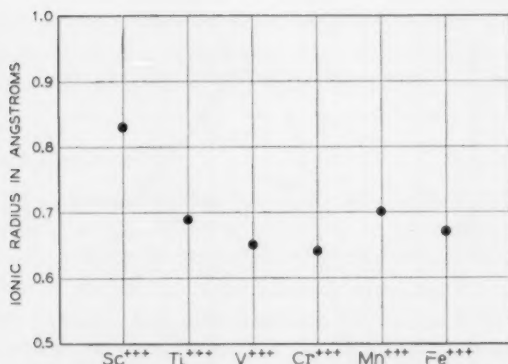


Fig. 9 — The rapid decrease in ionic radius with increasing atomic number for the first few members of the 3d series. This implies a contraction in the 3d wave functions and, therefore, a decrease in the amount by which they may overlap to form a 3d band. (Ionic radii from Goldschmidt, Ref. 44).

gested, on the basis of optical absorption, that there was evidence that such might be the case in  $\text{Ti}_2\text{O}_3$ . A comparison of the ionic radii of the trivalent cations plotted in Fig. 9 shows how rapidly the radius (and therefore the extent of the 3d wave functions) decreases with increasing atomic number in the first three members of the series. The abrupt increase in the radius of  $\text{Mn}^{+++}$  does not contradict this idea, since it is due to the addition of the first  $d\gamma$  electron. This, since it interacts with the electron cloud of the anion, increases the effective radius of the cation.<sup>29</sup> Since no transport information exists for  $\text{Sc}_2\text{O}_3$ , the data for the oxides of Ti and V will be examined for evidence of a 3d band.

#### 4.1 $\text{TiO}_2$ (Configuration $d^0$ )

In  $\text{TiO}_2$ , the electronic configuration of  $\text{Ti}^{++++}$  is  $3d^0$ , so that if a 3d band exists we expect it to be normally empty. We have, however, the possibilities of supplying electrons to the 3d band by excitation from imperfections or from the filled 2p band. Hall mobility of conduction electrons has been measured by Breckenridge and Hosler<sup>30</sup> in ceramic and single-crystal samples of  $\text{TiO}_2$  (rutile). The electrons were thermally excited from lattice defects introduced by slight reduction of the samples. Room-temperature mobility ranged from 0.1 to 1.0  $\text{cm}^2/\text{volt-sec}$  for all samples, the crystals tending to have the higher values. The mobility decreased in a normal way with increasing temperature. This mobility is 100 to 1000 times smaller than the electron mobility found in  $\text{ZnO}$ , and is precisely what is expected from transport in a 3d band.

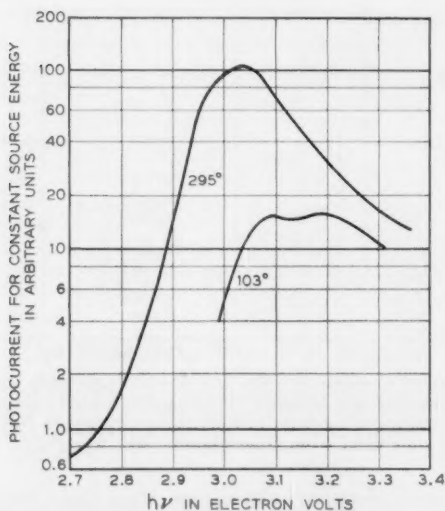


Fig. 10 — Photoconductivity in stoichiometric single crystal rutile. (After Cronmeyer, Ref. 31.)

Conductivity, photoconductivity and optical absorption have been measured by Cronmeyer<sup>31</sup> on pure stoichiometric single crystals of rutile. These data indicate an intrinsic forbidden energy gap of 3.05 ev. Above 1200°K, however, the conductivity temperature dependence suggests an increase in the energy gap to 3.67 ev. Presumably, the 3.05 ev represents an electronic transition from the filled  $2p$  band of the oxygen lattice to the empty  $3d$  band, which was indicated by Hall mobility to be the conduction band. The increase in the energy gap by as much as 0.6 ev at high temperature, suggests two possibilities: either the  $4s$  band of  $Ti^{++++}$  is near the upper edge of the  $3d$  band, and transitions to that band are also important, or the  $3d$  band is split into two sub-bands. Discussion in Section V shows that the  $4s$  band is probably too high in energy to play a role in conduction in the oxides. The second alternative —splitting of the  $3d$  band into  $d\epsilon$  and  $d\gamma$  sub-bands—seems to be the most likely.

The photoconductivity data, Fig. 10, only extend to 3.4 ev, presumably not high enough in energy to show the peak of the  $d\gamma$  band. At room temperature, photoconductivity shows a single absorption band having a maximum at 3.0 ev, probably the  $d\epsilon$  band, and a broad shoulder at higher energy which may be the beginning of the  $d\gamma$  band. The width of the main absorption band seems to be a few tenths of an



electron volt, which is very reasonable for a 3d band. At 103°K, this band gives an indication of splitting; this is not surprising, since the cation in the rutile structure is not at the center of a regular octahedron of anions.

#### 4.2 TiO (Configuration $d^2$ )

Besides TiO<sub>2</sub>, the only oxide for which there is fairly clear evidence of a 3d band is TiO. This oxide behaves like a metal, indicating the existence of a partially filled 3d band. According to Pearson,<sup>32</sup> room-temperature conductivity is 3500 ohm<sup>-1</sup>cm<sup>-1</sup> and increases slowly with decreasing temperature. Conductivity also decreases in a ratio of 7:12 when the oxygen content is increased from TiO<sub>0.7</sub> to TiO<sub>1.2</sub>. This is to be expected if the effect of changing the stoichiometry is to produce an equal change in the number of 3d electrons in the 3d band. If all the 3d electrons,  $6 \times 10^{22}$  for stoichiometric TiO, are assumed to be involved in conduction, the electron mobility can be calculated to be  $\mu = \sigma/qn = 3500 / (1.6 \times 10^{-19} \times 6 \times 10^{22}) = 0.36$  cm<sup>2</sup>/volt-sec at room temperature. This is comparable with the mobility in TiO<sub>2</sub> and suggests conduction in a 3d band in this case also.

#### 4.3 Ti<sub>2</sub>O<sub>3</sub> (Configuration $d^1$ ) and V<sub>2</sub>O<sub>3</sub> (Configuration $d^2$ )

Since these oxides contain, respectively, one and two 3d electrons per cation, metallic conduction is expected if a 3d band exists in them, just as in the case of TiO. Conductivity data for these oxides are shown in Figs. 11 and 12. The outstanding fact about these data is the large discontinuity in conductivity at  $T_N$  for a number of samples. (The lack of a discontinuity in some cases will be discussed later.) No other oxides have shown such behavior, and it is this behavior which suggests an energy band scheme that explains fairly well the information available for these oxides. To begin with, one expects the 3d band to be split by the crystal field into the  $d\gamma$  and  $d\epsilon$  sub-bands. It is proposed, further, that the  $d\epsilon$  band may be split by the magnetic exchange interaction into a lower filled band and an upper empty band. Thus, in a pure stoichiometric sample at temperatures below  $T_N$ , the Fermi level would be midway between the occupied  $d\epsilon$  band and the empty  $d\epsilon$  band. When the temperature of the sample is raised through  $T_N$ , the bands would collapse into a single partially filled band and cause metallic conduction. Sample A of V<sub>2</sub>O<sub>3</sub> behaves in this way. If it is assumed that carrier mobility does not change very much on going through  $T_N$ , and that the conductivity change is due only to the change in carrier concentration resulting from the collapsing of  $d\epsilon$  bands, the amount of discontinuity

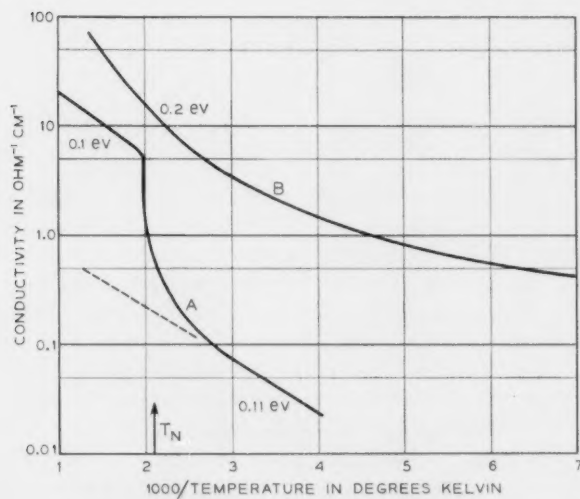


Fig. 11 — Conductivity of  $\text{Ti}_2\text{O}_3$  through the Néel temperature. (Sample A, Foëx and Loriens, Ref. 45; sample B, Pearson, Ref. 32.)

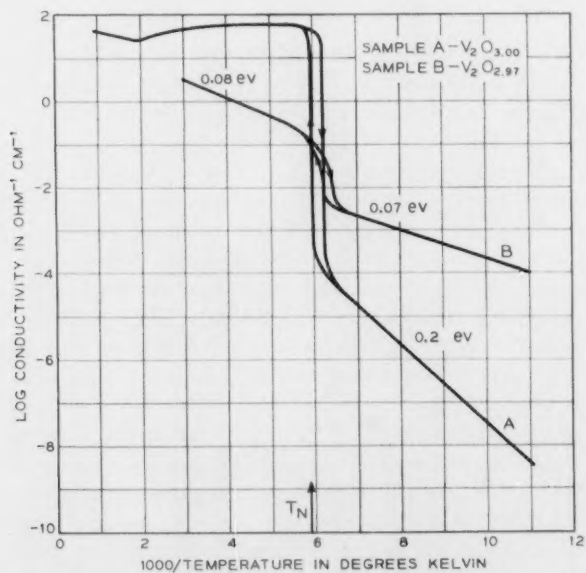


Fig. 12 — Conductivity of  $\text{V}_2\text{O}_5$  through the Néel temperature. (After Foëx, Ref. 46.)

to be expected in the conductivity of a pure stoichiometric sample can be estimated. This will be simply a factor of  $\exp(E_F/kT_N)$ , where  $E_F$  is taken to be the slope of the conductivity curve below  $T_N$ . For  $V_2O_3$  sample A, this factor is  $\exp(0.2/8.63 \times 10^{-5} \times 170) = 8 \times 10^5$ , which is very close to the measured discontinuity. For  $Ti_2O_3$  sample A, the factor is  $\exp(0.11/8.63 \times 10^{-5} \times 470) = 15$ , again very close to the observed discontinuity, although this sample does not show metallic conduction above  $T_N$ . A remarkable point about these two cases is that the Fermi energy is changed at the discontinuity by an amount considerably greater than the exchange energy  $kT_N$ .

If a sample departs from stoichiometry several effects can be imagined which would work to obscure the discontinuity: the odd, or missing, cations in the lattice will tend to decouple the spin system; they may break up the periodicity of the lattice and disrupt the 3d band; they will alter the conductivity by acting as donors or acceptors. Samples A and B of  $Ti_2O_3$  and  $V_2O_3$  sample B probably show these effects in varying degrees. With the band disrupted, transport probably occurs as in oxides such as NiO, and metallic conduction does not appear above  $T_N$ . The presence of donors or acceptors increases the conductivity below  $T_N$  and minimizes the effect of the magnetic transition on the conductivity.

An estimate of electron mobility for  $V_2O_3$  sample A above  $T_N$  gives  $\mu = \sigma/qn = 60/(8 \times 10^{22} \times 1.6 \times 10^{-19}) = 5 \times 10^{-3}$  cm<sup>2</sup>/volt-sec. Thus, mobility in a single crystal may be of the order of  $10^{-2}$  cm<sup>2</sup>/volt-sec, which is more than an order of magnitude less than in  $TiO_2$  so that the 3d band in  $V_2O_3$  is probably not much greater than  $kT$  in width at temperatures above  $T_N$ .

It seems reasonable to conclude from the considerations and results of this and the previous section that a 3d band exists in the oxides of scandium, titanium and vanadium, which probably goes to essentially zero width in chromium oxide. A schematic of this idea is shown in Fig. 13.

#### V. RELATIVE ENERGIES OF THE 4s, 3d AND 2p LEVELS

We saw in the last section that, of the 3d oxides, probably only those of Sc, Ti and V are like ordinary semiconductors in that their charge carriers are in energy bands. When we come to  $Cr_2O_3$  and the remaining 3d oxides we find an entirely new situation. The 2p and 4s bands are quite comparable to the bands in ZnO, for example, and can be represented on the usual one-electron energy diagram. However, the energy of conduction electrons and holes in the localized 3d levels must be

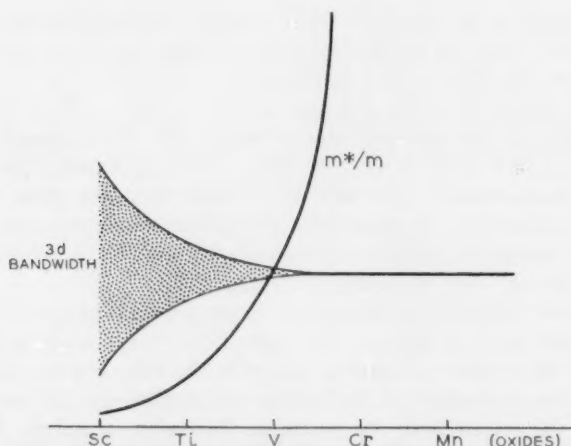
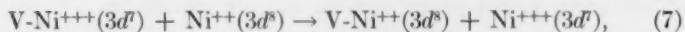
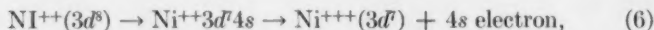
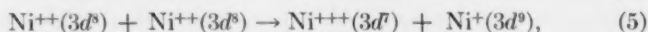
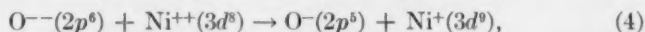


Fig. 13 — Schematic showing how 3d bandwidth goes to zero and effective mass,  $m^*/m$ , of charge carriers increases as 3d wave functions contract with increasing atomic number.

represented in a different way, since they are in excited states of the cation.

It is possible to find, in a very approximate way, the relative energies of the unbroadened 4s, 3d and 2p levels in an oxide by using data from the Born cycle, and spectroscopic data for the free ions and neglecting lattice polarization about an electron or hole. In Fig. 14, NiO is taken as an example to show how this is done.

Charge carriers are produced by the following reactions, in which the electronic states represented are separated by large distances in the crystal:



These reactions represent: (4) the formation of a hole in the 2p band and an electron in the 3d levels; (5) the formation of an electron-hole pair in the 3d levels; (6) the excitation of an electron to the 4s band and formation of a hole in the 3d levels; (7) the trapping of an electron at a lattice vacancy acceptor with the formation of a hole in the 3d

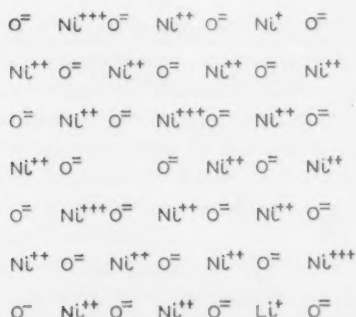


Fig. 14 — Lattice of NiO with  $\text{Ni}^{+++}$  acceptors near a cation vacancy and a substituted  $\text{Li}^+$ ,  $\text{Ni}^+$  electron and  $\text{Ni}^{+++}$  hole, and a  $\text{O}^-$  hole in the  $2p$  band.

levels; and (8) the trapping of an electron at a  $\text{Li}^+$  acceptor site with the formation of a hole in the  $3d$  levels. Consider first the energy necessary to remove an electron from  $\text{O}^{--}$  and place it on a distant  $\text{Ni}^{++}$  in the lattice, as shown by reaction (4). The total electron affinity of an oxygen atom ( $\text{O}$  going to  $\text{O}^{--}$ ), determined by the Born cycle, is repulsive and equals  $-7.5$  ev.<sup>33</sup> The affinity of  $\text{O}$  for the first electron is  $+2.2$  ev,<sup>34</sup> hence the negative affinity for both electrons is due to the affinity for the second electron ( $\text{O}^- \rightarrow \text{O}^{--}$ ), which therefore amounts to  $-9.7$  ev. This energy is plotted in Fig. 15 relative to the  $2p^5$  level plus a free electron on the left of the energy diagram. The ionization potential of  $\text{Ni}^+(3d^9)$  and the other spectroscopic data come from Ref. 28. This ionization potential is  $18.2$  ev, and it is plotted relative to the  $3d^8$  level in the diagram. (These energies are plotted with reversed signs, since in the process being investigated an electron is to be taken from  $\text{O}^{--}$  and placed on the  $\text{Ni}^{++}$ , and this is the reverse of the process for which the energies are quoted.) When the ions are brought together to form the lattice, the potential at the position of a positive ion due to all the other ions in the lattice is negative, and that at the position of the negative ion it is positive. As a result, the  $\text{O}^{--}$  level is depressed and the  $\text{Ni}^{++}$  level is raised (as shown in the diagram) by the amount of the Madelung potential<sup>35</sup> of NiO, which is  $23.8$  ev. Thus we find these levels moved to  $-14.1$  ev ( $2p^6$ ) and  $+5.6$  ev ( $3d^9$ ). The difference in energy of these two levels,  $19.7$  ev, is the energy of reaction (4), and it was arrived at by considering only free ion potentials, which are a measure of the energy necessary to remove an electron from a free ion out to infinity. In this process, the electron would experience the potential of the ion all the way to infinity. In the lattice, however, the process is carried out in a dielectric, so the energy required for the reaction is reduced by the di-

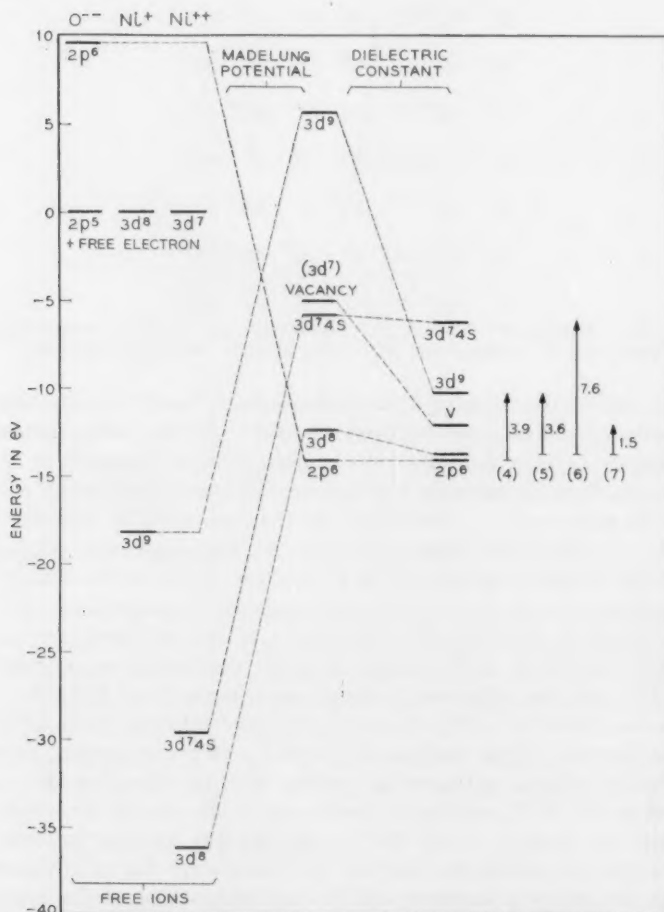


Fig. 15 — Energy level diagram calculated for NiO and showing the energy required for the reactions (4) through (7).

electric constant of NiO. Taking this constant to be about 5, the separation of the two levels is thus reduced to  $19.7/5 = 3.9$  eV, as shown on the diagram to the right in Fig. 15. This energy is probably reduced even further by broadening of the  $2p$  levels into a  $2p$  lattice band, so that the energy required to produce a free hole in the  $2p$  band and an electron in the  $3d$  levels is expected to be less than 3.9 eV, in NiO.

The next process of interest, given by reaction (5), is to take an electron

from a  $\text{Ni}^{++}$  and place it on another  $\text{Ni}^{++}$  far removed in the lattice. The  $3d^8$  level is located at  $-36.2$  ev, with respect to the  $3d^7$  level in the left of the diagram. Adding to this the Madelung potential raises it to  $-12.4$  ev. This lies  $18.0$  ev below the  $3d^9$  level calculated in a similar manner in the preceding paragraph. In the lattice, therefore, the transition will require  $18.0/5 = 3.6$  ev. Thus, on the right-hand side of the diagram the  $3d^8$  level is plotted  $3.6$  ev below the  $3d^9$  level which had been located in the first calculation.

Reaction (6) represents the transition of an electron from a  $\text{Ni}^{++}$  into the  $4s$  band. The first step in calculating the energy required for this process is to take an electron from the ground state,  $3d^8$ , to the first excited  $4s$  state, given by  $3d^7 4s$ . The location of this excited state with respect to the ground state is plotted to the left of the diagram, at  $-29.6$  ev, and in the center, at  $-5.8$  ev, by adding the Madelung potential, which places it  $6.6$  ev above the  $3d^8$  level. Thus, it required  $6.6$  ev to produce this excited state of the cation, which is a bound hole-electron pair. The additional energy required to separate this pair (essentially to remove the electron from the field of the cation) is given approximately by  $q^2/\epsilon a$ , where  $\epsilon$  is the dielectric constant and  $a$  is the distance between cations. This energy amounts to  $1.0$  ev, so that the energy required to free an electron from a cation and place it in a band of  $4s$  states is  $7.6$  ev. This is plotted with respect to the  $3d^8$  level at the right of the diagram. Due to broadening of the  $4s$  levels into a band, the actual separation will be reduced to something less than  $7.6$  ev.

Consider now the process (7), in which excess oxygen in the  $\text{NiO}$  lattice introduces vacant  $\text{Ni}^{++}$  lattice sites, which act as acceptors and produce conduction holes in the  $3d$  levels. The relative location in energy of such an acceptor level has been calculated by de Boer and Verwey,<sup>7</sup> although they neglected the effect of the dielectric constant of the solid. Their argument is as follows. Each vacant  $\text{Ni}^{++}$  site is surrounded by twelve  $\text{Ni}^{++}$  ions, and the situation to be considered is that in which two of these ions yield an electron each to form  $\text{Ni}^{+++}$  ions that compensate for the absence of the  $\text{Ni}^{++}$  ion. This is shown in Fig. 14. Each  $\text{Ni}^{+++}$  is surrounded by a normal lattice minus one  $\text{Ni}^{++}$  at a distance  $a\sqrt{2}/2$ , plus one positive charge ( $\text{Ni}^{+++}$ ) assumed to be at  $a\sqrt{2}$ , the greatest separation from the first  $\text{Ni}^{+++}$ . Hence, the potential at one  $\text{Ni}^{+++}$  site amounts to the normal Madelung potential plus  $2q^2/a\sqrt{2}/2 - q^2/a\sqrt{2} = 23.8 + 9.8 - 2.4 = 31.2$  ev. Thus, the level of this ion is raised  $7.4$  ev above that of the normal  $3d^8$  ions, as shown in Fig. 15. Considering the dielectric constant, the energy required to transfer an electron from a distant  $\text{Ni}^{++}$  ion to a  $\text{Ni}^{+++}$  next to a vacancy will be



$7.4/5 = 1.5$  ev. This level is plotted to the right in Fig. 15 with respect to the  $3d^8$  level. On this same basis, in reaction (8) a substitutional  $\text{Li}^+$  will produce a  $\text{Ni}^{+++}$  acceptor level at 0.5 ev above the  $3d^8$  level.

The calculated energies involving four of these reactions are shown by vertical arrows to the right of the diagram. They will be used in Sections VI and VII as guides in analyzing the data for  $\text{NiO}$  and  $\text{Fe}_2\text{O}_3$ . It will be seen in Section VI that these calculated energies are probably larger than the actual energies found in  $\text{NiO}$  by a factor of approximately two. Because of this, it is suggested that the dielectric constant of  $\text{NiO}$  is nearer to ten than to the value of five assumed in these calculations.

The Madelung potential is about the same for all the monoxides  $\text{CuO}$  through  $\text{TiO}$ . However, as we go from  $\text{CuO}$  to  $\text{MnO}$ , the second and third ionization potentials of the cation become progressively smaller. This raises the  $3d$  levels in energy with respect to the  $2p$  band. In  $\text{MnO}$ , for example, the  $3d^3$  level is about 4.5 ev above the  $2p$  band, as compared with a separation of 3.9 ev for the  $3d^9$  level in  $\text{NiO}$ , (assuming a dielectric constant of five in both cases). Therefore, conduction by  $2p$  holes may be less important in the oxides which are earlier in the series than is  $\text{NiO}$ .

Madelung constants are not available for the individual ions in the rhombohedral oxides where anions and cations do not occupy equivalent lattice sites. Therefore, the relative positions of the  $3d$  levels and the  $2p$  band in these oxides cannot be determined easily.

The location (as given in Ref. 22) of the  $3d^4 4s$  state with respect to the ground state in the free ion indicates that the  $4s$  band becomes farther removed from the  $3d$  levels as the charge on the cation is increased. Thus, the  $4s$  band probably plays no role in conduction in any of the oxides having cations with a charge  $+2$  or greater. The energy of the  $3d-3d$  transition is given by the difference in ionization energy of the ground states,  $3d^n$  and  $3d^{n+1}$ , divided by the dielectric constant of the oxide, as shown above for  $\text{NiO}$ . The only sesquioxide of interest here for which spectroscopic data are available is  $\text{Cr}_2\text{O}_3$  (which is one that does not have a  $3d$  band), for which the interval  $3d^3 - 3d^4$  is 18.6 ev. This is about the same as  $3d^8 - 3d^9$  in  $\text{NiO}$ .

The simple oxides, then, when pure and stoichiometric, can be expected to show conduction involving  $3d$  holes and electrons and  $2p$  holes, as a result of the processes shown in (4), (5) and (6). These are the processes corresponding to intrinsic conduction arising from excitation across the forbidden gap in the semiconductors discussed in earlier chapters. They will probably appear to be  $p$ -type, because conduction by high-mobility  $2p$  holes will predominate over the conduction by low-mobility electrons in the  $3d$  levels. On the other hand, when an oxide is impure or departs

from stoichiometry, as in (7) and (8), its type will depend, in addition to this intrinsic behavior, upon the particular valence state of the cation and upon the valence states available to the cation. It was shown above how excess oxygen or substitutional  $\text{Li}^+$  in  $\text{NiO}$  introduced  $\text{Ni}^{+++}$  acceptor levels near to the  $3d^8$  levels. In  $\text{TiO}_2$ , a departure from stoichiometry produces  $\text{Ti}^{+++}$  ions which are donors with respect to  $\text{Ti}^{++++}$  ions and introduce donor levels near to the  $3d$  band. In general, when the cations are in their lowest valence state, a defect will be such as to cause the oxide to be  $p$ -type and, when the cations are in their highest valence state, a defect will be such as to cause the oxide to be  $n$ -type. Oxides such as  $\text{Fe}_2\text{O}_3$ , in which the cations are in an intermediate valence state, can be made to go either into  $n$ -type or  $p$ -type. However, at high temperatures even impure oxides will tend towards  $p$ -type, because of conduction by high mobility  $2p$  holes. The energy levels discussed in Section III, of course, exist in addition to those shown in Fig. 15, but they are excited states which do not contribute to conduction.

#### VI. NICKEL OXIDE, $\text{NiO}$

Much more information is available for  $\text{NiO}$  than for the other cubic oxides, so it will be considered in detail. The structure of  $\text{NiO}$  has been described in Section II, and a possible electronic energy level scheme has

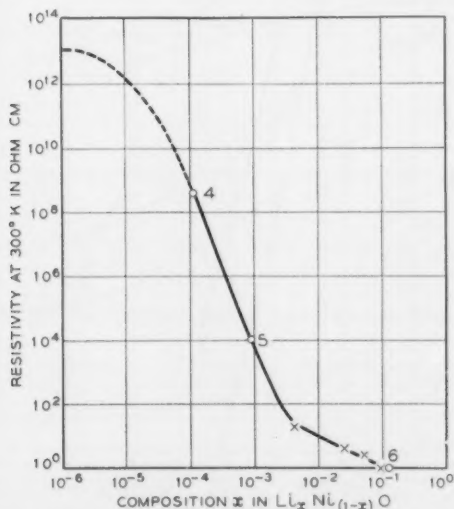


Fig. 16 — The resistivity of  $\text{NiO}$  as a function of Li content. (Sample o, Morin, Ref. 37; sample x, Verwey, Ref. 47.)

been discussed in Sections IV and V. Nickel oxide is a *p*-type semiconductor, apparently even when pure and stoichiometric, and no *n*-type form has been reported. Room-temperature resistivity for pure NiO is approximately  $10^{13}$  ohm-cm. This can be lowered to about 1 ohm-cm by the addition of Li, as shown in Fig. 16.

The transport data available for NiO are from Wright and Andrews,<sup>36</sup> taken on oxidized pure Ni films, and Morin,<sup>37</sup> taken on sintered bars

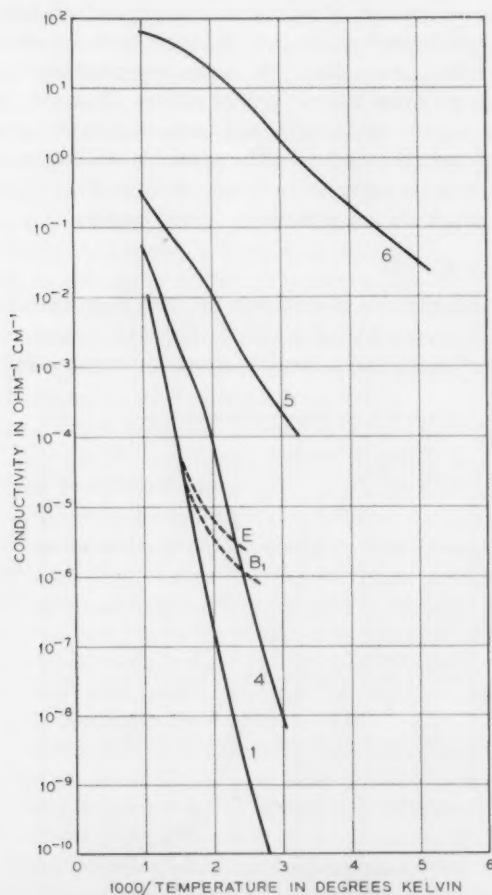


Fig. 17 — The conductivity of NiO (samples 1, B<sub>1</sub> and E) and of NiO containing Li (samples 4, 5 and 6; see Fig. 16). (Samples 1, 4, 5 and 6, Ref. 37; samples B<sub>1</sub> and E, Ref. 36.)

containing different amounts of Li and also presumed to vary in oxygen content. The data are shown in Figs. 17, 18 and 19. Samples 1 and B<sub>1</sub>, judging from the method of preparation (see Refs. 36 and 37), their color (pale green) and their electrical behavior, are considered to be the purest and most nearly stoichiometric. Conductivity and thermoelectric effect of the other samples approaches that for these at high temperatures. This occurs in a way typical of semiconductors when impurity centers become completely ionized and intrinsic conduction predominates. In the intrinsic range, both Hall effect and thermoelectric effect remain *p*-type.

According to the calculations of Section V, the energy level diagram, Fig. 20 can be constructed. Three parallel conduction processes are expected for NiO, from reactions (4) and (5):  $\sigma_1$ , high-mobility 2*p* holes;  $\sigma_2$ , low-mobility 3*d* holes; and  $\sigma_3$ , low-mobility 3*d* electrons, so that total conductivity is given by

$$\sigma = \sigma_1 + \sigma_2 + \sigma_3. \quad (9)$$

Carrier concentration will be given, choosing  $E_1 = 0$  as the zero of energy,

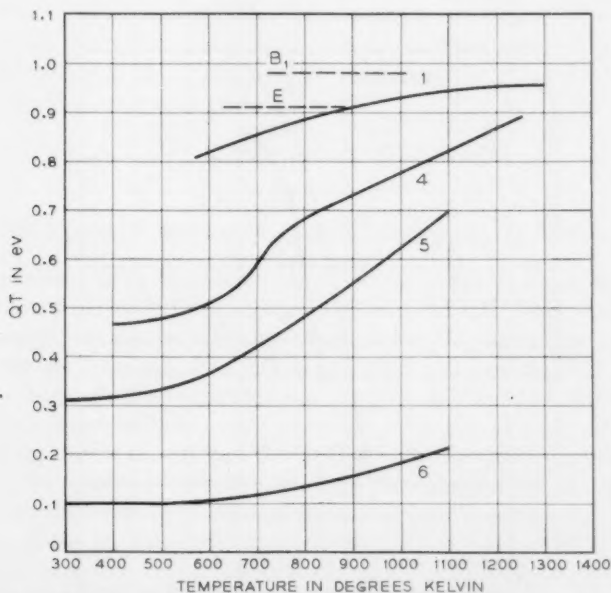


Fig. 18 — The Seebeck effect of NiO (samples 1, B<sub>1</sub>, and E) and NiO containing Li (samples 4, 5 and 6; see Fig. 16). (Samples 1, 4, 5 and 6, Ref. 37; samples B<sub>1</sub> and E, Ref. 36.)

by

$$p_1 = 2 \left( \frac{2\pi m^* kT}{h^2} \right)^{3/2} \exp(-E_F/kT), \quad (10)$$

$$p_2 = N \exp[-(E_F - E_2)/kT], \quad (11)$$

$$n_3 = N \exp[-(E_3 - E_F)/kT], \quad (12)$$

where  $N$  is the number of cations per cu cm. No Hall effect is expected from carriers  $p_2$  and  $n_3$  in localized  $3d$  levels, and none has been observed. Under conditions of sufficiently high purity and stoichiometry, or at elevated temperature where an appreciable fraction of the current is carried by  $2p$  holes, a Hall effect due to these holes is expected. Since such a Hall effect is due only to  $2p$  holes, but the current is carried by three kinds of carriers, the Hall coefficient is given by

$$R_H = \frac{p_1 \mu_1^2}{(p_1 \mu_1 + p_2 \mu_2 + n_3 \mu_3)^2 q}. \quad (13)$$

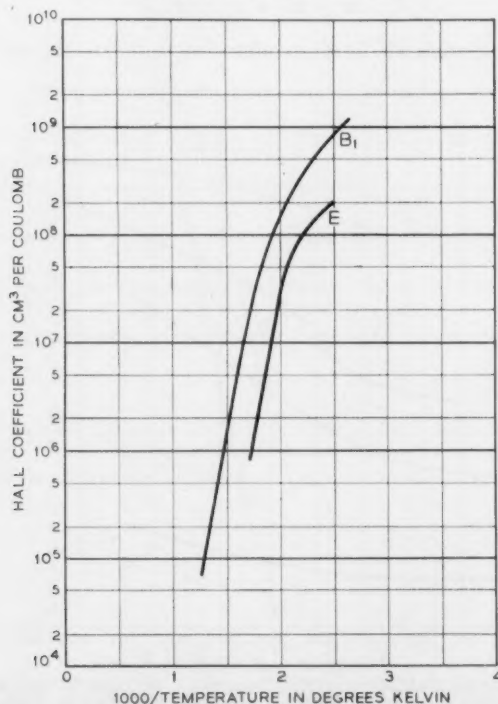


Fig. 19 — The Hall coefficient of NiO. (Samples B₁ and E, Ref. 36.)

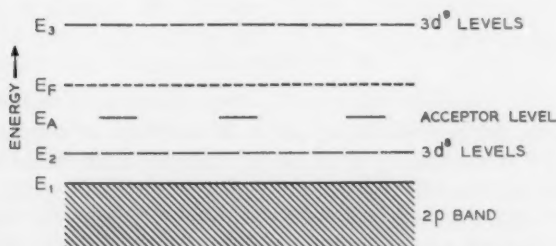


Fig. 20 — Energy level diagram proposed for NiO.

Because the 3d carriers give no Hall effect, their behavior has been studied using another tool, the Seebeck effect. In interpreting the Seebeck effect of the 3d oxides it is assumed that 3d carriers transport no kinetic energy, since they spend most of their time trapped on lattice sites. Therefore, there is no phonon drag effect associated with them, and their Seebeck effect is due only to their separation in energy from the Fermi level. For simplicity, it is assumed that there is no phonon drag effect associated with 2p holes. This assumption is probably a good one, since most of the data have been taken at elevated temperatures where this effect is at a minimum. The 2p holes are assumed to carry a kinetic energy of  $2kT$ . The over-all thermoelectric effect produced by three kinds of carriers is given by

$$QT\sigma = Q_1T\sigma_1 + Q_2T\sigma_2 - Q_3T\sigma_3 \quad (14)$$

or

$$QT\sigma = (E_F - E_1 + 2kT)\sigma_1 + (E_F - E_2)\sigma_2 - (E_3 - E_F)\sigma_3. \quad (15)$$

The problem is to determine three carrier concentrations and three mobilities from only three independent experiments. This complicated calculation will not be attempted here. Rather, two extreme situations will now be assumed: (a) NiO doped with so much Li that only 3d holes contribute to conduction, and (b) NiO so pure that 2p holes predominate in conduction.

In Fig. 16 it is shown that the conductivity changes in direct proportion to the amount of Li added, for high concentrations of Li. One infers from this that each Li added contributes one hole to conduction and that nearly all the impurity centers are ionized. Thus, conduction is entirely extrinsic and due to 3d holes. Under these simplified conditions, (9) and (14) reduce to

$$\sigma = \sigma_2 \quad (16)$$

and

$$QT = (E_F - E_s). \quad (17)$$

Knowing now, from (17), the location of the Fermi level with respect to the  $3d^8$  levels, the concentration,  $p_2$ , of  $3d$  holes can be calculated from equation (11) if the density of states,  $N$ , available to the holes is known. This is assumed to be the number of cations per cu cm of crystal, which is  $5.6 \times 10^{22}$  in NiO, since we are dealing with holes localized on the cations rather than in an energy band.

Now, with the measured  $\sigma$  and the hole concentration calculated in this way from  $QT$  for sample 6, the mobility,  $\mu_2$ , of the  $3d^8$  holes has been calculated and is plotted in Fig. 21. Both in magnitude and in temperature dependence this result is in accord with the ideas concerning transport in highly localized  $3d$  orbitals discussed in Sections I and VIII. Mobility at 300°K is 0.004 cm<sup>2</sup>/volt-sec and increases exponentially with temperature, with an activation energy of 0.10 ev. At low temperatures,  $QT$  (sample 6) is constant with temperature, at 0.10 ev. If the Fermi level lies halfway between the  $3d^8$  levels and the acceptor states, this would indicate then that the  $[\text{Li}^+ \text{Ni}^{+++}]$  acceptor levels are 0.20 ev above the  $3d^8$  levels in this sample, as compared with the value of 0.5 ev calculated in Section V and shown in Fig. 15. This suggests that a somewhat higher value should have been chosen for the dielectric constant

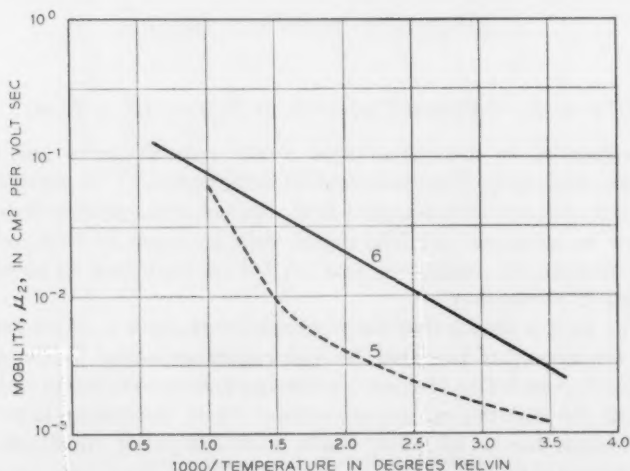


Fig. 21 — The mobility of holes in the  $3d^8$  levels of NiO obtained from measurement of conductivity and Seebeck effect. (See Fig. 16 for composition of samples 5 and 6.)



in these calculations. On the other hand, at the high density of defects existing in sample 6, interaction among defects may occur, and this would reduce their ionization energy.

A calculation of  $p_2$  and  $\mu_2$  has been made for sample 5, in which the  $[\text{Li}^+]$  is not in the range where  $\sigma_2$  is directly proportional to  $[\text{Li}^+]$  (see Fig. 16). The mobility results are shown as a dashed line in Fig. 21. At temperatures for which  $1/T$  is  $> 1.5 \times 10^{-3}$  they are parallel to, but much lower than, the results for sample 6; at higher temperatures they rise rapidly with temperature. It is assumed that transport of holes in the  $3d^8$  levels consists of  $\text{Ni}^{++}$  states drifting by jumps from one cation to a neighbor cation under the influence of the applied electric field. Therefore, it seems likely that mobility for this type of transport will be independent of impurity concentrations. In fact, this is suggested in Fig. 16 by the direct proportionality between conductivity and Li concentration for high-Li concentration. Consequently, the results on sample 5 probably mean that conduction in the  $2p$  band is appreciable in this sample and cannot be neglected in any sample containing less than a  $3 \times 10^{-3}$  atom fraction of Li (or approximately  $2 \times 10^{20}$  Li atoms/cm<sup>3</sup>). This suggests, further, that the  $2p$  band is not much farther below  $E_F$  than are the  $3d^8$  levels, in accord with the energy level diagram in Fig. 15.

Now assume the second situation, pure NiO, with only  $2p$  holes involved in conduction and  $\mu_1 = R_H\sigma$ . This result for sample *E* is shown in Fig. 22. Also, from this assumption (15) reduces to

$$QT = (E_F + 2kT). \quad (18)$$

From this,  $p_1$  can be calculated from (10), assuming  $m^*/m = 1$ . Since  $\sigma_1 = \sigma$ ,  $\mu_1$  can again be calculated. This has been done for samples 1 and B<sub>1</sub> and is also plotted in Fig. 22. There, the  $\mu_1$  results are compared with  $\mu_L$ , a lattice-scattering mobility considered reasonable for carriers in the wide band of an oxide. The high values found for  $\mu_1$  support the idea that  $2p$  holes are involved in the conduction. The temperature dependence that is found is quite far from a reasonable one, showing that the other conduction processes also play a role in these samples and cannot be neglected. These results, then, do not represent true  $2p$  hole mobility. They do indicate, however, that the energy level scheme proposed for NiO is a reasonable one. With this model in mind, the  $QT$  results of Fig. 18 can be understood in a qualitative way. At low temperature,  $E_F$  is midway between  $E_2$  and  $E_A$ , the acceptor levels, so that  $\sigma = \sigma_1 + \sigma_2$ . As the temperature is raised,  $E_F$  moves upward through  $E_A$  as acceptors become completely ionized, and  $QT$  increases accordingly.

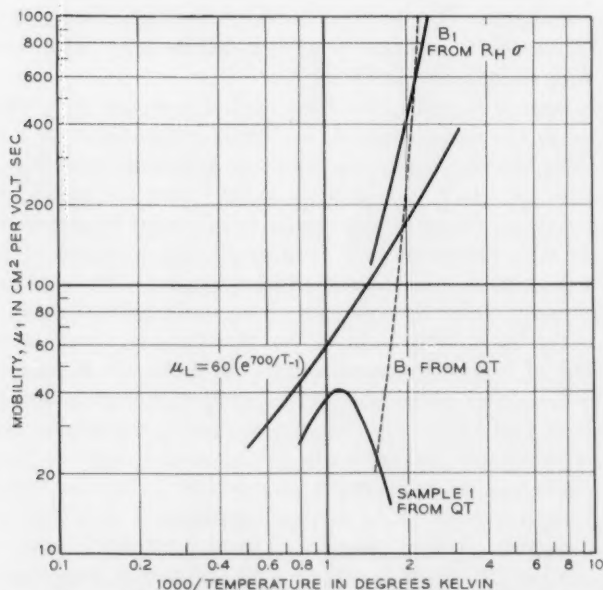


Fig. 22 — The mobility of holes in the  $2p$  band of stoichiometric NiO obtained from measurement of conductivity Hall effect and Seebeck effect.

Finally, at high temperatures, all the acceptors become ionized in the purest samples,  $E_F$  lies nearly midway between  $E_2$  and  $E_3$ , and  $QT$  becomes constant with temperature. Under these conditions,  $Q_2T\sigma_2 - Q_3T\sigma_3$  approaches zero, and  $QT$  is  $p$ -type, due largely to  $2p$  holes. At high temperature, measured  $QT$  for samples 1 and  $B_1$  is about 1 ev. Furthermore, the slope of the conductivity and Hall coefficient plots for these two samples is also about 1.0 ev at high temperature. These results suggest that the  $2p$  band is about 1.0 ev below the Fermi level in the intrinsic situation and, therefore, that the energy levels of Fig. 15 should be scaled down by a factor of one-half. This is also in fair agreement with the finding that the  $[Li^+ Ni^{+++}]$  acceptor level lies 0.2 ev above the  $3d^8$  level rather than 0.5 ev above, as was calculated. Evidently the value of ten would have been a better assumption for the dielectric constant of NiO.

#### VII. IRON OXIDE, $Fe_2O_3$

Magnetic and structural properties of the rhombohedral sesquioxide of iron have been described in Section II. Its semiconductor behavior is very similar to that of NiO, except that  $Fe_2O_3$  can exist as either  $n$ - or

*p*-type because the cation can take on a lower as well as a higher valence state. Oxidation causes pure  $\text{Fe}_2\text{O}_3$  to become *p*-type, probably due to the production of  $\text{Fe}^{++++}$  ions in the vicinity of cation vacancies. Reduction causes pure  $\text{Fe}_2\text{O}_3$  to become *n*-type, probably due to the production of excess cations in the form of  $\text{Fe}^{++}$  ions. With respect to the normal lattice of  $\text{Fe}^{++}$  ions,  $\text{Fe}^{++++}$  is a hole and  $\text{Fe}^{++}$  an electron. The room-temperature resistivity of  $\text{Fe}_2\text{O}_3$  is approximately  $10^{13}$  ohm-cm. This can be lowered to about 4 ohm-cm by the addition of Ti. It is known from an X-ray study<sup>38</sup> that, in the isomorphous compound  $\text{FeTiO}_3$ , the cations are  $\text{Fe}^{++}$  and  $\text{Ti}^{++++}$  at room temperature. Presumably then,  $\text{Ti}^{+++}$  in  $\text{Fe}_2\text{O}_3$  also ionizes, to give a 3d electron ( $\text{Fe}^{++}$ ) and a  $\text{Ti}^{++++}$  ion. The change in resistivity with added Ti is shown in Fig. 23. At high Ti concentrations the resistivity does not decrease with added Ti. This may be due to a shifting oxygen equilibrium with Ti content, which introduces acceptors that compensate for some of the donors.

Transport data<sup>18, 39</sup> available for  $\text{Fe}_2\text{O}_3$  have been obtained on sintered bars, and consist of conductivity, Fig. 24, and thermoelectric effect, Fig. 25. Samples 1 and A are identical in conductivity, but the thermoelectric effect shows that, due to the different conditions of sintering, sample 1 is *p*-type and sample A is *n*-type. The *QT* data also show that both of these samples tend to be *p*-type at high temperatures, which is in accord with (14) and the idea that the general energy level scheme which was developed in Section V for NiO is probably applicable to most of the simple oxides. However, in  $\text{Fe}_2\text{O}_3$ , *QT* is smaller in the intrinsic range than it is in NiO. This suggests that the 3d levels in  $\text{Fe}_2\text{O}_3$  are higher above the 2p band than they are in NiO.

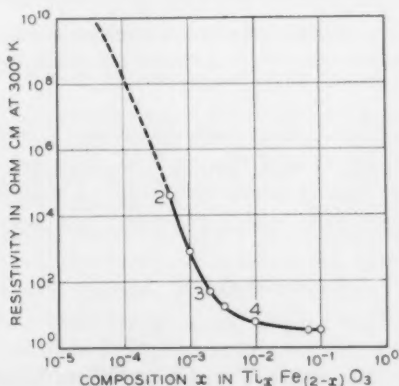


Fig. 23 — The resistivity of  $\text{Fe}_2\text{O}_3$  as a function of Ti content. (Ref. 18).

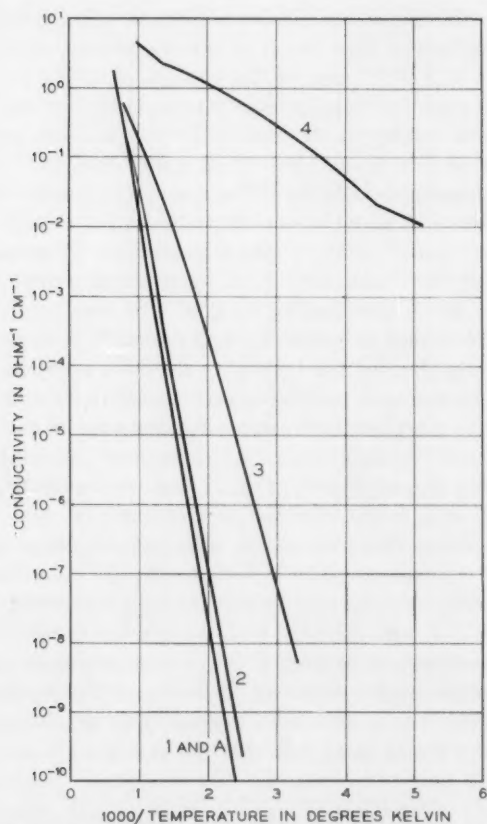


Fig. 24 — The conductivity of  $\text{Fe}_2\text{O}_3$  (samples 1, A and 2) and  $\text{Fe}_2\text{O}_3$  containing Ti (samples 3 and 4; see Fig. 23 for composition).

The situation in  $\text{Fe}_2\text{O}_3$ , where both donors and acceptors are present, is somewhat more complicated than in  $\text{NiO}$ . However, the simple case in which  $\text{Fe}_2\text{O}_3$  is so heavily doped with Ti that conduction is only by  $3d$  electrons can be dealt with. Such a situation is probably represented by sample 4, in which

$$\sigma = \sigma_3, \quad (19)$$

$$QT = (E_3 - E_F), \quad (20)$$

and  $n_3$  is given by (12), where  $N = 4.0 \times 10^{22} \text{ cm}^{-3}$ . From these equations and the data for sample 4,  $\mu_3$  has been determined. It is found to

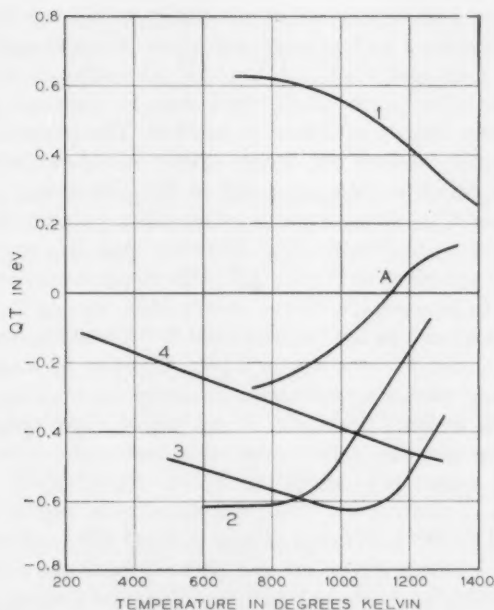


Fig. 25 — The Seebeck effect of  $\text{Fe}_2\text{O}_3$  (samples 1, A and 2) and  $\text{Fe}_2\text{O}_3$  containing Ti (samples 3 and 4; see Fig. 23 for composition).

be identical with the hole mobility for NiO sample 6, shown in Fig. 21. Thus the mobility of 3d electrons in  $\text{Fe}_2\text{O}_3$  is in accord, both in magnitude and temperature dependence, with the idea of transport in localized 3d levels. At  $T = 300^\circ\text{K}$ ,  $\mu_3 = 0.004 \text{ cm}^2/\text{volt-sec}$  and increases exponentially with temperature with an activation energy of 0.1 eV.

#### VIII. TRANSPORT IN THE 3d LEVELS

In Section V the processes were described by which conduction electrons or holes are created in the 3d levels. In NiO, for example, a 3d hole freed from a cation defect is presumed to consist of a  $\text{Ni}^{+++}$  with the cation neighbors for some distance around it normal  $\text{Ni}^{++}$  ions. The hole can diffuse about the cation lattice by exchanging an electron with a  $\text{Ni}^{++}$  neighbor until it moves next to an ionized defect site, receives an electron and becomes trapped, or until it becomes annihilated by recombination with a free electron. A net drift of such holes occurs when an external electric field is applied to the crystal, and thus an electric current is obtained.

In Sections VI and VII the mobility of 3d charge carriers was shown

to be very low and to increase exponentially with temperature. These results are consistent with a suggestion made 20 years ago by de Boer and Verwey<sup>7</sup> that conduction in NiO and  $\text{Fe}_2\text{O}_3$  occurs as outlined above and that a potential barrier exists which must be overcome for a charge carrier to jump from one cation to another. The potential barrier is assumed to arise because the charge carrier spends a time on a particular cation which is long compared to the vibrational frequency of the lattice, and this allows the ions surrounding a charge carrier to become displaced by its electric field. Evidence that this occurs in  $\text{Fe}_2\text{O}_3$  containing Ti was given in Section III. This displacement creates a field which tends to prevent the charge carrier from leaving its lattice site, and so the charge carrier has trapped itself.<sup>40, 41</sup> These ideas can be represented by two energy levels, one for a hole, the other for a normal cation neighbor, being moved up and down in energy by phonons. Whenever the two levels become the same, charge transfer can occur; thus, an exponential temperature dependence would be found for transport.

One might expect this charge transfer to depend upon the electron configuration of the cation. Using the diagram in Fig. 6 one can see that, if Hund's rule\* is followed, a hole in MnO and CuO will be in the  $d\gamma$  levels but a hole in FeO, CoO and NiO will be in the  $d\epsilon$  levels. Now, since the  $d\epsilon$  orbitals are directed between anions and towards neighboring cations while  $d\gamma$  orbitals are directed at anions, transport in the two levels may be quite different. For example, transport in the  $d\gamma$  levels, through an anion as in superexchange, will involve spin reversal below  $T_N$  regardless of crystal orientation. Transport in the  $d\epsilon$  levels will not involve spin reversal if it is in the (111) planes of parallel spins but will require spin reversal if it is perpendicular in the planes of parallel spin, and it so may produce an anisotropy in conductivity, at least within a magnetic domain.

If spin reversal is involved in transport, one might expect the activation energy for transport below  $T_N$  to be the sum of the polarization energy plus the exchange energy, and to be only the polarization energy above  $T_N$ . This would introduce an abrupt change in the temperature dependence of conductivity at  $T_N$ . Heikes and Johnston<sup>42</sup> believe that they have seen this effect in sintered samples of the oxides MnO, CoO, NiO and CuO which contained a large concentration of Li. However, the results described in Section VI for NiO containing Li (sample 6) show no change in the slope of mobility (Fig. 20) at  $T_N$ , but do show

\* That the  $d$  levels are filled with electrons in such a way as always to maintain a maximum spin multiplicity.



that the slope of conductivity is changing in this temperature region, because the Fermi level (Fig. 18) is beginning to move upward. It is evident that these questions can be answered only by transport studies on single crystals.

#### ACKNOWLEDGMENTS

The author wishes to thank P. W. Anderson, C. J. Ballhausere, A. D. Liehr and G. H. Wannier for many helpful discussions and N. B. Hannay for editing the manuscript.

#### REFERENCES

1. Becker, J. A., Pearson, G. L. and Green, C. B., *Trans. A.I.E.E.*, **65**, 1946, p. 711.
2. Gorter, E. W., *Proc. I.R.E.*, **43**, 1955, p. 1945.
3. Emmett, P. H., *Catalysis*, Vol. 2, Reinhold Publ. Co., New York, 1955.
4. Evans, U. R., *Metallic Corrosion, Passivity and Protection*, Edward Arnold & Co., London, 1937.
5. Slater, J. C., *Handbuch der Physik*, Vol. 19, J. Springer, Berlin, 1956.
6. Coster, D. and Kiestra, S., *Physica*, **14**, 1948, p. 175.
7. de Boer, J. H. and Verwey, E. J. W., *Proc. Phys. Soc. (London)*, **49**, 1937, p. 66.
8. Mott, N. F., *Proc. Phys. Soc. (London)*, **62A**, 1949, p. 416.
9. Nagamiya, T., Yosida, K. and Kubo, R., *Phil. Mag. Suppl.* **4**, 1955, p. 1.
10. Anderson, P. W., *Phys. Rev.*, **79**, 1950, p. 350.
11. Yamashita, J. and Kondo, J., *Phys. Rev.* **109**, 1958, p. 730.
12. Shull, C. G., Stauser, W. A. and Wollan, E. O., *Phys. Rev.*, **83**, 1951, p. 333; Brockhouse, B. N., *J. Chem. Phys.* **21**, 1953, p. 961.
13. McGuire, T. R., Scott, E. J. and Grannis, F. H., *Phys. Rev.* **102**, 1956, p. 1000.
14. Néel, L. and Pauthonet, R., *Comptes Rendus*, **234**, 1952, p. 2172.
15. Anderson, P. W., Merritt, F. R., Remeika, J. P. and Yager, W. A., *Phys. Rev.* **93**, 1954, p. 717.
16. Néel, L., *Ann. de Phys.* **4**, 1949, p. 249.
17. Dzyaloshinski, J. B., *J.E.T.P. (USSR)*, 1957, p. 1547; and *J. Phys. Chem. Solids*, **4**, 1958, p. 241.
18. Morin, F. J., *Phys. Rev.*, **83**, 1951, p. 1005.
19. Karplus, R. and Luttinger, J. M., *Phys. Rev.*, **95**, 1954, p. 1154.
20. Smart, J. S. and Greenwald, S., *Phys. Rev.* **82**, 1951, p. 113; Kanamori, J., *Prog. Theo. Phys.*, **17**, 1957, pp. 177 and 197.
21. Greenwald, S., *Nature*, **168**, 1951, p. 379.
22. Moffitt, W. and Ballhausen, C. J., *Ann. Rev. Phys. Chem.*, **1**, 1956, p. 197.
23. Van Vleck, J. H., *J. Chem. Phys.*, **3**, 1935, p. 807.
24. Pauling, L., *The Nature of the Chemical Bond*, Cornell Univ. Press, Ithaca, N. Y., 1948.
25. Orgel, L. E., *J. Chem. Phys.*, **23**, 1955, p. 1004.
26. Van Vleck, J. H., *J. Phys. Chem.*, **41**, 1941, p. 67.
27. Ilse, F. E. and Hartmann, H., *Z. für Physik. Chem.*, **197**, 1951, p. 239.
28. *Atomic Energy Levels*, N. B. S. Circular 467, Vols. 1949 and 1952.
29. Van Santen, J. H. and Van Wieringen, J. S., *Rec. Trav. Chem.*, **71**, 1952, p. 420; Hush, N. S. and Price, M. H. L., *J. Chem. Phys.*, **28**, 1958, p. 244.
30. Breckenridge, R. G. and Hosler, W. R., *Phys. Rev.*, **91**, 1953, p. 793.
31. Cronmeyer, D. C., *Phys. Rev.*, **87**, 1952, p. 376.
32. Pearson, A. D., M. I. T. Lab for Insul. Res. Tech. Report 120, 1957.
33. Sherman, J. J., *Chem. Revs.* **11**, 1932, p. 93.
34. Lozier, W. W., *Phys. Rev.*, **46**, 1934, p. 268.
35. Gilileo, M. A., *Phys. Rev.* **109**, 1958, p. 777.



36. Wright, R. W. and Andrews, J. P., Proc. Phys. Soc. (London), **62A**, 1949, p. 446.
37. Morin, F. J., Phys. Rev., **93**, 1954, p. 1199.
38. Barth, T. F. W. and Posnjak, E., Z. Krist. **88**, 1934, p. 265.
39. Morin, F. J., Phys. Rev., **93**, 1954, p. 1195.
40. Mott, N. F. and Gurney, R. W., *Electronic Processes in Ionic Crystals*, Clarendon Press, Oxford, England, 1950.
41. Yamashita, J. and Kunosawa, T., J. Chem. Phys. Solids, **5**, 1958, p. 34.
42. Heikes, R. R. and Johnston, W. D., J. Chem. Phys., **26**, 1957, p. 582.
43. Holmes, O. G. and McClure, D. S., J. Chem. Phys., **26**, 1957, p. 1686.
44. Goldschmidt, V. M., *Internationale Tabellen zur Bestimmung von Kristallstrukturen*, Vol. 2, Berlin, 1935.
45. Foëx, M. and Lorient, J., Comptes Rendus, **226**, 1948, p. 901.
46. Foëx, M., J. des Rech. du C.N.R.S., **21**, 1952, p. 237.
47. Verwey, E. J. W., Chem. Weekblad, **44**, 1948, p. 705.

## Recent Monographs of Bell System Technical Papers Not Published in This Journal\*

ANDERSON, O. L.

**Cooling Time of Strong Glass Fibers**, Monograph 2943.

ARCHER, R. J.

**Optical Measurement of Film Growth on Silicon and Germanium Surfaces**, Monograph 2962.

BACKENSTOSS, G.

**Conductivity Mobilities of Electrons and Holes in Heavily Doped Silicon**, Monograph 2944.

BAKER, A. N., and WEBBER, D. S.

**Hydrogen Vibration Spectra of Rochelle Salt**, Monograph 2963.

BEMSKI, G., see Bittmann, C. A.

BITTMANN, C. A. and BEMSKI, G.

**Lifetime in Pulled Silicon Crystals**, Monograph 2945.

BOZORTH, R. M.

**Magnetism**, Monograph 2942.

D'ASARO, L. A.

**Field Emission from Silicon**, Monograph 2946.

DISTLER, R. J. and STURZENBECKER, C.

**A Magnetic Amplifier Voltage-Current Overload Protection Circuit**, Monograph 2947.

EGAN, T. F., see Hermance, H. W.

\* Copies of these monographs may be obtained on request to the Publication Department, Bell Telephone Laboratories, Inc., 463 West Street, New York 14, N. Y. The numbers of the monographs should be given in all requests.

FELDMANN, W. L., see Pearson, G. L.

FRISCH, H. L.

**An Approach to Equilibrium, Monograph 2948.**

FULLER, C. S.

**Some Analogies Between Semiconductors and Electrolyte Solutions, Monograph 2961.**

FULLER, C. S. and LOGAN, R. A.

**Effect of Heat Treatment Upon Electrical Properties of Silicon Crystals, Monograph 2949.**

GILLES, M. A.

**Superexchange Interaction Energy for  $\text{Fe}^{3+}\text{-O}^{2-}\text{-Fe}^{3+}$  Linkages, Monograph 2951.**

GROSSMAN, A. J.

**Synthesis of Tchebycheff Parameter Symmetrical Filters, Monograph 2964.**

HERMANCE, H. W. and EGAN, T. F.

**Examination of Electrical Contacts by Plastic Replica Method, Monograph 2952.**

INGRAM, S. B.

**An Electrical Engineer's World—1957, Monograph 2931.**

JACCARINO, V., see Shulman, R. G.

LIEHR, A. D.

**Variation of Ethylene  $\pi$ -Electronic Energy Under Nuclear Displacements, Monograph 2953.**

LOCKWOOD, W. H., see Peters, H.

LOGAN, R. A. and PETERS, A. J.

**Effect of Oxygen on Etch-Pit Formation in Silicon, Monograph 2954.**

LOGAN, R. A., see Fuller, C. S.

LUNDY, W. R.

**Negative Impedance Circuits—Some Basic Relations and Limitations**, Monograph 2955.

MC DAVITT, M. B.

**6000-mc/sec Radio Relay System for Broad-Band Long-Haul Service**, Monograph 2956.

PEARSON, G. L., READ, W. T., JR. and FELDMANN, W. L.

**Deformation and Fraction of Small Silicon Crystals**, Monograph 2933.

PETERS, A. J., see Logan, R. A.

PETERS, H. and LOCKWOOD, W. H.

**Bonding Polyethylene to Rubber, Brass and Brass-Plated Metals**, Monograph 2932.

PRINCE, E.

**Crystal and Magnetic Structure of Copper Chromite**, Monograph 2960.

READ, W. T., JR.

**Dislocation Theory of Plastic Bending**, Monograph 2934.

READ, W. T., JR., see Pearson, G. L.

RONGVED, L. and FRASIER, J. T.

**Displacement Discontinuity in the Elastic Half-Space**, Monograph 2957.

SHULMAN, R. G. and JACCARINO, V.

**Nuclear Magnetic Resonance in Paramagnetic  $M_nF_2$** , Monograph 2958.

STURZENBECKER, C., see Distler, R. J.

WEBBER, D. S., see Baker, A. N.

## Contributors to This Issue

THOMAS M. BURFORD, B.S. in E.E., 1952, Washington University; M.S., 1953, and Ph.D., 1955, University of Wisconsin; Bell Telephone Laboratories, 1955—. Mr. Burford has been engaged in military systems analysis and mathematical research with application to communications. Member I.R.E., Sigma Xi.

IRA JACOBS, B.S., 1950, College of the City of New York; M.S., 1952, and Ph.D., 1955, Purdue University; Bell Telephone Laboratories, 1955—. Mr. Jacobs has concentrated on general systems analysis of military systems, including work on waveguides, propagation in non-uniform and anisotropic media, airborne radar display, missile trajectory shaping. Member American Physical Society, I. R. E., Phi Beta Kappa, Sigma Xi, Sigma Pi Sigma.

PAUL KISLIUK, B.S., 1943, Queens College; M.A., 1947, and Ph.D., 1952, Columbia University; Brookhaven Laboratory, 1947-48; Bell Telephone Laboratories, 1952—. Mr. Kisliuk has been engaged in research in contact and surface physics. Member American Physical Society, Sigma Xi.

DANIEL LEENOV, B.S., 1943, George Washington University; S.M., 1948, and Ph.D., 1951, University of Chicago; University of Chicago, 1952-55; University of Florida, 1955-56; Bell Telephone Laboratories, 1956—. Mr. Leenov has been engaged in testing and theory of microwave diodes and diode amplifiers. He took part in the National Defense Research Committee rocket research project at George Washington University in 1943-45. Member American Physical Society, Sigma Xi, Gamma Alpha.

JACK M. MANLEY, B.S. in E.E., University of Missouri, 1930; Columbia University, 1934; Bell Telephone Laboratories, 1930—. For a number of years, Mr. Manley was concerned mainly with theoretical and experimental studies of nonlinear electric circuits. Beginning in 1945, he spent about ten years working on new multiplex methods for

communication systems, and had a part in the first PCM trials in 1947. In 1956, he joined the group concerned with transmission line research. Senior member I.R.E., member A.I.E.E., American Association for the Advancement of Science, Sigma Xi.

F. J. MORIN, B.S. and M.S., 1939 and 1940, University of New Hampshire; University of Wisconsin, 1940-41; Bell Telephone Laboratories, 1941—. During World War II, Mr. Morin was engaged in research on elemental and oxide semiconductors and the development of thermistor materials. Since that time he has worked on fundamental investigations into the mechanism of conduction in silicon, germanium and oxide semiconductors. Mr. Morin is a member of the American Chemical Society and the American Physical Society.

GORDON RAISBECK, B.A., 1944, Stanford University; Ph.D., 1949, Massachusetts Institute of Technology; Bell Telephone Laboratories, 1949—. Mr. Raisbeck's early work at Bell Laboratories was in research in acoustics and underwater sound. From 1950 to 1953 he concentrated on research in transistor circuits and then took his present post in charge of a group engaged in transmission line research. Throughout his Laboratories career, Mr. Raisbeck has done additional work on information theory. He was a Rhodes Scholar at Oxford University in 1947. Senior member I.R.E.; member American Mathematical Society, Mathematical Association of America, Society for Industrial and Applied Mathematics, American Management Association, Sigma Xi.

C. L. RUTHROFF, B.Sc. in E.E., 1950, and M.A., 1952, University of Nebraska; Long Lines Department of the American Telephone and Telegraph Company, 1946-52; Bell Telephone Laboratories, 1952—. Mr. Ruthroff was a central office craftsman with Long Lines in Lincoln, Nebraska. Since transferring to Bell Laboratories, he has been a member of the Radio Research Department and has worked on FM problems.

WARREN SEMON, B.S., 1944, University of Chicago; M.A., 1948, and Ph.D., 1954, Harvard University. Mr. Semon is assistant director of the Harvard University Computation Laboratory and director of the University computation facility. He is also a lecturer on applied mathematics at Harvard and was an instructor in mathematics at Hobart College. Member I.R.E., Association for Computing Machinery, Society for Industrial and Applied Mathematics, Harvard Engineering Society.

ARTHUR UHLIR, JR., B.S., 1945, and M.S. in Ch.E., 1948, Illinois Institute of Technology; S.M., 1950, and Ph.D., 1952, University of Chicago; Armour Research Foundation, 1945-48; Bell Telephone Laboratories, 1951—. Mr. Uhler has worked on point-contact transistor theory, semiconductor surface protection and electrochemical properties of semiconductors and has developed an electrolytic micromachining technique of metals and semiconductors. He is now working on microwave semiconductor devices. Member I.R.E., American Physical Society, Sigma Xi, Phi Lambda Upsilon, American Association for the Advancement of Science.

HANS-GEORG UNGER, Dipl. Ing., 1951, and Dr. Ing., 1954, Technische Hochschule, Braunschweig (Germany); Siemens and Halske (Germany), 1951-55; Bell Telephone Laboratories, 1956—. Mr. Unger's work at Bell Laboratories has been in research in waveguides, especially circular electric wave transmission. He holds several foreign patents on waveguides and has published in German and American technical magazines. Member I.R.E., N.T.G. (German Communication Engineering Society).





